The Collision Dynamics of OH(A)+H_2

A thesis submitted for the degree of Doctor of Philosophy

Physical and Theoretical Chemistry

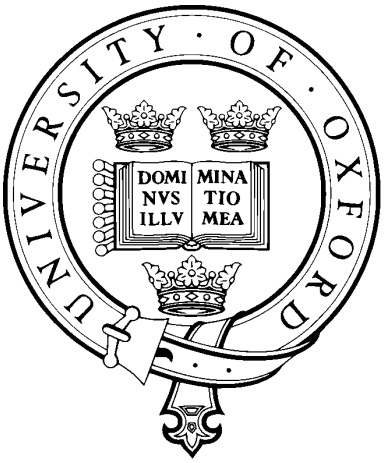

Scott Andrew Seamons

Jesus College, University of Oxford

Trinity Term, 2015

The Collision Dynamics of OH(A)+H_2

Scott Andrew Seamons, Jesus College
A thesis submitted for the degree of Doctor of Philosophy
Trinity Term, 2015

Abstract

This thesis presents a joint experimental and theoretical study of a bimolecular collision between OH(A) and H_2 diatoms. The study focuses on the relationship between the initial, $\boldsymbol{j}$, and final rotational angular momentum, $\boldsymbol{j}'$. This relationship is explored from both a scalar point of view by measuring rotational energy transfer (RET), and a vectorial viewpoint by considering the collisional depolarisation.

The experimental technique used in this investigation, Zeeman quantum beat spectroscopy, is first demonstrated by applying it to the determination of the lab-frame orientation of OH(X) photofragments following the photolysis of H_2O_2. The H_2O_2 is photolysed by circularly-polarised light at 248 nm, and Zeeman quantum beat spectroscopy probes the angular momentum orientation as a function of the photofragment spin-rotation level. The results of this experiment are compared with orientation parameters predicted by a simulation that couples the rotation of the parent molecule to the torsional motion during bond cleavage. The calculations from the model agree qualitatively with those from the experiment.

The Zeeman quantum beat spectroscopy technique is then used to monitor the evolution of angular momentum polarisation of OH(A) radicals during collisions with H_2. The technique allows for the determination of depolarisation cross sections for oriented and aligned distributions, as a result of collisions with H_2. Alongside this, cross sections for collisional quenching to non-reactive OH(X)+H_2 and reactive H_2O+H products are determined. By resolving the fluorescence with a monochromator the contributions to depolarisation from elastic collisions (the elastic depolarisation cross sections) are measured alongside cross sections for RET. Cross sections for total depolarisation and rotational energy transfer demonstrate only weak dependence on the rotational quantum number of the OH(A) radical, N_{OH}. Competing quenching processes that fall with N_{OH} are likely a considerable cause of this weak dependence. Furthermore, the polarisation of the angular momentum of OH(A) is randomised following RET. The elastic depolarisation cross sections make only a small contribution to the depolarisation and fall with increasing N_{OH}. Collectively these trends have not been seen previously in similar studies on OH(A) collisions with atomic colliders.

For the theoretical calculations, a four-atom quasi-classical trajectory (QCT) method has been developed, utilising Lagrangian multipliers to fix the OH(A) and H_2 bonds. The calculations demonstrate that collisions involving the formation of complexes that survive for several rotational periods are prevalent in this collision system, and that these lead to large amounts of depolarisation. The calculations also demonstrate that RET in the H_2 diatom supports higher levels of RET in OH(A) than seen in previous

triatomic systems. Additionally, when one diatom is depolarised the accompanying diatom is typically also depolarised. These trends, at least in part, are owed to the highly attractive and anisotropic potential energy surface (PES) describing the interaction.

The QCT calculations overestimate the experimentally-measured cross sections by more than a factor of 2. The calculations are adiabatic and do not account for the non-adiabatic activity associated with this collision system, and this is likely one cause of the discrepancies. In an attempt to further account for this overestimation, alternative angular momentum binning approaches for the QCT calculations are developed, but with limited success. Further exploration of the topology of the PES used in the calculations suggests that inadequacies in this surface are a major contributor to the discrepancies.

Publications

1. Molecular Photofragment Orientation in the Photodissociation of H_2O_2 at 193 nm and 248 nm.

Y.-P. Chang, M. Brouard, R. Cireasa, T. Perkins and S. A. Seamons, *Phys. Chem. Chem. Phys.*, **13**, 8213, (2011).

2. The Hyperfine Structure of NO(A).

M. Brouard, H. Chadwick, Y.-P. Chang, B. J. Howard, S. Marinakis, N. Screen, S. A. Seamons and A. La Via, *J. Mol. Spec.*, **282**, 42, (2012).

3. A New Potential Energy Surface for OH(A)-Kr: The van der Waals Complex and Inelastic Scattering.

H. Chadwick, M. Brouard, Y.-P. Chang, C. J. Eyles, T. Perkins, S. A. Seamons, J. Kłos, M. H. Alexander and F. J. Aoiz, *J. Chem. Phys.*, **137**, 154305, (2012).

4. Electronic Quenching of OH(A $^2\Sigma^+$) Induced by Collisions with Kr Atoms.

J. H. Lehman, M. I. Lester, J. Kłos, M. H. Alexander, P. Dagdigian, D. Herráez-Aguilar, F. J. Aoiz, M. Brouard, H. Chadwick, T. Perkins and S. A. Seamons, *J. Phys. Chem. A*, **117**, 13481, (2013).

5. The Collisional Depolarisation of OH(A) and NO(A) with Kr.

H. Chadwick, M. Brouard, Y.-P. Chang, C. J. Eyles, G. McCrudden, T. Perkins, S. A. Seamons, J. Kłos, M. H. Alexander, P. J. Dagdigian, D. Herráez-Aguilar and F. J. Aoiz, *J. Chem. Phys.*, **140**, 054306, (2014).

Future Publications

1. Experimental and quasi-classical trajectory studies of OH(A $^2\Sigma^+$)+H_2: rotational energy transfer and collisional depolarisation.

M. Brouard, H. Chadwick, J. Lawlor, T. Perkins, S. A. Seamons, P. Stevenson, F. J. Aoiz and J. M. Bowman.

2. Potential energy surface and classical dynamics of rotational energy transfer in OH(A $^2\Sigma^+$)+H_2.

M. Brouard, H. Chadwick, J. Lawlor, T. Perkins, S. A. Seamons, P. Stevenson, F. J. Aoiz and J. M. Bowman.

Acknowledgements

Firstly, I would like to thank my supervisor, Prof. Mark Brouard. In submitting this thesis, I reflect upon the ten years I have known Mark, from being seated adjacent to him at dinner the night before interviews as a wide-eyed, slightly overwhelmed 17 year old, through his time as my excellent tutor, to my time in the Brouard Group. He has been, throughout, a source of encouragement, support and enthusiasm.

My thanks also to the range of wonderful people I have had the privilege of getting to know and work with in the group over the years. Dr. Yuan-Pin Chang for teaching me the ways and woes of the experiment, Dr. Helen Chadwick for teaching me how to survive this world, my principal lab partner Dr. Tom Perkins for more than I could ever repay, and two talented Part II students: Paul Stevenson and John Lawlor for their enthusiasm and imagination. I am additionally grateful to Garreth McCrudden for making my final months in the lab enjoyable, and for the extensive proof reading of this thesis. I look forward to learning about the exciting experiments Garreth undertakes on the mini rig, and couldn't leave it in better hands.

Others I have not worked as closely with, but have been no less important in making the last few years a joy: Ewen, Chris, Sean, Ed, Balasz, Alex, Bethan, Craig, Ben and Wei Hao. They have provided great conversation at tea breaks, occasionally fantastic cake, and always the promise of a beer at the end of the week.

Further thanks are extended to collaborators further afield: Prof. Joel Bowman for supplying the OH(A)+H_2 PES, Prof. Javier Aoiz for his guidance on all matters QCT particularly with regards to Gaussian binning, and Dr. Raluca Cireasa for supporting me in the early stages of designing a new experimental rig. Thanks also to Prof. David Chandler and Dr. Stuart Greaves for sharing their experiences developing compact cross molecular beam machines.

I am also grateful for all the support received from technical staff in lab services and the workshops. Life would be a whole lot simpler if not everything that could go wrong, at some point did go wrong, but immeasurably harder without these guys to fix, make do or make new. In particular I would like to thank Andy Green, who worked tirelessly, and with enthusiasm producing multiple parts of the new experiment. More generally, the mechanical workshop is a fantastic resource for students in the chemistry department, allowing items to be built to tailor made instructions through direct contact with the manufacturers. The most enjoyable part of my studies was certainly designing, overseeing the production of, and assembling a new experiment and this facility made that possible.

There's probably a good 700 other people I need to thank and couldn't hope to add them all. However I should add my family for their support and general advice.

Finally, my thanks to Emma for her love and support, there is no way I could have done any of this without her. She has forever my love and gratitude.

Contents

Chapter 1

Introduction

Chemical processes vary in scale and complexity, from collisions and reactions between macromolecules, such as the interaction between a protein and a nucleic acid during RNA translation, to the outcome of collisions between two atoms in the gas phase. Reaction or molecular dynamics is concerned with obtaining a fundamental understanding of how these processes take place and how the interaction between particles directs the outcome.

The development of models to explain the experimentally-observed properties of chemical processes is a central goal of reaction dynamics and, in turn, experimental measurements can be used to test the adequacy of models developed to explain molecular processes. Rather than just reproducing the outcomes, successful models give an understanding of how a chemical process develops mechanically. Reaction dynamics focuses typically on the interaction of small molecular or atomic species in the gas phase, since such systems allow a meticulous comparison of theory and experiment. The hope remains, however, that the successful development of models to explain the dynamics in these simpler systems may lead to their successful application in interpreting, or predicting, results in more complex processes.

A central concept in molecular dynamics is the potential energy surface (PES) describing the potential energy associated with the geometry of the nuclei for a particular

electronic state, and determining the forces at work in the molecular process. Consequently, there is a great amount of work for theoreticians in calculating PESs to model the 'true potential' of a chemical system.

In this thesis, models are presented to explain the dynamics in two different processes. The first model tries to account for the preferred sense of rotation observed in molecular photofragments following the photolysis of hydrogen peroxide by considering the role of the rotation of the parent molecule. The second model investigated uses quasi-classical calculations to consider the outcome of collisions between the hydroxyl radical in its first excited-state, OH(A), and molecular hydrogen, H_2. This latter study is the principal investigation of this thesis and tests the suitability of both the theoretical PES describing this interaction, and the quasi-classical technique used to propagate trajectories on it.

This introduction chapter establishes key concepts and properties of interest to the molecular dynamicist, including scalar properties like the collision cross section, and vector correlations such as the differential cross section (DCS) and the rotational tilt. The OH radical provides a connection between the short study of H_2O_2 photolysis, and the extensive study of OH(A)+H_2 collision dynamics. As such, the electronic structure of the radical and its angular momentum couplings are set out. In both studies, the formation of a polarised angular momentum distribution with polarised light and the monitoring of this distribution with Zeeman quantum beat spectroscopy underpin the experimental methods; this chapter introduces these concepts.

The chapter then focuses on the central study of this thesis: the collision dynamics of OH(A)+H_2. In the first instance, previous experimental work on this system is discussed, before later introducing theoretical concepts. The basics of adiabatic and non-adiabatic theoretical formalisms are established, and previous theoretical studies of relevance to this investigation are briefly detailed.

1.1 Bimolecular Collision Systems

The outcome of bimolecular collisions is determined by both the scalar and vector properties of the colliding molecules, and likewise the resultant products are described by a combination of scalar and vector properties. A variety of experiments have been developed that control the initial properties and utilise detection arrangements sensitive to the product properties.

A bimolecular collision involving two diatoms, AD+BC, can be described by 6 vectors, the initial relative velocity, $\boldsymbol{k}$, the final relative velocity, $\boldsymbol{k}'$, and the initial and final angular momenta of each diatom: $\boldsymbol{j}_{\mathrm{AD}}$, $\boldsymbol{j}_{\mathrm{BC}}$, $\boldsymbol{j}'_{\mathrm{AD}}$, $\boldsymbol{j}'_{\mathrm{BC}}$. Alternatively, the system can be described by the initial and final bond orientation of each diatom: $\boldsymbol{r}_{\mathrm{AD}}$, $\boldsymbol{r}_{\mathrm{BC}}$, $\boldsymbol{r}'_{\mathrm{AD}}$, and $\boldsymbol{r}'_{\mathrm{BC}}$, along with the relative velocity vectors, $\boldsymbol{k}$ and $\boldsymbol{k}'$. These descriptions are as illustrated in figure 1.1.

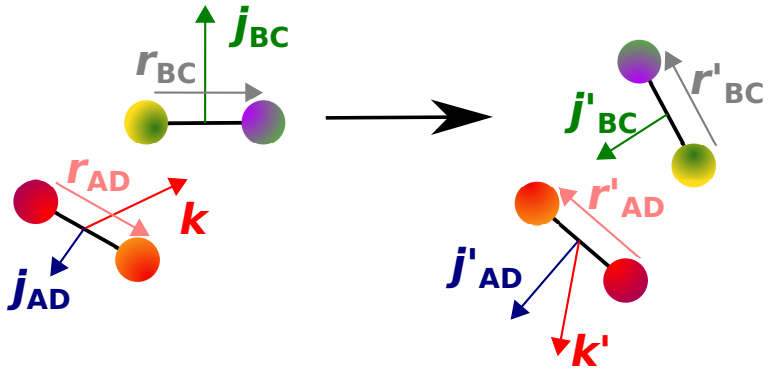

Figure 1.1: Illustration of the vectors involved in a diatom+diatom collision.

Development of crossed molecular beam experiments, similar to those described in the appendix of this thesis, lead to a well defined relative velocity, $\boldsymbol{k}$ [1–3]. The development of velocity mapped ion imaging enables the measurement of $\boldsymbol{k}'$, and therefore the $\boldsymbol{k}$-$\boldsymbol{k}'$ distribution or DCS [4–6]. The use of a static electric field enables the orientation of the initial bond axis, $\boldsymbol{r}$, as has been demonstrated for the OH radical in references [7–9]. However, there are no experimental methods to detect the orientation

of $\boldsymbol{r}'$. Similarly, a magnetic field can be used to control the direction of $\boldsymbol{j}$ [10–12]. Alternatively, as in the central studies of this thesis, polarised light can be used to create an anisotropic distribution of $\boldsymbol{j}$ for one of the diatoms [13]. $\boldsymbol{j}'$ can also be probed by a polarised laser, this technique has been used by Chandler and co-workers to explore collision induced alignment [14, 15], and collision induced orientation [16] through measuring the $\boldsymbol{k}$-$\boldsymbol{k}'$-$\boldsymbol{j}'$ correlation. A more common approach is to detect emitted radiation from $\boldsymbol{j}'$ through a polariser [17–21]. The relationship describing the rotational tilt of a diatom, $\boldsymbol{j}$-$\boldsymbol{j}'$, is of particular interest as it indicates the role of angular momentum polarisation on the outcome of a collision, and the resulting change in angular momentum polarisation after the collision. Unlike the $\boldsymbol{k}$-$\boldsymbol{k}'$ correlation, the rotational tilt cannot be measured directly. However, rate constants for the loss of an initially anisotropic distribution can be determined in a simple bulb experiment. Such measurements are a key observable in this study and this discussion continues in subsection 1.8.2.

1.2 The Collision Cross Section

The collision cross section, σ, is a central concept and parameter in reaction dynamics, expressing the efficiency of a process as an effective target area [22, 23]. In this thesis, the cross sections are often for non-reactive processes, such as inelastic collisions, electronic quenching and depolarisation, rather than for reactive processes. The cross section is the effective target area for a process and is independent of the orientation of the species involved, i.e. a 'dartboard' average of the probability of the process. The collision cross section is classically defined as [22, 23]

$$\sigma = \int_0^{b_{\max}} P(b) 2\pi b \mathrm{d}b, \tag{1.1}$$

where b is the impact parameter of the collision and $P(b)$ the opacity function. b is defined as the distance of closest approach between the paths of the two particles in the absence of an intermolecular potential. The impact parameter also classically defines the orbital angular momentum of the system via $|\boldsymbol{\ell}| = \mu \upsilon_{\mathrm{rel}} b$, where μ is the reduced mass of the system and υ_{rel} is the relative velocity between the two colliding species. $P(b)$ expresses the probability that a process will occur at a particular impact parameter b. b_{max} is the maximum impact parameter, above which there is zero probability of the process occurring.

In the theoretical calculations presented in this thesis, cross sections for processes are calculated directly, as the initial impact parameter is sampled as a dartboard average. However, in the experiments described in this thesis, it is various thermally-averaged rate constants, $k(T)$, rather than collision cross sections that are measured. A simpler rate constant at fixed collision energy for a specific process, x, can also be defined, k_x. This rate constant can be expressed in terms of the collision cross section for the process and the relative velocity as [22, 23]

$$k_x(\upsilon_{\mathrm{rel}}) = \upsilon_{\mathrm{rel}} \sigma_x(\upsilon_{\mathrm{rel}}). \tag{1.2}$$

This is the collision volume swept out by the collision particles per unit time, and as such is an easily interpreted property. However in the experiment the temperature, T, is definitive rather than the collision energy or relative velocity. In this way the thermally-averaged rate constant is determined from the distribution of velocities such that [22, 23]

$$\begin{aligned} k_x(T) = \langle k_x(\upsilon_{\mathrm{rel}}) \rangle &= \langle \upsilon_{\mathrm{rel}} \sigma_x(\upsilon_{\mathrm{rel}}) \rangle \\ &= \int_0^\infty \upsilon_{\mathrm{rel}} \sigma_x(\upsilon_{\mathrm{rel}}) f_{\mathrm{MB}}(\upsilon_{\mathrm{rel}}|T) \mathrm{d}\upsilon_{\mathrm{rel}}, \end{aligned} \tag{1.3}$$

where $f_{\mathrm{MB}}(\upsilon_{\mathrm{rel}}|T)$ is the Maxwell-Boltzmann distribution of relative velocities at temperature, T.

Similarly the thermally-averaged collision cross section is defined by [23, 24]

$$\begin{aligned} \sigma_x(T) &= \langle \sigma_x(\upsilon_{\mathrm{rel}}) \rangle \\ &= \int_0^\infty \sigma_x(\upsilon_{\mathrm{rel}}) f_{\mathrm{MB}}(\upsilon_{\mathrm{rel}}|T) \mathrm{d}\upsilon_{\mathrm{rel}}. \end{aligned} \tag{1.4}$$

Alternatively we can define a flux-averaged thermal cross section such that

$$\sigma_x = \frac{k_x(T)}{\langle \upsilon_{\mathrm{rel}} \rangle}. \tag{1.5}$$

With a Maxwell-Boltzmann distribution of relative velocities, as in the thermalised experiments here,

$$\langle \upsilon_{\mathrm{rel}} \rangle = \left(\frac{8 k_{\mathrm{B}} T}{\pi \mu} \right)^{\frac{1}{2}}, \tag{1.6}$$

where k_{B} the Boltzmann constant [25]. This flux-averaged thermal cross section is equivalent to the thermally-averaged cross section only in the event that the cross section is independent of the relative velocity. It is this flux-averaged thermal cross section defined in equation (1.5) that is the form of the experimentally-determined collision cross sections for quenching, RET and depolarisation processes in the experiments of this thesis, and shall typically be referred to simply as a 'cross section' throughout.

1.3 Polarisation

The anisotropic nature of collisions is indicated by the vector properties describing the collision partners [26]. The anisotropy of the spatial distributions of one or more vector properties is described as polarisation. Polarisation can simply be demonstrated with recourse to its two simplest forms - orientation and alignment [26].

Figure 1.2 gives a simplistic classical view of vector polarisation, displaying images indicative of isotropic and anisotropic vector distributions. The left-hand diagram in this figure demonstrates no preference for the direction of the vectors and is isotropic in nature. The middle diagram in the figure does not show a preferred direction with equal numbers of vectors pointing left and right or up and down, however there is a preferred axis. The vectors in this diagram have a clear preference for pointing to the sides of the page rather than up and down. This distribution is referred to as aligned [17, 26–28]. Vectors in the right-hand diagram have a preferred direction towards the top of the page, and this distribution is referred to as oriented. A distribution being aligned does not preclude it from being oriented and vice-versa.

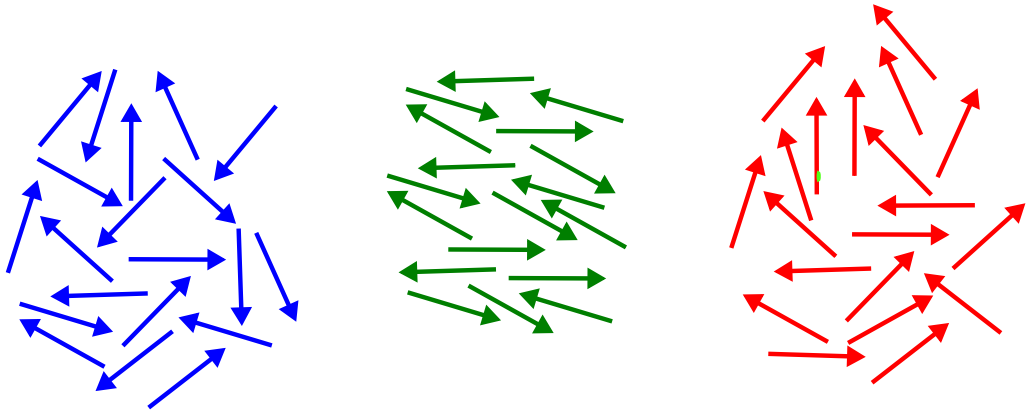

Figure 1.2: Ensemble of vectors to demonstrate isotropic (left) and anisotropic (middle and right) distributions. The middle diagram demonstrates an aligned distribution and the right diagram an oriented distribution.

It is the polarisation of the diatom angular momentum that is of interest in the studies described in this thesis. In quantum mechanics, the direction as well as the magnitude of angular momentum is quantised. For an angular momentum $\boldsymbol{J}$ there are $2J+1$ possible projections, M_J, onto any quantization axis. Figure 1.3 demonstrates the origin of oriented or aligned distributions of angular momentum in quantum mechanics as the distribution is described by the relative population of $|JM_J\rangle$ states [13]. In an aligned distribution there is a larger population in states with particular values of $|M_J|$, but the population for $-M_J$ and $+M_J$ states are equal. In figure 1.3 the left panel

displays an isotropic distribution where all states are populated equally. An aligned distribution is shown in the middle panel where there is a clear preference for high $|M_J|$ states. In oriented distributions, as in the right-hand panel of figure 1.3, there is a clear preference for particular signs of M_J, here there is a preference for + projections. With an aligned distribution, there is a preferred plane of rotation; with an oriented distribution, there is a preferred sense of rotation.

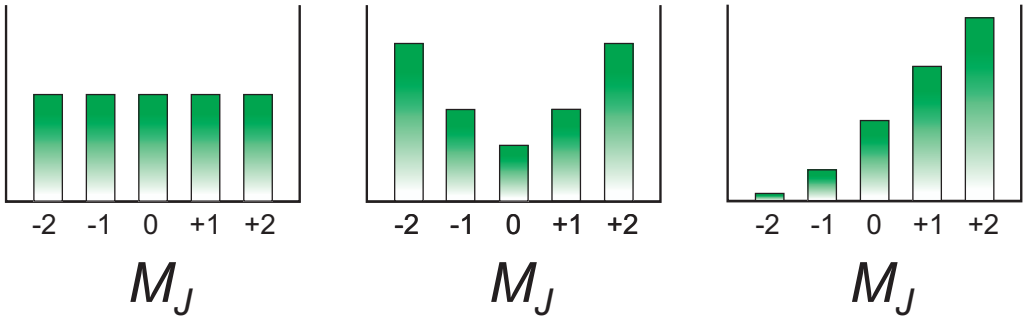

Figure 1.3: Pictoral representation of the population of the $|JM_J\rangle$ quantum states in an isotropic (left), aligned (middle) and oriented (right) distribution. In this case $J = 2$.

In the general case, where the system is non-cylindrically symmetric, a full density matrix formulation is needed to describe the distribution [10, 13, 29]. A wavefunction for the distribution can be expressed as

$$|\Psi\rangle = \sum_{M_J=-J}^{J} c_{M_J}|JM_J\rangle, \tag{1.7}$$

whilst the density operator is expressed as [29]

$$\hat{\rho} = \sum_{M_{J,1},M_{J,2}} c_{M_{J,1}} c^*_{M_{J,2}} |JM_{J,1}\rangle\langle JM_{J,2}|. \tag{1.8}$$

The resulting density matrix elements are given by [23, 29, 30]

$$\langle JM_J|\hat{\rho}|JM'_J\rangle = \sum_{M_{J,1},M_{J,2}} c_{M_{J,1}} c^*_{M_{J,2}} \langle JM_J|JM_{J,1}\rangle\langle JM_{J,2}|JM'_J\rangle = c_{M_J} c^*_{M'_J}, \tag{1.9}$$

where the diagonal elements express the populations of the various $|JM_J\rangle$ states in the distribution, and the off-diagonal elements the coherences between them.

1.4 Vector Correlations

As already mentioned, the vector properties of species in chemical processes (including photolysis and molecular collisions) are important in understanding the mechanisms involved. The relationships between two or more of these vectors are of particular interest. This thesis focuses heavily on the two-vector correlation $\boldsymbol{j}$-$\boldsymbol{j}'$ of molecular angular momentum before and after a collision, but also on the $\boldsymbol{k}$-$\boldsymbol{k}'$ correlation. Three-vector correlations are also briefly considered in the discussion of H_2O_2 photolysis. Both three- and two-vector correlations are described for a general case here.

1.4.1 Three-Vector Correlations

Taking one vector $\boldsymbol{a}$ as the reference z-axis, a second vector $\boldsymbol{b}$ is defined by the angles θ_{ab} and ϕ_{ab} relative to $\boldsymbol{a}$. A third vector, $\boldsymbol{c}$, is defined by the angles θ_{ac} and ϕ_{ac}, and this vector has a characteristic spatial distribution for each position of $\boldsymbol{b}$. This three-vector correlation can be expressed classically as [31–33]

$$\begin{aligned} P(\omega_{ab}, \omega_{ac}) &\equiv P(\theta_{ab}, \phi_{ab}, \theta_{ac}, \phi_{ac}) \\ &= \frac{1}{16\pi^2} \sum_{KQ} \sum_{k_1 k_2} [k_1][k_2] b_Q^K(k_1, k_2) B_Q^K(k_1, k_2; \omega_{ab}, \omega_{ac})^*, \end{aligned} \tag{1.10}$$

where $[x] = 2x + 1$, and the correlation is an expansion in terms of bipolar harmonics [13, 32] defined as

$$B_Q^K(k_1, k_2; \theta_{ab}, \phi_{ab}, \theta_{ac}, \phi_{ac}) = \sum_{q_1 q_2} (-1)^K \sqrt{2K+1} \begin{pmatrix} k_1 & K & k_2 \\ q_1 & -Q & q_2 \end{pmatrix} C_{q_1}^{(k_1)}(\theta_{ab}, \phi_{ab}) C_{q_2}^{(k_2)}(\theta_{ac}, \phi_{ac}). \tag{1.11}$$

where the term in large parentheses is a Wigner 3-j symbol which are closely related to Clebsch-Gordan coefficients according to [13, 34]

$$\langle j_1 m_1, j_2 m_2 | j m \rangle = (-1)^{m + j_1 - j_2} \sqrt{2j+1} \begin{pmatrix} j_1 & j_2 & j \\ m_1 & m_2 & -m \end{pmatrix}. \tag{1.12}$$

Clebsch-Gordan coefficients can be thought of as the probability amplitude that the composite parts of an angular momentum $\boldsymbol{j} = \boldsymbol{j}_1 + \boldsymbol{j}_2$, with magnitude j and a projection onto a given axis is m, have themselves projections of m_1 and m_2 onto that axis [13, 34]. Rather than a probability amplitude the related 3-j symbols have a magnitude related to that of the coupled vector j.

Returning to equation (1.10), the expansion coefficients, also known as the bipolar moments, are defined as

$$b_Q^K(k_1 k_2) = \langle B_Q^K(k_1, k_2; \omega_{ab}, \omega_{ac}) \rangle. \tag{1.13}$$

If the vector $\boldsymbol{b}$ is defined as lying in the xz plane the azimuthal dependence is removed, so $\phi_{ab} = 0$ and the sum is reduced to only terms where $Q = 0$. Consequently [31], it follows that

$$P(\theta_{ac}, \phi_{ac}, \theta_{ab}) = \frac{1}{16\pi^2} \sum_K \sum_{k_1 k_2} [k_1][k_2] b_Q^K(k_1 k_2) \sum_q \begin{pmatrix} k_1 & K & k_2 \\ q & 0 & -q \end{pmatrix} P_{k_1}(\cos\theta_{ab}) C_q^{(k_2)}(\theta_{ac}, \phi_{ac}). \tag{1.14}$$

Here the basis set is clearly the product of the k-th order Legendre polynomial (describing the correlation of $\boldsymbol{b}$ about $\boldsymbol{a}$) and the kq-th spherical harmonic (describing the relationship of the vector $\boldsymbol{c}$ to the zx plane).

1.4.2 Two-Vector Correlations

Classical Description

Three-vector correlations can prove difficult to visualise or interpret, and the lower order two-vector correlations are often considered instead, following integration over the third vector. In this way, the distribution of the vector b with respect to a is given by [13, 31, 33]

$$P(\theta_{ab}, \phi_{ab}) = \sum_{k=0}^{\infty} \sum_{q=-k}^{k} \frac{[k]}{4\pi} h_q^{(k)} C_q^{(k)}(\theta_{ab}, \phi_{ab})^*, \tag{1.15}$$

which is an expansion in terms of the complex conjugates of the modified spherical harmonics, $C_q^{(k)}(\theta_{ab}, \phi_{ab})^*$. The expansion coefficients are the expectation values of the modified spherical harmonics, $h_q^{(k)} = \langle C_q^{(k)}(\theta_{ab}, \phi_{ab}) \rangle$ [26]. These expansion coefficients are commonly referred to as polarisation moments since the distribution describes the polarisation of one vector with respect to the other. Since the spherical harmonics are complex functions, the polarisation moments must also take complex values to obtain a real distribution. These moments are often used in characterising the distribution and it can be useful to work with real values. In order to obtain real values the Hertel-Stoll normalisation is applied for $q > 0$ [35]:

$$h_{q+}^{\{k\}} = \frac{1}{\sqrt{2}} \left((-1)^q a_q^{(k)} + a_{-q}^{(k)} \right) \tag{1.16}$$

$$h_{q-}^{\{k\}} = \frac{1}{i\sqrt{2}} \left((-1)^q a_q^{(k)} - a_{-q}^{(k)} \right) \tag{1.17}$$

$$h_0^{\{k\}} = a_0^{(k)} \tag{1.18}$$

In this thesis, correlations involving an angular momentum $\boldsymbol{j}$ and a second vector are amongst the most important. The first of these is the $\boldsymbol{j}$ correlation in the space-fixed frame, relative to the lab Z-axis. In this case Z is also considered the projection axis, and $\boldsymbol{j}$ is cylindrically symmetric about Z. Consequently, the azimuthal dependence is lost, and the sum over $q \neq 0$ is removed [26],

$$P(\theta) = 2\pi \times P(\theta, \phi) = \frac{1}{2} \sum_{k} [k] h_0^{(k)} P_k(\cos\theta). \tag{1.19}$$

Note that $C^k_{q=0}(\theta_{zj}, \phi_{zj}) = P_k(\cos\theta)$ where $P_k(\cos\theta)$ is the kth order Legendre polynomial in $\cos\theta$. A similar distribution can be used to describe the $\boldsymbol{k}$-$\boldsymbol{k}'$ distribution. The case of the rotational tilt $\boldsymbol{j}$-$\boldsymbol{j}'$ shall be considered below.

Quantum Description

In reality $\boldsymbol{j}$ is a quantum object and there is uncertainty in its direction. In this case the distribution is better defined by a density matrix formulation. Continuing with a focus on $\boldsymbol{j}$ relative to a lab fixed Z-axis, the elements of the density matrix defined in equation (1.9) can be re-expressed in terms of Clebsch-Gordan coefficients [30, 36], such that

$$\langle jM_j|\hat{\rho}|jM_j'\rangle = \sum_{k=0}^{2j} \sum_{q=-k}^{k} \frac{2k+1}{2j+1} h_q^{(k)} \langle jM_j, kq|jM_j'\rangle, \tag{1.20}$$

where $\langle jM_j, kq|JM_j'\rangle$ are the Clebsch-Gordan coefficients [13]. On inversion the polarisation moments are obtained [30, 36],

$$a_q^{(k)} = \sum_{M_j M_j'} \langle jM_j|\hat{\rho}|jM_j'\rangle \langle jM_j, kq|jM_j'\rangle. \tag{1.21}$$

To more directly link this quantum description with the classical description, a minimum uncertainty state $|\theta_j, \phi_j\rangle$ is defined. Such a state is centralised around (θ_j, ϕ_j)

but is not defined by it as there is quantum uncertainty in the direction of $\boldsymbol{j}$. The state is consequently defined as [30, 36]

$$|\theta_j, \phi_j\rangle = R(\phi_j, \theta_j, 0)|jj\rangle - \sum_{M_j} |jM_j\rangle D^j_{M_j j}(\phi_j, \theta_j, 0) \tag{1.22}$$

where the state $|jj\rangle$ is rotated to the direction of interest. $D^j_{M_j j}(\phi_j, \theta_j, 0)$ is a Wigner rotation matrix defined in reference [13] and is equivalent to the overlap of the $|jM_j\rangle$ state with the minimum uncertainty state, i.e. $D^j_{M_j j}(\phi_j, \theta_j, 0) = \langle jM_j|\theta_j\phi_j\rangle$ [30, 36]. The population distribution is given by [30]

$$Q(\theta_j, \phi_j) = \frac{\langle\theta_j\phi_j|\hat{\rho}|\theta_j\phi_j\rangle}{\mathrm{Tr}(\hat{\rho})} = \frac{1}{4\pi}\sum_{k=0}^{2j}\sum_{k=-q}^{q}[k]h^{(k)}_q\langle jj, k0|jj\rangle C^{(k)}_q(\theta_j, \phi_j), \tag{1.23}$$

where in the high $\boldsymbol{j}$ limit the Clebsch-Gordan coefficient tends to unity, so that the correlation corresponds with the classical case. In the case where $\boldsymbol{j}$ is cylindrically symmetric about Z and the azimuthal dependence is removed, the summation over q reduces to only the $q = 0$ terms, and $h^{(k)}_0 = \langle P_k(\cos\theta)\rangle$.

Rotational Tilt - $\boldsymbol{j}$-$\boldsymbol{j}'$ Correlation

The $\boldsymbol{j}$-$\boldsymbol{j}'$ correlation, also known as the rotational tilt, is considered extensively both experimentally and theoretically in this study. This correlation gives information on the change in polarisation, or depolarisation, of the angular momentum upon collision. The $\boldsymbol{j}'$ vector is cylindrically symmetric about the $\boldsymbol{j}$ vector, and the distribution is given by [26, 37]

$$P(\theta_{jj'}) = \sum_k \frac{[k]}{2} a^{(k)}(j, j')P_k(\cos\theta_{jj'}). \tag{1.24}$$

The polarisation moments here are most frequently referred to as depolarisation parameters or moments throughout this thesis. These moments are given by

$$a^{(k)}(j, j') = \langle P_k(\cos\theta_{jj'})\rangle. \tag{1.25}$$

The odd order depolarisation parameters take limiting values of $-1 \leq a^{(k)}(j, j') \leq +1$, whilst even order depolarisation parameters take limiting values $-0.5 \leq a^{(k)}(j, j') \leq +1$ [37]. The +1 limiting value corresponds to the conservation of the initial k-th order polarisation of $\boldsymbol{j}$ following collisions. The $a^{(1)}$ moment is a measure of the loss of orientation, and the limiting value of -1 corresponds with $\boldsymbol{j}'$ lying anti-parallel to the initial $\boldsymbol{j}$. Likewise the $a^{(2)}$ moment is a measure of the loss of alignment, and the limiting value of -0.5 corresponds with $\boldsymbol{j}'$ perpendicular to $\boldsymbol{j}$. A value of 0 in either case indicates the final k-th order polarisation is randomised following the collision.

In quantum mechanics it can be shown that $a^{(k)}(j, j')$ is identical [37, 38] to Corey *et al.*'s tensor transfer coefficient $E^{(k)}(j, j')$ [39]. A quantum mechanical description of the rotational tilt can also be determined with recourse to the tensor cross sections. Tensor cross sections are defined as

$$\sigma_T^{(k)}(j, j') = a^{(k)}(j, j')\sigma_{jj'}, \tag{1.26}$$

where $\sigma_{jj'}$ is the inelastic collision cross section for the collision $\boldsymbol{j} \rightarrow \boldsymbol{j}'$, and the tensor cross section measures the degree of polarisation transferred in the collision. The tensor cross section has been defined quantum-mechanically as [40–44]

$$\sigma_T^{(k)}(j, j') = \frac{\pi}{k_i^2}\sum_{JJ'}\sum_{\ell\ell'}[J][J'](-1)^{\ell-\ell'-j-j'-2J}\begin{Bmatrix} j & j & k \\ J & J' & \ell \end{Bmatrix}\begin{Bmatrix} j' & j' & k \\ J & J' & \ell \end{Bmatrix} T^J_{j\ell j'\ell'}T^{J'*}_{j\ell j'\ell'}, \tag{1.27}$$

with ℓ the orbital angular momentum, J is the total angular momentum of the collision system, k_i is the wavevector - the linear momentum in the initial conditions divided by $\hbar$. T is the T-matrix element defined in references [39, 42, 45] and $\{...\}$ is a 6-j symbol. Whilst 3-j symbols describe the coupling between 2 vectors, the 6-j symbols describe the coupling between 3. 6-j symbols can be expressed in terms of 3-j symbols as [13]

$$\begin{Bmatrix} j_1 & j_2 & j_3 \\ j_4 & j_5 & j_6 \end{Bmatrix} = \sum_{allm} (-1)^{j_4-m_4+j_5-m_5+j_6-m_6} \times \begin{pmatrix} j_1 & j_2 & j_3 \\ m_1 & m_2 & m_3 \end{pmatrix} \begin{pmatrix} j_1 & j_5 & j_6 \\ m_1 & -m_5 & m_6 \end{pmatrix} \times \begin{pmatrix} j_4 & j_2 & j_6 \\ m_4 & m_2 & -m_6 \end{pmatrix} \begin{pmatrix} j_4 & j_5 & j_3 \\ -m_4 & m_5 & m_3 \end{pmatrix}, \tag{1.28}$$

or in terms of Clebsch-Gordan coefficients

$$\begin{Bmatrix} j_1 & j_2 & j_{12} \\ j_3 & j & j_{23} \end{Bmatrix} = \sqrt{\frac{1}{(2j_{12}+1)(2j_{23}+1)}} \langle j_{12} j_3 j | j_1 j_{23} j \rangle. \tag{1.29}$$

Wigner 6-j symbols are linked to the probability amplitude that a system described by the coupling scheme $\boldsymbol{j} = \boldsymbol{j}_{12} + \boldsymbol{j}_3$ is found in a state that can be described by the coupling system $\boldsymbol{j} = \boldsymbol{j}_1 + \boldsymbol{j}_{23}$.

A central quantity measured in this thesis is the collisional depolarisation cross section, $\sigma^{(k)}(j, j')$, which is directly related to the tensor cross section via the equation

$$\sigma^{(k)}(j, j') = \sigma_{jj'} - \sigma_T^{(k)}(j, j') = \sigma_T^{(0)}(j, j')[1 - a^{(k)}(j, j')]. \tag{1.30}$$

1.5 Angular Momentum Couplings and OH Electronic Structure

Ignoring for a moment the inclusion of the intrinsic nuclear spin angular momentum, $\boldsymbol{I}$, there are three sources of angular momentum in a diatom. The first is the spin angular momentum of the electrons, $\boldsymbol{S}$, the second the electronic orbital angular momentum arising from the electronic motion, $\boldsymbol{L}$, and the final contribution from rotation of the nuclear frame, $\boldsymbol{R}$. Hund's coupling cases describe different coupling schemes depending upon the varying strength of couplings between these angular momenta [46–49]. There is no 'correct' coupling scheme for any molecule, and real molecules contain characteristics of more than one scheme; the scheme chosen typically limits the size of off-diagonal elements in the molecular Hamiltonian [49].

The experimental and theoretical studies of this thesis focus on the OH radical in either the ground or first excited-states. The ground electronic state of OH(X $^2\Pi$) exists in two lambda doublets A' and A'' with the electronic configurations $1\sigma^2 2\sigma^2 3\sigma^2 1\pi_x^2 1\pi_y^1$ and $1\sigma^2 2\sigma^2 3\sigma^2 1\pi_x^1 1\pi_y^2$ respectively [50]. At varying points in this thesis, OH(X) is described by Hunds case (a) and (b), both of which are demonstrated in figure 1.4. Hund's case (b) is used exclusively in modelling the first excited-state, OH(A), so shall be introduced with that electronic state below.

In Hund's case (a) the electronic motion is strongly coupled to the electrostatic field arising from the nuclear framework, in this event the frequency of precession about the internuclear axis is so high that the magnitude of $\boldsymbol{L}$ is no longer defined, only its component or projection about the internuclear axis, $\Lambda\hbar$. Λ is a good quantum number that can take integer values of 0 or greater. The spin angular momentum $\boldsymbol{S}$ couples to the magnetic field arising from the electronic motion, although, unlike L, S remains a good quantum number with a projection upon the internuclear axis, Σ [48, 51]. Collectively, there is a resultant angular momentum projection $\Omega = |\Lambda + \Sigma|$

on the internuclear axis arising from the electronic orbital and electron spin angular momenta. For the OH(X) radical Ω can take a value of 3/2 (F_1) or 1/2 (F_2), leading to two spin-orbit levels separated by an energy of $140\,\mathrm{cm}^{-1}$, with F_1 lower in energy [46]. Both spin-orbit manifolds are considered in this thesis, and both are populated in thermal conditions. Ω is coupled to the nuclear rotational angular momentum $\boldsymbol{R}$, which lies perpendicular to the molecular bond. This coupling gives rise to the total angular momentum $\boldsymbol{j}$ and j is a good quantum number. At higher N, $\boldsymbol{S}$ is uncoupled from the internuclear axis and Hund's case (b) better describes the coupling in OH(X) [49].

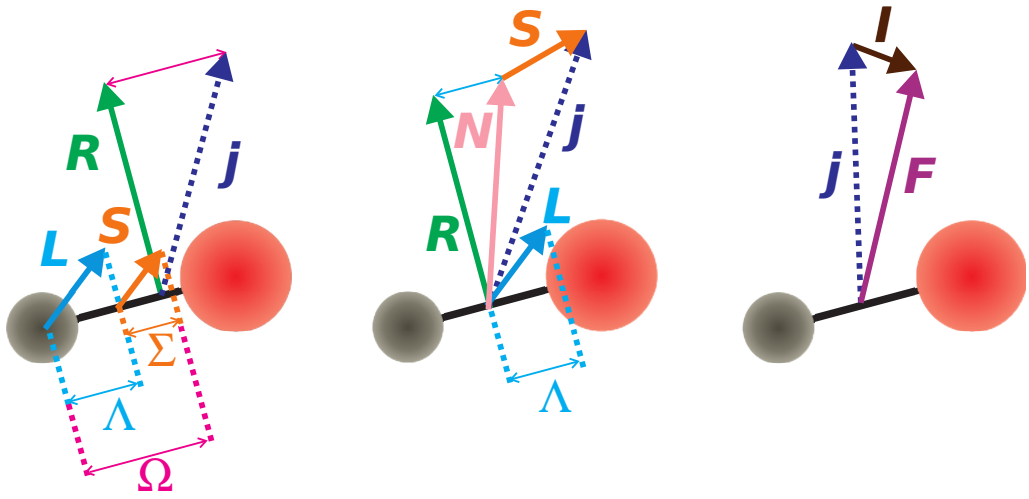

Figure 1.4: Diagram demonstrating angular momentum coupling schemes utilised in this thesis for the OH radical in its ground (X) and first excited-state (A). The left figure demonstrates the Hund's case (a) coupling scheme, the middle figure demonstrates the Hund's case (b) coupling scheme, and the right figure demonstrates the coupling of the nuclear spin. The labels are as described in the text.

Excitation of an electron from the 3σ orbital to a 1π orbital gives the first electronically excited-state: OH(A), with the electronic configuration $1\sigma^2 2\sigma^2 3\sigma^1 1\pi_x^2 1\pi_y^2$ [50]. The coupling of various angular momenta in this system is best described within the Hund's case (b) coupling regime, where spin-orbit coupling is weak and the spin is consequently only weakly coupled to the internuclear axis. $\boldsymbol{L}$ still precesses rapidly about

the internuclear axis with projection Λ, and Λ is coupled to $\boldsymbol{R}$ to give the resultant angular momentum $\boldsymbol{N}$ [51]. The electronic spin $\boldsymbol{S}$ is then coupled to $\boldsymbol{N}$ to give the total angular momentum $\boldsymbol{j}$, giving rise to spin-rotation levels: $f_1(j{=}N{+}S)$ and $f_2(j{=}N{-}S)$ split by the spin-rotation constant $\gamma = 0.2244\,\mathrm{cm}^{-1}$ [50]. Note this splitting is many orders of magnitude smaller than that arising from the spin-orbit splitting in Hund's case (a). In the case of OH(A) there is no orbital angular momentum $\boldsymbol{L}$, so the spin-orbit coupling is not only weak but necessarily non-existent. Additionally, since in this case $\boldsymbol{N}{=}\boldsymbol{R}$, $\boldsymbol{N}$ shall typically be referred to as the rotational angular momentum.

In both the OH(X) and OH(A) radicals the total angular momentum, $\boldsymbol{j}$, is further coupled to the nuclear spin angular momentum, $\boldsymbol{I}$, to give rise to the total angular momentum including nuclear spin, $\boldsymbol{F}$. The ^{16}O^{1}H isotopomer is by far the most abundant (^{1}H accounts for 99.9% and ^{16}O 99.8% of all naturally occurring hydrogen and oxygen respectively [52]) and is the only one considered here. Since a ^{16}O nucleus has no spin angular momentum, the nuclear spin angular momentum of the OH radical arises exclusively from the hydrogen atom, and so $I = 0.5$. The total angular momentum including nuclear spin, $\boldsymbol{F}$, is quantised and associated with the quantum number F. The experiments of this thesis are not resolved into hyperfine level F, and reference is instead made to j and N to describe the angular momentum of the OH(A) radical.

1.5.1 Lambda Doublets

As stated previously, in the case of OH(X) the differing populations of $1\pi_x$ and $1\pi_y$ molecular orbitals give rise to lambda doublets, as illustrated in figure 1.5. These lambda doublets are degenerate for a stationary molecule, but the degeneracy is lifted on molecular rotation [47–49]. In the high j limit this energy difference can simply be explained, arising from whether the molecule is rotating in the nodal plane of the

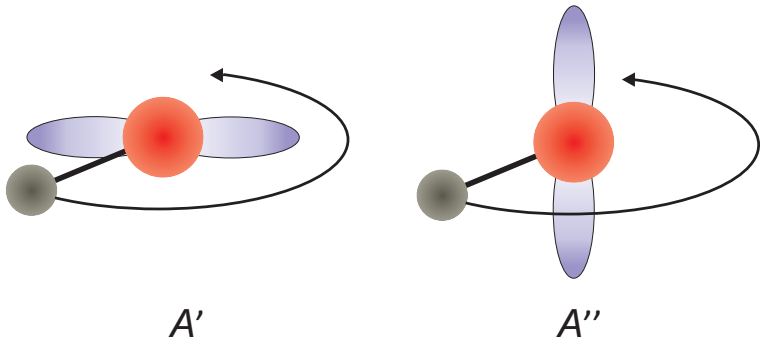

Figure 1.5: Figure demonstrating the origin of Λ-doublet states and their labelling.

singly-occupied π orbitals (A''), or perpendicular to it (A') [53]. The electronic wavefunction of the A' state is symmetric with respect to reflection in the plane of rotation, whilst the A'' state is antisymmetric. The degeneracy is lifted by a partial breakdown in the Born-Oppenheimer approximation, since the electronic motion does not instantaneously respond to the nuclear rotation [49]. Additionally, and highly relevant to the PESs that describe the OH(X)+H_2 collision system, even in the absence of rotation the degeneracy is lifted by the non-linear approach of a further atom or molecule.

1.6 Creation of Polarised Angular Momentum by Polarised Light

As stated earlier, polarised laser light is commonly used to create a polarised distribution of angular momentum $\boldsymbol{j}$ in an excited-state. This technique is used in the principal study of this thesis to produce oriented or aligned distributions of OH(A) radicals for use in the study of OH(A)+H_2 collisions.

The angular momentum of a species before laser excitation, $\boldsymbol{j''}$, is isotropically distributed, but the species absorbs light anisotropically on excitation to state, $\boldsymbol{j}$. The probability of absorbing the light is related to the correlation between the electric field vector of the light, $\boldsymbol{\epsilon}$, and the transition dipole moment, $\boldsymbol{\mu}$, of the absorbing species. The probability of absorption is proportional to $|\ \hat{\boldsymbol{\epsilon}} \cdot \hat{\boldsymbol{\mu}}\ |^2$, defined in terms of unit

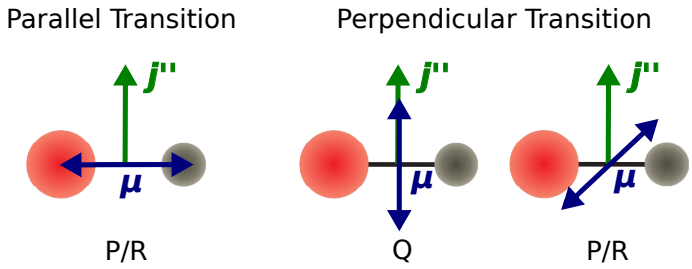

Figure 1.6: The relationship between the transition dipole moment $\boldsymbol{\mu}$ and the dipole bond axis for parallel and perpendicular transitions and the relationship with the total angular momentum $\boldsymbol{j''}$.

vectors. The relationship between $\hat{\boldsymbol{\mu}}$ and $\hat{\boldsymbol{j''}}$ is dependent on the transition branch, as shown in figure 1.6 [26].

1.6.1 Classical Description

In a classical description for the absorption of polarised light valid in the high j limit, first the projection of $\boldsymbol{j''}$ along an arbitrary molecular axis $\boldsymbol{z}$ (set perpendicular to the diatom intermolecular bond) $M_{j''}$, is set as equivalent to j''. In this way $\boldsymbol{j''}$ is directed along $\boldsymbol{z}$. With $\hat{\boldsymbol{k}}$ the unit vector for the propagation direction of the excitation laser, the intensity of P, Q and R branches can be expressed in terms of $\hat{\boldsymbol{j''}}$ [10]:

$$|\,\hat{\boldsymbol{\epsilon}}\cdot\hat{\boldsymbol{\mu}}\,|^2 = \begin{cases} \frac{1}{2}-\frac{1}{2}\,|\,\hat{\boldsymbol{j''}}\cdot\hat{\boldsymbol{\epsilon}}\,|^2+\frac{1}{2}s_3\hat{\boldsymbol{j''}}\cdot\hat{\boldsymbol{k}} & \text{(P)} \\ |\,\hat{\boldsymbol{j''}}\cdot\hat{\boldsymbol{\epsilon}}\,|^2 & \text{(Q)} \\ \frac{1}{2}-\frac{1}{2}\,|\,\hat{\boldsymbol{j''}}\cdot\hat{\boldsymbol{\epsilon}}\,|^2-\frac{1}{2}s_3\hat{\boldsymbol{j''}}\cdot\hat{\boldsymbol{k}} & \text{(R)} \end{cases}$$

where s_3 is a Stokes parameter varying from +1 to -1 depending on the degree of circular polarisation [10, 54]. $s_3 = +1$ for completely right-hand circularly-polarised light (negative helicity) or $s_3 = -1$ for perfectly left-hand circularly-polarised light (positive helicity). In this case the labels P, Q and R refer to the change in the total angular momentum on excitation from j'' to j, corresponding to $\Delta j = -1, 0, +1$, respectively.

For linearly-polarised light, if the electric field vector is defined as lying parallel to the lab-frame Z-axis, then the intensity is dependent on the azimuthal angle, $\theta_{jj'}$, of $\boldsymbol{j''}$ relative to Z, which is identical to the azimuthal angle in the excited-state, θ_j. In this case $s_3 = 0$, and for excitation via P or R branches:

$$\begin{aligned} |\, \hat{\boldsymbol{\epsilon}} \cdot \hat{\boldsymbol{\mu}} \,|^2 &= \frac{1}{2} - \frac{1}{2} \,|\, \hat{\boldsymbol{j''}} \cdot \hat{\boldsymbol{\epsilon}} \,|^2 \\ &= \frac{1}{2} - \frac{1}{2}\cos^2\theta_{j''} \\ &= \frac{1}{2}\sin^2\theta_{j''} \qquad \text{(P or R)} \end{aligned} \tag{1.31}$$

whilst for Q branches:

$$\begin{aligned} |\, \hat{\boldsymbol{\epsilon}} \cdot \hat{\boldsymbol{\mu}} \,|^2 &= |\, \hat{\boldsymbol{j''}} \cdot \hat{\boldsymbol{\epsilon}} \,|^2 \\ &= \cos^2\theta_{j''} \qquad \text{(Q)} \end{aligned} \tag{1.32}$$

For circularly-polarised light, the electric field vector is related to the propagation vector [10]:

$$|\, \hat{\boldsymbol{j''}} \cdot \hat{\boldsymbol{\epsilon}} \,|^2 = \frac{1}{2} - \frac{1}{2} \,|\, \hat{\boldsymbol{j''}} \cdot \hat{\boldsymbol{k}} \,|^2 \tag{1.33}$$

If the propagation vector is set parallel to the lab-frame Z-axis then once again the intensity is related to the azimuthal angle. So, for the P branch:

$$\begin{aligned} |\, \hat{\boldsymbol{\epsilon}} \cdot \hat{\boldsymbol{\mu}} \,|^2 &= \frac{1}{4} + \frac{1}{4} \,|\, \hat{\boldsymbol{j''}} \cdot \hat{\boldsymbol{k}} \,|^2 + \frac{1}{2} s_3 \hat{\boldsymbol{j''}} \cdot \hat{\boldsymbol{k}} \\ &= \frac{1}{4} + \frac{1}{4}\cos^2\theta_{j''} + \frac{1}{2} s_3 \cos\theta_{j''} \qquad \text{(P)} \end{aligned} \tag{1.34}$$

for the Q branch:

$$\begin{aligned} |\, \hat{\boldsymbol{\epsilon}} \cdot \hat{\boldsymbol{\mu}} \,|^2 &= \frac{1}{2} - \frac{1}{2} \,|\, \hat{\boldsymbol{j''}} \cdot \hat{\boldsymbol{k}} \,|^2 \\ &= \frac{1}{2}\sin^2\theta_{j''} \qquad \text{(Q)} \end{aligned} \tag{1.35}$$

and for the R branch:

$$\begin{aligned} |\,\hat{\boldsymbol{\epsilon}}\cdot\hat{\boldsymbol{\mu}}\,|^2 &= \frac{1}{4}+\frac{1}{4}\,|\,\hat{\boldsymbol{j''}}\cdot\hat{\boldsymbol{k}}\,|^2-\frac{1}{2}s_3\hat{\boldsymbol{j''}}\cdot\hat{\boldsymbol{k}} \\ &= \frac{1}{4}+\frac{1}{4}\cos^2\theta_{j''}-\frac{1}{2}s_3\cos\theta_{j''} \qquad \text{(R)} \end{aligned} \tag{1.36}$$

The polarisation of $\boldsymbol{j}$ arises from this intensity variation, and it can be shown that $|\,\hat{\boldsymbol{\epsilon}}\cdot\hat{\boldsymbol{\mu}}\,|^2$ is equivalent to the probability distribution of the azimuthal angle, $P(\theta_j)$, remembering that the azimuthal angles, θ_j and $\theta_{j''}$ are equivalent. Combining together the expressions above for P, Q and R branch excitation, a general expression is reached [37, 55]:

$$P(\theta_j)=\frac{1}{2}[1+3r_0^{(1)}(j)P_1(\cos\theta_j)+5r_0^{(2)}(j)P_2(\cos\theta_j)] \tag{1.37}$$

where $P_x(\cos\theta_j)$ is the xth-order Legendre polynomial and $r_0^{(x)}(j)$ is an extrinsic parameter dependent on the method of excitation [56] (P, Q or R transition, and nature of light polarisation) and equivalent to the expectation value of the xth-order Legendre polynomial of $\cos\theta_j$.

With purely linearly-polarised light $r_0^{(1)}(j)=0$ and $r_0^{(2)}(j)=2/5$ for Q branch transitions or $r_0^{(2)}(j)=-1/5$ for P or R branch excitation [57]. With purely circularly-polarised light $r_0^{(1)}(j)=0,+s_3/2$ or $-s_3/2$ whilst $r_0^{(2)}(j)=-1/5$ for Q branch excitation or $r_0^{(2)}(j)=1/10$ for P/R branch excitation [55]. Note that circularly-polarised light creates an aligned as well as oriented distribution but linearly-polarised light produces a distribution of angular momentum, $\boldsymbol{j}$, that is aligned only.

1.7 Quantum Beat Spectroscopy

In this work, angular momentum polarisation is monitored by quantum beat spectroscopy. Quantum beat spectroscopy is a Doppler-free technique arising from the creation of a coherent superposition of two or more eigenstates in an atom or molecule,

with the time evolution of the interference between these states measured by spectroscopy. Quantum beats were first demonstrated by Aleksandrov [58] and by Dodd *et al.* [59] in 1964. The coherently excited-states may arise from couplings between non-degenerate states that arise naturally, or on the application of an external field. Both Stark [60–62] and Zeeman fields [62–64] have been utilised in this way. The studies of this thesis focus on the use of Zeeman splitting to lift the degeneracy of different projections of the angular momentum on the field axis.

Early quantum beat studies focused on the measurement of hyperfine structure and Landé g factors in atomic species [65–68]. In 1979, studies were first extended by McDonald and co-workers to observe quantum beats in polyatomic molecules [69]. Quantum beat spectroscopy, particularly Zeeman quantum beat spectroscopy (ZQBS), has since been used extensively in the determination of spectroscopic quantities including the Landé g factor, energy level splittings and hyperfine coupling constants of molecules [62, 64, 70–79].

ZQBS can also be utilised in reaction dynamics and the study of molecular collisions [21, 80, 81]. The technique is primarily utilised in this thesis to study the collision dynamics of OH(A)+H_2. The technique has also been used in the study of half-collisions, measuring the angular momentum polarisation following photodissociative processes, for example, in ICN [82] and NO_2 [83]. The use of ZQBS in measuring angular momentum polarisation following H_2O_2 photolysis is demonstrated in chapter 2.

1.7.1 Qualitative Quantum Mechanical Description

Figure 1.7 illustrates the simplest system that the quantum beat phenomenon can arise from - a four level system [62]. $|a\rangle$, $|b\rangle$, $|i\rangle$ and $|f\rangle$ are eigenstates of the time-independent Schrödinger equation, $\hat{H}|n\rangle = E|n\rangle$.

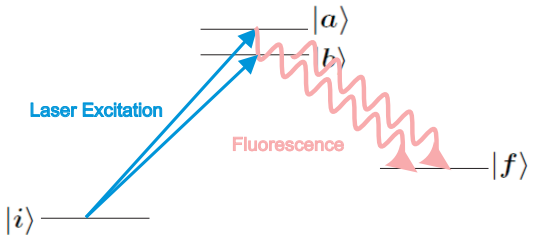

Figure 1.7: An energy diagram of a four level system where a coherent superposition of states $|a\rangle$ and $|b\rangle$ is created from photon absorption from the initial state, $|i\rangle$, and then fluoresces coherently to a final state, $|f\rangle$.

In the instant of preparation by excitation with a laser, $t = 0$, a superposition of states is created if the coherence width of the laser is larger than the energy spacing of those states:

$$|\Psi(0)\rangle = c_a|a\rangle + c_b|b\rangle. \tag{1.38}$$

Assuming that the laser pulse is short compared to the relaxation time of the two states in the coherent superposition, then the time evolution of each excited-state can be obtained from solving the time-dependent Schrödinger equation

$$i\hbar\frac{\partial}{\partial t}|\Psi(t)\rangle = \hat{H}|\Psi(t)\rangle, \tag{1.39}$$

with generic solution

$$|n(t)\rangle = |n(0)\rangle \mathrm{e}^{i\omega_n t}. \tag{1.40}$$

It follows that

$$|\Psi(t)\rangle = c_a|a\rangle \mathrm{e}^{-i\omega_a t} + c_b|b\rangle \mathrm{e}^{-i\omega_b t}, \tag{1.41}$$

where

$$\omega_x = \frac{2\pi E_x}{h}. \tag{1.42}$$

If the laser intensity is constant over the coherence width (or at least over the energy range containing $|a\rangle$ and $|b\rangle$), then the coefficients in the coherent superposition are proportional to the transition dipole moments, μ_{xi}, for excitation to $|a\rangle$ and $|b\rangle$. A

phenomenological constant γ_n is also introduced to account for decay of the population of each excited-state through fluorescence [70]

$$|\Psi(t)\rangle \propto \mu_{ai}|a\rangle \mathrm{e}^{-(i\omega_a+\frac{\gamma_a}{2})t} + \mu_{bi}|b\rangle \mathrm{e}^{-(i\omega_b+\frac{\gamma_b}{2})t}. \tag{1.43}$$

If the states in the superposition fluoresce to the same state, $|f\rangle$, the intensity of that fluorescence is proportional to $|\langle f|\hat{\boldsymbol{\mu}}|\Psi(t)\rangle|^2$, and so

$$\begin{aligned} I(t) &\propto |\mu_{ai}|^2|\mu_{af}|^2\mathrm{e}^{-\gamma_a t} + |\mu_{bi}|^2|\mu_{bf}|^2\mathrm{e}^{-\gamma_b t} \\ &+ |\mu_{ai}\mu_{af}\mu_{bi}\mu_{bf}|\mathrm{e}^{-\frac{(\gamma_a+\gamma_b)t}{2}}\cos(|\omega_a-\omega_b|t+\phi). \end{aligned} \tag{1.44}$$

The first two terms describe independent exponential decays of the two states, but the last term is a coherent term between these two states modulated by their energy difference $\omega_{ab} = |\omega_a - \omega_b|$. The term ϕ has been introduced to account for the phase at the start of the beat.

Assuming that the phenomenological constants and transition dipole moments are equal for the two states, the equation simplifies to

$$I(t) \propto [1+\cos(\omega_{ab}t+\phi)]\mathrm{e}^{-\gamma t}. \tag{1.45}$$

In this case the beat amplitude is the same as the amplitude of the decay. This is not typical and a further phenomenological constant, C, is introduced to adjust for this so that

$$I(t) \propto [1+C\cos(\omega_{ab}t+\phi)]\mathrm{e}^{-\gamma t}. \tag{1.46}$$

1.7.2 Zeeman Quantum Beats

In the presence of a magnetic field, degenerate magnetic sub levels are separated, and these are coherently excited in Zeeman quantum beat spectroscopy (ZQBS) [62]. ZQBS is used in these experiments to monitor angular momentum polarisation arising from the collision dynamics.

The interaction energy of the molecule in the magnetic field is given by [13]

$$E = -\boldsymbol{\mu}.\boldsymbol{H}, \tag{1.47}$$

where $\boldsymbol{H}$ is the applied magnetic field strength and $\boldsymbol{\mu}$ the magnetic dipole moment of the molecule. The largest contribution to the magnetic dipole is from electronic motion. For a Σ radical such as OH(A), the electronic orbital angular momentum, $\boldsymbol{l}$, is equal to 0. Consequently, the only contribution from electronic motion is from the electronic spin angular momentum, $\boldsymbol{S}$, [46]

$$\mu_e = -g_e \mu_B \sqrt{S(S+1)} \approx 2.002. \tag{1.48}$$

where μ_B is the Bohr magneton and g_e is the Landé g factor for a free electron. In the Hunds case (b) regime, $\boldsymbol{S}$ couples to $\boldsymbol{N}$, causing the time averaged magnetic moment to lie in the direction defined by $\boldsymbol{j}$. $\boldsymbol{j}$ itself couples to the nuclear spin, and the magnetic moment lies along the resulting total angular momentum, $\boldsymbol{F}$. The magnetic moment is

$$\mu_F = \mu_B g_F M_F, \tag{1.49}$$

where M_F is the quantum number for the magnetic sub level and g_F is the Landé g factor

$$g_F = g_j \frac{F(F+1) + j(j+1) - I(I+1)}{2F(F+1)} \tag{1.50}$$

and

$$g_j = g_e \frac{j(j+1) + S(S+1) - N(N+1)}{2j(j+1)}. \tag{1.51}$$

Combining equation 1.49 and equation 1.47, the interaction energy of each sub level, M_F, in a magnetic field, $\boldsymbol{H}$, becomes

$$E = -g_F \mu_B M_F H. \tag{1.52}$$

Provided the coherence width of the laser is larger than the spacing between magnetic sub-levels, it is possible for a superposition of those sub-levels to be excited. The levels that are coherently excited are dependent upon the selection rule, determined by the polarisation of the excitation laser. When circularly-polarised light is used, creating an oriented distribution of $\boldsymbol{F'}$, the magnetic quantum number selection rule is $\Delta M_F = 1$. Using equation 1.52 to calculate ω in equation 1.46

$$\omega = \frac{\Delta E}{\hbar} = \frac{g_F \mu_F H}{\hbar} = \omega_F \tag{1.53}$$

whilst for linearly-polarised light the selection rule is $\Delta M_F = 2$, so the frequency is

$$\omega = \frac{\Delta E}{\hbar} = \frac{2 g_F \mu_F H}{\hbar} = 2\omega_F. \tag{1.54}$$

So, the frequency in the alignment case is double that in the orientation case. ω_F is the Larmor frequency for the precession of the angular momentum distribution in the magnetic field. The beat amplitude is a measure of the degree of polarisation and is represented by the constant C in equation (1.46).

1.7.3 Classical Description

A classical description of ZQBS can also be useful in better understanding this phenomenon. In the presence of a weak magnetic field, $\boldsymbol{H}$, the magnetic moment of the OH radical precesses in the plane perpendicular to the field axis. Any anisotropy in the $\boldsymbol{j}$ distribution perpendicular to $\boldsymbol{H}$ similarly precesses about the field. The rate of this precession is given by the Larmor frequency for the state j, ω_j. The distribution of $\boldsymbol{j}$ about Z, where $Z \parallel H$, at time t is given by [13, 84]

$$P(\theta_j, \phi_j; t) = \boldsymbol{R}(0, \omega_j t, 0) P(\theta_j, \phi_j), \tag{1.55}$$

where $\boldsymbol{R}(0, \omega_j t, 0)$ is a rotation transformation and $P(\theta_j, \phi_j)$ is the $\boldsymbol{j}$ distribution at time 0. In the case where $\boldsymbol{j}$ is an excited-state angular momentum, at the point of excitation t is set to 0, and $P(\theta_j, \phi_j)$ is given by equation (1.37) leading to [13, 84]

$$P(\theta_j, \phi_j; t) = \frac{1}{2}\left[1 + 3r_0^{(1)} D_{p0}^{(1)}(0, \omega_L t, 0) C_p^{(1)}(\theta_j, \phi_j) + 5r_0^{(2)} D_{p0}^{(2)}(0, \omega_L t, 0) C_p^{(2)}(\theta_j, \phi_j)\right]. \tag{1.56}$$

where $D_{pq}^{(k)}$ are rotation matrices and $C_p^{(k)}$ are modified spherical harmonics.

In the case where this state fluoresces, the emission intensity is given by

$$I(t) = \int P(\theta_j, \phi_j; t) |\boldsymbol{\epsilon}_d \cdot \boldsymbol{\mu}_e|^2 \exp[-k_p t] \mathrm{d}\theta_j \mathrm{d}\phi_j, \tag{1.57}$$

where $\boldsymbol{\epsilon}_d$ is the preferred polarisation for emission detection defined by the optics preceding an experimental detector, and $\boldsymbol{\mu}_e$ is the transition dipole moment for the emission transition. The exponential term accounts for the decay of the excited-state population through fluorescence and collisional quenching. The evaluation of $|\boldsymbol{\epsilon}_d \cdot \boldsymbol{\mu}_e|^2$ proceeds as in section 1.6, and is dependent upon the emission branch and the sensitivity of the detection optics. When the polarised distribution, $P(\theta_j)$, is produced

by linearly-polarised light and the detector geometry is similarly linearly-polarised, the emission intensity is given by

$$I(t) = \begin{cases} A' \left[1 - \frac{1}{4} r_0^{(2)} \big(3\cos(2\omega_j t + \phi) + 1\big)\right] \exp(-k_p t) & \text{(P/R)} \\ A' \left[1 + \frac{1}{2} r_0^{(2)} \big(3\cos(2\omega_j t + \phi) + 1\big)\right] \exp(-k_p t) & \text{(Q)} \ . \end{cases}$$

Alternatively, if excited with circularly-polarised light and the detection geometry limits the sensitivity of the detector to only a certain helicity, the emission intensity is given by

$$I(t) = \begin{cases} A' \left[1 + \frac{3}{2} r_0^{(1)} \cos(\omega_j t + \phi) + \frac{1}{2} r_0^{(2)} P_2\big(\cos(\omega_j t + \phi)\big)\right] \exp(-k_p t) & \text{(P)} \\ A' \left[1 - r_0^{(2)} P_2\big(\cos(\omega_j t + \phi)\big)\right] \exp(-k_p t) & \text{(Q)} \\ A' \left[1 - \frac{3}{2} r_0^{(1)} \cos(\omega_j t + \phi) + \frac{1}{2} r_0^{(2)} P_2\big(\cos(\omega_j t + \phi)\big)\right] \exp(-k_p t) & \text{(R)} \ , \end{cases}$$

where ϕ is a phase factor accounting for the detection geometry and the relationship between $\boldsymbol{\epsilon}_d$ and $\boldsymbol{\epsilon}_{pr}$. It is clear that there are two terms in the emission intensity: the first a decay, and the second a modulation of that decay expressed as a cosine factor. This modulation gives rise to the 'beat' in quantum beat spectroscopy.

The emission intensity in the case of linearly-polarised excitation and detection can be re-expressed as [13]

$$I(t) = A''[1 - P(t)\cos(2\omega_j t + \phi)]\exp(-k_p t). \tag{1.58}$$

P is the degree of linear polarisation [13]

$$P(t) = \frac{I_{\parallel}(t) - I_{\perp}(t)}{I_{\parallel}(t) + I_{\perp}(t)}, \tag{1.59}$$

where $I_\perp$ and $I_\parallel$ define the relationship between $\boldsymbol{\epsilon}_d$ and $\boldsymbol{\epsilon}_{pr}$ as perpendicular or parallel, respectively.

In orientation experiments, the degree of orientation is defined as [13]

$$\mathcal{C}(t) = \frac{I_{\circlearrowleft\circlearrowleft}(t) - I_{\circlearrowleft\circlearrowright}(t)}{I_{\circlearrowleft\circlearrowleft}(t) + I_{\circlearrowleft\circlearrowright}(t)}, \tag{1.60}$$

where $I_{\circlearrowleft\circlearrowleft}(t)$ and $I_{\circlearrowleft\circlearrowright}(t)$ describe whether the emission signal and the detection geometry have same or opposite helicities. On consideration that the distributions following excitation with two opposite circular polarisations are separated by a phase factor of π and that $\cos(\theta + \pi) = -\cos(\theta)$ for P/R branch emission,

$$\begin{aligned} \mathcal{C}(t) &= \frac{3r_o^{(1)}\cos(\omega_j t + \phi)}{2 + r_0^{(2)} P_2\big(\cos(\omega_j t + \phi)\big)} \\ &\simeq \frac{3}{2} r_o^{(1)} \cos(\omega_j t + \phi). \end{aligned} \tag{1.61}$$

1.8 Previous Experimental Work

1.8.1 OH(A)+H_2

The collision dynamics of the excited-state hydroxyl radical, OH(A), have been the subject of considerable previous study, in part because the hydroxyl radical is an important species in combustion and atmospheric chemistry [85–89]. It is also a radical that can be readily observed through laser-induced fluorescence (LIF) experiments [86, 87]. Studies have considered both atomic and molecular colliders, and several such colliders readily electronically quench the radical to its ground-state OH(X) [90–95]. The H_2 molecule provides the simplest possible molecular collider, as well as one of importance in combustion chemistry [88, 96, 97].

Previous studies of this collision system, as with most OH(A) bimolecular collisions have focused on the outcome of electronic quenching [90–92, 94, 95]. In OH(A)+H_2 collisions there are two different quenching outcomes; the first is non-reactive quenching to the electronic ground-state of the OH radical [98]

$$OH(A) + H_2 \rightarrow OH(X) + H_2$$

Alternatively the radical may be quenched reactively [99]

$$OH(A) + H_2 \rightarrow H_2O + H$$

and this reaction may occur via an insertion or abstraction mechanism [98]. The experiments in this thesis only monitor the population of the excited-state radical, and the two quenching outcomes are therefore indistinguishable. Consequently, non-reactive and reactive quenching will often be collectively referred to as quenching or electronic quenching.

The earliest studies on OH(A)+H_2 utilised LIF to quantify this combined quenching cross section and its relationship with the collision energy (temperature) [94, 100] or OH(A) rotational state [90–92, 100]. The experiments performed in this thesis add to this previous work by presenting further cross sections for these combined processes.

More recent experiments have explored the branching ratio between the two quenching pathways and the product-state distribution [101]. Lester and co-workers have been heavily involved in exploring the outcomes of the quenching pathway in OH(A)+H_2, and their work is the subject of a recent review in reference [98]. Initially, studies focused on the reactive quenching pathway, using Doppler scans of the LIF spectrum of the H atom product [102, 103]. The experiments by Lester and co-workers [101, 102, 104, 105] study the collisions in a supersonic beam expansion, providing a

low collision energy of $\sim 0.005\,\mathrm{eV}$. The expanded gas consists of HNO_3 alongside He and the molecular hydrogen collider. OH(A) radicals are subsequently generated by a photolysis laser at 193 nm. Davis *et al.* used a crossed molecular beam arrangement and studied the differential cross section ($\boldsymbol{k}$-$\boldsymbol{k}'$ correlation) [106]. This study focused on the isotopologue collision system OH(A)+D_2 rather than OH(A)+H_2. This experiment used Rydberg tagging of the hydrogen or deuterium atom product. In this crossed molecular beam arrangement, the collision energy is superthermal in nature at $\sim 0.16\,\mathrm{eV}$. Collectively, the experiments by Davis *et al.* and Lester *et al.* indicate that the H_2O product is produced with a large degree of vibrational excitation in both stretching and bending modes. The experiments have provided evidence for the production of H_2O via both abstraction and insertion mechanisms. In the former case, the collisions are predominantly forward scattered, whereas forward-backward scattering is associated with the latter pathway [106]. It is also clear that the direct scattering abstraction mechanism dominates the process, at $\sim 75\%$ of the total.

More recent studies by Lester and co-workers have focused on the non-reactive quenching pathway, investigating the OH(X,ν'',j'') product-state distribution by probing the ground-state quenched products [104, 105, 107, 108]. These experiments demonstrated a clear non-statistical population distribution, with a strong preference for the A' lambda-doublet and rotational excitation of the OH(X) product. At the same time, relatively little vibrational excitation of OH(X) was observed.

Instead of considering the outcome in quenched collisions, the studies presented in this thesis will give a more extensive focus on the outcomes of the non-quenched collisions between OH(A) and H_2 than has been seen previously. Experimental measurements are taken to determine rotational energy transfer (RET) cross sections for collisions in which OH(A, $\nu = 0$, N_{OH})+H_2 $\rightarrow$ OH(A, $\nu = 0$, N'_{OH})+H_2 where $N'_{\mathrm{OH}} \neq N_{\mathrm{OH}}$. These are measured as a function of N_{OH}, and add considerably to previous measurements of this kind [109]. Going further than this, the studies described in this thesis

also explore the collisional depolarisation of the OH(A) angular momentum.

Recent works by Brouard, Lester, Aoiz and Dagdigian have attempted a unified description of the quenching, non-quenching RET, and collisional depolarisation processes for the OH(A)+Kr system. These studies utilised experiments and theory, employing both quantum mechanics and QCT calculations [93, 110, 111]. The work in this thesis strives towards a similar comprehensive analysis of the OH(A)+H_2 collision dynamics.

1.8.2 OH Depolarisation

Collisional depolarisation of the OH radical in both its ground, OH(X), and first excited-state, OH(A), with rare gas colliders has been the subject of considerable study [20, 24, 34, 37, 55, 57, 83, 93, 110–124]. These studies determine the cross section for the loss of polarisation, and as such provide a measure of the rotational tilt. Brinkman and Crosley carried out one of the earliest studies of OH(A) depolarisation using a simple one photon fluorescence approach [20]. This study was limited looking only at fluorescence from the $N = 4$, $j = 4.5$ quantum state, but did obtain depolarisation cross sections for molecular colliders - O_2, N_2, CO_2 and H_2O - alongside atomic colliders - He and Ar. Through employing a ZQBS technique (the concepts of which have been set out in section 1.7) Brouard and co-workers have added greatly to this area, studying the collisional depolarisation of OH(A) with rare gases [24, 34, 37, 55, 57, 83, 93, 110–117]. The results of these measurements are reviewed alongside the experimental results for OH(A)+H_2 in chapter 6.

McKendrick and co-workers have developed a polarisation spectroscopy (PS) technique to determine cross sections for the loss of bulk polarisation [38, 40, 125]. This is a non-linear coherent spectroscopic technique used in one and two colour variants that creates a polarised distribution in both the upper and lower states of a transition. Investigating the hydroxyl radical in its ground-state, OH(X), has tended to be the

focus of these depolarisation studies, and extensive work has been carried out on He, Ar [118–122] and Xe [123] rare gas colliders, but also on molecular collision partners, N_2 and O_2 [124]. Unlike the ZQBS technique, PS cannot separate out population decay and polarisation decay contributions to the bulk polarisation decay. However, the PS technique inherently has a higher resolution than ZQBS, allowing it to consider the polarisation decay from individual quantum states with ease [38, 114]. The PS technique also has the advantage of being more adaptable as it is able to investigate depolarisation in the ground-state. Due to their different strengths and weaknesses, the two techniques can be considered complementary. As such, using them together led to a greater understanding of depolarisation in OH(A)+He/Ar collisions [114]. Reference [38] reviews both ZQBS and PS approaches, whilst also considering the one photon fluorescence decay approach utilised by Brinkman and Crosley [20].

1.9 Theoretical Studies

In this thesis, theoretical calculations are performed to explore the non-quenching dynamics of OH(A)+H_2. The calculations use a quasi-classical trajectory (QCT) method to propagate trajectories on a calculated potential energy surface (PES) [126] that describes the potential energy governing the interaction. The calculation of cross sections for RET is of particular interest in these studies.

Whilst RET has been the subject of extensive theoretical study between a molecular and atomic collider, RET between two different molecular colliders has been covered in much less previous work [127–167]. No previous theoretical calculations have been performed to determine inelastic RET cross sections for OH(A)+H_2 collisions, or indeed any other OH(A) collisions with molecular species. However, there have been some previous studies of RET with molecular colliders involving the radical in its ground-state, OH(X). These include collisions with H_2 [128–133] and CO [134]. Most of these

theoretical studies of RET have tended to be quantum mechanical in origin, using either the coupled states approximation [136], or close-coupled calculations [135].

Due to its status as the most abundant molecule in the universe, and consequent importance in interstellar chemistry, there has been considerable interest in inelastic collisions involving H_2. The interest is typically in the RET induced in the accompanying molecular collider rather than the H_2, and this is the primary interest in this study too. Quantum scattering calculations have been performed to determine inelastic RET cross sections for a variety of electronic ground-state molecules with a H_2 collider, including H_2O [137–143] and its isotopologues [144, 145], as well as with NH_3 [146, 147], HCN [148–151], CN [152], HC_3N [153], SO [154], SO_2 [155], SiS [156], CO [157], O_2 [158], HCl [159] and with itself - H_2 [135, 160–163]. Many of these studies have made use of a reduced dimensional PES, for example, in the study by Vera *et al.*, where bond lengths and bond angles are fixed for H_2+HCN collisions reducing the PES to 4 dimensions [149]. A similar method was used in a study of O_2+H_2 by Kalugina *et al.* [158]. Many of these H_2 collision system studies are devoted to the differences in the RET products that arise from collisions with *para*-H_2 and *ortho*-H_2 [131, 147–150, 153, 156, 158, 159, 161]. In these QM scattering calculations parity changing *ortho*↔*para* collisions are restricted and typically cross sections with a change in the H_2 rotational angular momentum are small.

QCT studies focusing on bimolecular collisions and exploring RET, as in this thesis, are far fewer in number. The small number of exceptions include: a study by Wallis and Thompson on HF+CO collisions [164], studies on HF+HF collisions by Schwenke *et al.* [165], and H_2+H_2O collisions by Faure *et al.* [166]. The Faure *et al.* study considers the rotational de-excitation rate constants for H_2O with a H_2 collider, and since in this thesis QCT is used to calculate RET cross sections for OH(A) with H_2 the results and methodology are of interest. The molecular bond lengths are fixed in the Faure *et al.* study, as they will be in the present work [166]. Furthermore, the H_2

rotational state is chosen in each trajectory through a consideration of the population distribution, again as in the present work. The study reported good agreement between the QCT results and those from previous QM studies. However, the classification of good agreement was more modest than will be accepted in this study, as the QCT rate constants only agreed with the QM results to a factor of 1-3 [166], though agreement was better for calculations run at higher temperatures (greater than 100 K).

QCT studies of the OH(X)+CO by Kudla *et al.* provide an example of a QCT study of RET with an OH(X) collider [134, 168]. Here the PES is reduced to 3 dimensions by fixing the two bond lengths and forcing planar geometries [134]. The cross sections from the QCT calculations show excellent agreement with those from experiment despite this [134]. A further QCT study by Kłos *et al.* considered OH(X)+HCl collisions [167] using a reduced dimensionality 2D PES following averaging over torsional angle and orientation of the HCl diatom, directly analagous to the PES defining an atom-diatom collision.

No previous theoretical studies of depolarisation cross sections in bimolecular collisions have been identified. However, theoretical formalisms to determine depolarisation properties have been developed and applied to diatom collisions with atomic colliders. Brouard, Aoiz and co-workers have used both quantum mechanical and QCT methods to consider depolarisation in OH(A)+Rg collision systems [24, 37, 111, 113, 115, 116]. Alexander and Dagdigian have formulated approaches with quantum mechanics to determine depolarisation properties for OH(X)+Rg systems [169–171] as well as for the OH(A)+Kr collision system [93, 111].

1.9.1 Potential Energy Surfaces and the Born-Oppenheimer Approximation

The forces involved in determining the outcome of molecular collisions are described by the gradients of the PES for that system [23]. Theoretical calculations such as those in this thesis involve running trajectories on calculated PESs. Such calculations allow rate constants or cross sections for various processes to be determined, and an exploration of the mechanism involved.

The motion of nuclei and electrons in molecular collision systems are characterised by time-dependent wavefunctions, $\Psi(\boldsymbol{x}, \boldsymbol{X}, t)$, which are solutions of the time-dependent Schrödinger equation [23]

$$i\frac{\partial}{\partial t}\Psi(\boldsymbol{x}, \boldsymbol{X}, t) = \hat{H}\Psi(\boldsymbol{x}, \boldsymbol{X}, t), \tag{1.62}$$

where $\boldsymbol{x}$ and $\boldsymbol{X}$ describe the positions of the electrons and nuclei, respectively. The molecular Hamiltonian can be expressed as [23]

$$\hat{H} = \hat{T}_N + \hat{T}_e + \hat{V}_{eN} + \hat{V}_{ee} + \hat{V}_{NN}, \tag{1.63}$$

where $\hat{T}$ are kinetic energy operators and $\hat{V}$ potential energy operators, where e signifies electrons, and N nuclei. The potential energies depend solely upon the relative Cartesian co-ordinates of the particles - electrons and nuclei. Since the nuclear masses are many orders of magnitude larger than the mass of an electron, the terms from the nuclear kinetic energy operator, $\hat{T}_N$, are very small and are often considered as a perturbation. The electronic Hamiltonian, $\hat{H}_e$, is defined in the absence of $\hat{T}_N$, and eigenfunctions, $\psi_i(\boldsymbol{x}; \boldsymbol{X})$, for the electronic time-independent Schrödinger equation are such that [23]

$$\hat{H}_e\psi_i(\boldsymbol{x}; \boldsymbol{X}) = E_i(\boldsymbol{X})\psi_i(\boldsymbol{x}; \boldsymbol{X}). \tag{1.64}$$

With the nuclear kinetic energy operator considered a perturbation, the total wave-function can be expressed as [23]

$$\Psi(\boldsymbol{x}, \boldsymbol{X}) = \sum_{i=0}^{\infty} \psi_i(\boldsymbol{x}; \boldsymbol{X}) \phi_i(\boldsymbol{X}) \tag{1.65}$$

where the coefficients $\phi_i(\boldsymbol{X})$ are functions of the nuclear co-ordinates. Removing the co-ordinates $\boldsymbol{X}$ and $\boldsymbol{x}$ for simplicity and placing into the time-independent Schrödinger equation leads to [23]

$$\begin{aligned}
(\hat{T}_N + \hat{H}_e) \sum_{i=0}^{\infty} \psi_i \phi_i &= E \sum_{i=0}^{\infty} \psi_i \phi_i \\
\sum_{i=0}^{\infty} \left[\sum_{\alpha=1}^{N} -\frac{1}{2M_\alpha} \nabla_\alpha^2 + \hat{H}_e \right] \psi_i \phi_i &= E \sum_{i=0}^{\infty} \psi_i \phi_i \\
\sum_{i=0}^{\infty} \left\{ \sum_{\alpha=1}^{N} -\frac{\nabla_\alpha}{2M_\alpha} \left[\psi_i \nabla_\alpha \phi_i + \phi_i \nabla_\alpha \psi_i \right] + \phi_i \hat{H}_e \psi_i \right\} &= E \sum_{i=0}^{\infty} \psi_i \phi_i \\
\sum_{i=0}^{\infty} \left\{ \sum_{\alpha=1}^{N} -\frac{1}{2M_\alpha} \left[\psi_i (\nabla_\alpha^2 \phi_i) + 2(\nabla_\alpha \phi_i)(\nabla_\alpha \psi_i) + \phi_i (\nabla_\alpha^2 \psi_i) \right] + \phi_i E_i(\boldsymbol{X}) \psi_i \right\} &= E \sum_{i=0}^{\infty} \psi_i \phi_i,
\end{aligned} \tag{1.66}$$

where the summation across α accounts for the N nuclei present in the system. Pre-multiplying by ψ_j^* gives [23]

$$\begin{aligned}
\sum_{i=0}^{\infty} \left[\sum_{\alpha=1}^{N} -\frac{1}{2M_\alpha} \langle \psi_j | \psi_i \rangle \nabla_\alpha^2 \phi_i + 2(\nabla_\alpha \phi_i) \langle \psi_j | \nabla_\alpha | \psi_i \rangle + \phi_i \langle \psi_j | \nabla_\alpha^2 | \psi_i \rangle + \phi_i E_i(\boldsymbol{X}) \langle \psi_j | \psi_i \rangle \right] \\
= E \sum_{i=0}^{\infty} \langle \psi_j | \psi_i \rangle \phi_i.
\end{aligned} \tag{1.67}$$

Integrating over all the electronic co-ordinates and noting that different eigenstates are orthogonal leads to [23]

$$\sum_{\alpha=1}^{N} -\frac{1}{2M_\alpha}\nabla_\alpha^2\phi_j + E_j(\boldsymbol{X})\phi_j - \sum_{i=0}^{\infty}\sum_{\alpha=0}^{N}\frac{1}{2M_\alpha}\left[2\langle\psi_j|\nabla_\alpha|\psi_i\rangle(\nabla_\alpha\phi_i) + \langle\psi_j|\nabla_\alpha^2|\psi_j\rangle\phi_i\right] = E\phi_j. \tag{1.68}$$

The term in the second summation, $\frac{1}{2M_\alpha}[2\langle\psi_j|\nabla_\alpha|\psi_i\rangle(\nabla_\alpha\phi_i) + \langle\psi_j|\nabla_\alpha^2|\psi_j\rangle\phi_i]$, expresses the coupling of nuclear wavefunctions for the j-th electronic state to the nuclear wavefunctions of the i-th electronic state. It instead can be expressed as [23, 172]

$$\left[\hat{T}_N + E_j(\boldsymbol{X})\right]\phi_j - \sum_{i=0}\hat{\Lambda}_{ji}\phi_j = E\phi_j, \tag{1.69}$$

where $\hat{\Lambda}_{ji}$ is the coupling constant for the j-th and i-th electronic state, and these terms are neglected in the Born-Oppenheimer approximation. The approximation makes use of the considerably larger mass, and thus slower motion, of the nuclei relative to the electrons. Consequently, the nuclei are not considered to move on the timescale of electronic motion. The equation reduces to [23, 173]

$$\hat{H}\phi_j = \left[\hat{T}_N + E_j(\boldsymbol{X})\right]\phi_j = E\phi_j. \tag{1.70}$$

The $E_j(\boldsymbol{X})$ functions give adiabatic PESs to describe the interaction between molecules in the collision system. PESs are continuous functions, but their calculation usually involves first performing *ab-initio* calculations to find energies, their first derivatives (forces) and, commonly, their second derivatives at a series of nuclear coordinates. These *ab-initio* points are then fit to a functional form.

1.9.2 Non-Adiabatic Processes and Conical Intersections

In the event that values of $E_j(\boldsymbol{X})$ in equation (1.68) are close for different j electronic states, or indeed degenerate, the value of $\langle\psi_j|\nabla_\alpha|\psi_i\rangle$ becomes large and the term in parentheses in equation (1.68) can no longer be ignored - the Born-Oppenheimer approximation breaks down. This leads to non-adiabaticity in the description of the collision system, and the potential energy surface is then better described by diabatic potentials [23].

The coupling constant introduced in equation (1.69) can be expressed as [23]

$$\hat{\Lambda}_{ji} = \frac{1}{2M}\left(2\boldsymbol{F}_{ji}\cdot\nabla + \boldsymbol{G}_{ji}\right), \tag{1.71}$$

where [23, 173]

$$\boldsymbol{F}_{ji} = \langle\psi_j|\nabla|\psi_i\rangle = \frac{\langle\psi_j|\nabla\hat{H}_e|\psi_i\rangle}{E_i(\boldsymbol{X}) - E_j(\boldsymbol{X})}, \tag{1.72}$$

and [23]

$$\boldsymbol{G}_{ji} = \langle\psi_j|\nabla^2|\psi_i\rangle. \tag{1.73}$$

The later second derivative couplings are typically very small so the $\boldsymbol{F}_{ji}$ terms are critical [23, 173]. When ψ_i and ψ_j are degenerate the $\boldsymbol{F}_{ji}$ term becomes infinite. The derivative coupling terms are at their largest when the electronic wavefunction changes rapidly with small changes in the nuclear co-ordinates. This tends to occur in regions of near degeneracy and close to avoided crossings between PESs. In these regions, electronic motion is not able to re-arrange on the timescale of nuclear motion to ensure the lowest energy configuration results. As a consequence, the nuclear motion may progress onto another PES. Such behaviour is non-adiabatic and in this case particle motion is best described by diabatic PESs [23]. The wavefunctions, $\psi_i^{(0)}$, are no longer eigenstates of the electronic Hamiltonian and the potential energy matrix has non-zero off-diagonal elements, whilst the nuclear kinetic energy matrix is diagonal [23].

If we assume just two orthonormal diabatic states, $\psi_1^{(0)}$ and $\psi_2^{(0)}$, which are eigenfunctions of the Hamiltonian $\hat{H^{(0)}}$, related to the electronic Hamiltonian via

$$\hat{H}_{el} = \hat{H^{(0)}} + \hat{V} \tag{1.74}$$

where $\hat{V}$ is a matrix defining the couplings between states, the eigenfunctions of the electronic Hamiltonian (the adiabatic states) can be described as a linear combination of the orthonormal diabatic states

$$\psi_{\pm} = c_1\psi_1^{(0)} + c_2\psi_2^{(0)}. \tag{1.75}$$

Therefore

$$\begin{aligned} \hat{H}_{el}\psi_{\pm} &= E_{\pm}\psi_{\pm} \\ c_1\hat{H}_{el}\psi_1^{(0)} + c_2\hat{H}_{el}\psi_2^{(0)} &= E_{\pm}(c_1\psi_1^{(0)} + c_2\psi_2^{(0)}). \end{aligned} \tag{1.76}$$

premultiplying by $\langle\psi_1^{(0)}|$ or $\langle\psi_2^{(0)}|$ and integrating over all space yields the 'secular equations' [23, 173]

$$\begin{aligned} c_1(H_{11} - E_{\pm}) - c_2H_{12} &= 0 \\ c_1H_{21} + c_2(H_22 - E_{\pm}) &= 0, \end{aligned} \tag{1.77}$$

with solutions found through solving the quadratic equation

$$\begin{aligned} E_{\pm}^2 - (H_{11} + H_{22})E_{\pm} + H_{11}H_{22} - H_{21}H_{12} = 0 \\ E_{\pm} = \frac{1}{2}(H_{11} + H_{22}) \pm \frac{1}{2}\sqrt{(H_{11} - H_{22})^2 + 4H_{12}H_{21}}. \end{aligned} \tag{1.78}$$

$E_{\pm}$ are the adiabatic PESs. Assuming that couplings are only non-zero between different diabatic states such that

$$V_{11} = V_{22} = 0 \tag{1.79}$$

$$V_{12} \neq 0 \tag{1.80}$$

$$H_{11} = H_{11}^{(0)} = E_1^{(0)} \tag{1.81}$$

$$H_{22} = H_{22}^{(0)} = E_2^{(0)}, \tag{1.82}$$

at a point of degeneracy for the diabatic states ($H_{11} = H_{22}$) the adiabatic states would only be degenerate such that $E_+ = E_-$ if $H_{12}H_{21} = |H_{12}|^2 = 0$. Since $H_{12} = V_{12}$, if the couplings between diabatic states are non-zero, then the adiabatic states undergo an avoided crossing. In the case of a diatomic molecule where there is only one degree of freedom and the coupling operator is of a totally symmetric nature, non-zero coupling terms arise when diabatic states are of the same symmetry. A further inference is that adiabatic states of different symmetry can cross. This gives rise to the well-known non-crossing rule that states of the same symmetry cannot cross [23, 173, 174].

It is a common misconception of the non-crossing rule that states of the same symmetry cannot cross in any case, and this is the subject of some discussion in reviews by Yarkony [172, 175]. In reality, the additional degrees of internal freedom that arise in polyatomic cases mean states of same symmetry can cross [172, 173, 175]. These crossings lead to conical intersections connecting different adiabatic PESs and allowing passage from one surface to another in the dynamics, i.e. non-adiabatic activity. Despite the conclusion that intersections are not limited by symmetry constraints, conical intersections can be more easily identified when they are symmetry-induced [23, 173]. Furthermore, the identification of symmetry-induced conical intersections is often a useful first step in identifying a wider seam of conical intersections [175]. Discussion will now turn to identifying symmetry-induced conical intersections in simple triatomic

systems. Symmetry-induced conical intersections arise when, in a limited range of geometries, the symmetry point group for the nuclei is of a higher order. Exclusively in this region, the two electronic wavefunctions have different symmetry. Under these circumstances, a conical intersection can be induced if the diabatic wavefunctions are degenerate, since the coupling element $V_{12} = 0$ on symmetry grounds [23, 172, 173, 175].

Examples of conical intersections in triatomic systems are provided by the OH(A)+Rg systems that are often the subject of comparison in this thesis [93]. In most geometries, the system is described by the C_s point group. The excited electronic state and ground electronic state, with OH(X) in its A' lambda doublet, transform as A' irreducible representations of the C_s point group, and the states are described as the OH(A)+Rg $2^2A'$ and OH(X)+Rg $1^2A'$ respectively. At points of degeneracy between diabatic states, the adiabatic states typically undergo an avoided crossing [93]. In linear geometries, the system has higher order symmetry described by the $C_{\infty v}$ point group. In this case the ground and excited-states transform as Π and Σ irreps of the point group respectively, and the states are described as OH(X)+Rg $^2\Pi$ and OH(A)+Rg $^2\Sigma^+$ [93]. As the states are of different symmetry, they are allowed to cross and a conical intersection between them is observed - these crossings do not however, have to be energetically accessible.

Returning to the more general case, the region of conical intersections can be described by two orthogonal types of coordinate [23, 172, 173]. These coordinates are 3 dimensional displacement vectors for all the nuclei in the system. The first is a 'tuning coordinate' along which the movement of nuclei maintains the symmetry of the intersection. This motion is totally symmetric in nature and typically moves to and then away from the point of degeneracy and crossing. In the simple two state system described above, this lifts the condition $H_{11} = H_{22}$ [173]. The second coordinate is a 'coupling coordinate' and involves non-totally symmetric motion so that the adiabatic states undergo an avoided crossing, as the condition $V_{12} = 0$ is no longer met [173].

Along the remaining $(N^{\text{int}} - 2)$ coordinates, where N^{int} is the number of internal degrees of freedom, there is a $(N^{\text{int}} - 2)$-dimensional seam of intersections, although the energy at the point of degeneracy varies. If a point of intersection is plotted in the plane defined by the tuning and coupling coordinate, known as either the branching [176] or g-h plane [175], it takes the appearance of a double cone (as shown in figure 1.8) and hence is known as a conical intersection [23]. Recourse to the rule that the conical intersection is maintained along $(N^{\text{int}} - 2)$ coordinates is useful in interpreting and understanding the shape of seams of intersection.

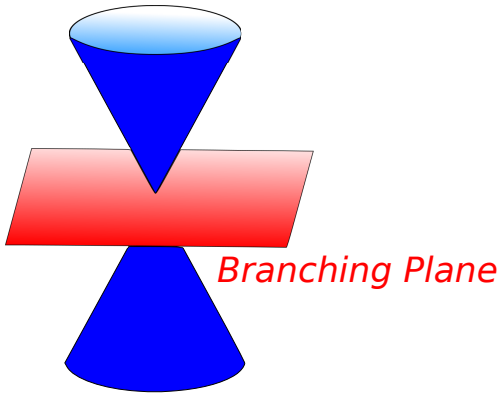

Figure 1.8: Model conical intersection shown in the branching plane defined by orthogonal tuning and coupling coordinates.

1.9.3 OH(A)+H_2

Seams of intersections between electronic states describing the dynamics in the H_3O system have been identified [107, 177, 178]. These funnel the system from the first excited-state surface describing the OH(A $^2\Sigma^+$)+H_2 potential to either the non-reactive products OH(X $^2\Pi$)+H_2 or reactive products $H_2O(\tilde{X}^1A_1)$+H. These two alternative electronic quenching pathways are illustrated in a qualitative picture in figure 1.9 [98]. The ground-state surface is subject to lambda doubling, but coupling between the A' doublet ground-state and the first excited-state is most significant in determining the outcome of collisions in the excited-state.

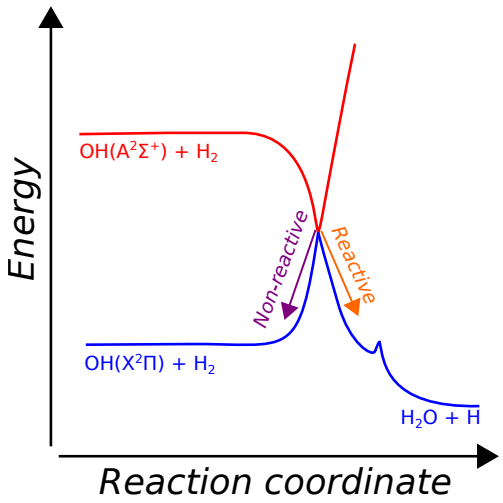

Figure 1.9: Qualitative picture of the conical intersection between ground and excited-states in the OH+H_2 collision system showing electronic quenching routes to reactive and non-reactive products. Adapted from reference [98].

The description of these three states is dependent on the geometry of the nuclei: for general C_1 geometries, the states are 1,2,3, ^2A; for colinear $C_{\infty v}$ geometries, the ground-states are $1^2\Pi$ and the excited-state is $1^2\Sigma^+$; for C_{2v} geometries, the states are 1^2B_1, 1^2B_2 and 1^2A_1; and for other coplanar C_s geometries, the states are $1^2A''$, $1^2A'$ and $2^2A'$ [178]. For simplicity, the coupled states shall be referred to in this discussion as either the ground and excited-state, or the $1^2A'$ and $2^2A'$ state, using the terminology of the C_s geometries. The ground-state $1^2A'$ PES alone has been the subject of considerable study [179–186], particularly because of the presence of a reactive pathway to H_2O. The excited-state surface has been the subject of fewer studies, although some have focused on the area around the conical intersection [105, 107, 178]. Only two dynamics studies have been performed for the OH(A)+H_2 collision system [187–189], but more work has been done to explore the shape of this PES. These different studies are reviewed in this section.

One of the earliest theoretical studies of the OH(A)+H_2 system by Clary *et al.* calculated *ab initio* points for the H-end C_{2v} geometry (T-shaped configuration with the hydrogen atom of the radical pointed at the H_2 diatom) [130, 190]. This configuration

forms a van der Waals complex, but the conical intersections in this geometry are not energetically accessible. Further on in this study the electronic spectra for $OH(X^2\Pi,\, \nu = 0 \rightarrow A^2\Sigma^+,\, \nu = 1)$ transitions were calculated.

Lester *et al.* carried out the earliest calculations on a region associated with electronic quenching, focusing exclusively on the $C_{2v}(1^2B_2\text{-}2^2A_1)$ seam of intersections, with a barrierless pathway found [105, 107]. Discussions have otherwise tended to focus on this and the $C_{\infty v}(1^2\Pi\text{-}1^2\Sigma^+)$ seam of intersections, but studies by Yarkony have identified a seam of intersections in the C_s point group between states: $1^2A'\text{-}2^2A'$ [177]. Whilst these are two states of the same symmetry, their crossing is allowed. Since $N^{\text{int}} = 6$, it follows that the seam of intersections must be 4-dimensional and cannot be restricted to limited C_{2v} and $C_{\infty v}$ subspaces. Yarkony and co-workers have demonstrated that, rather than 3 different seams of intersections that occasionally coincide, this is one continuous seam of intersections with C_{2v}, $C_{\infty v}$ and C_s components [177, 178].

Figure 1.10 demonstrates tuning and branching coordinates ($\boldsymbol{g}$ and $\boldsymbol{h}$ vectors) for exemplar conical intersection points in each of the three geometries. The examples in the figure are drawn from reference [178]. Whilst it is somewhat of an oversimplification, minimum energy conical intersections can generally be thought to occur when the two diatoms lie in the same plane and the oxygen atom of the OH diatom is directed at the H_2 diatom. The study by Hoffman and Yarkony calculated points on the potential energy surface and characterised the seams of intersections, but did not carry out dynamics calculations [178].

The studies by Hoffman and Yarkony conclude by considering the topology of the conical intersection, noting that the outcome of H_2O+H or OH(X)+H_2 products depends on whether the system moves away from the conical intersection in the $+\boldsymbol{g}$ or $-\boldsymbol{g}$ direction respectively. A strong $\boldsymbol{g}$ component in the direction of the systems dynamics post the intersection is anticipated as the cone is much steeper with respect to the $\boldsymbol{g}$

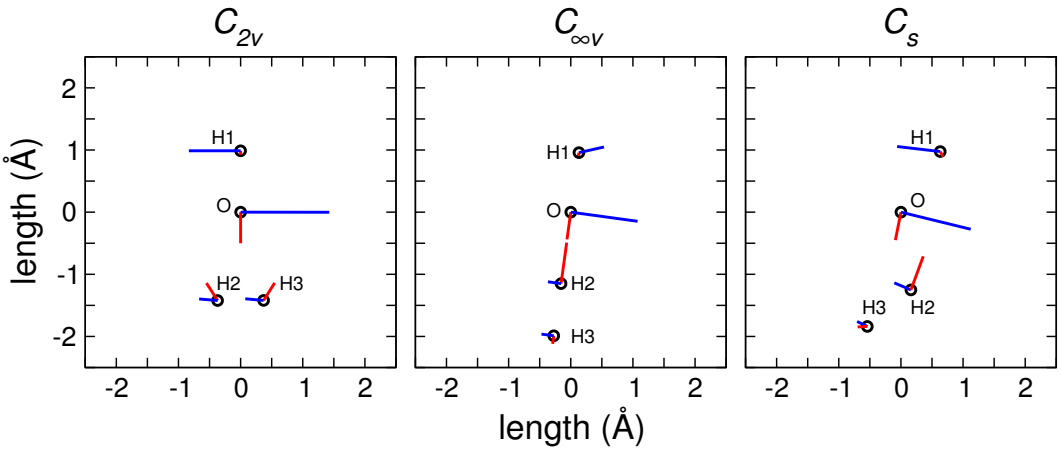

Figure 1.10: Representation in cartesian coordinates of the positions of oxygen and hydrogen atoms in the H_3O system at representative conical intersections between $1^2A'$ and $2^2A'$ states. Conical intersections are chosen for C_{2v}, $C_{\infty v}$ and C_s portions of the seam of intersections. The black circles plot the position of each atom as labelled, with the O atom set at the origin. $\boldsymbol{g}$ (red) and $\boldsymbol{h}$ (blue) vectors are shown for each atom though are scaled up by factors of 10.0 and 30.0 respectively. The positive direction for each of these vectors is away from the atom. These representative points were taken from those provided in reference [178].

rather than the $\boldsymbol{h}$ vector. The tilt of the cone was seen to bias the system towards the non-reactive quenching products, though this leads to the opposite conclusion to that observed exprimentally where reactive products are favoured.

Han *et al.* carried out non-adiabatic quantum scattering calculations on reduced forms of the PESs such that the tetra-atomic system was restricted to a plane (dihedral angle fixed at 0°). These dynamics studies focused on the branching ratio between reactive and non-reactive quenching, the rotational and vibrational distribution of the non-reactive products, and the dependence of these factors on the collision energy for both $OH+H_2$ [187] and its isotopologue system $OH+D_2$ [188]. Typically, excellent agreement was seen with available experiments, and the topology of the surface was used to explain product-state distributions. Non-reactive quenching OH(X) products tend to be rotationally excited due to the strong dependence of the PESs on the angle the OH(A) radical makes with the intermolecular vector. As in the Yarkony study, in the excited-state a geometry with the O-end of the OH(A) diatom pointing at the

H_2 diatom is necessary to enter a conical intersection. However, this geometry is an energy maximum on the ground surface, inducing a torque after travelling through the intersection and rotationally exciting the OH(X) product. At the point of intersection, the bond length of OH is close to its equilibrium value, explaining the lack of vibrational excitation in this product. In contrast, the H_2 diatom product of non-reactive quenching is rotationally cold and vibrationally hot. Again, this is demonstrated in the study as a result of the topology of the PESs. Firstly, the seam of conical intersections is independent of the H_2 orientation, leading to little rotational excitation. Secondly, the minimum energy pathway through a conical intersection typically involves stretching the H_2 bond from its equilibrium geometry, leading to vibrational excitation in the ground-state. Conical intersections do exist in this PES with the H_2 bond at its equilibrium bond length but, in this study, are of a higher energy than those with a stretched H_2 bond.

Bowman *et al.* have calculated complete 6-dimensional PESs for both the excited and coupled ground electronic states [126, 191]. The ground-state surface was used for QCT studies, with trajectories initiated at the selected intersection points identified by Hoffman and Yarkony. The branching ratio for non-reactive and reactive quenching was once again explored along with product-state distributions, with typically good agreement with experiments. The accompanying excited-state surface was generously donated for the studies in this thesis. The topology of the PES and the results of this study by Bowman *et al.* are discussed in chapter 3.

An *ab initio* quasi-diabatic potential energy matrix study by Collins *et al.* is also of note [189]. In this study a non-diagonal diabatic potential energy matrix for the OH+H_2 system was calculated. The calculation was non-exact as it only considered the coupling between 3 states, although couplings to other states are likely to be weak. The calculation included consideration of over 700 configurations for long range interactions where the two diatoms were separated by between 3.7 Å and 7.4 Å. In total, just under

3000 data points were calculated for this system, significantly smaller than the 23,000 data points used in fitting the PES for the study of this thesis. The Collins *et al.* study observed no barriers to accessing points associated with conical intersections, relative to the OH(A)+H_2 long range asymptote [189]. Classical trajectories were propagated using a surface hopping process similar to that developed by Tully [192] at collision energies between 0.013 and 0.2 eV. In this study, hopping between $2^2A'$ and $1^2A'$ states was three times as likely as hopping between $2^2A'$ and $1^2A''$. The outcomes of non-reactive and reactive quenching collisions were investigated and compared with results from the experiments of Davis *et al.* [106] and Lester *et al.* [108] already described in subsection 1.8.1. The Collins *et al.* calculations of the OH(A)+D_2 isotopologue system give good agreement with experimentally-observed HOD+D scattering angles and D atom translational energy distributions from the Davis laboratory [106]. However, the total quenching cross sections are much smaller than those measured experimentally, for example, by Heard and Henderson [100]. Furthermore, the branching ratio for non-reactive to reactive quenching products in the Collins study was around 5:1, yet in the Lester and co-workers experimental studies, reactive quenching products are favoured [108]. This Collins study remains the only full 3 state 6-dimensional nuclear dynamics study, yet limited numbers of trajectories are run and relatively few configurations are considered in calculating the diabatic potential energy matrix. These limitations are likely the origin of the disagreements with experimentally-observed properties.

1.10 This Thesis

The bulk of this thesis investigates the OH(A)+H_2 collision system, using theoretical and experimental techniques to measure cross sections for quenching, RET and depolarisation. The investigation considers the impact of the non-adiabaticity on not only collisions that lead to electronic or reactive quenching, but also on inelastic and elastic

collisions that remain in the excited-state. The theoretical calculations allow for the measurement of other properties that cannot be measured in the current experiment such as differential cross sections and opacity functions. The theoretical cross sections also consider the potential role of parity constraints on RET in the H_2 diatom.

By way of illustrating the capabilities of the ZQBS method, Chapter 2 extends a previous study by Chang [55] investigating the lab-frame orientation observed in OH(X) photofragments following photolysis of H_2O_2 with circularly-polarised light. The earlier study looked at the orientation following photolysis with a 193 nm laser; here, a lower energy 248 nm laser is used. This study demonstrates the ZQBS technique and introduces much of the experimental apparatus that is later used in the experimental measurements of OH(A)+H_2 collisions. A model for considering the contribution of the parent molecule rotation to the photofragment orientation is presented, and a simulation of this model tested against the experimental results.

Chapter 3 presents the theoretical methods used in the study of OH(A)+H_2 collisions. Firstly, the method used by Bowman and co-workers to develop the PES is briefly recounted. The shape of this excited-state PES is then described for a number of configurations. Quasi-classical trajectories have been run on this PES and a new 4-atom QCT code has been developed for this study. This 4-atom code has the potential for application to other diatom-diatom collision systems in the future. Chapter 3 presents this new method and concludes by detailing the calculations used in analysing the trajectories.

Chapter 4 presents the results of these QCT calculations on the OH(A)+H_2 PES. Inelastic cross sections and depolarisation moments are both measured alongside opacity functions and differential cross sections. The dependence of these properties on the rotational angular momentum, $\boldsymbol{N}$, of each diatom is considered. Finally, this chapter considers the role of the second diatom, since previous similar studies have focused on OH(A) collisions with atomic species.

Chapter 5 details the adaptations required to the experiment, first presented in chapter 2, to experimentally measure OH(A)+H_2 collisions. The ZQBS technique enables the measurement of total depolarisation cross sections alongside quenching cross sections. When the emission is resolved with a monochromator, further cross sections for RET and elastic depolarisation are determined. The fitting procedure for the LIF decays recorded in the experiment is also presented.

Chapter 6 presents the results from these experiments and compares them with those from previous ZQBS studies on OH(A)+Rg including He, Ar and Xe. He provides a comparison with similar kinematics, and Ar a collision system with more similar dynamics as the PES is both attractive and anisotropic. The Xe comparison provides a system also associated with sizeable electronic quenching cross sections owing to its accessible conical intersection.

Chapter 7 compares the cross sections for RET, total depolarisation and elastic depolarisation measured in the experiment with those determined from the QCT calculations. The theoretical analysis is then extended to assess to what extent the adiabatic QCT can account for electronic quenching by considering the topology of the excited-state surface. Finally, the chapter considers alternative binning procedures based on Gaussian functions and the impact this has on the QCT results.

Chapter 8 draws final conclusions for the OH(A)+H_2 studies and postulates future work to extend the study. This chapter concludes with a short description of the design and development of a new compact crossed-molecular-beam experimental system for use in future chemical dynamics studies. The chapter deals with the concept behind the design and demonstrates that the resultant molecular-beam is rotationally cold. Finally, velocity-mapped ion images following OCS photolysis are presented.

Chapter 2

H_2O_2 Photolysis

Molecular photolysis is a fundamental chemical process and the subject of considerable previous study. The determination of vector properties, such as the photofragment recoil velocity, $\boldsymbol{v}$, and photofragment angular momentum, $\boldsymbol{j}$, along with the correlations between them, can provide a strong indicator of the nuclear and electronic motion during bond cleavage [193–199]. The polarisation of the angular momentum and the anisotropy of the recoil direction are sensitive to the electronic states associated with dissociation, and any quantum interference effects between them. The photolysis of diatoms producing atomic photofragments has been extensively studied previously, and the photofragment angular momentum, $\boldsymbol{j}$, is entirely electronic in origin [196–200]. Polyatomic photodissociation leads to molecular photofragments and there is a nuclear rotation contribution to the photofragment angular momentum. In this case, internal motion in the parent molecule, whether through rotation or vibration, can have an impact on the photodissociation dynamics and the vector properties of the photofragment. The photolysis of H_2O_2 is potentially influenced by this range of factors: photolysis occurs via two electronic states, with the potential for interference between them, and the system has parent rotation and bending motions, which correlate with fragment spin.

The photolysis of H_2O_2 is typically described with recourse to three electronic states of the parent molecule. In its ground electronic state $H_2O_2(\tilde{X}^1A)$ is described as a bent 'open book' molecule with C_2 symmetry, and a dihedral angle between the two OH bonds of $\phi = 111.5°$ [201–203] as shown in figure 2.1. The electronic configuration is [204]

$$\tilde{X}^1A_{(g)}...4a^2_{(g)}5a^2_{(u)}4b^2_{(g)},$$

where all the orbitals are localised on the oxygen atoms.

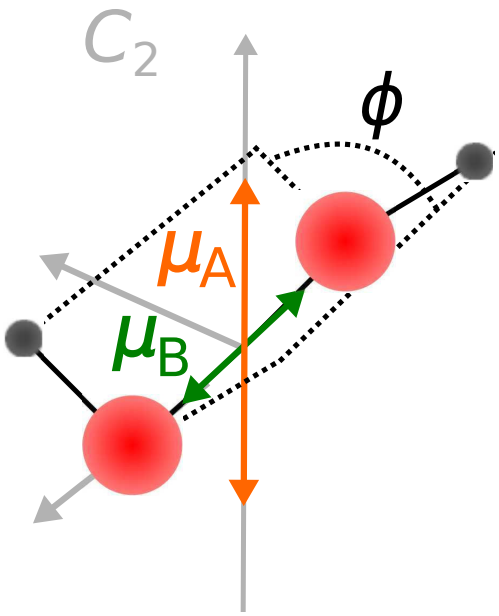

Figure 2.1: Geometry of H_2O_2 ground electronic state, $\tilde{X}^1A$. The molecular-frame axis set is shown, with x the C_2 symmetry axis and z defined by the O-O bond axis. Transition dipole moments are shown for the $\tilde{X} \rightarrow \tilde{A}$ and $\tilde{X} \rightarrow \tilde{B}$ photolytic excitations.

Excitation to the first excited electronic state involves promoting an electron to the anti-bonding $5b_{(u)}$ orbital giving the electronic configuration [204]

$$\tilde{A}^1A_{(u)}...4a^2_{(g)}5a^2_{(u)}4b^1_{(g)}5b^1_{(u)}.$$

The lowest energy conformer of $H_2O_2(\tilde{A}^1A)$ has a trans geometry with dihedral angle,

$\phi = 180°$ [204, 205]. The transition dipole moment for this transition, $\boldsymbol{\mu}_{\mathrm{A}}$, lies perpendicular to the O-O bond and parallel to the C_2 symmetry axis.

Excitation to the higher energy $H_2O_2(\tilde{\mathrm{B}}^1B)$ electronic state involves a transition dipole moment, $\boldsymbol{\mu}_{\mathrm{B}}$, close to parallel to the O-O bond [206]. The electronic configuration [204],

$$\tilde{\mathrm{B}}^1B_{(g)}...4a^2_{(g)}5a^1_{(u)}4b^2_{(g)}5b^1_{(u)},$$

arises from excitation of an electron from a lower energy orbital than in exciting to $\tilde{\mathrm{A}}^1A$. The $\tilde{\mathrm{B}}$ state has a cis geometry, and $\phi = 0°$ in its lowest energy conformer. The two excited electronic states are unstable and the O-O bond breaks following excitation. The lowest energy conformer in either excited state is significantly different to the equilibrium geometry in the ground state with a greater dependence on torsional angle. Consequently, a large torsional torque is applied following excitation and during fragmentation. This torque is believed to be the main source of rotational excitation in the OH(X) photofragments [207–209].

2.1 Previous Work

The relative contribution of the $\tilde{\mathrm{A}}$ and $\tilde{\mathrm{B}}$ states is dependent upon the photolysis wavelength, λ_{photo}. Photolysis at 193 nm provides sufficient energy to excite H_2O_2 to both the $\tilde{\mathrm{A}}$ and $\tilde{\mathrm{B}}$ states, and the work of Gericke *et al.* concluded that photofragments are generated from these states in approximately a 0.68:0.32 ratio [210].

At longer wavelengths (than 193 nm) insufficient energy is provided to excite the $\tilde{\mathrm{X}} \rightarrow \tilde{\mathrm{A}}$ transition from the $\tilde{\mathrm{X}}$ state equilibrium geometry. Instead photolysis at longer wavelengths requires excitation away from the equilibrium O-O bond length and the Franck-Condon region [211, 212]. The dependence of the potential upon the O-O bond

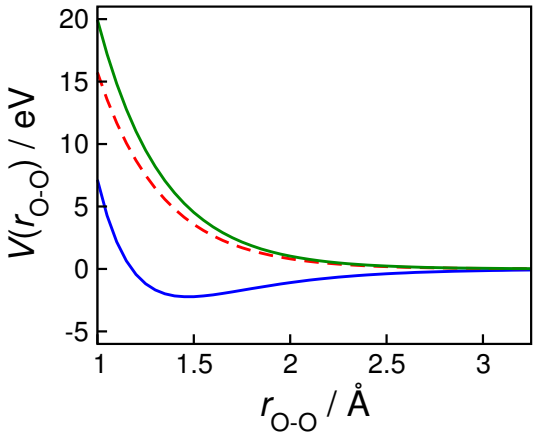

Figure 2.2: Dependence of the potential energy of H_2O_2 on the O-O bond length r_{O-O}. The ground $\tilde{X}$ potential energy curve is shown in blue, the $\tilde{A}$ state is shown with a broken red line, and the $\tilde{B}$ state in green.

length, r_{O-O}, for each electronic state of H_2O_2 is shown in figures 2.2 and 2.3. The figures make clear that at larger bond lengths the energy differences between the ground and higher electronic states are reduced, allowing for excitation at longer wavelengths. At wavelengths of 248 nm [211, 213], 266 nm [204, 214] and 308 nm [205] excitation is predominantly to the $\tilde{A}$ state, as the excitation energy is insufficient to reach the $\tilde{B}$ state. At still longer wavelengths the transition must occur with still larger O-O bond lengths, reducing the energy gap between the $\tilde{A}$ and $\tilde{B}$ excited states considerably. Consequently, both states can be excited as indicated in figure 2.3 [211, 212]. At longer wavelengths, including 351 nm and 465 nm, excitation to the $\tilde{B}$ state becomes more prevalent [205, 215].

It has also been postulated that when $\lambda_{photo} > 193$ nm, excitation requires torsional excitation and occurs via torsional hot bands [205]. The population of vibrational levels above the ground state for the torsional bending mode, ν_4, is around 22% at 300 K [204]. Along with reduced torsional dependence for larger r_{O-O} this results in reduced torsional torque following excitation at longer λ_{photo}, and accounts for the reduced levels of rotational excitation observed at longer wavelengths experimentally [204, 205]. Both factors are illustrated in figure 2.3. In progressively higher ν_4 vibrational levels

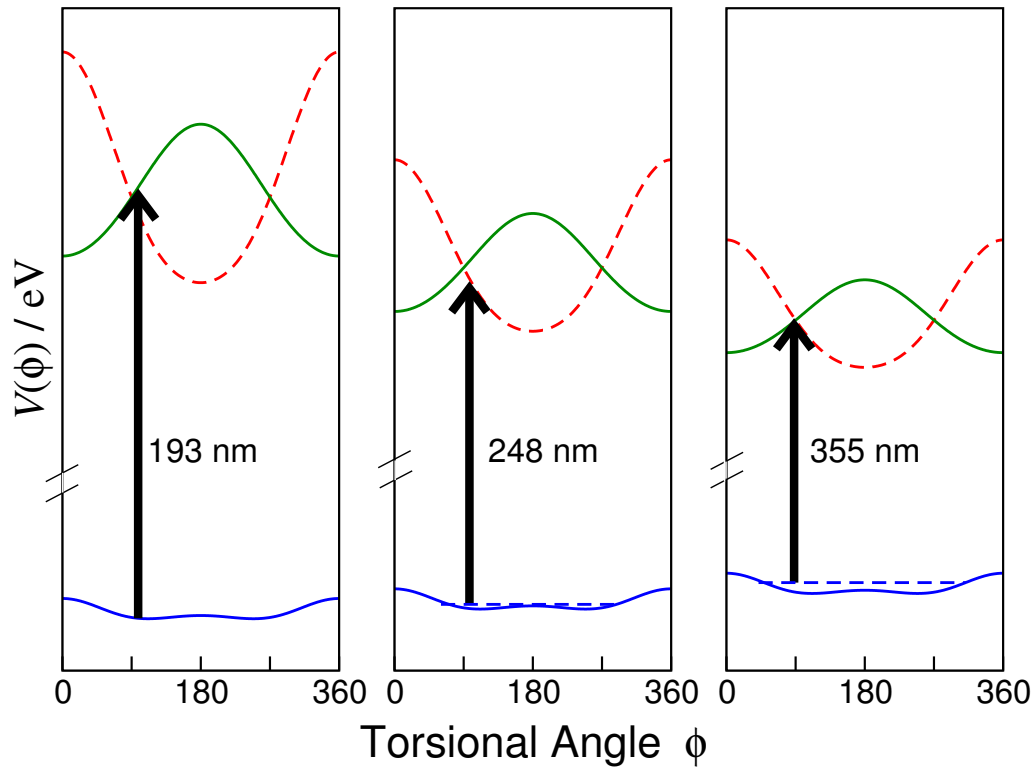

Figure 2.3: Variation in the H_2O_2 PESs with dihedral angle, ϕ, with increasing O-O bond length, r_{O-O}, for each panel from left to right. The potentials qualitatively demonstrate the changing shape of the three potentials with changing excitation wavelength, and the r_{O-O} involved in that excitation. The arrows demonstrate the states excited with differing photolysis wavelength as labelled. The ground $\tilde{X}$ potential energy curve is shown in blue, the $\tilde{A}$ state is shown with a broken red line, and the $\tilde{B}$ state in green. Dashed blue lines indicate the increasing role played by excitation of the torsional bending mode at longer photolysis wavelength. This diagram is based on that presented in reference [205] and is qualitative in nature, as such the bond lengths used are not listed.

the Franck-Condon region moves to more cis-like geometries, facilitating excitation to the $\tilde{B}$ state. Again, this is illustrated qualitatively in figure 2.3.

Semi-classical calculations on an *ab initio* PES by Drozd *et al.* give good agreement with experimentally-observed $\tilde{A}$:$\tilde{B}$ ratios in the range 190-300 nm [216]. However, this study did not predict the resurgence in excitation to the $\tilde{B}$ state at yet longer wavelengths. Within this work, Drozd *et al.* suggested that the increased role of the $\tilde{B}$ state at longer wavelengths is actually a consequence of an intersystem crossing mechanism involving excitation to the $H_2O_2(\tilde{B}^3B)$ state [216].

2.1.1 Vector Correlations

Previous studies have also quantified the value of moments describing a number of vector correlations relating to the dissociation process. One of the simplest correlations is the polarisation of the photofragment $\boldsymbol{j}$ relative to the lab Z-axis, where the lab Z-axis is parallel to the electric field vector, $\boldsymbol{\epsilon}_{\mathrm{ph}}$, for photolysis with linearly-polarised light, or parallel to the propagation axis for left-hand-circularly-polarised photolysis light, $\boldsymbol{k}_{\mathrm{ph}}$. If Z is also defined as the projection axis, there is no azimuthal dependence, and it follows classically that

$$P(\theta_{jZ}) = \sum_{k=0}^{\infty} \frac{[k]}{2} h_0^{(k)} P_k(\cos\theta_{jZ}), \tag{2.1}$$

as given in section 1.19. The moments $A_0^{(k)}$ are commonly used to describe this distribution. If k is odd $A_0^{(k)} = h_0^{(k)} = \langle P_k(\cos\theta_{jZ})\rangle$ and the limits are -1 ($\boldsymbol{j}$ anti-parallel to Z) and +1 ($\boldsymbol{j}$ parallel to Z). If k is even, $A_0^{(k)} = 2h_0^{(k)} = 2\langle P_k(\cos\theta_{jZ})\rangle$ and the limits are -1 ($\boldsymbol{j}$ perpendicular to Z) and +2 ($\boldsymbol{j}$ parallel or anti-parallel to Z).

Three-vector correlations take into account the mutual correlation of the transition dipole moment, $\boldsymbol{\mu}$, with the photofragment velocity, $\boldsymbol{v}$, and angular momentum, $\boldsymbol{j}$, and are described in generic terms in section 1.4.1. A semi-classical expression for the $\boldsymbol{v}$-$\boldsymbol{j}$ distribution in the molecular (body-fixed) frame has been formulated by Dixon [32],

$$P(\omega_{vz}\omega_{jz}) = \sum_{K,Q,k_1,k_2} \frac{[k_1][k_2]}{16\pi^2} b_Q^K(k_1k_2) B_Q^K(k_1k_2;\omega_{vz}\omega_{jz}), \tag{2.2}$$

where typically $z \parallel \boldsymbol{\mu}$. However, properties are measured in the lab-frame rather than a body-fixed-frame, and in the case of the experiments in this chapter involve photolysis with circularly-polarised light. For this case a further three-vector correlation Z-$\boldsymbol{v}$-$\boldsymbol{j}$

(where the Z-axis is parallel to the propagation direction) has been formulated [32],

$$P(\omega_{vZ}\omega_{jZ}) = \frac{1}{16\pi^2}\left[\sum_k [k] b_0^0(kk) B_0^0(kk;\omega_{vZ}\omega_{jZ}) + \frac{s_3}{5}\sum_{k_1,k_2}[k_1][k_2] b_0^1(k_1k_2) B_0^1(k_1k_2;\omega_{vZ}\omega_{jZ})\right], \tag{2.3}$$

where the relationship between $\boldsymbol{\epsilon}$ and $\boldsymbol{\mu}$ is readily characterised as excitation to a single state is assumed [32]. Furthermore the Z-$\boldsymbol{v}$-$\boldsymbol{j}$ correlation can be described in terms of molecular-frame bipolar moments $b_q^k(k_1k_2)$. In the case of photolysis by linearly-polarised light, the factor $s_3/5$ is replaced by $+2/5$. This formalism by Dixon is semi-classical in nature so is a poor description at low $\boldsymbol{j}$. Additionally, the formalism requires photolysis to occur via a single state.

Costen and Hall [82] formulated an alternative semi-classical expression using renormalised lab-frame bipolar moments, $\beta_Q^K(k_1k_2)$. These moments follow from the expression of bipolar harmonics in terms of angular momentum spherical tensors, $T_q^{(k)}(\boldsymbol{j})$ [13, 29, 217], rather than the classical spherical harmonics, $C_q^{(k)}(\omega_{jZ})$, in equation 1.11 [82]. Table 2.1 details some of the key renormalised laboratory-frame bipolar moments, $\beta_0^K(k_1k_2)$, extending the list in references [82, 218]. The table gives the equivalent body-fixed-frame bipolar moment - $b_Q^K(k_1k_2)$, the nature of the mutually correlated vectors either moment describes, and references for experimental measurements of these parameters following H_2O_2 photolysis at different wavelengths.

The study of H_2O_2 photolysis in this chapter considers photolysis wavelength of 248 nm and 193 nm, and it is worth highlighting the results of previous experimental work to determine key vector correlation moments at these wavelengths. Work by August *et al.* at 248 nm measured an anisotropy parameter $\beta = -0.86 \pm 0.16$, indicating that excitation occurs almost exclusively via a perpendicular transition [211], implying excitation solely to the $\tilde{A}$ state. The theoretical study by Drozd *et al.* also calculated almost exclusive excitation to the $\tilde{A}$ state following photolysis at 248 nm [216]. A similar anisotropy parameter of $\beta = -0.71 \pm 0.08$ has been observed at the

$\beta_Q^K(k_1k_2)$	$b_Q^K(k_1k_2)$	Correlated Vectors	Notes	References
$\beta_0^0(22)$	$=\sqrt{5}b_0^0(22)$	$\boldsymbol{v}$, $\boldsymbol{j}$	$=\langle P_2(\boldsymbol{j}\cdot\boldsymbol{v})\rangle$	248 nm - [211], 193 nm - [210, 212, 219], 266 nm - [204, 211]
$\beta_0^1(01)$	$=b_0^1(01)$	$\boldsymbol{k}_{\rm ph} \parallel Z$, $\boldsymbol{j}$	Linked to the lab-frame orientation, $A_0^{(1)}$	355 nm - [215] 248 nm - this work, 193 nm - [55]
$\beta_0^2(02)$	$=b_0^2(02)$	$\boldsymbol{\epsilon}_{\rm ph} \parallel Z$, $\boldsymbol{j}$	Linked to the lab-frame alignment, $\frac{5}{4}A_0^{(2)}$	355 nm - [215]
$\beta_0^2(20)$	$=b_0^2(20)$	$\boldsymbol{\epsilon}_{\rm ph} \parallel Z$, $\boldsymbol{v}$	Linked to translational anisotropy $\frac{1}{2}\beta$	248 nm - [211], 193 nm - [210, 212, 219], 266 nm - [204, 211]
$\beta_0^1(21)$	$=-\sqrt{\frac{2}{5}}b_0^1(21)$	$\boldsymbol{k}_{\rm ph} \parallel Z$, $\boldsymbol{v}$, $\boldsymbol{j}$	Higher order orientation parameter	193 nm - [55]
$\beta_0^2(22)$	$=-\frac{i2\sqrt{10}}{3}b_0^2(22)$	$\boldsymbol{\epsilon}_{\rm ph} \parallel Z$, $\boldsymbol{v}$, $\boldsymbol{j}$	Mutual correlation	248 nm - [211], 193 nm - [210, 212, 219], 266 nm - [204, 211]
$\beta_0^1(23)$	$=-\frac{3}{\sqrt{35}}b_0^1(23)$	$\boldsymbol{k}_{\rm ph} \parallel Z$, $\boldsymbol{v}$, $\boldsymbol{j}$	Higher order orientation parameter	193 nm - [55]
$\beta_0^0(00)$	$=b_0^0(00)$		Normalised population (=1)	

Table 2.1: Renormalised lab-frame bipolar moments, $\beta_0^K(k_1k_2)$, of interest in photodissociation studies, shown with the equivalent body-fixed-frame bipolar moment, $b_Q^K(k_1k_2)$. A simplistic view of the vector correlation being considered in each case is also listed, note that $\boldsymbol{k}_{\rm ph}$ is the propagation direction of left-hand-circularly-polarised photolysis light. $\boldsymbol{\epsilon}_{\rm ph}$ is the electric field vector of linearly-polarised photolysis light. References indicate studies where these correlations have been measured experimentally previously for H_2O_2.

slightly longer photolysis wavelength of 266 nm employed by Gericke and co-workers [204]. Further work by Gericke *et al.* [210] at the shorter photolysis wavlength of 193 nm found $\beta = 0.00 \pm 0.02$, indicating transitions via both the $\tilde{\mathrm{A}}$ and $\tilde{\mathrm{B}}$ state as explained earlier.

The body-fixed-frame bipolar moment $\beta_0^0(22)$ quantifies the alignment of the photofragment angular momentum $\boldsymbol{j}$ with respect to the recoil velocity $\boldsymbol{v}$ following photolysis. Large positive values are measured for this moment at 193 nm, 248 nm and 266 nm [204, 211–213], indicating a strong preference for $\boldsymbol{j}$ to align parallel with $\boldsymbol{v}$, with the photofragments flying apart with 'propeller'-like motion. The strong torque applied on excitation is considered the source of this correlation [207–209].

2.2 Measuring Orientation

The experiment described here moves away from the study of alignment parameters following photolysis by linearly-polarised light (see reference [205]), to the study of orientation parameters following photolysis by circularly-polarised-light. A similar study has been performed at 355 nm by Alexander [215, 220].

The experiment described here was first used by Chang [55] to record the lab-frame orientation, $A_0^{(1)}$, following the photolysis of H_2O_2 at 193 nm. In that study, Doppler scans of the (1+1) LIF peaks allowed for the determination of higher order orientation parameters $\beta_0^{(1)}(21)$ and $\beta_0^{(1)}(23)$. The lab-frame orientation can be expressed in terms of the renormalised lab-frame bipolar moments as [82]

$$A_0^{(1)}(\omega_{vz}) = \frac{1}{4\pi}\left[\beta_0^1(01) + 5\beta_0^1(21)P_2(\cos\omega_{vZ})\right], \tag{2.4}$$

where $\omega_{vz} = \theta_{vZ}\phi_{vZ}$ is the angle between the recoil velocity and the lab-frame Z-axis. This can easily be converted to the Doppler shift, x_{D} [82],

$$A_0^{(1)}(x_{\mathrm{D}}) = \frac{1}{2}\left[\beta_0^1(01) + 5\beta_0^1(21)P_2(x_{\mathrm{D}})\right] \tag{2.5}$$

Integrating over x_{D} between -1 and +1 gives $A_0^{(1)} = \beta_0^1(01)$. This integration is equivalent to the simple experiment used in this study in which the full LIF peak is integrated. Consequently, later in this chapter $A_0^{(1)}$ and $\beta_0^1(01)$ can be (and are) used interchangeably.

Molecular-frame polarisation parameters, $a_q^k(p)$, were first formulated by Rakitzis and Zare [221]. The label (p) indicates the transition excited during photolysis and whether it is parallel, perpendicular or mixed $(\parallel, \perp)$. The molecular-frame orientation parameters, $a_0^1(\perp)$ and $\mathrm{Re}[a_0^1(\parallel, \perp)]$, can be determined from renormalised lab-frame bipolar moments, including the anisotropy parameter, β [82],

$$a_0^1(\perp) = \frac{2\beta_0^1(01) + 10\beta_0^1(21)}{2-\beta}, \tag{2.6}$$

$$Re[a_1^1(\parallel, \perp)] = \frac{5\beta_0^1(21) - 2\beta_0^1(01)}{\sqrt{(1+\beta)(2-\beta)}}. \tag{2.7}$$

In the diatomic case transitions are either parallel or perpendicular, so parameters with $(p) = (\parallel, \perp)$ are considered as resulting from coherent excitation of both a parallel and perpendicular transition and thus the involvement of more than one excited state. A general formalism for the interpretation of these molecular-frame polarisation parameters following polyatomic photodissociation has been proposed by Rakitzis and Alexander [222, 223]. However, H_2O_2 is often considered a 'pseudo-diatomic' and the molecular-frame polarisation parameters are interpreted as in the diatomic case. In

this way the $a_0^1(\perp)$ parameter can be uniquely associated with the perpendicular transition to the $\tilde{A}$ state, and the $\mathrm{Re}[a_1^1(\parallel,\perp)]$ parameter with coherent excitation to $\tilde{A}$ and $\tilde{B}$ states. In Chang's study at 193 nm, Doppler resolved scans were performed in order to determine these molecular orientation parameters [55, 224]. Although these Doppler resolved scans have not been repeated at 248 nm these parameters have still been introduced as they arise in the discussion of the dynamics following photolysis at 248 nm as well as at 193 nm.

Chang *et al.* proposed a mechanism to account for the involvement of the parent molecular rotation in determining the observed lab-frame orientation [55, 224]. A simulation based on this mechanism was formulated, and predictions of values for $A_0^{(1)}$, $a_0^1(\perp)$ and $\mathrm{Re}[a_1^1(\parallel,\perp)]$ following photolysis at 193 nm calculated [55, 224]. Experiments in this thesis extend this investigation to record the lab-frame orientation following photolysis at 248 nm. The simulation has been adapted to account for photolysis at this wavelength, and the calculated values compared with the experimental results, although with reduced success. The entirety of this work was presented in reference [224].

2.3 The Experiment

Three techniques are used to measure the lab-frame orientation in these experiments. The first records 1+1 LIF emission spectra following photolysis by left- and right-circularly-polarised laser radiation, with the difference between these two spectra used to determine the lab-frame orientation. The second and third methodologies use the Zeeman quantum beat spectroscopy (ZQBS) technique introduced in section 1.7.2. Most of the experimental set-up is common to these three methods and the differences will be explained as and when needed.

2.3.1 Reaction Chamber and Introduction of H_2O_2

The reaction chamber consists of a stainless steel central cylinder of diameter 250 mm, which height 250 mm and the reagent gas enters via a short arm. The chamber is pumped by a Leybold Trivac D40B 40 m^3/hr vacuum pump which achieves a background pressure of approximately 1×10^{-1} mTorr. The pressure within the chamber is measured via a baratron positioned close to the interaction region.

Attached to either side of the chamber are two 250 mm stainless steel side arms, also under the same vacuum. The lasers enter and exit these side arms through flat silica windows. A series of stainless steel baffles within the side arms limit the scattering of light back into the central chamber.

A 50:50 mixture of water and hydrogen peroxide, H_2O_2, is prepared in a fume hood and added to a 250 ml vacuum-sealed glass bomb. The bomb is attached to the vacuum chamber via a teflon tube and entry into the chamber is controlled by an inlet valve. The pressure in the chamber is below the vapour pressure of the water, and peroxide, so the gases slowly enter. On initially pumping down the experimental set-up, some time is left to drive off excess water. The partial pressure of the gas from the bomb is maintained at around 50 mTorr throughout the experiments.

2.3.2 Magnetic Field

For the ZQBS based methods, a magnetic field is generated by a pair of Helmholtz coils held 50 mm apart at the centre of the reaction chamber - the interaction region. The current through the coils is tunable and a field of $\lesssim$50 Gauss is generated for these experiments. The field is set perpendicular to the detection direction [83] for the orientation experiments carried out here. The magnetic field is pulsed but the field is uniform at the point of photolysis and over the course of the fluorescence decay.

The coils are surrounded by μ-metal shielding to remove the influence of external magnetic fields such as the Earth's magnetic field and stray fields. Any inhomogeneity in the magnetic field would lead to radicals precessing at different rates [225] in different regions and the emission decay from the precessing radicals would no longer be a measure of their resultant polarisation. A Hall probe was previously used to measure the magnetic field directly, confirming the magnitude of the field and its homogeneity within the interaction region [226].

2.3.3 Laser System

The H_2O_2 is photolysed by a laser pulse generated by a Lambda Physik Compex excimer laser. Either an excimer mix for ArF is used to generate a 193 nm laser pulse as in the experiments by Chang [55], or a KrF mix is used to generate a 248 nm laser pulse as in the experiments here. The initial laser is partially linearly-polarised, but it passes through a Glan-Taylor polariser on its route to entering the reaction chamber. The Glan-Taylor polariser purifies the initial polarisation from the laser, transmitting only the polarisation parallel to its optical axis, whilst the other is reflected. Following this polariser, the photolysis laser passes through a photoelastic modulator (PEM) along the path to the reaction chamber. The voltage applied to the PEM is selected so that the laser flips between left- and right-circularly-polarised light on alternate laser shots. The necessary PEM setting is found by observing the quality of the separation of the two polarisations after the light passes through a Fresnel rhomb and Rochon polariser. The Rochon polariser separates mutually perpendicular polarisations into different directions.

A delay of 20 ns is allowed before a subsequent probe laser excites the OH(X) radicals to their first excited state OH(A). Care is taken to ensure that these laser pulses

overlap at the centre of the interaction region, so that the nascent products of photolysis are probed. The probe laser is generated by a tunable Lambda Physik LPD3000 dye laser. The second harmonic (532 nm) of a Continuum Surelite III Nd:YAG laser is used to pump a Rhodamine 101 dye which is tunable in the usable range 612-619 nm. This is then frequency doubled via an FL30 doubling crystal to produce laser light in the range 306-309.5 nm corresponding with OH(A $\leftarrow$ X) transitions. The energy of the probe laser is kept below 0.1 mJ and the laser linewidth is around 0.75 cm^{-1}. Both lasers operate at a repetition rate of 10 Hz.

Stanford DG 535 digital delay generators synchronise the timing between the pulsing of the lasers, the PEM, the magnetic field (if used), the oscilloscope and other devices. The laser grating positions for particular A$\leftarrow$X transitions are found by scanning the laser wavelength and comparing with data from LIFBASE [227] - a computer program that simulates electronic spectra for simple diatomic molecules. The scanning is controlled by a PC via an RS245 interface with a Stanford box car averaging system, this is linked to the delay generator to deliver a trigger pulse for the dye laser grating and crystal control interface.

2.3.4 Detection and Data Recording

OH(A) radicals fluoresce back to their ground electronic state, and this fluorescence can leave the chamber via a window placed orthogonally to the axis of the pump and probe laser propagation. The fluorescence is focused on the entrance of a monochromator, by a pair of lenses. Before entering the monochromator but subsequent to the lenses, the fluorescence passes through one or two polarisers depending on the experiment.

The monochromator grating is positioned so that the experiment is sensitive to emission from one particular emission branch, and the slit width is large enough to capture all of the emission from occupied rotational levels in that branch. As will be

shown later the sensitivity of the emission to orientation is opposite in the P and R branches, so it is important that the monochromator isolates the emission from one of these branches only. Eliminating emission from the Q branch is less important in practice as this emission does not exhibit sensitivity to orientation.

Following passage through the monochromator, the emission is focused onto the entrance of a UV sensitive photomultiplier tube (PMT) via a bi-convex lens. The PMT converts photon flux into an electric current. The signal from the PMT is sent to a Tektronix TDS 3032B digital oscilloscope, which records the signal before it is passed to a PC utilising LabVIEW software [228].

Figure 2.4 details the different experimental geometries used in the three methodologies for measuring lab-frame orientation. The left-hand picture shows the set-up used in recording absorption quantum beats and the basic recording of the 1+1 LIF spectrum. The magnetic field, $\boldsymbol{H}$, is not present for the basic 1+1 LIF measurements. In this set-up, the probe laser is circularly-polarised by first passing through a Rochon polariser to purify the initial linear polarisation from the dye laser, and then through a Fresnel rhomb to convert this to right-hand-circularly-polarised light. This same combination of optics is used in setting up the circular polarisation of the photolysis laser, so that the right-hand-circularly-polarised photolysis laser is of the same helicity as the probe laser. With counter-propagating lasers of the same helicity the electric field vectors of their photons are rotating in opposite directions and the resultant emission signal is labelled $I_{\circlearrowleft\circlearrowleft}$. For counter-propagating lasers the electric field vectors rotate synchronously and the emission signal is labelled $I_{\circlearrowleft\circlearrowleft}$. In this geometry a linear polariser is placed ahead of the monochromator. This polariser is set for the preferred alignment of light for the monochromator.

The right-hand panel displays the experimental geometry used in recording emission quantum beats. Here the probe laser is linearly- rather than circularly-polarised and its electric field vector, $\boldsymbol{\epsilon}_{\mathrm{pr}}$, is aligned in the axis perpendicular to the detection

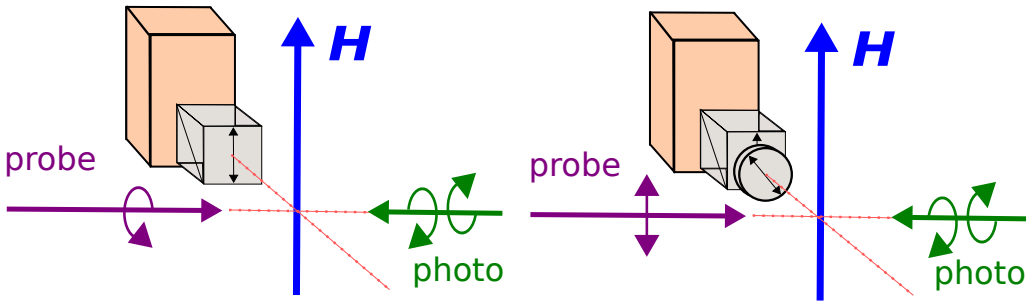

Figure 2.4: Experimental geometries used in the investigation of the lab-frame orientation parameter following H_2O_2 photolysis. The magnetic field, $\boldsymbol{H}$, is only applied when recording quantum beats. The orange box represents the monochromator and PMT and the grey circle and cube polarised optics along the detection axis.

axis and parallel to the applied magnetic field, $\boldsymbol{H}$. Additionally, there is a quarter wave plate as well as a linear polariser prior to the monochromator and detector. The probe laser excites all OH(X,$\nu = 0$,j) in the plane of rotation equally, so the oriented distribution from photolysis is effectively transferred to the excited state, from which it fluoresces.

2.3.5 1+1 LIF Spectrum

In this simple technique, no magnetic field is applied, and the LIF emission signal is recorded as the probe laser is scanned over a region of the (0,0) vibrational band of the OH(A←X) transition, for each photolysis laser polarisation. The laser scan range is over the observable lines in the R_{11} and R_{22} absorption branches. The lines are labelled as $\Delta N_{F_\Pi f_\Sigma}(N'')$ where N'' is the ground state rotational quantum number, ΔN is O, P, Q, R, S for $\Delta N = -2, -1, 0, 1, 2$ respectively, F_Π gives the spin-orbit manifold of the ground electronic state: 1 for $^2\Pi_{3/2}$ and 2 for $^2\Pi_{1/2}$, and f_Σ the spin-rotation manifold: 1 for $j = N + S$ or 2 for $j = N - S$. Over the scan range used here, excitation from both spin-orbit levels is explored.

The photolysing laser is switched between left- and right-hand circular polarisations on alternate laser shots, whilst the probing laser remains left-hand-circularly-polarised. Signal on alternate laser shots is recorded in separate channels on the oscilloscope. The

spectrum is scanned in steps of 0.0005 nm and the signal averaged over 64 shots for each polarisation, at each point on the spectrum. The scanning is controlled by a PC, which sets the scan length and the number of repeat measurements via a purpose-built LabVIEW program [55, 228]. The signal is only integrated over the first 200 ns after the probe laser to limit the influence of collisions. Figure 2.5 shows a spectrum of the LIF spectrum recorded in this way.

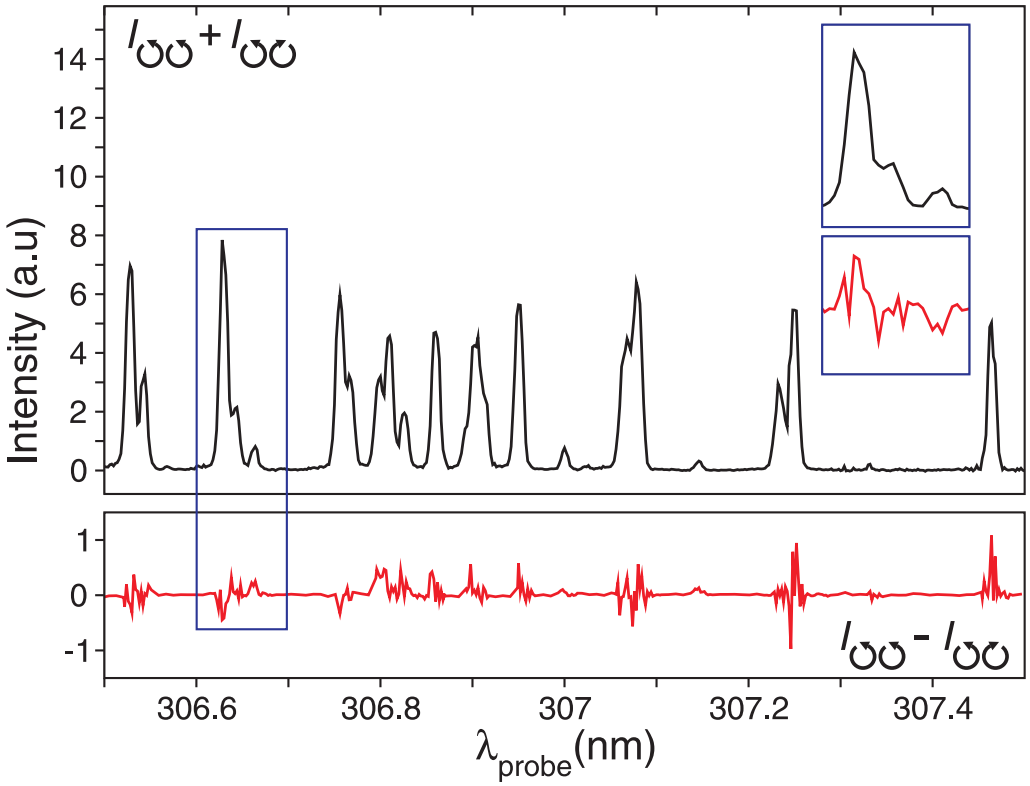

Figure 2.5: Figure demonstrating a section of the experimental scan of the 1+1 LIF spectrum following 248 nm photolysis of H_2O_2 and then probing the A $\leftarrow$ X of the OH photofragments transition with a tunable dye laser, at the wavelength λ_{probe}. The top panel shows the sum of emission signals following 1+1 LIF where the photolysing and probing photons have the same helicity $I_{\circlearrowleft\circlearrowleft}$ and where the photolysing and probing photons have opposite helicity, $I_{\circlearrowleft\circlearrowright}$. The lower panel shows the difference of the two signals in red. The insert zooms in on the peaks indicated. These peaks correspond with $R_{11}(5)$, $R_{21}(5)$ and $R_{11}(13)$ transitions from left to right, with the first two peaks overlapping.

The intensity for each transition is found by integrating across the whole LIF peak, leading to a pair of LIF intensities, $I_{\circlearrowleft\circlearrowleft}$ and $I_{\circlearrowleft\circlearrowright}$, for each peak. The difference is

shown in the lower panel of figure 2.5. Along with the sum of intensities, this is used in measuring the degree of circular polarisation, $C(j)$, for the OH(X) photofragment in rotational state j [229]. $C(j)$ is directly linked to the lab-frame orientation, $A_0^{(1)}(j)$ [56, 229]. For P/R branch excitation and the experimental geometry used here it follows that

$$C(j) = \frac{I_{\circlearrowleft\circlearrowleft}(j) - I_{\circlearrowleft\circlearrowright}(j)}{I_{\circlearrowleft\circlearrowleft}(j) + I_{\circlearrowleft\circlearrowright}(j)} = \frac{\tilde{S}_0^{(1)} A_0^{(1)}}{\tilde{S}_0^{(0)} A_0^{(0)} + \tilde{S}_0^{(2)} A_0^{(2)}}, \tag{2.8}$$

where $A_0^{(0)}$ represents the population and is normalised to unity and the lab-frame alignment parameter, $A_0^{(2)}$, is taken from previous measurements with linearly-polarised photolysis light. $A_0^{(2)}$ is found to be independent of the photo-fragment rotational angular momentum, j, with a value of 0.00±0.05 [210] following photolysis at 193 nm or 0.10±0.05 following photolysis at 248 nm [211]. These values are used in this analysis, although they are first multiplied by -$\frac{1}{2}$ to account for the transformation of the lab fixed Z-axis to that defined in these studies [32]. $\tilde{S}_0^{(k)}$ is the monochromator adjusted k-th order line strength factor. The 1+1 LIF line strength factors are adjusted from those derived from a theoretical line strength formula, formulated by Kummel, Sitz and Zare, $S_0^{(k)}$ [56]. The adjustment here accounts for the uneven detection efficiency owing to the use of the monochromator. A Gaussian weighting function, $W_{\mathrm{m}}(\lambda_{\mathrm{m}} - \lambda_{\mathrm{e}})$ is applied to model the monochromator's transmittance, and $\tilde{S}_0^{(k)}$ is calculated according to [224]

$$\tilde{S}_0^{(k)} = \sum_{\lambda_{\mathrm{e}}} S_0^{(k)}(\lambda_{\mathrm{e}}) W_{\mathrm{m}}(\lambda_{\mathrm{m}} - \lambda_{\mathrm{e}}), \tag{2.9}$$

where λ_{m} is the monochromator position, and the FWHM of the Gaussian is set as 7.7 nm. λ_{e} is the wavelength for the emission, and all the emission branches for j (P, Q, and R) are summed over. The monochromator is fixed at the position of the $R_{22}(7)$ transition, as this allows for the detection of most R branch emission. An additional demonstration of how the use of the monochromator is accounted for is given in reference [224]. The 1+1 LIF line strength factors are dependent upon the

initial angular momentum, the angular momentum after excitation, and the angular momentum after LIF emission [56].

As stated earlier, in the case in which $A_0^{(1)}$ is evaluated by integrating the signal across a peak, $A_0^{(1)}$ is equivalent to the renormalised lab-frame bipolar moment $\beta_0^1(01)$. Positive values of $\beta_0^1(01)$ indicate $\boldsymbol{j}$ is oriented along the lab $+Z$ direction. Each segment of the 1+1 LIF spectrum was scanned at least 4 times and the average value of $C(j)$ determined for each peak, the error bars represent the 95% confidence limits when these data are used in determining the standard deviation of $C(j)$.

2.3.6 Quantum Beats

As well as the 1+1 LIF spectrum recording technique, techniques based upon Zeeman quantum beat spectroscopy can be used in studying photofragment polarisation. A Faraday rotation technique, similar to a ZQBS technique, was previously used by Vasyutinskii *et al.* to investigate the photofragment orientation following the photodissociation of RbI [230, 231]. More recently, quantum beats have been observed in polyatomic photodissociation, exploring the orientation of the photodissociation of ICN [232] and NO_2 [55, 83]. As part of the studies presented here, two techniques are described and utilised to demonstrate photofragment orientation.

The first technique involves the recording of quantum beats in the emission. In these experiments the emission is resolved into the P, Q or R branches by the monochromator, and the full LIF decay is recorded following excitation of a particular transition $N, j \rightarrow N_e, j_e$. The photolysis laser is switched between left- and right-circularly-polarised light on alternate laser shots, and the signal recorded on separate channels of the oscilloscope. The optics along the detection axis are as discussed earlier and shown in the right panel of figure 2.4. The oscilloscope averages over 256 shots per polarisation before sending the signals to a computer operating a purpose-built LabVIEW

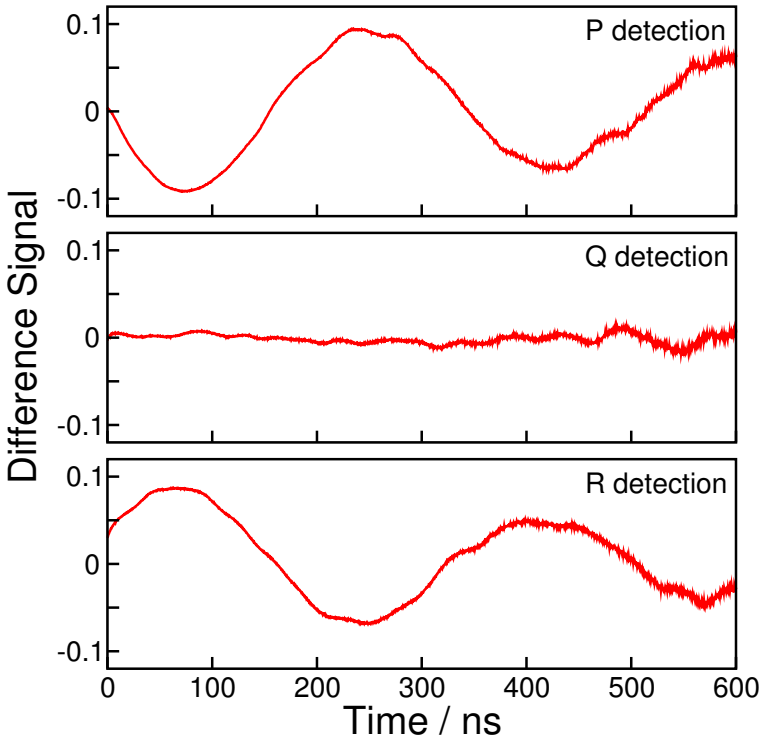

Figure 2.6: Zeeman quantum beats observed in the LIF emission decay following excitation of photofragments produced at 193 nm [55] in a $R_{22}(15)$ transition. The normalised difference of emission intensities following photolysis by left- or right-circularly-polarised light is shown. This normalised difference is equivalent to the degree of circular polarisation $\mathcal{C}$. A magnetic field of 30 Gauss was applied and emission data resolved into P, Q and R branches as shown.

program [228], which in turn averages over 10 of these oscilloscope averaged decays.

Figure 2.6 displays the degree of circular polarisation (see equation (2.8)) recorded for each emission branch following probing a particular transition OH(X,$N, j \rightarrow$ A,N_e, j_e). From the figure there is a clear modulation of the difference signal in the P and R emission branches, but there is no significant difference (discounting noise) in the LIF signal recorded in the Q branch. Additionally, the modulations in the P and R branches are out of phase with one another. This behaviour is characteristic of an oriented sample. Since the probe laser is linearly-polarised and incapable of bringing about the observed orientation signal, this observed orientation must instead result from the initial photolysis process. The oriented distribution produced on photolysis with circularly-polarised light has been transferred to the first excited state

on probing with linearly-polarised light. In these experiments the degree of circular polarisation, now labelled $\mathcal{C}$, becomes time dependent

$$\mathcal{C}(t) = \frac{A_0^{(1)} \tilde{S}_0^{(1)}(t)}{A_0^{(0)} \tilde{S}_0^{(0)}(t) + A_0^{(2)} \tilde{S}_0^{(2)}(t)} \tag{2.10}$$

where the time dependency is accounted for in the line strength factors, which are a function of the experimental geometry and the magnetic field strength. The experimental geometry for the emission element of the 1+1 LIF process is rotated by $\omega_{j_e} t$ in time t, where $t = 0$ is the time of the probe laser pulse, and ω_{j_e} is the Larmor frequency for the excited state, j_e. Note also that the line strengths in the above equation differ from those in equation (2.8), not just in the rotation of the lab-frame geometry with respect to j_e, but also because the polarisation of the probe laser and detection optics differ, as shown in figure 2.4. On evaluation the above equation will yield lab-frame orientation moments from these experimental data. In the example of figure 2.6, $A_0^{(1)} = 0.052 \pm 0.006$, which compares very favourably to the data from the 1+1 LIF difference spectra, $A_0^{(1)} = 0.058 \pm 0.010$ [55].

The second method of using quantum beat spectroscopy, absorption quantum beats, takes advantage of the precession of the initially produced OH(X) photofragment angular momentum, $\boldsymbol{j}$, in the applied magnetic field. There is consequently a precession of the transition dipole moment for excitation to the OH(A) state in the lab-frame, and therefore a variation in the probability of excitation by the left-hand-circularly-polarised probe laser with pump-probe time delay, t_{d}. Finally, this leads to a variation of the LIF emission recorded with t_{d} and an oscillation in the degree of circular polarisation $\mathcal{C}$.

Figure 2.7 displays the variation in the degree of polarisation $\mathcal{C}$ with the delay time in the presence and absence of a magnetic field. The data points were determined from the normalised difference in the LIF intensity for the first 200 ns following the probe

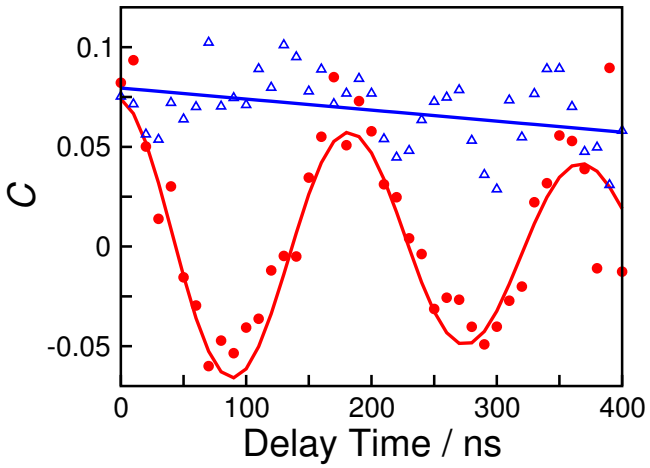

Figure 2.7: Variation of the degree of circular polarisation, $\mathcal{C}(N)$ with delay time between the photolysis and probe laser for the $R_{22}(11)$ transition following photolysis at 248 nm. The blue triangles with line of best fit in blue are data recorded in the absence of the magnetic field (equivalent to the simple 1+1 LIF method). The red circles, with red line of best fit, are data recorded in the presence of a magnetic field of strength 50 Gauss.

pulse for the different photolysis laser polarisations. The pump-probe time delay was varied in steps of 10 ns between each data point. As anticipated, the figure shows a clear oscillation when a magnetic field is present. This demonstrates the presence of an oriented distribution in the ground state following photolysis. Here the linestrength factors used in determining $\mathcal{C}$ are dependent on t_{d}, and the impact this has on the initial ground state, $\boldsymbol{j}$. In this case the experimental geometry for the probe laser excitation is rotated by $\omega_j t_{\mathrm{d}}$, with ω_j the Larmor frequency for the ground electronic state, j. Once again the lab-frame orientation can be determined by utilising equation (2.10). The observed beats have a period of $\sim$ 100 ns in the 50 G field, i.e. the time taken for the oriented angular momentum to precess to the opposite direction to that of the nascent OH(X) products. $\mathcal{C}$ clearly declines in the absence of the field, which is due to the loss of the initial orientation generated in the photolysis through depolarising collisions or the interaction with stray magnetic fields. The beat amplitude at $t_{\mathrm{d}} = 0$ gives the degree of polarisation in the nascent products comparable to the result from 1+1 LIF experiments. The fit in the figure gives a value of $A_0^{(1)} = 0.056 \pm 0.022$, which

is within the errors of the result from 1+1 LIF of $A_0^{(1)} = 0.064 \pm 0.015$.

2.3.7 Comparing the Experimental Methods

It has been demonstrated that the lab-frame orientation can be measured using either of the Zeeman quantum beat techniques described or by measuring the LIF absorption spectra. The limited quantum beat measurements taken are valuable, in that they confirm that the differences observed in the 1+1 LIF signals are a consequence of angular momentum polarisation. However, the quantum beat measurements bring little additional benefit in terms of experimental precision, with error bars of the same order of magnitude as those from the 1+1 LIF measurements. There is also no benefit in terms of accuracy, as the results from 1+1 LIF absorption spectra agree with those from the beat techniques within their respective error bars. Consequently, the time consuming nature of the beat measurement techniques leads to the absorption spectra technique being chosen for collecting experimental results.

For each experimental run approximately 5000 laser shots are required to determine the lab-frame orientation of a particular individual spin-rotation level of the OH(X) photofragment from the emission beat technique. Alternatively, approximately 20,000 laser shots are used to determine the lab-frame orientation from the absorption beat technique. Conversely, approximately 550,000 laser shots are required to determine the entire absorption spectra (including all 21 spin-rotation levels investigated in this experiment at 248 nm) or approximately 25,000 laser shots per spin-rotation level. On first observation this would indicate that the 1+1 LIF spectra method is most time consuming, however given that the first stage of measuring the lab-frame orientation via either quantum beat method would require the determination of the probe laser wavelength for each individual spin-rotation level through scanning the spectrum anyway, there is in practice little benefit. Additionally, on repeat measurements the requirement

of 128 shots per point in the spectrum was relaxed in regions far away from a transition to 32 shots, this reduced requirement affected around 50% of the total spectrum recorded, reducing the experimental time to around 15,000 laser shots per spin-rotation level. The 1+1 LIF spectra technique is additionally much less time consuming for the experimentalist, allowing the entire spectrum of 21 spin-rotation levels to be observed in one experimental run.

Whilst the simple 1+1 LIF absorption spectra measurements are in practice used in determining the experimental results presented here, there are experiments for which the beat techniques are necessary. This necessity would arise when the experimental geometry is insensitive to the polarisation moment being explored, such a restriction is removed by the magnetic field which rotates the lab-frame with respect to the polarisation.

2.4 Experimental Results

Having recorded the full 1+1 LIF spectra, the intensity across the observed peaks is integrated, and the degree of circular polarisation fit with equation (2.8), and the lab-frame polarisation $A_0^{(1)}$ determined using the line strength factors for each peak with corresponding OH(X) quantum state j, N.

Figure 2.8 compares the experimentally-determined $A_0^{(1)}$ moments following photolysis at 248 nm with those following photolysis at 193 nm recorded by Chang [55]. For the most part, the $A_0^{(1)}$ orientation parameters increase with the rotational quantum number N_{OH}, of the probed OH(X) photofragment. The main exception to this is the pattern at lower N_{OH} for 193 nm photolysis; at the lowest N_{OH} the parameter is near zero and falls slightly until around $N_{\mathrm{OH}} = 7$, before rising continually thereafter. With 193 nm photolysis the orientation parameter crosses from negative to positive at $N_{\mathrm{OH}} = 12$, whilst this occurs at a lower N_{OH} following 248 nm photolysis. In the 248 nm

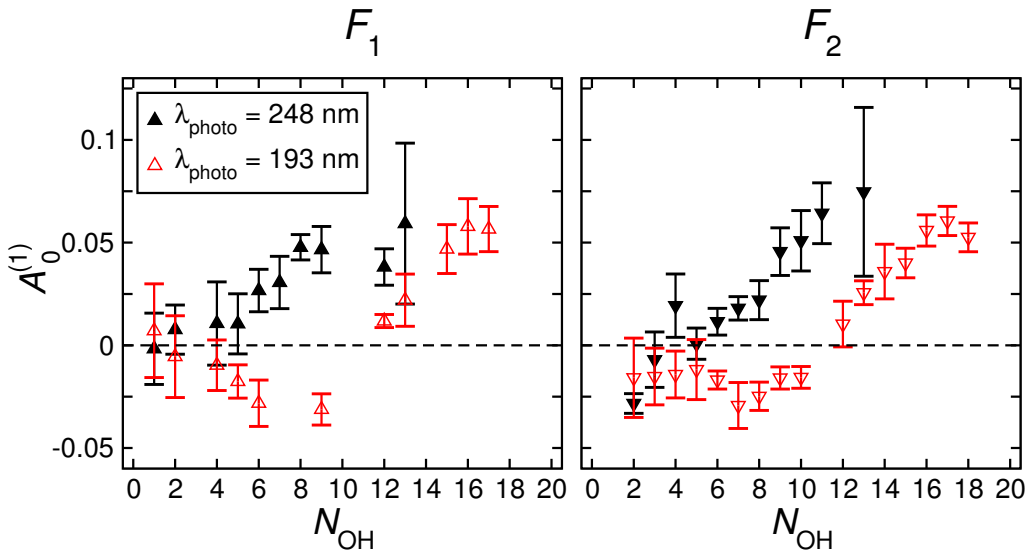

Figure 2.8: Experimental lab-frame orientation parameters, $A_0^{(1)}$, following photodissociation of H_2O_2 at 193 nm [55] shown with red open triangles, and at 248 nm with black filled triangles. Data are presented in terms of N_{OH}, the rotational quantum number of the OH(X) radical photofragment probed. The left-hand panel shows data for the photofragments in the OH($X^2\Pi_{1/2}$) spin-orbit level, whilst the right-hand panel is for photofragments in the OH($X^2\Pi_{3/2}$) spin-orbit level.

data there is not this same region where the orientation parameter is clearly negative, but rather the parameter is near zero until around $N_{OH} = 5$, when it begins to increase. The $A_0^{(1)}$ orientation parameters are typically more positive following 248 nm photolysis than 193 nm photolysis. However, at low N_{OH} the orientation parameters tend to be similar. Following photolysis at either wavelength, $A_0^{(1)}$ parameters are very similar for the two different spin-orbit manifolds, suggesting that spin is largely a spectator and that the rotational rather than electronic part of j is oriented. $A_0^{(1)}$ parameters are measured for a smaller range of N_{OH} following 248 nm photolysis than 193 nm. The peak in the population following photolysis at 248 nm is at a lower $N_{OH} \approx 7$ [211], as compared to $N_{OH} = 12$ following 193 nm photolysis [219]. More generally the population distribution following photolysis at 248 nm is rotationally colder than following 193 nm photolysis, and there is insufficient population at higher N_{OH} to record a LIF spectrum.

2.5 Simulation of Parent Rotation Involvement

Chang *et al.* proposed a mechanism to account for the contribution of H_2O_2 parent molecule rotation to the observed lab-frame orientation following photolysis at 193 nm [224]. In this study, this model has been adjusted to consider photolysis at 248 nm and compare with the new experimental results presented in this thesis. The model used here is similar to that developed previously by Gericke *et al.* to explain the rotational distribution of the OH(X) photofragments [219], and draws upon the classical calculations of Schinke *et al.* [207, 208, 233].

The model makes the axial recoil approximation with photofragment velocity assumed to lie parallel to the breaking O-O bond. Photofragment rotational excitation predominantly arises from the torsional impulse during dissociation and so to a first approximation the rotational angular momentum, $\boldsymbol{R}$, is parallel or anti-parallel to the recoil velocity, $\boldsymbol{v}$. $\boldsymbol{R}$ is defined in the Hund's case (b) coupling case in section 1.5. On photolysis two OH(X) photofragments are produced, labelled either A or B. Photofragment A possesses rotational angular momentum $\boldsymbol{R}_{\mathrm{A}}$ parallel to its velocity of $+\boldsymbol{v}$, whilst photofragment B possesses rotational angular momentum $\boldsymbol{R}_{\mathrm{B}}$ parallel to its velocity of $-\boldsymbol{v}$. On absorption of circularly-polarised light the parent H_2O_2 molecule's total angular momentum $\boldsymbol{J'}$ is oriented in space. Rotation about the O-O bond couples efficiently to the torsional motion during dissociation and is reflected in the rotational excitation of the photofragments. This simulation accounts for the role of orientation of the parent molecule in determining photofragment orientation [224].

In the limit of 0 K there is no contribution from parent molecule rotation to the rotation of the OH(X) photofragments. Under these conditions, this model assumes that the only contributor to fragment rotation is from the torsional impulse applied during bond cleavage. This torque is also assumed to be shared equally between the two photofragments - A and B. The rotational angular momentum in each photofragment

under these conditions has magnitude $|\boldsymbol{R}_i|$. The final rotational angular momentum of photofragment A is $\boldsymbol{R}_{\mathrm{A},f} = \boldsymbol{R}_i$ and for photofragment B, $\boldsymbol{R}_{\mathrm{B},f} = \text{-}\boldsymbol{R}_i$, as demonstrated on the left-hand side of figure 2.9. These photofragments make angles of θ_{R_A} and θ_{R_B} respectively with the lab-frame Z-axis. The lab-frame orientation is expressed as a function of R [224],

$$A^{(1)}(R) = \frac{R}{\sqrt{R(R+1)}} \frac{\langle \cos\theta_{R_\mathrm{A}} \rangle P(R)_\mathrm{A} + \langle \cos\theta_{R_\mathrm{B}} \rangle P(R)_\mathrm{B}}{P(R)_\mathrm{A} + P(R)_\mathrm{B}}, \tag{2.11}$$

where $P(R)_\mathrm{X}$ is the population of photofragment X with rotational angular momentum $\boldsymbol{R}$. $\langle \cos\theta_{R_\mathrm{X}} \rangle$ is the ensemble average of the anisotropy of $\boldsymbol{R}$ for the photofragment X. In the absence of parent rotation, there are an equal number of photofragments with equal and opposite angular momentum, $P(R)_\mathrm{A} = P(R)_\mathrm{B}$ and $\langle \cos\theta_{R_\mathrm{A}} \rangle = -\langle \cos\theta_{R_\mathrm{B}} \rangle$. Consequently there is no resultant orientation in the lab-frame.

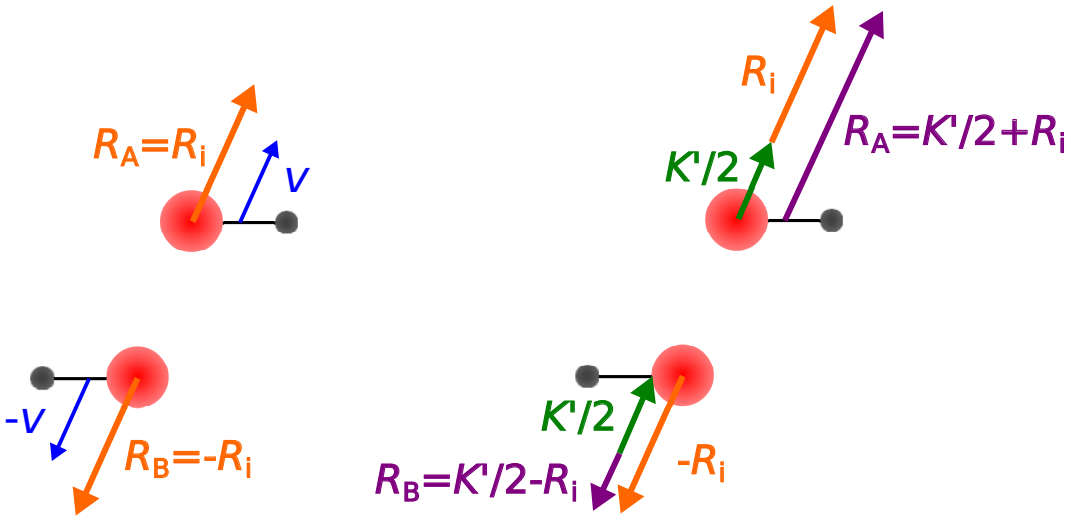

Figure 2.9: Dissociation dynamics as modelled in the simulation based on parent rotation presented here. On the left the dynamics in the absence of parent rotation or those associated with 0 K. On the right coupling with the parent rotation angular momentum projection along the O-O bond axis, $\boldsymbol{K}'$.

Above 0 K, and directly following photon excitation to the $\tilde{\mathrm{A}}$ or $\tilde{\mathrm{B}}$ state of the parent molecule, H_2O_2 has total rotational angular momentum $\boldsymbol{J}'$. $\boldsymbol{J}'$ has projection $\boldsymbol{K}'$ along the O-O bond axis [234], with associated quantum number $\pm K'$. $\boldsymbol{K}'$ makes an angle

$\theta_{K'Z}$ with the lab fixed Z-axis. On dissociation we assume that $\boldsymbol{K'}$ is shared equally between the two OH(X) photofragments, and that this transfer is efficient into the rotational angular momentum of those photofragments. Components of $\boldsymbol{J'}$ orthogonal to the O-O bond axis, contribute principally to the orbital angular momentum of the two OH(X) photofragments about their common centre of mass, rather than their internal rotational angular momentum. Typically $K'/2 < R_{\rm i}$, and in this case the final angular momenta associated with the photofragments are $\boldsymbol{R}_{{\rm A},f} = \boldsymbol{K}/2 + \boldsymbol{R}_i$ and $\boldsymbol{R}_{{\rm B},f} = \boldsymbol{K}/2$ - $\boldsymbol{R}_i$, as demonstrated on the right-hand side of figure 2.9. The rotational population distributions of the two photofragments are no longer the same with the peak positions shifted by $K'/2$ and $-K'/2$ for A and B respectively. Summing across both OH moieties, the effect is to broaden the population distribution, but its peak position will remain as before. Additionally, whereas at 0 K for any value of R there were an equal number of A and B fragments contributing, there are more of fragment B at low R and more of fragment A at high R. Since these fragments are oriented in opposite directions, there is an overall lab-frame orientation observed as a function of R. The population of photofragment A in state R is given by $P(R)_{\rm A} = P_{0{\rm K}}(R - K'/2)$, and for B, $P(R)_{\rm B} = P_{0\,{\rm K}}(R + K'/2)$, where $P_{0\,{\rm K}}(R)$ is the population at 0 K. The orientation of the angular momenta of the two photofragments remain equal and opposite, and make an angle of magnitude $\theta_{K'Z}$ with the lab-frame Z-axis. Therefore $\langle\cos\theta_{R_{\rm A}}\rangle = -\langle\cos\theta_{R_{\rm A}}\rangle = \langle\cos\theta_{K'Z}\rangle$. The resultant lab-frame orientation is expressed as [224]

$$\begin{aligned} A_0^{(1)}(R) &= \frac{R}{\sqrt{R(R+1)}}\frac{P(R)_{\rm A} - P(R)_{\rm B}}{P(R)_{\rm A} + P(R)_{\rm B}}\langle\cos\theta_{K'Z}\rangle \\ &= \frac{R}{\sqrt{R(R+1)}}\frac{P_{0{\rm K}}(R - K'/2) - P_{0\,{\rm K}}(R + K'/2)}{P_{0{\rm K}}(R - K'/2) + P_{0\,{\rm K}}(R + K'/2)}\langle\cos\theta_{K'Z}\rangle. \end{aligned} \quad (2.12)$$

The simulation requires the use of 0 K populations, $P_{0\,\mathrm{K}}(R)$. In the 193 nm case these were estimated from 20 K populations studied under beam conditions by Gericke *et al.* [219]. At 248 nm no beam condition studies were available, so instead data were taken from a computational study, with predictions of the 0 K distribution, by Cai *et al.* [209].

The case in which there is a larger contribution to the OH(X) rotational angular momentum from parent molecular rotation than from dissociative torsion, is also considered in the simulation, i.e. where $K'/2 > R_i$. This case is generally rare as populations of high K' are generally low, although since $\boldsymbol{R}_i$ is on average smaller at 248 nm, it does provide a more important contribution at 248 nm than following 193 nm photolysis. Expressions including this contribution are described in detail in reference [55]. Additionally, it should be noted that these expressions are used regardless of whether photolysis occurs via the $\tilde{\mathrm{A}}$ or the $\tilde{\mathrm{B}}$ state. This seems reasonable as the population distributions following 193 nm photolysis via either pathway are very similar [210]. It can also be shown that the expressions here apply equally to both conformers of $H_2O_2(\tilde{\mathrm{A}}/\tilde{\mathrm{B}})$ [55].

The evaluation of equation (2.12) requires the determination of the relative populations and orientation of the K' states of the parent molecule following absorption of circularly-polarised light. The determination of $\langle\cos\theta_{K'Z}\rangle$ proceeds with the spherical harmonic addition theorem [235],

$$\langle\cos\theta_{K'Z}\rangle = \langle\cos\theta_{K'z}\rangle\langle\cos\theta_{zZ}\rangle. \tag{2.13}$$

The angles are as shown in figure 2.10 and the latter term is the polarisation of the molecular bond in the laboratory-frame [236],

$$\langle\cos\theta_{zZ}\rangle = \frac{\pm K'M'}{J'(J'+1)}. \tag{2.14}$$

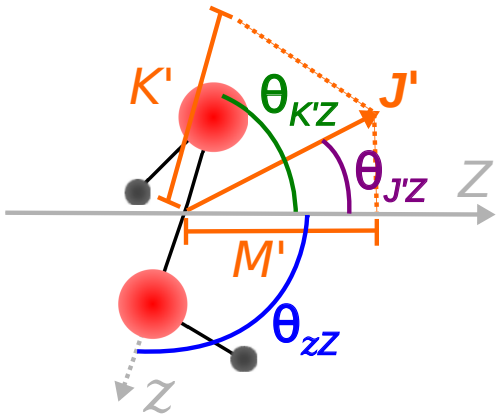

Figure 2.10: Pictorial description of the lab (XYZ) and molecular (xyz) frames associated with H_2O_2. The vectors and the angles associated with treating the parent molecule as a symmetric top are also shown.

$\langle \cos\theta_{zZ} \rangle$ has different signs for $+K'$ and $-K'$, yet these states are equally populated. Consequently, the bond is not oriented on absorption of circularly-polarised light. Since the first term $\langle \cos\theta_{K'z} \rangle = \pm K'/K'$ it follows that

$$\langle \cos\theta_{K'Z} \rangle = \frac{M'K'}{J'(J'+1)}. \tag{2.15}$$

M' determines the sign of $\langle \cos\theta_{K'Z} \rangle$, and is thus responsible for orientation of the rotation about the bond axis in the laboratory-frame, whilst (for a given J') the magnitude of this orientation is determined by the magnitude of K'. The above equation is only valid in the case of predissociation, where the O-O bond is cylindrically symmetric in the lab-frame [224]. However, H_2O_2 undergoes a direct dissociation so that at the instant of absorption the principal molecular axis (z) is constrained by the transition probability $|\boldsymbol{\mu} \cdot \boldsymbol{\epsilon}|^2$ as evaluated in section 1.6. Consequently, in addition to the constraint set out in equation (2.14) the probability distribution of the z-axis in the lab-frame is confined by $4\pi P(\omega_{zZ}) = 3\cos^2\theta_{\mu\epsilon}$. For excitation via a perpendicular transition to the $\tilde{A}$ state it can be shown that [224]

$$4\pi P(\omega_{zZ}) = 1 + P_2(\cos\theta_{zZ})/2, \tag{2.16}$$

and via a parallel transition to the $\tilde{\mathrm{B}}$ state

$$4\pi P(\omega_{zZ}) = 1 - P_2(\cos\theta_{zZ}). \tag{2.17}$$

Consequently, direct dissociation can lead to a more oriented $\boldsymbol{K'}$ than implied by equation (2.15) , which is appropriate only for a long-lived symmetric top.

Further evaluation of $\langle\cos\theta_{zZ}\rangle$ for direct dissociation of a symmetric top is demonstrated in reference [224], but the resulting equation for $\langle\cos\theta_{K'Z}\rangle$ following direct dissociation via the $\tilde{\mathrm{A}}$ state is

$$\langle\cos\theta_{K'Z}\rangle = \left(1 + \frac{2\sin^2\theta_{J'z}\sin^2\theta_{J'Z}}{2 + sin^2\theta_{J'z}\sin^2\theta_{J'Z} + 2\cos^2\theta_{J'z}\cos^2\theta_{J'Z}}\right) \times \frac{K'M'}{J'(J'+1)}, \tag{2.18}$$

and via the $\tilde{\mathrm{B}}$ state

$$\langle\cos\theta_{K'Z}\rangle = \left(1 - \frac{2\sin^2\theta_{J'z}\sin^2\theta_{J'Z}}{2 - sin^2\theta_{J'z}\sin^2\theta_{J'Z} - 2\cos^2\theta_{J'z}\cos^2\theta_{J'Z}}\right) \times \frac{K'M'}{J'(J'+1)}. \tag{2.19}$$

However, these equations must be averaged over the population of the $|J'K'M'\rangle$ state. The probability of an H_2O_2 molecule being excited on absorption of polarised radiation to the state $|J'K'M'\rangle$, when treated as a symmetric top molecule, is proportional to the square of the Wigner coefficient $\langle JK, 1\rho|J'K'\rangle^2\langle JM, 1\rho|J'M'\rangle^2$ [13, 237], where $\langle JKM|$ is the lower state, and ρ is the polarisation of the radiation. With left-hand-circularly-polarised light, $\rho = +1$ [13, 220].

The $H_2O_2(\tilde{\mathrm{A}}/\tilde{\mathrm{B}})$ population for each state $|J'K'M'\rangle$ must be calculated. These populations are proportional to the population of $H_2O_2(\tilde{\mathrm{X}})$ in a particular state $|JKM\rangle$, and the Einstein coefficient for absorption, $B_{KJ\rightarrow K'J'}$. The population of the state

$|JKM\rangle$ is given by,

$$\mathcal{P}^{JK}_{\mathrm{H_2O_2(\tilde{X})}} = g_{J,K}\exp\left[\frac{-BJ(J+1)-(A-B)K^2}{k_{\mathrm{B}}T}\right], \tag{2.20}$$

where A and B are rotational constants for a prolate symmetric top and $g_{J,K}$ is a statistical weight [238]. The Einstein coefficient is proportional to the line strength factor, and in the case of a symmetric top this is simply given by the Hönl-London factor, $\mathcal{S}(J'K', JK)$, divided by $2J+1$ [13, 238]. Consequently, the population of the doublet state $\pm K'$ for $\tilde{\mathrm{A}}/\tilde{\mathrm{B}}$ is given by

$$\mathcal{P}(K')^{\Delta J,\Delta K}_{\mathrm{H_2O_2(\tilde{A}/\tilde{B})}} = D^{\Delta K}_{\tilde{\mathrm{A}}/\tilde{\mathrm{B}}}\sum_J \frac{g_{J,K}}{2J+1}\exp\left[\frac{-BJ(J+1)-(A-B)K^2}{k_{\mathrm{B}}T}\right]\mathcal{S}(J'K', JK), \tag{2.21}$$

where $D^{\Delta K}_{\tilde{\mathrm{A}}/\tilde{\mathrm{B}}}$ is the probability of a $\tilde{\mathrm{X}} \rightarrow \tilde{\mathrm{A}}/\tilde{\mathrm{B}}$ transition. ΔJ is restricted to 0, ± 1 and the selection rule for ΔK depends on the electronic transition. For the $\tilde{\mathrm{X}} \rightarrow \tilde{\mathrm{A}}$ transition ΔK is restricted to ± 1, whilst for $\tilde{\mathrm{X}} \rightarrow \tilde{\mathrm{B}}$ ΔK is restricted to 0. In the simulation the values of $D_{\tilde{\mathrm{A}}}$ and $D_{\tilde{\mathrm{B}}}$ are scaled to reflect the relative contributions at each photolytic wavelength [210], 1:0 at 248 nm and 0.62:0.38 at 193 nm. In the simulation, this summation is over J between $J = K' - \Delta K$ and $J = 60$ [224].

Finally, returning to $\langle\cos\theta_{K'Z}\rangle$, which should be averaged over J, J', M, and M', weighted by the population of the initial state and the square of the Wigner coefficient $\langle JK, 1\rho|J'K'\rangle^2\langle JM, 1\rho|J'M'\rangle^2$, to give the orientation of the K' state $\langle\cos\theta^{\Delta J\Delta K}_{K'Z}\rangle$. This orientation can be written as

$$\begin{aligned}\langle\cos\theta^{\Delta J\Delta K}_{K'Z}\rangle \;=\; & \sum_{J'JM'M}\frac{3D^{\Delta K}_{\tilde{\mathrm{A}}/\tilde{\mathrm{B}}}g_{J,K}\mathcal{S}(J'K', JK)}{(2J+1)(2J'+1)\mathcal{P}(K')^{\Delta J,\Delta K}_{\mathrm{H_2O_2(\tilde{A}/\tilde{B})}}}\langle\cos_{K'Z}\rangle \\ & \times\langle JM, 1\rho|J'M'\rangle^2\exp\left[\frac{-BJ(J+1)-(A-B)K^2}{k_{\mathrm{B}}T}\right],\end{aligned} \tag{2.22}$$

where $\langle \cos_{K'Z} \rangle$ is evaluated via equations (2.18) and (2.19).

Returning to equation (2.12) and by including consideration of the population and orientation of K' leads to a fuller expression for the lab-frame orientation

$$\begin{aligned} A_0^{(1)}(R) \equiv \beta_0^1(01)(R) &= \frac{R}{\sqrt{R(R+1)}} \frac{1}{P(R)_{300\,K}} \sum_{K'\Delta K\Delta J} \left[\mathcal{P}(K')^{\Delta J \Delta K}_{\mathrm{H_2O_2(\tilde{A})}} + \mathcal{P}(K')^{\Delta J \Delta K}_{\mathrm{H_2O_2(\tilde{B})}} \right] \\ &\quad \times \left[P(R - K'/2)_{0\,K} - P(R + K'/2)_{0\,K} \right] \langle \cos \theta^{\Delta J \Delta K}_{K'Z} \rangle, \end{aligned} \tag{2.23}$$

where

$$P(R)_{300\,K} = \sum_{K'\Delta K\Delta J} \left[\mathcal{P}(K')^{\Delta J \Delta K}_{\mathrm{H_2O_2(\tilde{A})}} + \mathcal{P}(K')^{\Delta J \Delta K}_{\mathrm{H_2O_2(\tilde{B})}} \right] \left[P(R - K'/2)_{0\,K} + P(R + K'/2)_{0\,K} \right]. \tag{2.24}$$

These equations are evaluated using equations (2.22) and (2.21).

In the $\tilde{\mathrm{A}}$ state, with transitions restricted to $\Delta K = \pm 1$, larger Hönl-London factors are seen for high K [13] and a high degree of orientation results. In the $\tilde{\mathrm{B}}$ state, with transitions restricted to $\Delta K = 0$, low K absorption dominates [13] and there is relatively little orientation. Consequently, this model predicts that observed orientation is primarily due to photolysis via the $\tilde{\mathrm{A}}$ state.

Finally, equations can also be derived to express the molecular-frame orientation parameters [224],

$$\begin{aligned} \left(1 - \frac{\beta}{2}\right) a_0^1(\perp)(R) &= \frac{3}{P(R)_{300\,\mathrm{K}}} \frac{R}{\sqrt{R(R+1)}} \sum_{K'\Delta K\Delta J} \mathcal{P}(K')^{\Delta J, \Delta K}_{\mathrm{H_2O_2(\tilde{A})}} \\ &\quad \times \left[P(R - K'/2)_{0\,\mathrm{K}} - P(R + K'/2)_{0\,\mathrm{K}} \right] \langle \cos \theta^{\Delta J, \Delta K}_{K'Z} \rangle, \end{aligned} \tag{2.25}$$

and

$$\sqrt{(1+\beta)(2-\beta)}\mathrm{Re}[a_1^1(\parallel,\perp)(R)] = \frac{-3}{P(R)_{300\,\mathrm{K}}}\frac{R}{\sqrt{R(R+1)}}\sum_{K'\Delta K\Delta J}\mathcal{P}(K')^{\Delta J,\Delta K}_{\mathrm{H_2O_2(\tilde{B})}} \times [P(R-K'/2)_{0\,\mathrm{K}} - P(R+K'/2)_{0\,\mathrm{K}}]\,\langle\cos\theta^{\Delta J,\Delta K}_{K'Z}\rangle, \quad (2.26)$$

where it is noted that the $\tilde{\mathrm{B}}$ state is unable to contribute to the $a_0^1(\perp)$ parameter, and consequently is associated exclusively with $\mathrm{Re}[a_1^1(\parallel,\perp)]$.

In the simulation, the equations detailed here are adapted to account for the true quantum nature of the angular momenta by applying semi-classical theory, accounting firstly for the breakdown in the approximation that $\boldsymbol{R}$ is parallel or anti-parallel to $\boldsymbol{v}$ [204]. In this way the semi-classical model does not restrict the angle between $\boldsymbol{R}$ and the transition dipole moment vector, $\boldsymbol{\mu}$, to 0°, or 90°, instead determining this angle on the basis of a Gaussian distribution for $\boldsymbol{R}$ centred on these angles. The model is further adapted to account for the coupling in the OH(X) photofragment, accounting for the coupling of the electronic angular momentum projection Λ, to $\boldsymbol{R}$ to create $\boldsymbol{N}$, and further coupling to the intrinsic spin angular momentum $\boldsymbol{S}$, to create $\boldsymbol{j}$. This adaptation makes use of the Hund's case (b) coupling regime. These adaptations to the model presented only briefly here, are detailed in reference [55] and are based on models by Gericke *et al.* [204] and Dixon *et al.* [239].

2.6 Comparison of Simulation and Experiment

Figure 2.11 compares the experimentally-observed lab-frame orientation parameters with those from the simulation considering the contribution of parent rotation. Data are shown following photolysis at 193 nm and 248 nm. Calculated orientation parameters from an alternative simulation (introduced later) are also shown.

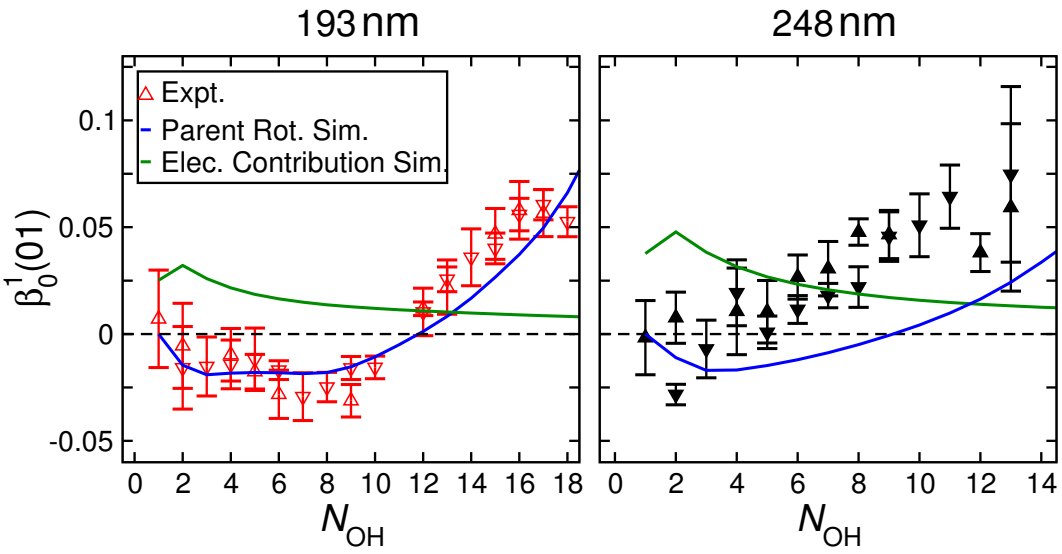

Figure 2.11: Comparison of the experimentally-determined bipolar moment, $\beta_0^1(01)$, with those from two different simulations. On the left are data for 193 nm photolysis [55], and on the right data following 248 nm photolysis. Experimental data are shown with triangles and error bars. The blue lines are predicted $\beta_0^1(01)$ data from the simulation described here to account for the contribution to lab-frame orientation from the parent molecule's rotation. The green lines give the simulated contribution from the electronic angular momentum. The simulated data are calculated for discrete rotational quantum numbers and the connected lines do not indicate that they are continuous. Experimentally, upwards pointing triangles are used for photofragments in the OH($X^2\Pi_{3/2}$) spin-orbit level, whilst the downwards pointing triangles are for photofragments in the OH($X^2\Pi_{1/2}$) spin-orbit level. Simulated data are averaged over spin-orbit levels.

At 193 nm there is good agreement between the results from the parent rotation simulation and the experiment. The simulation correctly predicts the changing sign of the orientation between low and high N_{OH}, and that this occurs at $N_{OH} \approx 11$. The agreement is quantitative as well as qualitative. The exception is that the simulation slightly underestimates the strength of the negative orientation in the mid range of N_{OH} = 6-9. This agreement implies that it is the rotational element of $\boldsymbol{j}$ that is oriented through coupling of the circularly-polarised photon and the H_2O_2 parent rotation. This is mostly attributed to the incoherent molecular-frame polarisation parameter, $a_0^1(\perp)$, and excitation to the $\tilde{A}$ state. Indeed both the simulation and experiment calculate near zero values for the coherent molecular-frame orientation parameter, $\mathrm{Re}[a_1^1(\parallel,\perp)]$ as shown in reference [224].

In contrast, the simulation provides only a qualitative prediction of the lab-frame orientation following photolysis at 248 nm. Generally the simulation underpredicts the size of the orientation, though the disagreement appears to increase at larger N_{OH}. The simulation also predicts negative orientation up to $N_{OH} \approx 9$, but negative orientation is not seen above $N_{OH} = 3$ experimentally.

Unlike the 193 nm simulation, the simulated data for 248 nm are not based on an experimentally-measured, near 0 K, population distribution, but a simulated distribution [209]. This simulated distribution is very similar to that observed at 300 K in the experiments of Docker, Hodgson and Simons [213]. In contrast, at 193 nm there are notable differences in the population distribution at 300 K and that measured in molecular beam conditions at 20 K. This might suggest that the simulated distribution is not accurate. Certainly it would be advantageous to have access to an experimental population distribution measured at a near 0 K temperature, comparable to that available for 193 nm photolysis.

Figure 2.12 explores the effect of changing the OH(X) rotational population distribution used as the 0 K population distribution in the simulation. The figure gives four different population distributions; one from theory by Cai *et al.* used in the initial simulation above [209], another measured experimentally by Docker *et al.* at 300 K [213], and finally two utilising the population distribution used in the 193 nm simulation [219] but shifting the distribution to lower N_{OH}. In the first of these the peak coincides with that in the Cai study at $N_{OH} = 8$, and in the second at $N_{OH} = 7$ so the distribution looks similar to that from Docker *et al.*. The right panel shows that whilst these different population distributions do change the simulated orientation, the differences are not substantial and there is no real improvement in the comparison with the experimentally-determined results. Consequently, it is clear that unlike following 193 nm photolysis, the orientation observed following 248 nm photolysis cannot exclusively be explained by the parent molecule rotation coupling to the torsional impulse.

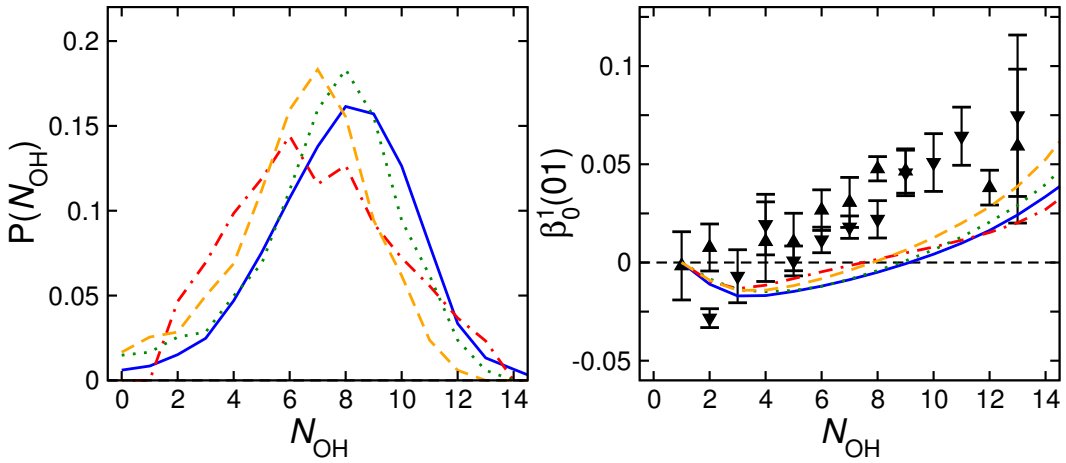

Figure 2.12: The left panel shows four alternative 0 K population distributions used as the basis of the parent rotation simulation. The blue full line is the population distribution determined in the theoretical study of Cai *et al.* [209], and the red line broken into dots and dashes is the population determined experimentally, though at 300 K, by Docker *et al.* [213]. The orange dashed line takes the 0 K distribution following 193 nm photolysis determined by Gericke [219] and shifts the population peak to $N_{\rm OH} = 7$ (nominally that of the Docker *et al.* study) and the dotted green line shifts this spectrum so the population peak is at $N_{\rm OH} = 8$. The right panel uses the same colours to display the simulated values of the bipolar moment, $\beta^1_0(01)$, with these different population distributions. Experimental data are shown with black triangles and error bars. Once again, experimentally upwards pointing triangles are used for photofragments in the OH($X^2\Pi_{3/2}$) spin-orbit level, whilst the downwards pointing triangles are for photofragments in the OH($X^2\Pi_{1/2}$) spin-orbit level. Simulated data are averaged over spin-orbit levels.

2.6.1 Possible Alternative Origins for Observed Orientation

Electronic Contribution

An alternative mechanism for the observed orientation was proposed by Alexander in a study at 355 nm [215], focusing on the action of circularly-polarised photons on the electronic rather than nuclear rotation. In this study most of the orientation was attributed to the incoherent molecular-frame polarisation parameter, $a^1_0(\perp)$, with the coherent term, $\mathrm{Re}[a^1_1(\parallel,\perp)]$, only of significant size at $j = 0.5$ [215]. In the model proposed here the incoherent molecular-frame orientation parameter $a^1_0(\perp)$, is derived from direct mapping of the photon angular momentum onto the electronic motion of

the OH(X) photofragment [217, 240]. As such [13, 215],

$$|a_0^1(\perp)| = \frac{m_{ph}}{\sqrt{j(j+1)}}, \tag{2.27}$$

where m_{ph} is the contribution from the projection of the photon angular momentum onto the molecular-frame z-axis, and j the total angular momentum quantum number for the OH(X) photofragment. Within this model the photon angular momentum is assumed to be shared equally between the two photofragments, each receiving $m_{ph} = 0.5\hbar$.

Figure 2.11 includes the orientation that results from this electronic contribution alongside the experimental results and the simulated orientation from parent rotation. The contribution of $a_0^1(\perp)$ to the lab-frame orientation, $A_0^{(1)}$, is given by [82, 223]

$$A_0^{(1)} \equiv \beta_0^1(01) = \frac{1}{6}\left[(2-\beta)a_0^1(\perp) - 2\sqrt{(1+\beta)(2-\beta)}\mathrm{Re}[a_1^1(\|,\perp)]\right]. \tag{2.28}$$

At 193 nm β is set to 0.00 (experimental measurement of 0.00±0.02 [210]) so $\beta_0^1(01) = \frac{1}{6}\{a_0^1(\perp) - 2\sqrt{2}\mathrm{Re}[a_1^1(\|,\perp)]\}$. At 248 nm β is set to -1 (experimental measurement is -0.86±0.10 [211]), to account for the fact that the only contribution to H_2O_2 photolysis is from perpendicular transitions through the $\tilde{A}$ state, consequently $\beta_0^1(01) = \frac{1}{4}a_0^1(\perp)$. The deviation from -1 in the experimental measurement of β is believed to arise from the rotation of the parent molecule in the interval between the moment of photon absorption and the subsequent fragment separation [205].

These expressions are adapted to account for the true quantum nature of angular momenta by the application of a semi-classical approach (see reference [224]). The resultant electronic contribution from the semi-classical expression is included in figure 2.11. Only the magnitude of this contribution should be considered, not its sign as equation (2.27) only refers to the modulus of the $a_0^1(\perp)$ orientation parameter [215].

This electronic contribution is unable to explain the observed pattern of orientation parameters in either the 193 nm or 248 nm case. The electronic contribution cannot account for the increasing parameter at high N_{OH}, instead predicting this to fall.

Whilst the sign of the electronic contribution should not be considered, the fact that this model is unable to predict the changing sign of the orientation parameter between high and low N_{OH} is worth reflecting upon. Recent experiments by Alexander *et al.* observed a change in sign of the orientation parameter with j following the photolysis of Cl_2 [200]. Since in this case the parent molecule is a diatomic, there is no rotational part of the photofragment angular momentum and the changing sign is thought to arise from the involvement of different exit channel dynamics for different j. The involvement of alternative exit channel dynamics could also lie behind the observed change of sign in the orientation parameter following H_2O_2 photolysis. One possible explanation is provided by the proposed involvement of excitation to the $H_2O_2(\tilde{B}^3B)$ state [241]. The involvement of this triplet state is used to explain the observed preference for the formation of photofragments in the A'' Λ-doublet in studies by Morita and Kato [241]. However, the studies performed in this investigation only probe the A' state, as absorption is via either R_{11} or R_{22} transitions. Consequently, it seems unlikely that the $\tilde{B}^3B$ state is involved in this case, and this alternative electronic state does not provide an explanation for the observed sign change in the lab-frame orientation.

Figure 2.13 compares the experimentally-determined $\beta_0^1(01)$ parameters with the combined orientation contributions from the parent molecule rotation simulation and the electronic contribution simulation. For 193 nm photolysis the inclusion of the electronic contribution worsens the agreement with the experimental values, when compared to the simulation only accounting for parent rotation contributions. However, for 248 nm photolysis the inclusion of the electronic contribution brings the simulated and experimental data closer together. Despite this there is still far from qualitative and quantitative agreement between the experiment and the simulation.

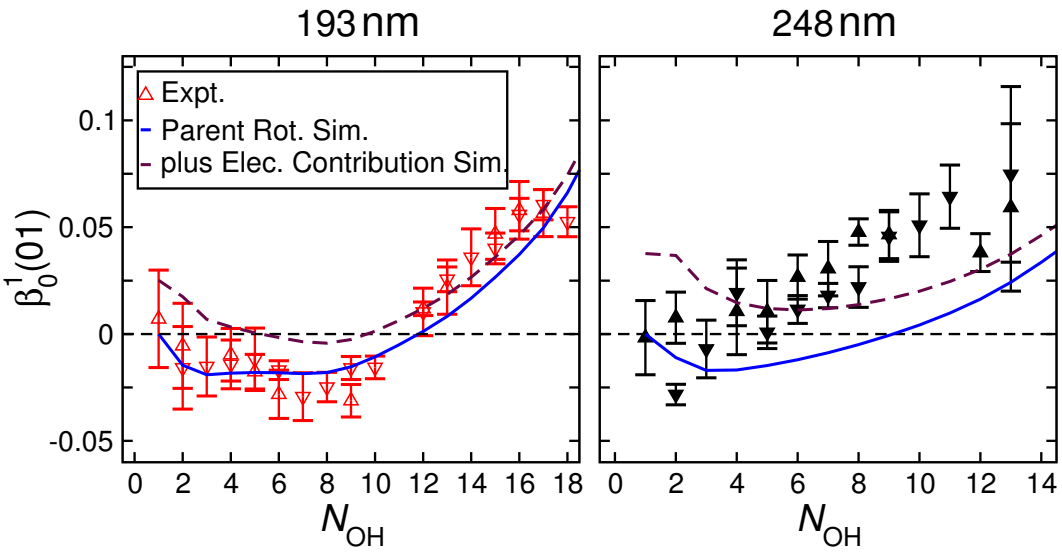

Figure 2.13: These graphs compare the experimentally-determined bipolar moment, $\beta_0^1(01)$, with those from the parent rotation simulation, shown as blue full lines, and the results from this simulation combined with a model for the electronic contribution to orientation described by Alexander [215] shown with purple dashed lines. On the left are data for 193 nm photolysis [55], and on the right data following 248 nm photolysis. Experimentally, upwards pointing triangles are used for photofragments in the OH($X^2\Pi_{3/2}$) spin-orbit level, whilst the downwards pointing triangles are for photofragments in the OH($X^2\Pi_{1/2}$) spin-orbit level. Simulated data are averaged over spin-orbit levels.

Bending Impulse

Although the torsional impulse is believed to be the main origin of the photofragment rotational excitation [207–209], there is still a smaller contribution from a bending impulse during the photodissociation. The recoil impulse along the breaking bond induces a component of rotation in each OH(X) photofragment orthogonal to the O-O bond. Since geometrically the rotation from this impulse behaves like an OOH bend in the instant of dissociation, it shall be referred to as a bending impulse. The fraction of the available energy that is disposed into rotation through the bending impulse can be estimated through the use of a simple direct impulsive model proposed by Tuck *et al.* [242]. According to this model, the majority of the energy (94.1%) is disposed into translational excitation of the photofragments. This dominant disposal of energy as translation has been confirmed in a number of experiments [205, 210, 211]. The

rotational energy disposed into each photofragment can be calculated via [242]

$$E_{\mathrm{R}}^{\mathrm{bend}} = E_{\mathrm{avl}} \frac{m_{\mathrm{H}}}{m_{\mathrm{O}}} \sin^2 \chi \tag{2.29}$$

where m_{X} is the mass of atom X, and χ is the OOH bond angle (109.5° for $H_2O_2(\tilde{\mathrm{X}})$ at equilibrium). E_{avl} is the available energy per photofragment, determined from the energy of the absorbed photon, $h\nu$, minus the bond dissociation energy, $D_0^0(\mathrm{HO-OH}) \approx 17300 \pm 800\,\mathrm{cm}^{-1}$ [243]. By evaluating the second and third terms, the fraction of energy disposed as rotation is estimated as 5.6%.

Table 2.2 lists E_{avl} and $E_{\mathrm{R}}^{\mathrm{bend}}$ for a variety of photolysing wavelengths. The table also gives experimentally-measured average rotational energies for OH(X) photofragments, following photodissociation at each wavelength. These values were collected together by Simons *et al.* [205], but the original references are listed in the table.

λ_{photo}	$E_{\mathrm{avl}}/\mathrm{cm}^{-1}$	$E_{\mathrm{R}}^{\mathrm{bend}}/\mathrm{cm}^{-1}$	$\langle E_{\mathrm{R}} \rangle/\mathrm{cm}^{-1}$	Reference
193 nm	17300	960	2750	[210]
248 nm	11500	640	1250	[211]
266 nm	10100	560	1050	[204]
351 nm	5600	310	445	[205]
390 nm	4200	230	-	N/A

Table 2.2: E_{avl} gives the available energy transferred in the recoil impulse during O-O bond cleavage for different photodissociating wavelengths, λ_{photo}. The energy provided by the this impulse to rotation, according to a simple direct impulsive model [242], is given by $E_{\mathrm{R}}^{\mathrm{bend}}$. $\langle E_{\mathrm{R}} \rangle$ lists the experimentally-determined average rotational energy for OH(X) photofragments, measured at each wavelength in the experiments listed in the references.

The energy transferred to the rotation is a constant fraction of the reducing available energy. However, the contribution to photofragment rotation from the torsional

impulse is also falling with increasing wavelength. For photolysis at 193 nm, the bending impulse can contribute 35% of the total rotational energy observed experimentally, whilst for 248 nm photolysis the bending impulse contribution is estimated as 51% and higher still at 70% for 351 nm photolysis. According to the direct impulsive model, the contribution from the recoil impulse to the rotational energy observed in the OH(X) photofragments increases with photolysis wavelength. The conclusion that the bending impulse is increasingly important to the dissociation dynamics at photolysis wavelengths greater than 193 nm has been noted previously [55, 204, 205, 210, 215, 217]. However, the conclusion here that at 248 nm and longer photolytic wavelengths the bending impulse is the main origin of the rotational excitation goes much further than previous studies. Previous work, as already discussed, has proposed that the torsional impulse continues to be the main contributor to OH(X) photofragment rotational excitation at higher photolytic wavelengths, and it should be noted that the direct impulsive model is particularly crude. However, in anycase this increased role of the bending impulse presents a clear challenge to the simulation utilised in this study.

The competitive bending impulse contributes angular momentum to the photofragments perpendicular to the axial recoil direction, $\boldsymbol{v}$, and also perpendicular to the angular momentum arising from torsional motion. The $\beta_0^0(22)$ modified lab-frame bipolar moment considers the mutual alignment of $\boldsymbol{v}$ and $\boldsymbol{j}$ in the lab-frame, so by considering its value the assumption in the simulation that $\boldsymbol{j}$ is parallel to $\boldsymbol{v}$ can be evaluated. In the event that $\boldsymbol{v}$ and $\boldsymbol{j}$ are parallel, $\beta_0^0(22)$ takes the limiting value of +1 (classically), whilst a perpendicular relationship would lead to a limiting value of -1/2.

Experimentally-determined $\beta_0^0(22)$ moments are listed in table 2.3. The parameter decreases with increasing wavelength as the correlation between $\boldsymbol{j}$ and $\boldsymbol{v}$ becomes progressively less co-parallel. This is as expected by both the direct impulsive model, and the reduced torsional impulse resulting from the reduced torsional dependence of excited state PESs as demonstrated earlier in figure 2.3.

λ_{photo}	$\beta_0^0(22)$	Reference
193 nm	0.70 ($N_{\text{OH}} = 12 - 17$)	[210]
248 nm	0.38 ($N_{\text{OH}} = 14$)	[211]
266 nm	0.33 ($N_{\text{OH}} = 14$)	[204]
351 nm	0.00 ($N_{\text{OH}} = 6$)	[205]
390 nm	0.00 ($N_{\text{OH}} = 5$)	[205]

Table 2.3: Example $\beta_0^0(22)$ parameters experimentally-measured for OH(X) photofragments following photolysis at λ_{photo} from a variety of experiments. The $\beta_0^0(22)$ parameter effectively measures the co-alignment of $\boldsymbol{v}$ and $\boldsymbol{j}$ relative to the lab-fixed Z-axis.

However, the interest of this study is not strictly the origin of the photofragment angular momentum but rather the origin of its orientation. It is unclear if the bending motion could couple to parent rotation, though if possible this would dramatically change the model presented here to account for the role of parent rotation in the observed orientation. $\tilde{\text{X}} \rightarrow \tilde{\text{A}}$ excitation is most intense in high K states, where the parent molecule angular momentum is strongly oriented about the O-O bond axis. Necessarily high K state parent molecules have relatively weak orientation about axes perpendicular to the O-O bond. This presents a challenge to the possibility that OH photofragment orientation arises from oriented parent molecule angular momentum perpendicular to the O-O bond coupling to the bending impulse.

Vibrational Motion

Finally, the suggestions made so far have only accounted for the contribution from the internal rotation of the parent molecule, not the potential role of parent vibration. The effect of zero-point energy or excitation of the torsional bend, ν_4, is accounted for in the model proposed in this study. This kind of motion will act to change the degree of torsional torque following excitation and it is this torque that is coupled to parent rotation in the model.

However, the role of zero point energy associated with OOH bending vibration (varying the angle between the O-O and O-H bonds) has not been considered, and this could couple with the bending torque induced by mutual repulsion at the point of photolysis [211]. Gericke *et al.* estimated that zero point energy from parent molecule OOH bending vibration (modes ν_2 and ν_6) contributes $\approx$330 cm^{-1} to the final rotation per OH photofragment [204]. However, this estimation follows photolysis from equilibrium geometries and is likely reduced at the larger O-O bond lengths associated with photolysis at longer wavelengths. In anycase it is unclear what role vibrational zero point energy would have on photofragment orientation.

2.7 Concluding Remarks

Studies have been performed to measure the orientation of the OH(X) photofragments produced following photolysis of H_2O_2 with circularly-polarised light at 193 nm by Chang [55], and here at 248 nm. A simulation was developed to account for the impact of the parent H_2O_2 molecule rotation on the orientation of the OH(X) photofragments in the lab-frame [55, 224]. The simulation coupled the parent rotation about the O-O bond to the torsional impulse during bond cleavage. This mechanism accounted well for the observed orientation at 193 nm, considerably better than a model assuming that the orientation results from the electronic part of the angular momentum rather than the rotational part [55]. However, at 248 nm the model was not able to quantitatively explain the observed orientation. The inclusion of a simple model for the incoherent orientation, $a_0^1(\perp)$, arising from the coupling of the photon angular momentum to the electronic orbital angular momentum, did not significantly improve the estimation either. As already mentioned, the lack of availability of a 0 K OH(X,N_{OH}) population distribution following 248 nm photolysis is inconvenient. However, as demonstrated, it

is unlikely that an alternative distribution will significantly improve the model's estimation of $\beta_0^1(01)$ values.

Consideration of the impact of parent rotation is sufficient to interpret $\beta_0^1(01)$ following 193 nm photolysis, but an alternative or additional mechanism seems to be at play at the longer wavelength of 248 nm. The possibility that this arises from the involvement of intersystem crossing to a further surface $H_2O_2(\tilde{B}^3B)$ has been suggested, though the preference for the OH(X) A' Lambda-doublets suggests otherwise. Another possibility is that coupling of the parent rotation to the bending impulse plays an increasing role at longer wavelengths. Finally, the possibility of a role for vibrational motion, specifically the zero point energy, of the H_2O_2 molecule was mentioned.

In order to further this study the development of a new simulation to account for the impact of the bending impulse, zero point energy of bending vibrations, and the coupling of parent rotation to the bending impulse, would be worthwhile. Alternatively, a full QCT study may prove more informative such as on the PESs calculated by Drozd *et al.* [216].

This investigation can also be furthered by carrying out the photolysis in a molecular beam. The experimental measurement of the rotational population of OH(X) photofragments following 248 nm photolysis under molecular beam conditions would provide an estimate of the 0 K population, comparable to that available for 193 nm photolysis. Measurement of the lab-frame orientation under molecular beam conditions, following both 193 nm and 248 nm photolysis, would also be useful since this will all but eliminate the role of parent rotation yet leave contributions from vibrational zero point energy and bending and torsional impulses. This study could also be extended to higher photolysis wavelengths, 266 nm, 355 nm etc. The new molecular-beam machine introduced in the final chapter of this thesis would be capable of performing these experiments either through a LIF technique or utilising a REMPI scheme for the OH(X) photofragment [244–248].

Part of the motivation of this study was to demonstrate the ability of Zeeman quantum beat spectroscopy to probe angular momentum polarisation. Having successfully demonstrated this with two approaches, the method will be used more extensively in the experimental measurement of collisional depolarisation in the OH(A)+H_2 system as detailed in Chapter 5.

Chapter 3

Theoretical Methods

Having established the Zeeman quantum beat spectroscopy method as a tool for measuring angular momentum polarisation, we now turn to the central topic of this thesis: the collision dynamics of OH(A)+H_2.

In this chapter the quasi-classical trajectory (QCT) method used in exploring collisions on an *ab-initio* OH(A)+H_2 potential energy surface (PES) is described. The PES used in these calculations was calculated by Bowman *et al.* [126] and the basics of their methodology are described in this chapter, building on the short description of their studies in 1.9.3. The shape of the potential energy surface is explored as this will prove extremely important in explaining the results of the QCT calculations in chapters 4 and 7.

The QCT calculations are broken down into three stages: the selection of the initial conditions of the two diatoms; the propagation of the trajectory; and the quantisation of the final states. The final positions and angular momenta of the two diatoms are recorded and these are analysed to calculate experimentally observable parameters such as RET cross sections and depolarisation cross sections. A tensor opacity formalism has been used to account for the open shell nature of the OH(A) diatom.

This work adds to the previous theoretical studies of the OH(A)+H_2 collision system by Yarkony *et al.* [177, 178], Zhang *et al.* [187, 188], Clary *et al.* [130, 190], Lester

et al. [105, 107], and Collins *et al.* [189] described in 1.9.3. Note again, though, that whilst those studies were interested in exploring the topography of ground, as well as excited state surfaces in the region of conical intersections, or propagating trajectories with the aim of exploring the outcome of quenched collisions, this study is adiabatic in nature and restricts collisions to the excited state surface.

3.1 OH(A)+H_2 Potential Energy Surface

The OH(A)+H_2 PES used in these calculations was produced by Bowman *et al.* [126]. A detailed description of how this surface, and another for the ground state $1^2A'$, was calculated is given in reference [126], and shall only be described here briefly. The ground state PES includes the products of reactive (H_2O+H) and non-reactive (OH(X)+H_2) quenching.

In constructing the surfaces, a selection of data points for fitting were first determined using direct-dynamics calculations [249, 250]. The calculations used a complete-active-space second-order multireference perturbation theory approach (CASPT2) [251] with a correlation-consistent-augmented-double zeta basis set (aVDZ) [252]. 16,000 molecular configurations and accompanying electronic energies were determined from calculations initiated at or near 13 previously identified conical intersections from the work of Yarkony and Hoffman [178]. A further 7000 configurations were added by considering the product channels and the reactive (ground state) saddle point [126]. These 23,000 configurations span the ground state $1^2A'$ and excited state $2^2A'$ potential.

Further data points were calculated *ab initio* using the state-averaged complete active space self-consistent field (CASSCF) method [253, 254] and these calculations were followed by multi-reference configuration interaction (MRCI) calculations [254]. These electronic structure calculations were identical to those performed by Alexander, Lester and co-workers in determining an alternative PES [105].

The PES's of the ground OH(X)+H_2 $1^2A'$ surface, and the excited state OH(A)+H_2 $2^2A'$ surface are fit to these data points by a standard linear least-squares fitting method to find the appropriate coefficients for each function. The functional form of the PESs are polynomial expansions in Morse-like variables of the internuclear distances, r_{ij}, between any pair of atoms i and j so that

$$y_{ij} = \exp(-r_{ij}/a), \tag{3.1}$$

where $a = 2.0$ bohr. The compact polynomial basis set is invariant upon permutation of like atoms [126, 255, 256]. A total of 235 free coefficients emerge for each PES [126].

The two PESs are adiabatic in nature, whilst the MRCI energies calculated are diabatic calculations. In presenting the surfaces Bowman *et al.* compared the energies from MRCI calculations with those in the PES for a number of geometries. Understandably for an adiabatic potential, the PESs do not exhibit the correct cusp conditions at the conical intersection, instead showing rounded minima in the case of the excited state OH(A)+H_2 surface or rounded maxima in the case of the ground state surface. However only slightly displaced from the conical intersection (of the order of 0.1-0.2 bohr) the PES and MRCI energy are in excellent agreement. Figures 2, 3, and 4 of reference [126] make clear the quality of the agreement between the MRCI calculations and generated PES. However, although not mentioned in the text, there does appear to be some possible small disagreement at larger separation distances in some of the geometries (particularly the C_{2v} O-end approach geometry).

The ground state surface, calculated alongside the excited state surface utilised in the QCT studies of this thesis, was compared firstly with results from experimental measurements, and secondly with a high level (UCCSD(T)/aVQZ) full dimensional ground state PES generated by Yang *et al.* [257]. The experimental measurements: bond angles, bond lengths and bond harmonic frequencies from Herzberg and Huber

[238, 258] agreed well with those generated from the PES. Likewise, there was good agreement with the PES of Yang *et al.* [257]. Finally, Bowman *et al.* ran quasi-classical trajectories on the ground state potential $1^2A'$, initiated at the site of the 13 identified conical intersections of Hoffman and Yarkony [178] (it should be stated these are a demonstrative set of conical intersection configurations, not a comprehensive list). From these QCT calculations [126, 191, 259], quenching product branching ratios and rovibrational distributions of the OH(X) products were determined and agreed well with the values determined from experiment [101, 108]. There was also good qualitative agreement with the translational energy distributions of the H atom products from the reactive quenching pathway [103, 260]. The only notable disagreement with the experiment is that the QCT calculations overestimate the ratio of abstraction to insertion reactions responsible for reactive quenching. It has been postulated that this disagreement arises because the initial conical intersection configurations are sampled equally and this is unlikely to be realistic [102].

The excited state surface used in the QCT studies of this thesis has not been the subject of dynamic studies before. To some extent it can be seen as a by-product of the ground state PES, which was more heavily scrutinised and utilised by Bowman and co-workers [126, 191, 259]. However, the generally good agreement with the MRCI energies does give some confidence in using this surface in the QCT calculations here.

Diagrams have been produced in figures 3.1 and 3.2 to demonstrate portions of the PES and the sensitivity to the orientation of the OH(A) and H_2 diatoms. Both 3D projections and contour plots have been produced. In the calculations of this thesis, the bond lengths of the two diatoms are fixed at their equilibrium values: $r_{\mathrm{OH}} = 1.012\,\text{Å}$ and $r_{\mathrm{H_2}} = 0.741\,\text{Å}$, and so the bond lengths in these projections are restricted to these values also. With the bond lengths fixed the potential, V, is dependent upon the distance between the centre of mass of the two diatoms, R_{CM}, and three angles: θ, γ and ϕ. In this way the 6-dimensional PES has been reduced to a 4-dimensional PES. In

this section θ is the angle between the OH(A) diatom bond r_{OH} and R_{CM}, such that $\theta = 0°$ when the H atom end is directed along R_{CM} towards the hydrogen molecule, and $\theta = 180°$ with the O atom end directed along R_{CM}. γ is the angle between the H_2 diatom and R_{CM} and is equal to 0° or 180° with the H_2 diatom directed along R_{CM} or 90° when orthogonal to it. The dihedral angle, ϕ, is the relevant angle between the two bond vectors $\boldsymbol{r}_{\mathrm{OH}}$ and $\boldsymbol{r}_{\mathrm{H_2}}$ and is 0° or 180° when the molecules are co-planar.

Figure 3.1 shows cuts of the OH(A)+H_2 PES, where θ and R_{CM} are varied for different fixed $\gamma = 0°$ and 90°. This effectively illustrates the dependence of the potential on the OH(A) diatom orientation. In both cases the potential is highly anisotropic with respect to OH orientation.

The global minimum of the surface is at $R_{\mathrm{CM}} = 3.14\,\mathrm{bohr}$, $V = -10158\,\mathrm{cm}^{-1}$ for a C_{2v} geometry with the oxygen atom pointed towards a side-on H_2 molecule. This is extremely attractive and comparable in size to a covalent bond; for example, the I_2 bond is $\approx 12500\,\mathrm{cm}^{-1}$ [46]. This H_2 side-on slice of the PES has a second minimum at 0° at $R_{\mathrm{CM}} = 3.0\,\mathrm{bohr}$, $V = -3882\,\mathrm{cm}^{-1}$. Whilst considerably less attractive than the oxygen end approach, this is still a very attractive region. Indeed this is more attractive than global well depths associated with OH(A)+Rg systems that have been the subject of similar previous studies: Kr ($V \sim -6100\,\mathrm{cm}^{-1}$) [110], Ar ($V \sim -1700\,\mathrm{cm}^{-1}$) [113] and He ($V \sim -120\,\mathrm{cm}^{-1}$) [261] and the former system is considered highly attractive. The two wells in the OH(A)+H_2 PES are separated by a heavily repulsive wall and it would not be possible to pass from one to another with rotation alone at 300 K thermal energies. A third attractive well is seen in the surface with a minimum of $V = -2656\,\mathrm{cm}^{-1}$ at $R_{\mathrm{CM}} = 5.45\,\mathrm{bohr}$ and an angle, $\theta = 53°$. Despite these very attractive regions the surface still has considerable regions which are repulsive including at larger separation distances, $R_{\mathrm{CM}} > 8\,\mathrm{bohr}$, and this variation indicates a very anisotropic surface and sensitivity to the orientation of the OH(A) diatom in a collision.

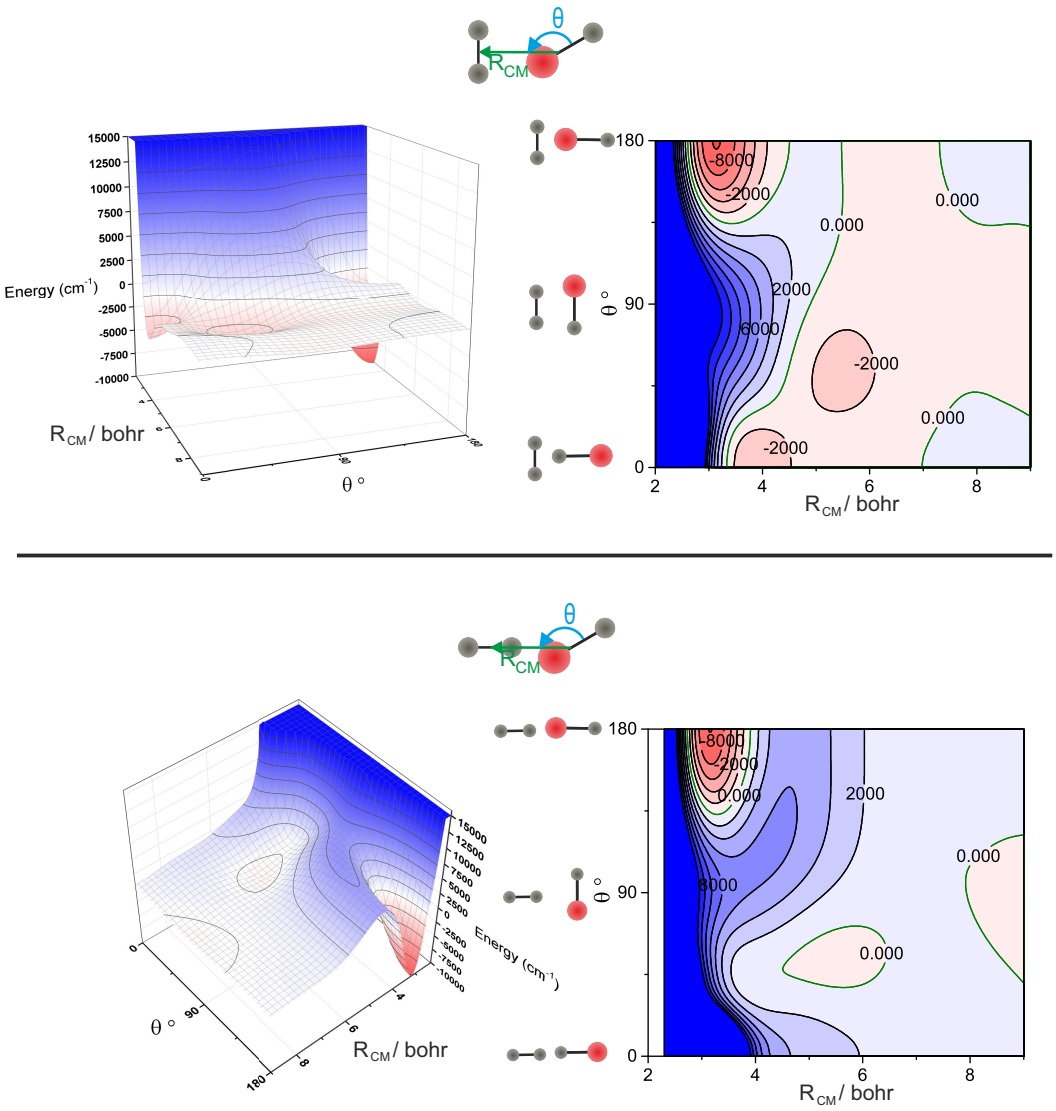

Figure 3.1: 3D projections of the OH(A)+H_2 PES and corresponding 2D contour plots. These sections of the PES vary the angle θ as shown in the accompanying drawings. For the top panel the angle $\gamma = 0°$ and the bottom panel $\gamma = 90°$. The dihedral angle, ϕ, is set to zero in all cases. Energies are given relative to the infinite separation of OH(A) and H_2 in cm^{-1}. Succesive contours are separated by $2000\,cm^{-1}$. Red/redish regions of the potential signify areas which are attractive relative to the infinitely separated diatoms and blue/bluish regions are repulsive; the strength of this colouring indicates the size of the attractive or repulsive potential involved.

The second slice of the surface displayed, with the H_2 molecule approached head-on, has a very similar minimum of $V = -10046\,\mathrm{cm}^{-1}$ at $R_{\mathrm{CM}} = 3.16\,\mathrm{bohr}$. The hydrogen approach in this case is repulsive but there is a second minimum of depth $V = -605\,\mathrm{cm}^{-1}$ at $R_{\mathrm{CM}} = 5.49\,\mathrm{bohr}$ at an angle, $\theta = 53°$. This slice of the surface is even more anisotropic with more marked repulsive regions than the slice for approaching a side-on H_2 molecule.

Figure 3.2 shows cuts of the OH(A)+H_2 PES where γ and R_{CM} are varied for different fixed θ. This effectively indicates the dependence of the potential on the H_2 diatom orientation. Note that there are a number of geometries in these slices of the PES that are equivalent to those in the previous pair of slices (varying the angle θ). Additionally the surfaces are symmetric about $\gamma = 90°$.

The first slice in this figure demonstrates that the deeply attractive regions of the PES are associated with approaching the oxygen end of the diatom. At around $R_{\mathrm{CM}} = 3.00$-$3.50\,\mathrm{bohr}$ there is an attractive valley, so at low separation distances the potential is isotropic. At larger separation distances there is a repulsive wall which is anisotropic varying from $5606\,\mathrm{cm}^{-1}$ at head-on geometries to $432\,\mathrm{cm}^{-1}$ for a side-on hydrogen molecule approach at $R_{\mathrm{CM}} = 4.73\,\mathrm{bohr}$. The potential is sensitive to the H_2 approach orientation and is highly anisotropic, just as with respect to the OH(A) approach orientation.

The second slice in the figure portrays the potential variation with the H_2 approaching a side-on OH(A) radical. This potential has a well depth of $V = -1297\,\mathrm{cm}^{-1}$ when the H_2 molecule is also approaching side-on at a separation of $R_{\mathrm{CM}} = 5.74\,\mathrm{bohr}$. Note this well is at a larger separation distance than others for this system, and generally this approach geometry is more repulsive than others. Once again the potential is anisotropic with respect to the H_2 approach orientation, but not as strongly as with the previous slice, or the slices in figure 3.1 varying OH(A) orientation.

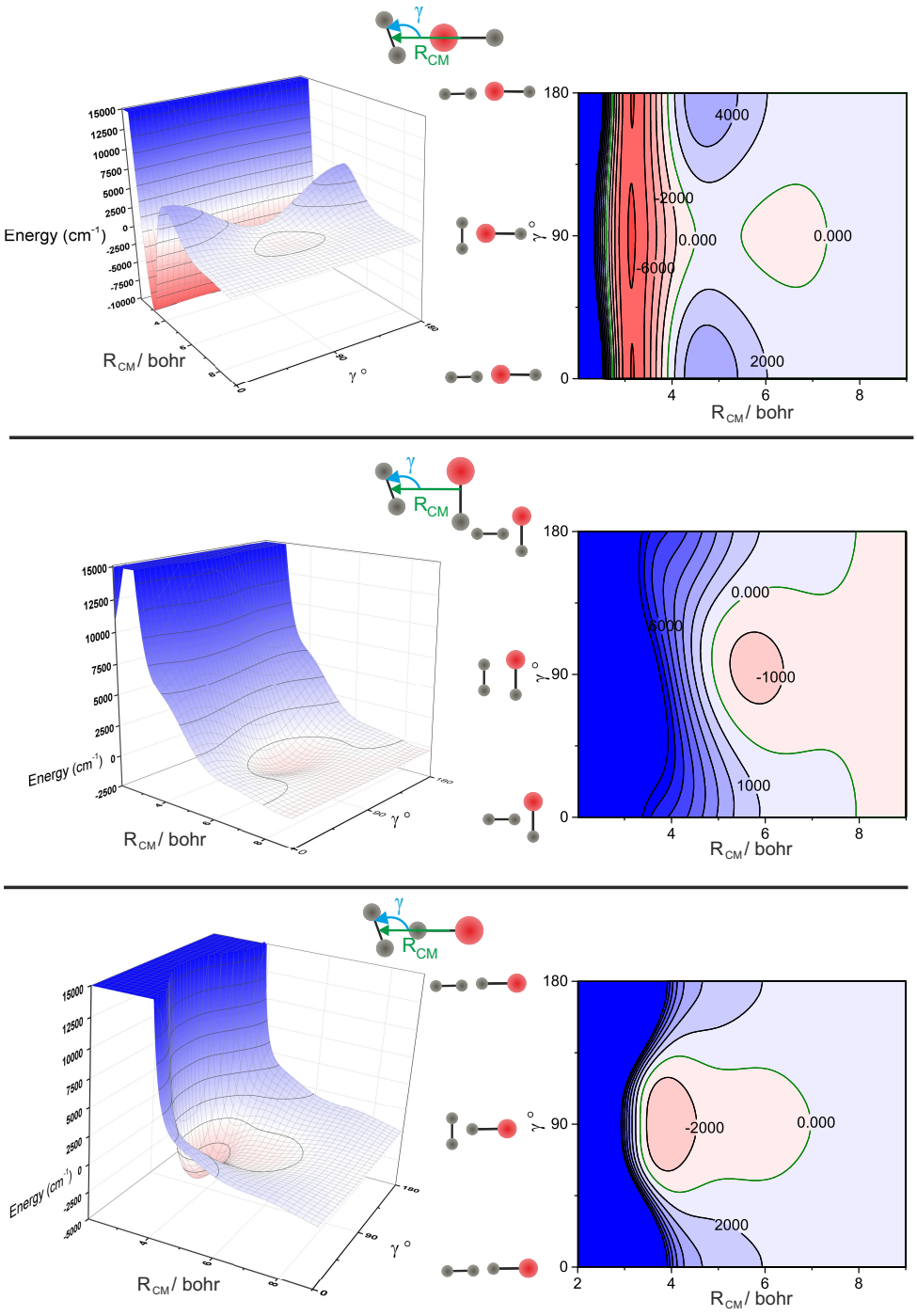

Figure 3.2: 3D projections of the OH(A)+H_2 PES and corresponding 2D contour plots. These sections of the PES vary the angle γ as shown in the accompanying drawings. For the top panel the angle $\theta = 180°$, the middle panel $\theta = 90°$, and the bottom panel $\theta = 0°$. The dihedral angle, ϕ, is set to zero in all cases. Energies are given relative to the infinite separation of OH(A) and H_2 in cm^{-1}. Successive contours in the top and bottom panels are $2000\,cm^{-1}$ apart, and $1000\,cm^{-1}$ apart in the middle panel. Red/redish regions of the potential signify areas which are attractive relative to the infinitely separated diatoms and blue/bluish regions are repulsive; the strength of this colouring indicates the size of the attractive or repulsive potential involved.

The final slice in the figure looks at the variation of the PES with γ, for an approach head-on with the hydrogen end of the OH radical. The potential well is as seen in the top slice of the PES in figure 3.1. The surface again shows anisotropy with respect to H_2 bond rotation.

The slices displayed in figures 3.1 and 3.2 are all planar with the dihedral angle, $\phi = 0°$. However, unlike studies by Zhang and co-workers [187, 188], the dynamic studies presented here allow ϕ to vary over the course of the trajectory also. So, whilst slices with varying ϕ have not been included here in the interests of brevity, they are no less significant in the dynamics. Changes in ϕ of 10° or 20° away from planar geometries tend to produce surfaces that resemble of those for the starting planar geometries though with shallower wells. Barriers to these regions also tend to be averaged out. For example, on increasing ϕ from 0° the barrier at around R_{CM} = 3.00-3.50 bohr in the top slice of figure 3.2 tends to become higher at $\gamma = 90°$ but lower at $\gamma = 0°$ and 180°. The overall outcome is that the surface tends to become less anisotropic with respect to θ and γ as ϕ increases away from 0°. Near $\phi = 45°$ the surface can appear considerably more isotropic with respect to θ or γ, whilst attractive regions still exist in the surface they tend to be shallower and entry into them is prevented by repulsive barriers. At $\phi = 90°$ the surface regardless of θ or γ tends to be highly repulsive. Taking these trends together, it is clear that the PES is highly anisotropic with respect to ϕ, as with θ and γ. The fact that the anisotropy with respect to θ and γ is lost on changing ϕ, should not detract from the conclusion that the potential is highly sensitive to all three angles, and consequently the orientation of both diatoms.

3.2 Quasi-Classical Trajectory Method

Having introduced the PES, the QCT method for propagating trajectories is now described. The QCT method used here is a new 4-atom adaptation of a 3-atom QCT code

originally formulated by Aoiz and co-workers [262, 263]. The 3-atom QCT code has been used by Aoiz, Brouard and co-workers in the consideration of NO(A) or OH(A) radical collisions with rare gas atoms, Rg [37, 110, 111, 113–116, 261, 264]. These earlier studies focused on inelastic cross sections and collisional depolarisation, mirroring the main interests of this OH(A)+H_2 study.

The initial conditions of the classical trajectory are either randomly selected or fixed on the basis of the values allowed by energy quantisation. The trajectory is propagated classically over the course of the PES until the trajectory is complete. Once the trajectory is complete the final rotational angular momentum is binned to a quantum-mechanically allowed energy level. This is the basis of the quasi-classical method used - initial and final quantisation of the energy level with classical evolution during the course of the trajectory.

QCT techniques take no account of quantum mechanical effects such as resonances or tunnelling. The exclusion of these effects has not proven important when comparing QCT and quantum mechanical (QM) calculations in a number of atom-diatom collision systems explored by Brouard and co-workers including NO(A)+Ar [115, 116, 264], OH(A)+Ar [37, 113, 116], OH(A)+He [34, 114] and OH(A)+Kr [111, 117]. RET and depolarisation cross sections from QCT and QM calculations in these cases agree within errors. However, OH(A)+H_2 could be more problematic, for reasons that will become apparent.

3.2.1 Co-ordinate System

In earlier diatom-atom studies, the calculated PES is a function of the distance between the diatom centre-of-mass and that of the atom, $\boldsymbol{R}_{\mathrm{CM}}$, and the angle, θ, between this vector and that of the diatom bond, $\boldsymbol{r}$ [110, 113]. In the OH(A)+H_2 case, the potential is defined in terms of the Cartesian co-ordinates of the four atoms. However, the bond

lengths of each diatom are constrained in the classical trajectories.

The Cartesian position co-ordinates of the atoms in a diatom-diatom collision AD+BC are given by $x_i, i = 1...12$, whilst their conjugate momenta are labelled $\wp_i, i = 1...12$. Atom B is described by coordinates $i = 1, 2, 3$, C by $i = 4, 5, 6$, A by $i = 7, 8, 9$ and D by $i = 10, 11, 12$.

The internal Jacobi co-ordinates analogous to those used in previous diatom-atom studies [117, 265] are thus, for $i = 1$ to 3,

$$q_i = x_{i+3} - x_i, \tag{3.2}$$

$$q_{i+6} = x_{i+6} - x_{i+9}, \tag{3.3}$$

$$q_{i+3} = \frac{m_{\rm A}x_{i+6} + m_{\rm D}x_{i+9}}{m_{\rm A} + m_{\rm D}} - \frac{m_{\rm B}x_i + m_{\rm C}x_{i+3}}{m_{\rm B} + m_{\rm C}}, \tag{3.4}$$

$$q_{i+9} = \frac{1}{M_{\rm tot}}(m_{\rm B}x_i + m_{\rm C}x_{i+3} + m_{\rm A}x_{i+6} + m_{\rm D}x_{i+9}), \tag{3.5}$$

where $m_{\rm A}$, $m_{\rm B}$, $m_{\rm C}$ and $m_{\rm D}$ are the masses of the four atoms, and $M_{\rm tot}$ is the total mass of the system. (q_1, q_2, q_3) describes the position of C with respect to B (here the hydrogen atom with respect to the oxygen atom in the OH radical); (q_4, q_5, q_6) the centre of mass of AD with respect to the centre of mass of BC; (q_7, q_8, q_9) describes the position of D with respect to A; (q_{10}, q_{11}, q_{12}) describes the position of the centre of mass of the system. The momenta, $p_i, i = 1, ...12$, are the corresponding momentum components, and are once again given for $i = 1$ to 3 as

$$p_i = \mu_{\rm BC}\dot{q}_i = \frac{m_{\rm B}\wp_{i+3} - m_{\rm C}\wp_i}{m_{\rm B} + m_{\rm C}}, \tag{3.6}$$

$$p_{i+6} = \mu_{\rm AD}\dot{q}_{i+6} = \frac{m_{\rm A}\wp_{i+9} - m_{\rm D}\wp_{i+6}}{m_{\rm A} + m_{\rm D}}, \tag{3.7}$$

$$p_{i+3} = \mu_{\rm BC,AD}\dot{q}_{i+3} = \frac{\wp_{i+6} + \wp_{i+9}}{m_{\rm A} + m_{\rm D}} - \frac{\wp_i + \wp_{i+3}}{m_{\rm B} + m_{\rm C}}, \tag{3.8}$$

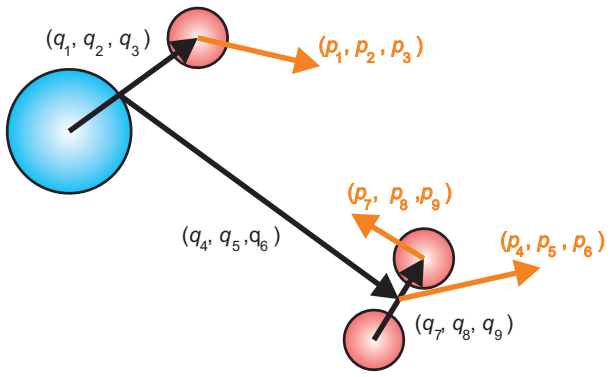

Figure 3.3: The Jacobi co-ordinate system as applied to OH+H_2 system and used to solve Hamilton's equations of motion.

where μ_{BC} and μ_{AD} are the reduced masses of the BC and AD diatoms respectively, whilst $\mu_{\mathrm{BC,AD}} = \frac{(m_{\mathrm{B}}+m_{\mathrm{C}})(m_{\mathrm{A}}+m_{\mathrm{D}})}{M_{\mathrm{tot}}}$. These position and momenta co-ordinates are shown in figure 3.3.

3.2.2 Initial Conditions

Figure 3.4 shows the space-fixed frame used in defining initial conditions and in propagating the trajectories, the origin of this system is the centre-of-mass of the OH(A) diatom. The trajectory is propagated in the space-fixed frame, Hamilton's equations of motion are solved in terms of Jacobi co-ordinates (see subsection 3.2.3) and the PES is described in terms of the Cartesian co-ordinates of the 4 atoms. The trajectory propagation program written in Fortran77 converts between these co-ordinate systems as necessary.

The centre-of-mass of the H_2 collider lies in the yz-plane and the initial relative velocity, v_{rel}, is parallel to the z-axis. Consequently, the orbital angular momentum of the system, ℓ, is initially directed along the x-axis. θ and ϕ describe the orientation of the OH(A) diatom bond in space whilst η defines the rotational phase of the radical. Likewise γ and δ define the orientation of the H_2 bond and α its rotational phase.

Initial position and momenta are assigned at the start of each trajectory by randomly sampling the angles θ, ϕ, η, γ, δ and α. These angles are constrained by the

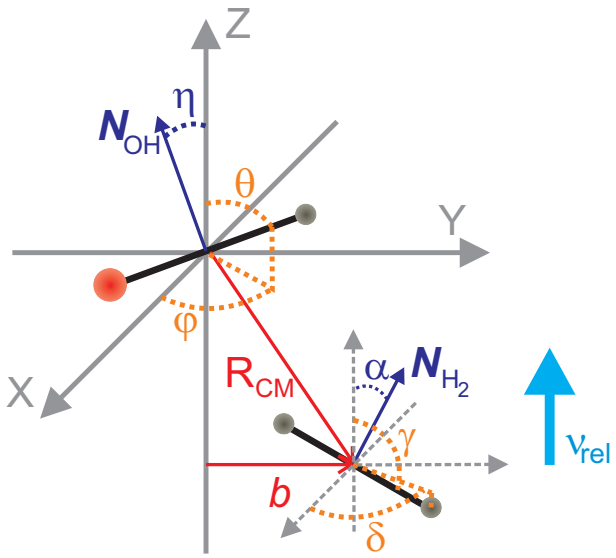

Figure 3.4: Space-fixed frame used in running QCT calculations and randomising initial conditions.

fixing of bond lengths to their equilibrium values, and the requirement that the rotational angular momentum of each diatom is of a fixed initial value. The orientation of the two diatoms with respect to one another, and to the direction of their angular momenta are randomised within these constraints.

The initial impact parameter, b, is randomly selected, and dartboard averaged such that $b = \xi^{1/2} b_{\max}$ where ξ is a random number between 0 and 1 [37, 266]. $b_{\max}$ is found such that in a sizeable sample any value of b larger than $b_{\max}$ leads to no RET or depolarisation.

Since the collision dynamics are propagated classically, intrinsic spins of nuclei and electrons are not accounted for in the trajectory. The Hund's case (b) rotational angular momentum $\boldsymbol{N}$, as defined in section 1.5, does however vary classically over the course of the trajectory. This initial rotational angular momentum is quantised and set at the start of each trajectory for each diatom. In the case of the OH(A) radical, batches of trajectories are run with the same starting rotational quantum number, $N_{\mathrm{OH}} = 0...14$. The OH(A) radical has the corresponding rotational energy $E_{\mathrm{rot,OH}}(N_{\mathrm{OH}}) = B_{\mathrm{OH}} N_{\mathrm{OH}}(N_{\mathrm{OH}} + 1)$. The outcome of the classical trajectory is highly

dependent on the initial conditions, and in determining properties associated with a particular initial N_{OH} it is necessary to average over other properties - the angles θ, ϕ, η, γ, δ and α. A large number of trajectories are run to achieve this, typically 1×10^5. Larger numbers of trajectories were run in some cases, and their calculated properties agreed with those following 1×10^5 trajectories, consequently the results were deemed to have converged after 1×10^5 trajectories.

The distribution of the rotational angular momentum quantum number for the H_2 diatom, $N_{\mathrm{H_2}}$, is determined from a thermal statistical distribution - a product of the nuclear spin statistics for a pair of fermions with nuclear spin $I = 1/2$, and the Boltzmann distribution [47]. So the probability of the initial H_2 angular momentum quantum number being $N_{\mathrm{H_2}}$ is given by

$$P(N_{\mathrm{H_2}}) = W_{\mathrm{ns}}(N_{\mathrm{H_2}}) \frac{(2N_{\mathrm{H_2}} + 1)\exp\left(-E_{\mathrm{rot,H_2}}(N_{\mathrm{H_2}})/k_{\mathrm{B}}T\right)}{\sum\limits_{N_{\mathrm{H_2}}} \exp\left(-E_{\mathrm{rot,H_2}}(N_{\mathrm{H_2}})/k_{\mathrm{B}}T\right)}, \tag{3.9}$$

where W_{ns} is the weighting due to nuclear spin statistics, and
$E_{\mathrm{rot,H_2}}(N_{\mathrm{H_2}}) = B_{\mathrm{H_2}} N_{\mathrm{H_2}}(N_{\mathrm{H_2}} + 1)$.

Nuclear spin statistics arise from the application of the Pauli exclusion principle to the H_2 diatom. Within the Pauli exclusion principle, the total wavefunction ψ must be antisymmetric with respect to the exchange of an identical pair of fermions - as here with H [49] in H_2. The total H_2 wavefunction can be broken down into components with electronic, vibrational, rotational and nuclear spin degrees of freedom, such that

$$\psi = \psi^{\mathrm{E}} \psi^{\mathrm{V}} \psi^{\mathrm{R}} \psi^{\mathrm{N}}. \tag{3.10}$$

ψ^{E} for H_2 is the ground state, ${}^1\Sigma_g^+$, which is symmetric with respect to exchange of nuclei. For a harmonic oscillator the exchange $x \to -x$ accompanies nuclear exchange and the wavefunction ψ^V changes by a factor of $(-1)^\nu$, where ν is the vibrational

quantum number. In these studies the H_2 diatom is vibrationally cold and $\nu = 0$ so ψ^V is symmetric with respect to interchange. On rotation through 180° the nuclei are exchanged and the rotational wavefunction, ψ^{R}, is multiplied by $(-1)^{N_{\mathrm{H_2}}}$. The nuclear spin wavefunction, ψ^{N}, is multiplied by +1 for exchange with parallel (↑↑) spin states or by -1 for exchange with antiparallel spin (↑↓) spin states.

If $N_{\mathrm{H_2}}$ is odd, the spins must be parallel for the total wavefunction to be anti-symmetric with respect to exchange. There are 3 possible parallel spin states and so $W_{\mathrm{ns}} = 3$ for odd $N_{\mathrm{H_2}}$. If $N_{\mathrm{H_2}}$ is even, the spins must be antiparallel for the total wavefunction to conform with the Pauli principle, and since there is only 1 such possible antiparallel spin state $W_{\mathrm{ns}} = 1$.

The initial $N_{\mathrm{H_2}}$ angular momentum for each trajectory is sampled randomly with the weighted distribution shown in equation (3.9). This thermal distribution of $N_{\mathrm{H_2}}$ allows for direct comparison with the experimental results, where the rotation of the H_2 diatom is thermalised. However, in much of the theoretical analysis the initial rotational angular momenta of both diatoms are specified. The output file of the trajectory calculations allows for the separation of trajectories into different initial H_2 rotational angular momenta and analysis of each subset. Much of the analysis focused on collisions with $N_{\mathrm{H_2}} = 1$, the most populated state at 300 K, making up approximately 66% of the total trajectories.

The experimental studies were performed under thermal conditions at 300 K, where the initial relative velocity is distributed by the Maxwell-Boltzmann distribution,

$$P(v_{\mathrm{rel}})\mathrm{d}v = 4\pi \left(\frac{\mu}{2\pi k_{\mathrm{B}} T}\right)^{3/2} v_{\mathrm{rel}}^2 \exp\left(-\frac{\mu v_{\mathrm{rel}}^2}{2k_{\mathrm{B}} T}\right) \mathrm{d}v. \tag{3.11}$$

The mean relative velocity at $T = 300\,\mathrm{K}$ is given by

$$\langle v_{\mathrm{rel}} \rangle = \left(\frac{8k_{\mathrm{B}} T}{\pi \mu}\right)^{1/2} \approx 1876\,\mathrm{ms}^{-1}, \tag{3.12}$$

this corresponds to a collision energy of $E_{\text{col}} = \frac{3}{2}k_{\text{B}}T \approx 39\,\text{meV}$. In previous QCT studies, including for OH(A)+Ar and NO(A)+Ar collision systems, there is little difference between RET and depolarisation cross sections determined using a fixed collision energy of 39 meV and those calculated with varying collision energy sampled by the Maxwell-Boltzmann distribution for 300 K [37, 57, 114, 264]. Given these previous results, the studies here were carried out at a fixed collision energy of 39 meV, so the trajectories all start with the same mean relative velocity. In QCT studies of OH(A)+Kr collisions where surface hopping is included to account for electronic quenching to the ground states OH(X)+Kr [93], there is some evidence that this fixed energy approximation is less appropriate. This arises because passage through the conical intersection, and thus quenching, are significantly more probable at lower collision energies [93]. The study of OH(A)+H_2 carried out here is restricted to a single surface so it seems likely that fixing collision energy will once again be adequate for the present purposes.

3.2.3 Trajectory Propagation

After the initial conditions are set, the course of the trajectory over the PES is determined by solving Hamilton's equations of motion. In terms of the Jacobi co-ordinates in figure 3.3, the Hamitonian for relative motion of the OH(A)+H_2 system is given by [265]

$$H = \sum_{i=1}^{3}\left(\frac{p_i^2}{2\mu_{\text{H}_2}} + \frac{p_{i+6}^2}{2\mu_{\text{OH}}} + \frac{p_{i+3}^2}{2\mu_{\text{OH,H}_2}}\right) + V. \tag{3.13}$$

The terms p_{10}, p_{11} and p_{12}, relate to the centre of mass of the whole system and are constants that do not appear in the Hamiltonian for relative motion [265]. V is the potential energy of the system and is determined from the PES where it is defined in terms of the cartesian co-ordinates, $x_i, i = 1...12$.

In these trajectory calculations the bond lengths are fixed at their equilibrium values, this reduces the computational requirements of the calculation but also eliminates

the need to account for, and quantise, vibrational motion throughout the trajectory. Particular problems can arise with regards to the zero point energy of each bond, since if the bonds are allowed to vary in length this can leak into other degrees of freedom. Such leakage is ultimately non-physical and through bond length fixing can be avoided. The disadvantage to fixing the bond is that the trajectory is no longer probing the entire 6-dimensional PES, reducing it instead to 4-dimensions. This may mean that regions and behaviour important to the collision dynamics is not explored.

In order to fix the bond lengths of the two diatoms over the course of a trajectory Lagrangian multiplier terms are incorporated into the equations of motion [266–268]. These multipliers are used to maximise or minimise a function, $f(x, y)$, subject to a constraint, $g(x, y) = c$, solving

$$\frac{\mathrm{d}f}{\mathrm{d}x} - \lambda\frac{\mathrm{d}g}{\mathrm{d}x} = 0 \tag{3.14}$$

$$\frac{\mathrm{d}f}{\mathrm{d}y} - \lambda\frac{\mathrm{d}g}{\mathrm{d}y} = 0, \tag{3.15}$$

where λ is the Lagrangian multiplier. The constraint can be thought of as a restoring force applied to each bond, l, to stop its length changing such that [266–268]

$$\begin{aligned} F_i^l &= \lambda_l \frac{\partial g_l}{\partial q_i} && i = 1, 2, 3, 7, 8, 9 \\ &= 0 && i = 4, 5, 6, 10, 11, 12. \end{aligned} \tag{3.16}$$

In this case the constraining functions applied to each bond are

$$g_{\mathrm{OH}} = \sum_{i=1}^{3} q_i^2 - |\boldsymbol{r}_{\mathrm{OH}}|^2 = 0, \tag{3.17}$$

$$g_{\mathrm{H_2}} = \sum_{i=1}^{3} q_{i+6}^2 - |\boldsymbol{r}_{\mathrm{H_2}}|^2 = 0, \tag{3.18}$$

where it is clear these constraints hold the bond length constant. It follows that

$$\frac{\mathrm{d}g_{\mathrm{OH}}}{\mathrm{d}q_i} = q_i \tag{3.19}$$

$$\frac{\mathrm{d}g_{\mathrm{H_2}}}{\mathrm{d}q_{i+6}} = q_{i+6}, \tag{3.20}$$

and

$$\frac{\mathrm{d}g_{\mathrm{OH}}}{\mathrm{d}t} = 2\sum_{i=1}^{3} q_i\dot{q}_i = 0 \implies \sum_{i=1}^{3} q_i\dot{q}_i = 0, \tag{3.21}$$

$$\frac{\mathrm{d}g_{\mathrm{H_2}}}{\mathrm{d}t} = 2\sum_{i=1}^{3} q_{i+6}\dot{q}_{i+6} = 0 \implies \sum_{i=1}^{3} q_{i+6}\dot{q}_{i+6} = 0. \tag{3.22}$$

Focusing just on the OH diatom it follows that

$$\begin{aligned} \frac{\mathrm{d}}{\mathrm{d}t}\sum_{i=1}^{3} q_i\dot{q}_i = \sum_{i=1}^{3}\dot{q}_i^2 + \sum_{i=1}^{3} q_i\ddot{q}_i &= 0 \\ \sum_{i=1}^{3}\frac{p_i^2}{\mu_{\mathrm{OH}}^2} + \sum_{i=1}^{3} q_i\frac{\dot{p}_i}{\mu_{\mathrm{OH}}} &= 0 \end{aligned} \tag{3.23}$$

Therefore

$$\sum_{i=1}^{3} q_i\dot{p}_i = -\sum_{i=1}^{3}\frac{p_i^2}{\mu_{\mathrm{OH}}}, \tag{3.24}$$

and similarly for the H_2 diatom

$$\sum_{i=1}^{3} q_{i+6}\dot{p}_{i+6} = -\sum_{i=1}^{3}\frac{p_{i+6}^2}{\mu_{\mathrm{H_2}}}. \tag{3.25}$$

In Lagrangian mechanics the equations of motion can be written as

$$\frac{\mathrm{d}}{\mathrm{d}t}\frac{\partial L}{\partial q_i} - \frac{\partial L}{\partial q_i} - F_i^{\mathrm{OH}} = 0 \implies \dot{p}_i + \frac{\partial V}{\partial q_i} - \lambda_{\mathrm{OH}} q_i = 0 \tag{3.26}$$

$$\frac{\mathrm{d}}{\mathrm{d}t}\frac{\partial L}{\partial q_{i+6}} - \frac{\partial L}{\partial q_{i+6}} - F_{i+6}^{\mathrm{H_2}} = 0 \implies \dot{p_{i+6}} + \frac{\partial V}{\partial q_{i+6}} - \lambda_{\mathrm{H_2}} q_{i+6} = 0, \tag{3.27}$$

multiplying equation (3.26) by q_i and summing over $i = 1 \rightarrow 3$ gives

$$\sum_{i=1}^{3} q_i \dot{p}_i + \sum_{i=1}^{3} q_i \frac{\partial V}{\partial q_i} - \lambda_{\mathrm{OH}} \sum_{i=1}^{3} q_i^2 = 0, \tag{3.28}$$

using equation (3.24)

$$-\sum_{i=1}^{3} \frac{p_i^2}{\mu_{\mathrm{OH}}} + \sum_{i=1}^{3} q_i \frac{\partial V}{\partial q_i} - \lambda_{\mathrm{OH}} \sum_{i=1}^{3} q_i^2 = 0, \tag{3.29}$$

which rearranges to give

$$\lambda_{\mathrm{OH}} = \left(\sum_{i=1}^{3} q_i^2 \right)^{-1} \left(\sum_{i=1}^{3} q_i \frac{\partial V}{\partial q_i} - \sum_{i=1}^{3} \frac{p_i^2}{\mu_{\mathrm{OH}}} \right), \tag{3.30}$$

and for H_2

$$\lambda_{\mathrm{H_2}} = \left(\sum_{i=1}^{3} q_{i+6}^2 \right)^{-1} \left(\sum_{i=1}^{3} q_i \frac{\partial V}{\partial q_{i+6}} - \sum_{i=1}^{3} \frac{p_{i+6}^2}{\mu_{\mathrm{OH}}} \right), \tag{3.31}$$

Either Lagrangain multiplier has the form

$$\lambda_l = \frac{1}{|\boldsymbol{r}_l|^2} \left(\boldsymbol{r}_l \nabla_{r_l} V - \frac{\boldsymbol{p}_l \cdot \boldsymbol{p}_l}{\mu_l} \right) \tag{3.32}$$

Note that constraining the diatom bond lengths in this way means there is no vibrational energy associated with the bonds, and zero point energy cannot leak out to other degrees of freedom.

The alternative Hamilton's equations of motion in Jacobi co-ordinates are given by [265]

$$\frac{\mathrm{d}q_i}{\mathrm{d}t} = \frac{\partial H}{\partial p_i} = \frac{p_i}{\mu_{\mathrm{OH}}} \quad ; \quad \frac{\mathrm{d}p_i}{\mathrm{d}t} = -\frac{\partial V}{\partial q_i} + \lambda_{\mathrm{OH}} q_i, \tag{3.33}$$

$$\frac{\mathrm{d}q_{i+6}}{\mathrm{d}t} = \frac{\partial H}{\partial p_{i+6}} = \frac{p_{i+6}}{\mu_{\mathrm{H_2}}} \quad ; \quad \frac{\mathrm{d}p_{i+6}}{\mathrm{d}t} = -\frac{\partial V}{\partial q_{i+6}} + \lambda_{\mathrm{H_2}} q_{i+6}, \tag{3.34}$$

$$\frac{\mathrm{d}q_{i+3}}{\mathrm{d}t} = \frac{\partial H}{\partial p_{i+3}} = \frac{p_{i+3}}{\mu_{\mathrm{OH,H_2}}} \quad ; \quad \frac{\mathrm{d}p_{i+3}}{\mathrm{d}t} = -\frac{\partial V}{\partial q_{i+3}}. \tag{3.35}$$

The trajectory is propagated by solving these coupled equations of motion in order to determine the forces on each atom, and the velocity and acceleration in each dimension at regular time steps (of the order of 10-100 attoseconds chosen such that results converge) starting with the initial conditions [117, 265]. This is continued over the course of the trajectory until it is considered complete.

Given that the potential in this study is defined in terms of the cartesian coordinates introduced earlier the partial differentials of the potential in Hamilton's equations of motion can be written instead as

$$\frac{\partial V}{\partial q_i} = \frac{\partial V}{\partial x_{i+3}} - \frac{\partial V}{\partial x_i}, \tag{3.36}$$

$$\frac{\partial V}{\partial q_{i+6}} = \frac{\partial V}{\partial x_{i+9}} - \frac{\partial V}{\partial x_{i+6}}, \tag{3.37}$$

$$\frac{\partial V}{\partial q_{i+3}} = \frac{m_{\mathrm{H_2}}}{m_{\mathrm{H}}}\frac{\partial V}{\partial x_{i+9}} + \frac{m_{\mathrm{H_2}}}{m_{\mathrm{H}}}\frac{\partial V}{\partial x_{i+6}} - \frac{m_{\mathrm{OH}}}{m_{\mathrm{H}}}\frac{\partial V}{\partial x_{i+3}} - \frac{m_{\mathrm{OH}}}{m_{\mathrm{O}}}\frac{\partial V}{\partial x_i} \tag{3.38}$$

3.2.4 Final States

The trajectory is deemed complete when the separation of the two diatoms is greater than the initial separation, at large enough values that the remaining forces are negligible ($\approx 10\,\text{Å}$). The position and momenta of the diatoms is recorded at the end of each trajectory along with the initial positions and momenta. With these data, collision properties can be evaluated. Final rotational angular momentum quantum numbers for OH(A) are determined from

$$|\boldsymbol{N}'_{\mathrm{OH}}| = \hbar\sqrt{N'_{\mathrm{OH}}(N'_{\mathrm{OH}}+1)}, \tag{3.39}$$

and histogram binned to the nearest integer to obtain the quasi-classical final rotational angular momentum quantum number, N'_{OH}.

To maintain the antisymmetric nature of the total wavefunction for the H_2 diatom any odd change in the rotational angular momentum, ΔN_{H_2}, must be accompanied by a change in spin state [49, 269]. Typically this is forbidden as the magnetic moment of the diatom is weak, and the impact of external perturbations small and incapable of bringing about a spin flip. However, given that the OH(A) collider is paramagnetic, it is unclear if this restriction should be applied, since paramagnetic molecules are known to act as spin-flip catalysts [270, 271].

In the following section, some N'_{H_2} resolved cross sections account for this parity conservation restriction and others do not. Whether or not this restriction is applied is a matter of choice in the calculation. Where the restriction is not considered, the values from an equation analagous to equation (3.39), N'_{H_2}, are rounded to their nearest integer. If the restriction is applied, N'_{H_2} is rounded to the nearest odd integer when the initial angular momentum N_{H_2} was odd, or rounded to the nearest even integer when N_{H_2} was even.

3.3 Analysis

The final positions and momenta of the diatoms are recorded so that various properties of the collision system can be calculated. These include experimentally observable properties such as collision cross sections and depolarisation cross sections, but also non-observable properties such as opacity functions and the differential cross section (DCS).

3.3.1 State Resolved Cross Sections

The number of trajectories that begin in rotational levels N_{OH}, N_{H_2}, and are histogram binned to final rotational angular momentum quantum numbers N'_{OH}, N'_{H_2}, is given by $\mathcal{N}(N_{OH}N_{H_2}N'_{OH}N'_{H_2})$. $\mathcal{N}(N_{OH}N_{H_2})$ is the total number of trajectories with starting

rotational angular momentum, N_{OH} and $N_{\mathrm{H_2}}$. Together these form a fraction which replaces $P(b)$, equivalent to the opacity function, in the definition of the integral cross section in equation (1.1). Therefore, the state-resolved cross section for $N_{\mathrm{OH}}, N_{\mathrm{H_2}} \rightarrow N'_{\mathrm{OH}}, N'_{\mathrm{H_2}}$ is given by [37, 261]

$$\sigma_{N_{\mathrm{OH}}N'_{\mathrm{OH}}N_{\mathrm{H_2}}N'_{\mathrm{H_2}}} = \frac{\pi b^2_{\mathrm{max}} \mathcal{N}(N_{\mathrm{OH}}N'_{\mathrm{OH}}N_{\mathrm{H_2}}N'_{\mathrm{H_2}})}{\mathcal{N}(N_{\mathrm{OH}}N_{\mathrm{H_2}})}. \tag{3.40}$$

State-to-state integral elastic cross sections, where $N_{\mathrm{OH}} = N'_{\mathrm{OH}}$ and $N_{\mathrm{H_2}} = N'_{\mathrm{H_2}}$ cannot be calculated. This is because there is no classical limit on how small the deflection angle can be, and so the cross sections cannot be converged. However, cross sections which are elastic in one diatom but not the other can be converged. Additionally, through the use of a tensor opacity formalism (see section 3.4.1), elastic depolarisation cross sections can be converged.

If the final state resolution of only one diatom is of interest, typically OH(A), the final rotational angular momentum of the other diatom is summed over to give a number of trajectories, $\mathcal{N}(N_{\mathrm{OH}}N'_{\mathrm{OH}}N_{\mathrm{H_2}})$, and the cross section is given by

$$\sigma_{N_{\mathrm{OH}}N'_{\mathrm{OH}}}(N_{\mathrm{H_2}}) = \frac{\pi b^2_{\mathrm{max}} \mathcal{N}(N_{\mathrm{OH}}N'_{\mathrm{OH}}N_{\mathrm{H_2}})}{\mathcal{N}(N_{\mathrm{OH}}N_{\mathrm{H_2}})}. \tag{3.41}$$

In the experiment the initial angular momentum of only the OH is selected and the H_2 collider is present with a thermal population distribution. The experimentally-observed RET cross sections are averaged over the thermalised rotational population of H_2. Comparable cross sections from QCT calculations are calculated following averaging over the thermally weighted population of $N_{\mathrm{H_2}}$. Since the initial angular momentum of H_2 in each trajectory is determined via a statistical distribution, this can be achieved by averaging over the total number of trajectories, $\mathcal{N}_{\mathrm{tot}}$, which is equal to $\mathcal{N}(N_{\mathrm{OH}})$.

The resultant cross section is

$$\sigma_{N_{\mathrm{OH}}N'_{\mathrm{OH}}} = \frac{\pi b_{\mathrm{max}}^2 \mathcal{N}(N_{\mathrm{OH}}N'_{\mathrm{OH}})}{\mathcal{N}_{\mathrm{tot}}}. \tag{3.42}$$

Whilst experiments of this type are possible in principle, in the current experiments state resolved cross sections of this kind are not measured. Instead only total RET cross sections, σ_{RET}, where all inelastic $N'_{\mathrm{OH}} \neq N_{\mathrm{OH}}$ collisions are included are measured. These are calculated theoretically by summing over all $N'_{\mathrm{OH}} \neq N_{\mathrm{OH}}$, such that

$$\sigma_{\mathrm{RET}} = \sum_{N_{\mathrm{OH}}N'_{OH}} \sigma_{N_{\mathrm{OH}}N'_{\mathrm{OH}}} = \sum_{N_{\mathrm{OH}}N'_{OH}} \frac{\pi b_{\mathrm{max}}^2 \mathcal{N}(N_{\mathrm{OH}}N'_{\mathrm{OH}})}{\mathcal{N}_{\mathrm{tot}}}. \tag{3.43}$$

3.3.2 Differential Cross Section

The remaining properties in this section can be determined with respect to either the OH or H_2 diatom, and can also be resolved in both. Here formulations for calculating the properties shall use generic quantum numbers, e.g. N rather than N_{OH} or $N_{\mathrm{H_2}}$.

Differential cross sections (DCS) can typically be measured in molecular beam experiments, in which the initial velocity, $\boldsymbol{k}$, is well defined. However, here in a bulb experiment, this is not possible. However, this property is calculated theoretically using QCT methods.

The differential cross section measures the dependence of a collision cross section on the scattering angle $\omega_{kk'}$ and is a measure of the $\boldsymbol{k - k'}$ correlation. The differential cross section for the inelastic state resolved collision $N \rightarrow N'$ is defined as [272]

$$\frac{\mathrm{d}\sigma_{NN'}}{\mathrm{d}\omega_{kk'}}, \tag{3.44}$$

where $\sigma_{NN'}$ is a state resolved collision cross section, which could also be resolved with respect to both diatoms. $\mathrm{d}\omega$ is the solid scattering angle defined by $\theta_{kk'}$ to $\theta_{kk'} + \mathrm{d}\theta_{kk'}$,

$\phi_{kk'}$ to $\phi_{kk'} + \mathrm{d}\phi_{kk'}$. It follows that $\mathrm{d}\omega_{kk'} = \sin\theta \mathrm{d}\theta_{kk'}\mathrm{d}\phi_{kk'}$.

Since the scattering is cylindrically symmetric about $\boldsymbol{k}$, the DCS is independent of $\phi_{kk'}$. The DCS is calculated for a given $N \rightarrow N'$ transition from the QCT calculations by the histogram binning of trajectories into bins either of width $\Delta\theta_{kk'}$ or $\Delta\cos\theta_{kk'}$, with the number of trajectories in the bin equal to $\mathcal{N}_{NN'}(\theta_{kk'})$, such that [117]

$$\frac{\mathrm{d}\sigma_{NN'}}{\mathrm{d}\omega_{kk'}} = \frac{\pi b_{\mathrm{max}}^2}{2\pi\cos\Delta\theta_{kk'}} \frac{\mathcal{N}_{NN'}(\theta_{kk'})}{\mathcal{N}_{\mathrm{tot}}}. \tag{3.45}$$

3.3.3 Depolarisation Moments

The rotational tilt of the rotational angular momentum over the course of a collision for either diatom $\boldsymbol{N}$-$\boldsymbol{N'}$ is defined in equation (1.24) as an expansion in terms of Legendre polynomials of $\cos\theta_{NN'}$. The expansion coefficients are the depolarisation moments $a^{(k)}(N, N)$, defined in equation (1.25), which can be calculated in QCT calculations. The k-th order depolarisation moment associated with collisions $N \rightarrow N'$ is given by the average k-th order Legendre polynomial for such collisions from the QCT, such that [37, 261]

$$a^{(k)}(N, N') = \frac{1}{\mathcal{N}_{NN'}} \sum_{i=0}^{\mathcal{N}_{NN'}} P_k(\cos\theta_{NN'}^i), \tag{3.46}$$

where $\theta_{NN'}^i$ is the tilt angle for the i-th trajectory and is given by [37]

$$\cos\theta_{NN'}^i = \frac{\boldsymbol{N}^i.\boldsymbol{N'}^i}{|\boldsymbol{N}^i||\boldsymbol{N'}^i|}. \tag{3.47}$$

Equation (3.46) expresses the depolarisation moment for product state resolved collisions, $N \rightarrow N'$. The depolarisation moment associated with RET collisions, $N \rightarrow N'$, for all $N' \neq N$ is also of interest. This moment is found by averaging over the k-th order Legendre polynomials for all inelastic trajectories starting in N.

The dependence of a cross section on the rotational tilt $\boldsymbol{N}$-$\boldsymbol{N'}$ can be described with a property analagous to the DCS,

$$\left|\frac{\mathrm{d}\sigma_{NN'}}{\mathrm{d}\theta_{NN'}}\right| = \frac{\sin\theta_{NN'}\sigma_{NN'}P(\theta_{NN'})}{2\pi}\,. \tag{3.48}$$

Similar to the DCS, this can be calculated by binning trajectories in bins of width $\Delta\cos\theta_{NN'}$, so that

$$\frac{\mathrm{d}\sigma_{NN'}}{\mathrm{d}\theta_{NN'}} = \frac{\mathcal{N}_{NN'}(\theta_{NN'})}{\mathcal{N}_{\mathrm{tot}}}\frac{\pi b_{\mathrm{max}}^2}{2\pi\Delta\cos\theta_{NN'}}. \tag{3.49}$$

However, to obtain a smooth correlation with small bin widths, a large number of trajectories are required. Instead the distribution can be expressed in terms of a Legendre polynomial expansion using the depolarisation moments obtained as in equation 3.46 [115], such that

$$\frac{\mathrm{d}\sigma_{NN'}}{\mathrm{d}\theta_{NN'}} = \frac{\sin\theta_{NN'}\sigma_{NN'}}{4\pi}\sum_k [k]a^{(k)}(N,N')P_k(\cos\theta_{NN'}). \tag{3.50}$$

A similar expression summing over Legendre polynomials $P_k(\cos\theta_{kk'})$ can be obtained for the DCS.

3.3.4 Depolarisation Cross Sections

Depolarisation cross sections for particular collisions $N \rightarrow N'$ can be calculated from the collision cross section, $\sigma_{NN'}$, and depolarisation moment, $a^{(k)}(N,N')$, for that process using the following relation [37, 38, 169]:

$$\sigma^{(k)}(N,N') = \sigma_{NN'}(1 - a^{(k)}(N,N')). \tag{3.51}$$

This relation is arrived at classically through consideration of the depolarisation of an initially polarised distribution later in section 5.1. The closed shell total inelastic

depolarisation cross section can be elucidated from the equation above by summing over N'. The total depolarisation cross section requires the inclusion of contributions from elastic depolarising collisions where $N' = N$ and a method for doing this, in which spin is treated as a spectator, will be detailed in section 3.4.1.

3.3.5 Opacity Functions

The outcome of a collision is dependent upon the initial impact parameter, b, of the trajectory. The probability of a particular collision, $N \rightarrow N'$, at a given b is expressed in the opacity function, $P^{(0)}_{NN'}(b)$, defined in section 1.2 such that

$$\sigma_{NN'} = \int_0^{b_{\max}} P^{(0)}_{NN'}(b) 2\pi b \mathrm{d}b. \tag{3.52}$$

Opacity functions can be determined from QCT calculations by histogram binning trajectories into bins of width Δb, with the number of trajectories in the bin equal to $\mathcal{N}_{NN'}(b)$, such that

$$P^{(0)}_{NN'}(b) = \frac{\mathcal{N}_{NN'}(b)}{\Delta b \mathcal{N}_{\mathrm{tot}}}. \tag{3.53}$$

Opacity functions for collisional depolarisation, $P^{(k)}_{NN'}(b)$, can also be found through

$$P^{(k)}_{NN'}(b) = P^{(0)}_{NN'}(b) \left(1 - a^{(k)}(b; N, N')\right), \tag{3.54}$$

where $a^{(k)}(b; N, N')$ is calculated from the average of the Legendre polynomial moment for collisions starting with an impact parameter within the bin width of b, such that

$$a^{(k)}(b; N, N') = \frac{1}{\mathcal{N}_{NN'}(b)} \sum_{i=0}^{\mathcal{N}_{NN'}(b)} P_k(\cos\theta^i_{NN'}(b)). \tag{3.55}$$

Given $a^{(k)}$ values can be negative, $P^{(k)}_{NN'}(b)$ is not limited to 1. Since the sum of the elastic and inelastic depolarisation opacity functions do not sum to unity, these are

not true opacity functions as they are not probabilities for depolarising collisions. The consideration of these $P^{(k)}_{NN'}(b)$ functions is however useful in assessing the variation in the depolarisation accompanying a collision with the impact parameter.

With the method above a very large number of trajectories are required for each bin to have sufficient trajectories to produce a smooth opacity functions. Instead, the QCT calculated opacity functions presented in this thesis are formed from a Legendre polynomial expansion in terms of a variable β such that [24, 34, 263]

$$P^{(0)}_{NN'}(b) = \frac{2\sigma_{NN'}}{\pi b^2_{\max}} g(\beta) \tag{3.56}$$

where $g(\beta)$ is a truncated Legendre expansion defined as [24, 34, 263]

$$g(\beta) = \frac{1}{2} + \sum_{n=1}^{M} \alpha_n P_n(\beta), \tag{3.57}$$

$$\alpha_n = \frac{2n+1}{2} \frac{1}{\mathcal{N}_{NN'}} \sum_{i=1}^{\mathcal{N}_{NN'}} P_n(\beta^{(i)}, \tag{3.58}$$

$$\beta = \frac{2b^2}{b^2_{\max}} - 1, \tag{3.59}$$

where the number of Legendre polynomials summed over, M, is determined by a Kolmogorov-Smirnov statistical test but, quantum-mechanically, cannot exceed $2N$ [262, 263].

3.4 Consideration of Electron Spin

Since OH(A) is an open shell radical, rather than a closed shell diatom, a method for the inclusion of both electron and nuclear spin ($\boldsymbol{S}$ and $\boldsymbol{I}$ respectively) has been developed. An assumption is made in this treatment that the intermolecular interactions are entirely electrostatic in nature and independent of the intrinsic spin angular

momenta [43, 273]. As such, the spin is considered a spectator to the collision. This assumption corresponds with the energy sudden limit, where the spin-rotation constant does not change on complex formation. In this formalism, depolarisation and inelastic cross sections for $\boldsymbol{j}$ or $\boldsymbol{F}$, defined by the Hund's case (b) coupling scheme described in section 1.5, can be determined.

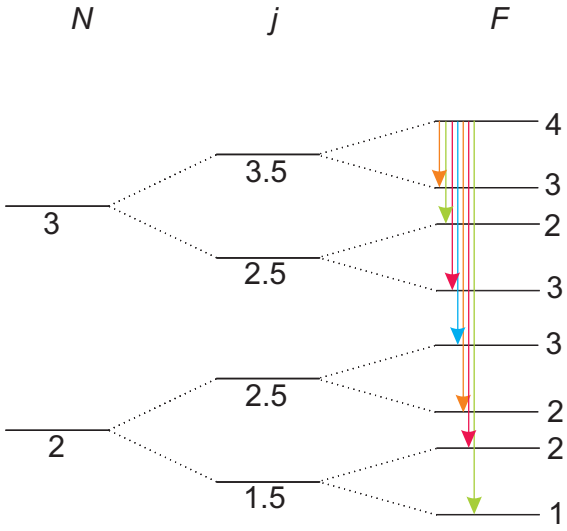

Figure 3.5: Energy level diagram for OH(A) radical with a variety of transitions from the $N = 3$, $j = 3.5$ and $F = 4$ level taken from sources [51, 57]. The colours of the arrows indicate the type of transition and are as described in table 3.1.

The inclusion of coupling of $\boldsymbol{N}$ to intrinsic spins, $\boldsymbol{S}$ and $\boldsymbol{I}$, leads to the possibility of several different types of inelastic collisions. The types of potential collision transitions are described in table 3.1 and examples of their meaning shown in figure 3.5.

3.4.1 Tensor Opacity Formalism

In the formalism, inelastic cross sections and depolarisation moments for $\boldsymbol{j}$ or $\boldsymbol{F}$ can be factorised into a geometrical contribution accounting for the angular momentum coupling and a tensor opacity term, $P^K_{NN'}$ [39, 45, 261, 274]. The tensor opacity defines the probability of having an angular momentum transfer vector, K, associated with the collision $N \rightarrow N'$. This tensor opacity formalism also allows for the elucidation of

Transition	...in quantum numbers	...in Figure 3.5
Spin-Rotation and Hyperfine level conserving	$\Delta N = \Delta j, \Delta j = \Delta F$	Blue
Spin-Rotation level conserving and Hyperfine level changing	$\Delta N = \Delta j, \Delta j \neq \Delta F$	Orange
Spin-Rotation level changing and Hyperfine level conserving	$\Delta N \neq \Delta j, \Delta j = \Delta F$	Red
Spin-Rotation and Hyperfine level changing	$\Delta N \neq \Delta j, \Delta j \neq \Delta F$	Green

Table 3.1: Table detailing various types of transitions between levels in the excited state these are shown pictorially for OH(A) in figure 3.5.

elastic depolarisation cross sections.

An angular momentum $\boldsymbol{\kappa}$ is defined as that transferred during a collision, $\boldsymbol{N} \rightarrow \boldsymbol{N'}$, where ($\boldsymbol{\kappa} = |\boldsymbol{N} - \boldsymbol{N'}|$) as shown in figure 3.6. It follows that

$$|\boldsymbol{\kappa}|^2 = |\boldsymbol{N}|^2 + |\boldsymbol{N'}|^2 - 2|\boldsymbol{N}||\boldsymbol{N'}| \cos\theta_{NN'}, \tag{3.60}$$

where using the semiclassical quantization rule as with other angular momenta [37]

$$|\boldsymbol{\kappa}|^2 = (\kappa + 1/2)^2\hbar^2. \tag{3.61}$$

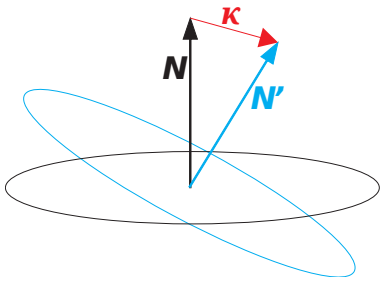

Figure 3.6: $\boldsymbol{\kappa}$ is the angular momentum transferred during a collision where the rotational angular momentum changes from $\boldsymbol{N}$ to $\boldsymbol{N}'$.

The distribution of κ is related to the $\boldsymbol{N}$-$\boldsymbol{N'}$ correlation and the rotational tilt such that [37, 115]

$$P(\kappa) = P(\cos\theta_{NN'}) \left| \frac{\mathrm{d}\cos\theta_{NN'}}{\mathrm{d}\kappa} \right|. \tag{3.62}$$

In this case κ and N' are considered real and continuous and the last term is the Jacobian of the transformation [37]. Given equations 3.60 and 3.61, it follows that

$$\left| \frac{\mathrm{d}\cos\theta_{NN'}}{\mathrm{d}\kappa} \right| = \frac{2(2\kappa+1)}{(2N+1)(2N'+1)}. \tag{3.63}$$

In the case in which N is binned to its nearest integer value, and likewise κ is binned to its nearest integer K, and the distribution is discrete [115],

$$P(K) = \frac{\mathcal{N}_{NN'}(K)}{\mathcal{N}_{NN'}}. \tag{3.64}$$

where $\mathcal{N}_{NN,}(K)$ is the number of trajectories $N \rightarrow N'$ with a momentum transfer κ binned to K. This expression is really the $P(K, M_N)$ correlation with M_N the quantum number for the projection of $\boldsymbol{N}$ onto an arbitary axis, whilst equation (3.62) is the $P(\kappa, \cos\theta_N)$ correlation with $\cos\theta_N$ the angle between $\boldsymbol{N}$ and the same reference axis. The relationship between the two is given by [37]

$$P(M_N) = P(\cos\theta_N)\frac{\mathrm{d}\cos\theta_N}{\mathrm{d}M_N} = P(\cos\theta_N)\frac{2}{2N+1}. \tag{3.65}$$

For an isotropic distribution $P(\cos\theta_N) = 1/2$ the distribution of interest is actually $P^K_{NN'} = (2N+1)P(K)$. The treatment is extended to consider the conditional probability of K for a given orbital angular momentum, ℓ, such that [37]

$$P_{NN'}(K|\ell) = \frac{\mathcal{N}_{NN'}(K,\ell)}{\mathcal{N}_{NN'}(\ell)}. \tag{3.66}$$

This joint probability can also be expressed as [37]

$$P^{K}_{NN'}(\ell) = (2N+1)P_{NN'}(K|\ell)P_{NN'}(\ell), \tag{3.67}$$

where

$$P_{NN'}(\ell) = \frac{\mathcal{N}_{NN'}(\ell)}{\mathcal{N}_{N}(\ell)}, \tag{3.68}$$

which is identical to the opacity function for $N \rightarrow N'$ collisions. The sampling of orbital angular momentum is given by [37]

$$\mathcal{N}_{N}(\ell) = \mathcal{N}_{N}\frac{2\ell+1}{(\ell_{\max}+1)^2}. \tag{3.69}$$

Combining equation (3.66) to equation (3.69) leads to

$$P^{K}_{NN'}(\ell) = (\ell_{\max}+1)^2(2N+1)\frac{\mathcal{N}_{NN'}(K,\ell)}{(2\ell+1)\mathcal{N}_{N}}. \tag{3.70}$$

In order to obtain the classical tensor opacity function it is necessary to sum over ℓ, such that

$$P^{K}_{NN'} = \sum_{\ell}(2\ell+1)P^{K}_{NN'}(\ell) = (\ell_{\max}+1)^2(2N+1)\sum_{\ell}\frac{\mathcal{N}_{NN'}(K,\ell)}{\mathcal{N}_{N}}. \tag{3.71}$$

With $k_i^2 b_{\max} \approx (\ell_{\max}+1)^2$ and including the inelastic cross section as defined in subsection 3.3.1 obtains

$$P^{K}_{NN'} = \frac{k_i^2}{\pi}(2N+1)\sigma_{NN'}(K), \tag{3.72}$$

where these classical cross sections can be derived directly from the QCT data so that

$$\sigma_{NN'}(K) = \pi b^2_{\max}\frac{\mathcal{N}_{NN'}(K)}{\mathcal{N}_{N}}. \tag{3.73}$$

In the opacity formalism, open shell inelastic cross sections are calculated by [115, 261]

$$\sigma_{jj'} = \sum_K [j'][N] \begin{Bmatrix} N & N' & K \\ j' & j & S \end{Bmatrix}^2 \sigma_{NN'}(K), \tag{3.74}$$

where $\{...\}$ is a 6-j symbol [13] that describes the angular momentum coupling. RET cross sections directly comparable to those from experiment are given by

$$\sigma_{\mathrm{RET}} = \sum_{j' \neq j} \sigma_{jj'}, \tag{3.75}$$

and depolarisation moments by

$$a^{(k)}(j,j') = (-1)^{k-j-j'}[j]^{\frac{1}{2}}[j']^{\frac{1}{2}} \frac{\sum_K (-1)^{-K} \begin{Bmatrix} j & j & k \\ j' & j' & K \end{Bmatrix} \begin{Bmatrix} N & N' & K \\ j' & j & S \end{Bmatrix}^2 \sigma_{NN'}(K)}{\sum_K \begin{Bmatrix} N & N' & K \\ j' & j & S \end{Bmatrix}^2 \sigma_{NN'}(K)}. \tag{3.76}$$

By extending to depolarisation cross sections

$$\sigma^{(k)}_{jj'} = \sum_{K>0} \sigma_{NN'}(K) \left(1 - (-1)^{k-K-N-N'}[N]^{\frac{1}{2}}[N']^{\frac{1}{2}} \begin{Bmatrix} N & N & k \\ N' & N' & K \end{Bmatrix} \right). \tag{3.77}$$

In this expression, $K = 0$ corresponds to the 'pure elastic' case where there is no change in the direction as well as no change in the magnitude of the angular momentum $\boldsymbol{N}$ upon collision. Elastic collision cross sections and depolarisation moments cannot be calculated as trajectories with $K = 0$ cannot be converged, but elastic depolarisation cross sections can be converged as the summation does not include the $K = 0$ term. As such the tensor opacity formalism allows for the calculation of elastic depolarisation cross sections for experimental comparison. Total depolarisation cross sections are

given by

$$\sigma_d^{(k)} = \sum_{j'} \sigma_{jj'}^{(k)}. \tag{3.78}$$

Coupling to the intrinsic nuclear spin, $I = 1/2$, can be accounted for similarly [37], but since the experiments are not hyperfine resolved this is not necessary in this analysis, and consequently not carried out.

3.5 Summary

This chapter has described the OH(A)+H_2 PES used in the QCT calculations. The method for classically propagating the trajectories has been outlined. Techniques have also been described for calculating various experimentally observable properties such as RET and depolarisation cross sections, along with some properties that are non-observable in these experiments, such as the DCS and opacity functions. A tensor opacity formalism, based on previous studies, has been presented that allows for the calculation of elastic depolarisation cross sections and the consideration of the effects of electron spin.

Chapter 4 presents results from QCT calculations for the various properties listed here. Chapter 7 compares these results with those from experimental measurements presented separately in chapter 6. Chapter 7 also presents data on the regions of the PES explored by the trajectories. Since electronic quenching is associated with particular regions of the PES, this discussion allows for an indirect qualitative consideration of the extent to which the QCT and adiabatic treatment accounts for the prevalence of the electronic quenching pathway. Since the theoretical calculations are adiabatic and restricted to a single surface the quenching products cannot be accounted for directly. Finally, chapter 7 considers and evaluates the potential sources of error in the calculations.

Chapter 4

OH(A)+H_2 Theoretical Results

The results in this chapter are calculated from propagating quasi-classical trajectories (QCT) on an adiabatic OH(A)+H_2 potential energy surface (PES). Chapter 3 demonstrated that the calculated potential is characterised by marked anisotropy. There are potential wells of considerable depth, $\sim 10000\,\mathrm{cm}^{-1}$, but large repulsive barriers to the rotation of either the OH(A) or H_2 diatom in approaching them. Repulsive regions are also seen at larger separations, as well as at short intermolecular distances. Together with the kinematics of the system, the nature of this surface is central in determining the end products of the QCT. Furthermore, this represents the first time this methodology has been used to investigate a four-atom system. The impact the presence of a second diatom will have on the result of the calculations is of particular interest.

Cross sections for inelastic collisions are calculated, along with disorientation and disalignment cross sections. These depolarisation cross sections are separated into their elastic and inelastic contributions. The opacity functions for depolarisation and inelastic collisions are also presented. The first and second rank depolarisation moments are recorded, and these form the first few moments in the expansion of the $\boldsymbol{N}$-$\boldsymbol{N}'$ correlation. This correlation is presented here, along with the $\boldsymbol{k}$-$\boldsymbol{k}'$ differential cross section (DCS).

The tensor opacity formalism has allowed for the determination of open shell properties - inelastic cross sections and depolarisation moments. The dependence of these factors on whether collisions are spin-rotation conserving or changing is also explored.

Depolarisation and rotational energy transfer (RET) in the colliding H_2 diatom is also considered, along with the influence this has on depolarisation and RET in the OH(A) diatom. In doing so, a weak propensity for anti-correlated transfers is observed, where either the increase in angular momentum in one diatom leads to a decrease in angular momentum in the other, or there are opposite changes in the angular momentum polarisation in each diatom.

4.1 Inelastic Cross Sections

4.1.1 Closed Shell

In a closed shell diatomic molecule, the energy associated with the rotation of the nuclear framework is given by

$$E_{\text{rot}} = BN(N+1), \tag{4.1}$$

where B is the rotational constant for the diatom. The energy spacing between rotational levels is given by

$$\Delta E_{\text{rot}} = B\Delta N(2N + \Delta N + 1) \tag{4.2}$$

where N is the initial rotational level, N' is the final rotational level after the collision and $\Delta N = |N' - N|$.

Inelastic collisions must obey conservation of energy such that

$$E_{\text{tot}} = E_{\text{coll}} + E_{\text{rot,OH}} + E_{\text{rot,H}_2} = E'_{\text{trans}} + E'_{\text{rot,OH}} + E'_{\text{rot,H}_2}, \tag{4.3}$$

where E_{coll} is the initial collision energy and initial translational energy, and E'_{trans} is the translational energy after the collision. This conservation restriction is not strictly obeyed following the binning of rotational angular momenta from classical trajectories to their nearest quantum numbers, but the rule is nonetheless useful in discussion of results. Similarly, the total angular momentum is conserved in the classical trajectory such that

$$\boldsymbol{J} = \boldsymbol{N}_{\text{OH}} + \boldsymbol{N}_{\text{H}_2} + \boldsymbol{\ell} = \boldsymbol{N}'_{\text{OH}} + \boldsymbol{N}'_{\text{H}_2} + \boldsymbol{\ell}', \tag{4.4}$$

where $\boldsymbol{J}$ is the total angular momentum and $\boldsymbol{\ell}$ is the orbital angular momentum of the system. Classically $|\boldsymbol{\ell}| = \mu|\boldsymbol{v}_{\text{rel}}|b$ where b is the impact parameter for the collision, $\mu = 1.802\,\text{amu}$ is the reduced mass of the collision system, and $\boldsymbol{v}_{\text{rel}}$ is the relative velocity.

Inelastic cross sections for collisions $N_{\text{OH}} \rightarrow N'_{\text{OH}}$ are resolved into N'_{OH} in figure 4.1. Cross sections are presented for trajectory calculations starting in $N_{\text{OH}} = 2$, 5 and 10, all with a collision partner with initial rotational angular momentum $N_{\text{H}_2} = 1$. These are closed shell cross sections, and in all panels the cross section decreases as ΔN_{OH} increases in magnitude, since, as noted in equation (4.2), more energy transfer is required for a higher ΔN_{OH}. Energy and momentum transfer takes place either with the internal energy of the second diatom or the system's orbital angular momentum, effectively the translational energy as demonstrated in equation (4.3). Translational to rotational energy transfer is more efficient at smaller impact parameters so smaller cross sections result.

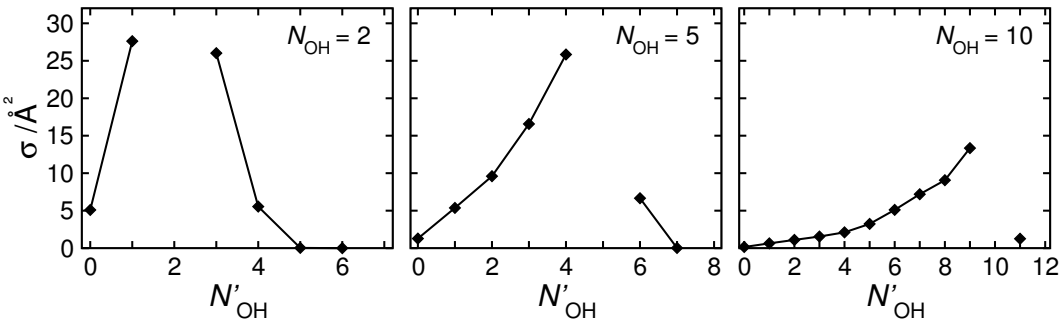

Figure 4.1: Closed shell inelastic cross sections for $N_{\mathrm{OH}} \rightarrow N'_{\mathrm{OH}}$ for $N_{\mathrm{OH}} = 2$ (left panel), $N_{\mathrm{OH}} = 5$ (middle panel) and $N_{\mathrm{OH}} = 10$ (right panel) with $N_{\mathrm{H_2}} = 1$.

For $N_{\mathrm{OH}} = 2$, collisions are observed with $\Delta N_{\mathrm{OH}} = +2$, +1, -1 and -2 with appreciable cross sections. For $N_{\mathrm{OH}} = 5$ reasonable cross sections are seen for collisions that reduce the OH(A) radical rotational angular momentum, but only for $N'_{\mathrm{OH}} = 6$ when N'_{OH} is being increased. Furthermore, for $N_{\mathrm{OH}} = 10$, only reductions in the rotational angular momentum of the OH(A) diatom have sizeable cross sections. Increasing rotational quantum number at higher initial N_{OH} is less likely as there is limited energy available for transfer. For example, the transition $N_{\mathrm{OH}} = 10 \rightarrow N_{\mathrm{OH}} = 11$ requires an energy transfer of $374\,\mathrm{cm}^{-1}$ yet the thermal collision energy is only $315\,\mathrm{cm}^{-1}$ (though in the case of histogram binned final states only an increase to $N_{\mathrm{OH}} = 10.5$ is required for the trajectory to be histogram binned to final state $N_{\mathrm{OH}} = 11$). Whilst these cross sections only include trajectories with a H_2 collider with $N_{\mathrm{H_2}} = 1$, the patterns observed are largely independent of the initial H_2 rotational angular momentum.

Figure 4.2 sums the inelastic cross sections for all collisions $N_{\mathrm{OH}} \rightarrow N'_{\mathrm{OH}}$, where $N'_{\mathrm{OH}} \neq N_{\mathrm{OH}}$, to give closed shell total RET cross sections. Accompanying closed shell QCT data is given from previous investigations with Ar [37] and Kr [117] colliders.

As with the atomic colliders, the RET cross sections with a H_2 collider fall with increasing N_{OH}. This follows firstly from the increased energy spacing between rotational levels at higher N_{OH}. Additionally, all three PESs are highly anisotropic, and this sensitivity to the orientation of the approaching OH(A) diatom leads to an OH

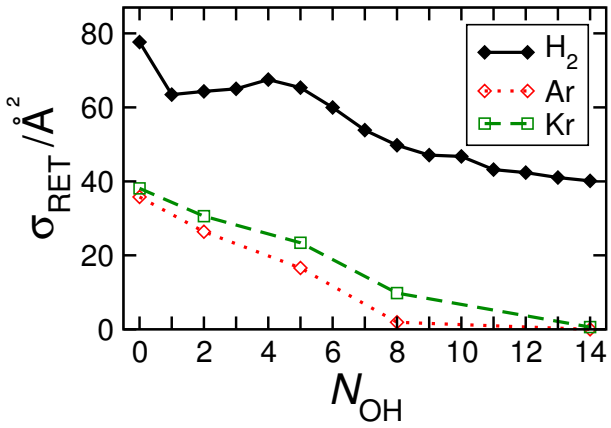

Figure 4.2: Closed shell RET cross sections for the OH(A) radical where $N_{\mathrm{OH}} \rightarrow N'_{\mathrm{OH}}$ and $N'_{\mathrm{OH}} \neq N_{\mathrm{OH}}$ with various collider species. The green dashed data with open squares are from QCT calculations with a Kr collider [117], the red open diamonds with dotted lines for QCT results with an Ar collider [37] and finally the black diamonds with black lines are data from this investigation with a H_2 collider and $N_{H_2} = 1$.

rotational level dependence. The collision system is drawn away from diatom orientations that are repulsive in nature and towards attractive regions of the PES associated with particular geometries of the diatom(s). This process induces torque in one diatom or the other (or both), leading to changes in both the magnitude and polarisation of the angular momentum. As the OH(A) radical rotates faster the potential experienced by the incoming H_2 diatom is increasingly averaged or 'washed out' and consequently the levels of RET will fall.

Whilst the cross sections with Kr and Ar colliders are fairly similar, those with a H_2 collider are substantially bigger. This may in part be a consequence of the more attractive and anisotropic PES involved with the deepest wells in the OH(A)+H_2 PES at $V = -10158\,\mathrm{cm}^{-1}$ compared to $V = -6079\,\mathrm{cm}^{-1}$ [93] for OH(A)-Kr. However, the Kr surface is substantially more attractive than the Ar surface (deepest well depth of $V = -1717\,\mathrm{cm}^{-1}$ and the difference in RET cross sections between the two rare gas colliders is comparatively small. It is more likely that the substantial difference in OH(A) RET cross sections with rare gas colliders compared to with a H_2 collider results from the additional possibility of transferring rotational energy and angular

momentum between the two diatoms.

The fall in cross section with increased N_{OH} is also less pronounced with H_2 than the other colliders. This may be due to the continued availability of energy transfer between the two diatoms at high N_{OH}. Furthermore, the PES of OH(A)+H_2 is considerably more anisotropic to begin with, reducing the impact of washing out. It is likely that even at high N_{OH}, the approaching H_2 still experiences pronounced anisotropy (depending upon approach geometry), with the interaction still creating torque and a mechanism for RET.

4.1.2 The Influence of a Diatomic Collider - H_2

The presence of a second diatom leads to the additional possibility of RET between rotational levels in that diatom. H_2 RET cross sections are shown in figure 4.3 for a series of different initial starting rotational angular momentum quantum numbers in the accompanying OH(A) collider, N_{OH}. Data are shown in which a condition had been placed on the histogram binning that the parity of the diatom remained fixed, and as such ΔN_{H_2} was limited to even values. Cross sections resulting from calculations where this constraint was not applied are also presented. The component of these cross sections in which there was RET in both diatoms is also shown.

The H_2 RET cross sections are smaller than those for OH(A). This is unsurprising given the much larger rotational constant, $B_{H_2} = 60.92\,\mathrm{cm}^{-1}$, [46] compared to $B_{OH} = 17.36\,\mathrm{cm}^{-1}$ [46], leading to energy levels that are much more widely spaced. The vast majority of H_2 RET collisions are accompanied by RET in OH(A), especially when parity must be conserved. This suggests that transfer of rotational energy between the two diatoms is important in bringing about RET in the H_2 diatom, however it does not necessarily mean that transfer of rotational energy between the two diatoms is necessary to bring about RET in OH(A). RET cross sections for H_2 are larger when

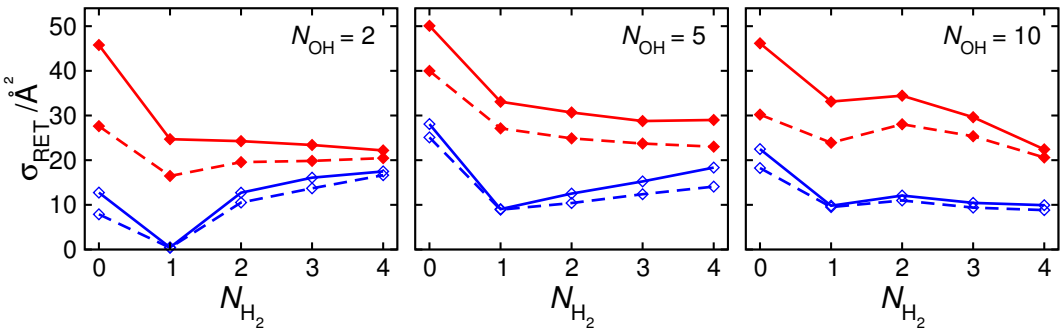

Figure 4.3: RET cross sections for $N_{H_2} \rightarrow N'_{H_2}$, where $N_{H_2} \neq N'_{H_2}$, as a function of the initial H_2 angular momentum, N_{H_2}. The accompanying OH(A) radical has initial rotational angular momentum $N_{OH} = 2$ (left-hand panel), $N_{OH} = 5$ (middle panel) and $N_{OH} = 10$ (right-hand panel). The blue open diamonds are cross sections resulting from calculations where parity was conserved following the collision and the red filled diamonds where parity was allowed to change. The data connected with complete lines are the total RET cross sections whilst data connected with dashed lines the components which were also inelastic in OH(A), i.e. RET occurred in both diatoms in the collision.

accompanied by an OH(A) collider with $N_{OH} = 5$, than with $N_{OH} = 2$, because of the availability of more rotational angular momentum for exchange. The cross sections are slightly reduced for $N_{OH} = 10$, potentially because the faster rotating OH(A) diatom means the PES anisotropy is partially washed out. As a result, less torque is experienced in collisions and there is less RET.

Cross sections are significantly smaller when the requirement for nuclear spin conservation is applied during the histogram binning of the final angular momentum. Trajectories binned to $\Delta N_{H_2} = \pm 1$ are the dominant component of RET when parity is not conserved. With the parity conservation restriction, these are either reassigned to $\Delta N_{H_2} = \pm 2$ or, as in the majority of cases, $\Delta N_{H_2} = 0$. In the latter case the trajectory has instead been considered elastic in H_2. It should be emphasized that the binning of trajectories such that ΔN_{H_2} is even has no effect on the OH(A) RET cross sections.

The dip in H_2 RET cross sections with parity conservation at $N_{H_2} = 1$ is of note. For this initial state, only collisions to higher N_{H_2} are allowed, and increasing to $N'_{H_2} = 3$ requires considerable energy transfer. Consequently, these H_2 RET cross sections are

the smallest, especially when N_{OH} is low, and there is limited rotational energy available for transfer. When nuclear spin is allowed to change, the RET cross sections for H_2 fall with N_{H_2} due to the increasing energy spacing and washing out effect. The RET cross sections are substantially larger at $N_{H_2} = 0$, where the only RET that can occur is increasing the rotational level of H_2. This is clearly quite a prevalent process as the cross sections are large, indicating the rotational motion of H_2 will readily act as a sink for energy in the trajectory. This suggests that H_2 readily assists in the reduction of N_{OH}.

Figure 4.4 gives the RET cross sections for OH for a variety of different starting N_{H_2}, along with cross sections where RET occurs in both diatoms. These latter cross sections are calculated both with, and without, the application of the parity conservation constraint on N'_{H_2}. Unlike in the case of H_2 diatom RET, there is a significant amount of RET in OH(A) that is not accompanied by RET in H_2. The data suggest that a significant fraction of collisions which are inelastic in OH(A) are elastic in H_2. This is not surprising as the smaller energy spacing in OH(A) allows RET to occur through the transfer of translational energy alone.

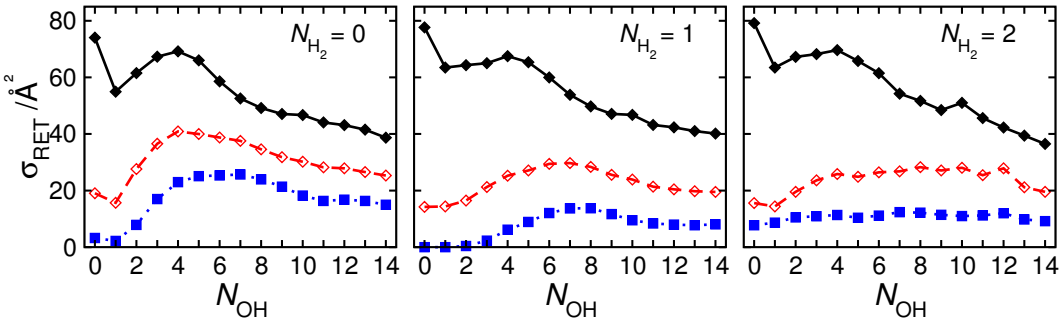

Figure 4.4: RET cross sections for $N_{\mathrm{OH}} \rightarrow N'_{\mathrm{OH}}$ where $N_{\mathrm{OH}} \neq N'_{\mathrm{OH}}$ as a function of the initial OH(A) angular momentum N_{OH}. The accompanying H_2 diatom has initial rotational angular momentum: $N_{H_2} = 0$ (left panel), $N_{H_2} = 1$ (middle panel) and $N_{H_2} = 2$ (right panel). The black filled diamonds connected by full lines show the closed shell RET cross sections for OH(A), and the red open diamonds connected by broken lines are the cross sections for OH(A) RET where the collision is also inelastic in the H_2 diatomic molecule. The blue filled squares connected by dotted lines show the cross sections for OH(A) RET in which the collision is also inelastic in the H_2 diatomic molecule and in which the latter transitions conserve parity.

The relative importance of OH(A) RET collisions that are also inelastic in H_2 increases with N_{OH}. For the $N_{H_2} = 1$ panel, this increase is from less than about a quarter of the total contribution at $N_{OH} = 0$, to more than half at $N_{OH} = 14$ (when parity is allowed to change). At low N_{OH} there is insufficient energy available in the rotational motion of OH(A) to bring about an increase in N_{H_2} without a substantial additional contribution from the translational motion. Consequently, at low N_{OH} a smaller fraction of collisions are inelastic in both H_2 and OH(A). To consider this from a different point of view, at high N_{OH} there is insufficient energy in the relative translational motion alone to excite OH(A) rotationally, and so H_2 rotation becomes a necessary source of energy. However, this argument is flawed, because it has been noted in figure 4.1 that at high N_{OH} most RET involves a reduction rather than an increase in N_{OH}. This reduction requires the H_2 rotational motion, or the translational motion, to readily act as an energy sink. The increased importance of collisions that are also inelastic in H_2 at high N_{OH} suggests that H_2 rotation acting as a sink plays a substantial role. Moreover, in cases in which only the transfer of energy to translational motion is available, e.g. in the OH(A)+Rg studies, the cross sections fall more dramatically with N_{OH}.

Figure 4.4 also displays the data for three different initial N_{H_2} values: the data do not vary greatly in this respect. The $N_{H_2} = 1$ and $N_{H_2} = 2$ data sets are extremely similar, the implication being that increased rotational energy in the H_2 collider has little impact on the degree of RET in the OH(A) diatom. However, the left-hand panel where $N_{H_2} = 0$ does display slight differences. In this case, the H_2 has no initial rotational energy to exchange with the OH(A) diatom. As a consequence, the total RET cross sections at low N_{OH} are smaller than with higher N_{H_2}. At high N_{OH} where H_2 is primarily required to act as an energy sink, the three panels differ little as these do not require the H_2 to have angular momentum initially.

Figure 4.5 displays the cross sections for various inelastic collisions where RET occurs in one or both diatoms. The left panel shows the results from scattering where OH(A) is initially in $N_{\mathrm{OH}} = 2$ and H_2 initially in $N_{H_2} = 1$, whilst in the right panel the initial levels are $N_{\mathrm{OH}} = 5$ and $N_{H_2} = 1$, respectively. In this analysis the requirement for parity conservation is not considered. Note that the collisions which are elastic in H_2 dominate the inelastic scattering process. The figures demonstrate that RET favours small angular momentum transfer collisions in OH(A) and H_2. Looking at collisions that are inelastic in H_2, an anti-correlation is observed between the RET collisions of H_2 and OH(A). If the quantum number of H_2 is increased during the collision, there is a strong propensity for a decrease in the rotational quantum number of OH(A). Likewise when $\Delta N_{H_2} < 0$ there is a propensity, albeit far weaker, for there to be a increase in the rotational quantum number of OH(A).

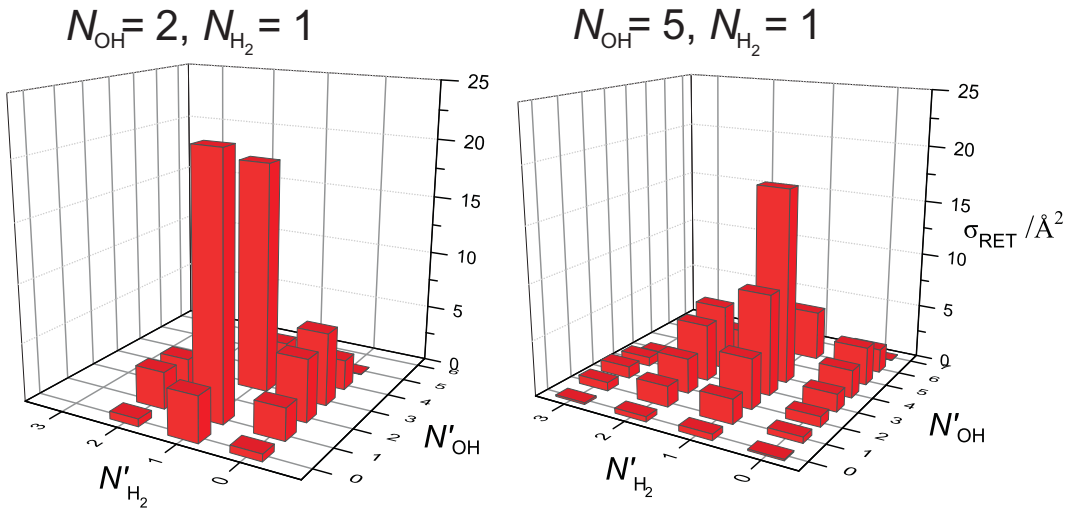

Figure 4.5: Bar chart showing RET cross sections resolved into various combinations of final N state for each diatom. Final rotational angular momentum of H_2 and OH(A) are N'_{OH} and N'_{H_2} respectively. The initial quantum numbers are $N_{\mathrm{OH}} = 2$ and $N_{H_2} = 1$ (left panel) and $N_{\mathrm{OH}} = 5$ and $N_{H_2} = 1$ (right panel). Parity has been allowed to change in H_2 in forming this figure.

Whilst the majority of collisions which are inelastic in OH(A) are elastic in H_2, there may still be a significant amount of angular momentum transfer, K_{H_2}, in the H_2 diatom. This transfer leads to a reorientation of the H_2 angular momentum, but

not necessarily a change in its magnitude. Similarly, in the rare cases where there is no RET in OH(A) accompanying RET in H_2, there may still be angular momentum transfer in OH(A), i.e. accompanying elastic depolarisation in OH(A) ($K_{OH} \neq 0$). Figure 4.6 explores this relationship showing the QCT calculated RET cross sections for OH(A), resolved in the angular momentum transfer K_{H_2} (left panel), and for H_2, resolved in K_{OH} (right panel).

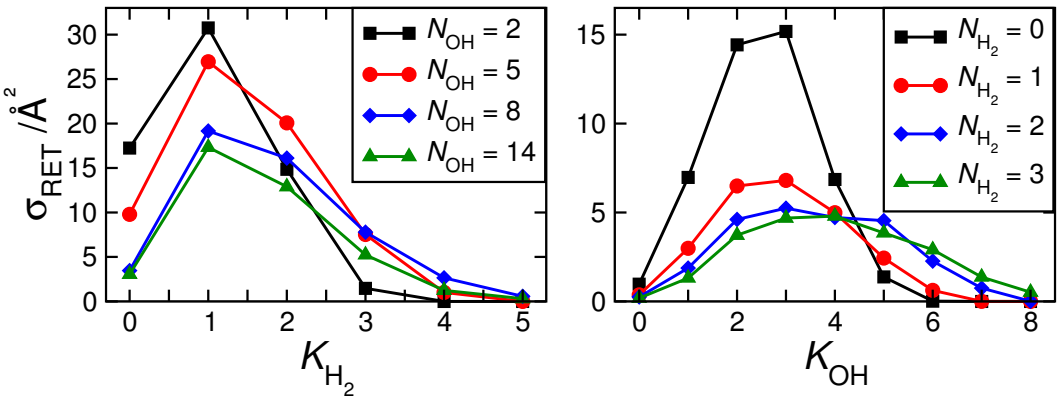

Figure 4.6: Left panel: Closed shell total OH(A) RET cross-sections for $N_{OH} = 2$ (black squares), $N_{OH} = 5$ (red circles), $N_{OH} = 8$ (blue diamonds), and $N_{OH} = 14$ (green triangles) resolved in K_{H_2}, the angular momentum transferred in H_2 during collision, which was initially in $N_{H_2} = 1$. Right panel: As for the left panel, but showing total H_2 RET cross sections for $N_{H_2} = 0$ (black squares), $N_{H_2} = 1$ (red circles), $N_{H_2} = 2$ (blue diamonds), and $N_{H_2} = 3$ (green triangles) resolved in K_{OH}, the angular momentum transferred during collision in OH(A), which was initially in $N_{OH} = 2$.

As expected, given earlier observations from figures 4.3 and 4.4, the RET cross sections are seen to decrease with increasing N_{OH} or N_{H_2}. For all initial OH(A) states, the cross sections are at their maximum when $K_{H_2} = 1$, before falling with increasing K_{H_2}. The rate of this decline decreases at higher N_{OH}. The H_2 RET cross sections peak around $K_{OH} = 3$ to 5, but involve an increasing range of K_{OH} as N_{H_2} increases. This figure reveals that the majority of OH(A) and H_2 RET in the QCT calculations, is accompanied by significant rotational angular momentum transfer in the collision partner, if not RET. RET collisions of OH(A) with H_2 tend to involve angular momentum transfer in both molecules, with neither OH(A) nor H_2 behaving like an atomic species. This behaviour becomes increasingly prominent as N_{OH} or N_{H_2} increases.

In this QCT analysis, H_2 cannot be thought of as behaving like an atom in collisions with OH(A). Instead the extent of angular momentum transfer to H_2 accompanying OH(A) RET can be considered indicative of the level of H_2 depolarisation during the collision. The fact that H_2 cannot be treated as a simple atomic species is perhaps surprising, but is largely a consequence of the highly anisotropic nature of the OH(A)+H_2 PES.

4.1.3 Rotational Energy Transfer - Open Shell Treatment

The tensor opacity method allows for the calculation of open shell properties from QCT calculations. Figure 4.7 displays open shell RET cross sections for the OH(A) diatom in OH(A)+H_2. Open shell RET cross sections include an additional component, of which the spin-rotation level changes but the rotational level is preserved ($j'_{OH} \neq j_{OH}$, $N'_{OH} = N_{OH}$). Inclusion of this component delivers RET cross sections directly comparable with those determined from the experiments outlined in chapter 5. There is no such spin-rotation changing contribution at $N_{OH} = 0$, as there is only one spin-rotation level, f_1 ($j = N + S$). Consequently, there is a dip in total RET cross section at $N_{OH} = 0$ for the f_1 spin-rotation level, but subsequent to $N_{OH} = 1$ the cross sections generally decline with increasing N_{OH}, as seen with the closed shell RET calculations. The contributions of pure spin-rotation changing collisions to the RET cross sections are seen to be relatively small.

The f_2 RET cross sections are typically larger than those for f_1, though this difference is greater at low N_{OH}. This is as found in previous OH(A) QCT collision studies with He [34], Ar [37] and Kr [117]. This difference arises from the difference in the size of the cross section for j_{OH} changing, N_{OH} conserving collisions. As expressed in

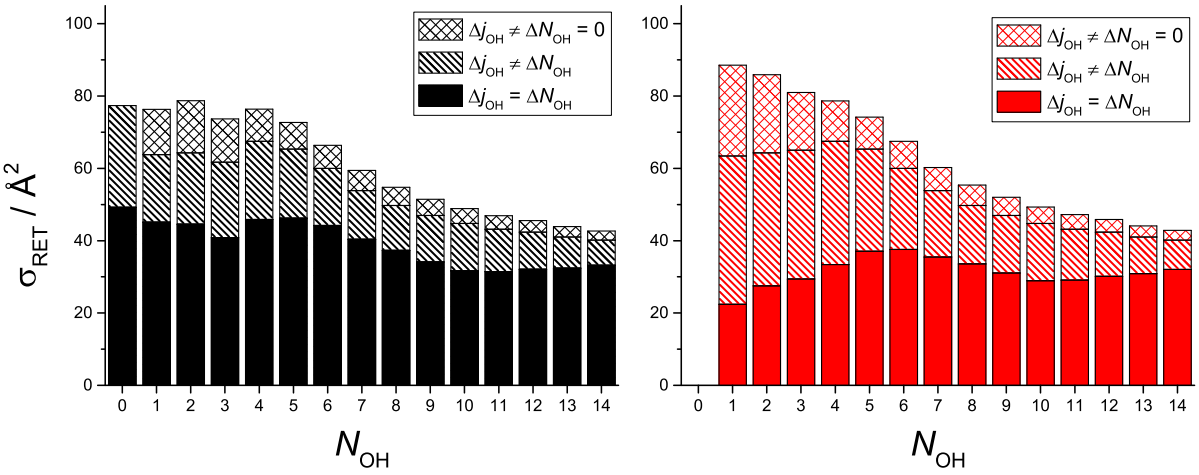

Figure 4.7: The composition of open shell RET cross sections determined from theoretical QCT calculations for OH(A)+H_2. The solid colour segments are the contribution to the RET cross sections from spin-rotation conserving collisions ($\Delta j_{\rm OH} = \Delta N_{\rm OH} \neq 0$). The stripped colour segments are the contribution to the RET cross sections from spin-rotation changing collisions ($\Delta j_{\rm OH} \neq \Delta N_{\rm OH} \neq 0$). The hashed coloured segment correspond with pure spin-rotation changing collisions without a change in $N_{\rm OH}$ ($\Delta N_{\rm OH} = 0$, $\Delta j_{\rm OH} = \pm 1$). The left-hand panel is for OH(A) radicals initially in the f_1 spin-rotation level and the right-hand panel for OH(A) radicals initially in the f_2 spin-rotation level. These cross sections follow trajectories with the H_2 diatom being in the initial rotational level, $N_{\rm H_2} = 1$.

section 3.4.1, open shell inelastic cross sections are given by

$$\sigma_{jj'} = \frac{\pi}{k_i^2}[j'_{\rm OH}] \sum_K \left\{ \begin{array}{ccc} N_{\rm OH} & N'_{\rm OH} & K_{\rm OH} \\ j'_{\rm OH} & j_{\rm OH} & S \end{array} \right\}^2 P^{K_{\rm OH}}(N_{\rm OH}, N'_{\rm OH}). \qquad (4.5)$$

When $N'_{\rm OH} = N_{\rm OH}$, given that the Wigner 6-j symbols are invariant under the permutation of any two columns, the difference between the pure spin-rotation changing cross sections for $j_{\rm OH} = N_{\rm OH} + S \rightarrow j'_{\rm OH} = N_{\rm OH} - S$ and $j_{\rm OH} = N_{\rm OH} - S \rightarrow j'_{\rm OH} = N_{\rm OH} + S$, is given by the ratio of the $[j'_{\rm OH}]$ terms. This ratio tends to unity in the high $j'_{\rm OH}$ limit. Consequently, the pure spin-rotation changing cross section for the f_2 spin-rotation level at $N_{\rm OH} = 1$ is twice that for f_1, and 1.5 times at $N_{\rm OH} = 2$. In the case where

$N'_{\mathrm{OH}} \neq N_{\mathrm{OH}}$, the variation in the ratio of cross sections for spin-rotation changing collisions to spin-rotation conserving collisions for f_1 and f_2 can be explained with similar recourse to this equation, though the ratio is not such a simple one. The degree of spin-rotation changing collisions is consistently greater in f_2 than f_1.

The figure also shows that at higher N_{OH}, there are fewer spin-rotation changing collisions. Spin is treated as a spectator in this analysis. As a consequence, to change spin-rotation level on average there needs to be a large change in the direction of N_{OH} upon collision. It is more difficult to change the direction of a faster rotating diatom so the cross sections for this process will fall with N_{OH}. Note that this is closely linked to the degree of molecular depolarisation.

4.2 Differential Cross Sections

As shown in section 3.3.2, the differential cross section (DCS), $\sigma_{N_{\mathrm{OH}}N'_{\mathrm{OH}}}P(\theta_{kk'})$, is a measure of the $\boldsymbol{k}$-$\boldsymbol{k}'$ correlation. Figure 4.8 presents QCT DCSs multiplied by a factor of $\sin(\theta_{kk'})$ since otherwise the function is dominated by small $\theta_{kk'}$ contributions. The data displayed correspond to the DCS for collisions that are inelastic in OH(A) on the left, and elastic on the right. The data shown are for initial $N_{\mathrm{OH}} = 2$ and 10 with $N_{\mathrm{H_2}} = 1$.

The inelastic DCSs show that inelastic collisions are slightly more likely to be forward scattered than anything else, as they decline at larger $\theta_{kk'}$. However, on the whole the DCSs appear relatively isotropic given their strong resemblance to the $\sin(\theta_{kk'})$ factor. This isotropy is characteristic of collision systems that form complexes which survive long enough to randomise the final relative velocity direction, $\boldsymbol{k}'$, with respect to $\boldsymbol{k}$. The large number of deep potential wells (associated with a variety of molecular geometries) are regions of the PES that would lead to complex formation, as has been seen with other systems with attractive regions such as OH(A)+Ar [116].

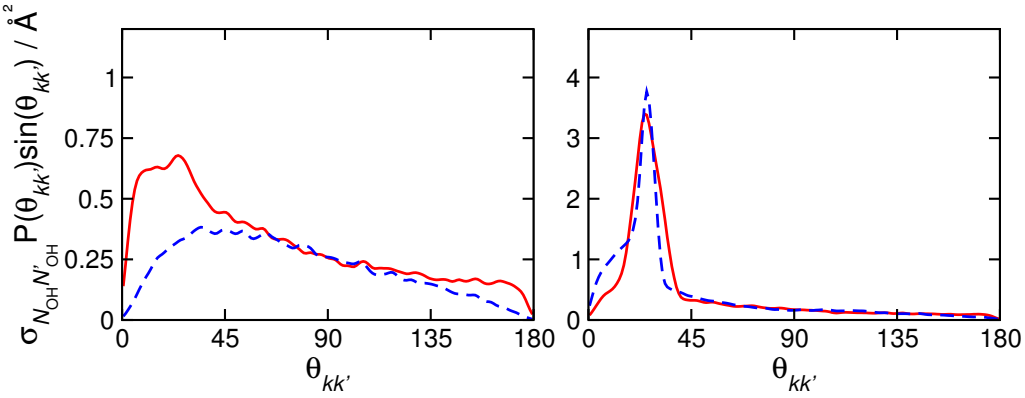

Figure 4.8: These panels display QCT calculated DCSs for the OH(A)+H_2 collision system, multiplied by $\sin(\theta_{kk'})$. The left-hand panel contains contributions from trajectories where the collision was inelastic in OH(A). The right-hand panel shows the DCS for collisions that were elastic in OH(A). Full red lines correspond to initial $N_{\mathrm{OH}} = 2$, and blue dashed lines to $N_{\mathrm{OH}} = 10$. For all trajectories $N_{\mathrm{H_2}} = 1$.

Though not shown here, when the DCS is resolved into N'_{OH} the function more and more closely resembles the shape of its sine dependence with increasing ΔN_{OH}, i.e. it becomes more isotropic. Likewise, the inelastic DCS is more isotropic at higher N_{OH}, as demonstrated in the comparison between $N_{\mathrm{OH}} = 10$ and 2 in the figure. This is a consequence of the greater energy transfer involved in RET at larger N_{OH} and ΔN_{OH}. As discussed, the energy transfer is either from translational motion or H_2 rotational angular momentum. In the former case this corresponds to a change in the relative velocity, which must be greater at larger N_{OH}. This larger change in velocity is less likely to result from a 'glancing blow' collision, but will originate from a collision at smaller impact parameters with a greater change in the direction, as well as size, of $\boldsymbol{k}$. Indeed at high N_{OH} relatively few trajectories would appear to be of a glancing nature, instead involving complex formation. In contrast, at $N_{\mathrm{OH}} = 2$ collisions of a glancing nature would appear to play a role in RET in some cases.

The elastic DCSs are dominated by forward scattering and are similar for $N_{\mathrm{OH}} = 2$ and 10. There is a slightly greater dominance of forward scattering at $N_{\mathrm{OH}} = 10$ because the colliding H_2 diatom experiences a more rotationally averaged PES which exerts a limited force on either diatom, preserving the direction of $\boldsymbol{k}$. There is a

notable feature in the elastic DCSs at $\theta_{kk'} \approx 25°$, this provides evidence of rainbow scattering, and suggests that attractive regions of the potential play a role in elastic collisions [22]. It seems likely that these trajectories will lead to elastic depolarisation. In contrast, the very small $\theta_{kk'}$ collisions are typically very long range collisions, without any accompanying angular momentum depolarisation. These can broadly be considered purely elastic as opposed to elastic depolarising collisions.

4.2.1 Deflection Function: b vs $\theta_{kk'}$

Figure 4.9 will further demonstrate the role of complex formation in OH(A)+H_2 collisions. This figure plots the deflection function: the scattering angle, $\theta_{kk'}$, as a function of the impact parameter for elastic and inelastic trajectories. The data in the left-hand panels are for OH(A)+Kr collisions at $N_{\mathrm{OH}} = 2$ and provide a useful comparison [117].

It is helpful to consider the pattern that would emerge for elastic collisions between structureless particles governed by a Leonard-Jones type potential [23]. At large impact parameters, the forces between particles are negligible and no deflection occurs giving $\theta_{kk,} = 0°$ at high b. As b is reduced the particles increasingly experience attractive forces and are drawn towards one another in the trajectory with increasing $\theta_{kk,}$. This reaches a peak at the rainbow impact parameter, when attractive forces have their largest effect and the particles are deflected towards one another by a characteristic maximum angle, known as the rainbow scattering angle [23]. As b is reduced below the rainbow scattering parameter, the repulsive regions of the potential begin to play a role and act to reduce the deflection resulting from the initial attraction. When the repulsive and attractive forces are in balance the particles emerge from the trajectory without deflection, $\theta_{kk,} = 0°$, this is glory scattering [23]. As the impact parameter is reduced to less than the glory scattering parameter, the repulsive forces start to dominate and the particles are driven apart increasing $\theta_{kk,}$ once more. This reaches a

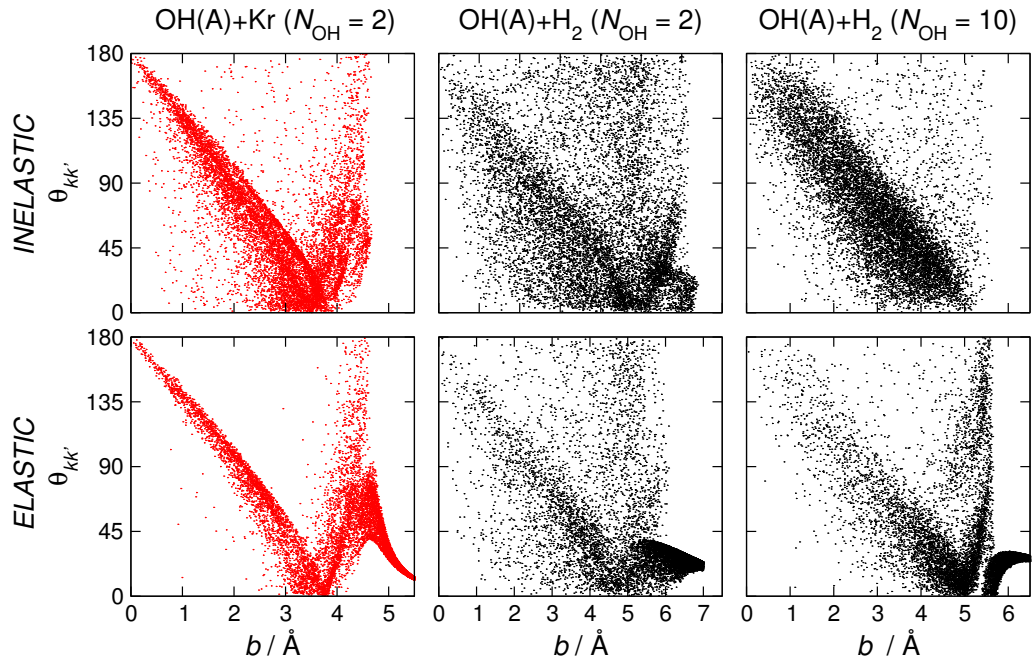

Figure 4.9: These panels present scatter plots of the scattering angle, $\theta_{kk'}$, for the trajectory against its initial impact parameter, b, from QCT calculations. Data are shown for OH(A)+Kr in the left-hand panels [117], and for OH(A)+H_2 in the middle and right-hand panels. The middle panels are for trajectories with $N_{\rm OH} = 2$ (as for the OH(A)+Kr example on the left) and the right-hand panels are for trajectories with $N_{\rm OH} = 10$. The top panels display trajectories that are inelastic in OH(A), i.e $N'_{\rm OH} \neq N_{\rm OH}$, whilst the bottom panels are elastic in OH(A), i.e. $N'_{\rm OH} = N_{\rm OH}$. A random sample of 10,000 trajectories are shown in each panel (typically 10% of the full set). For all OH(A)+H_2 trajectories $N_{\rm H_2} = 1$.

maximum for a head on collision where $b = 0$ and the deflection angle is $\theta_{kk'} = 180°$ with the particles backward scattered [23].

The OH(A)+Kr data follow a pattern not dissimilar to that for the model case described above. At small impact parameters large scattering angles dominate, since these trajectories probe the inner repulsive wall of the PES leading to back scattering. The scattering angle falls to zero as the impact parameter is increased, before increasing again. The second (rainbow scattering) peak arises because of the increased role of the attractive region of the PES at larger b. At these larger impact parameters, the Kr atom is pulled off course somewhat by attraction to the OH(A) diatom, leading to forward scattered products [116, 117]. The discernible two band structure of the OH(A)+Kr panels corresponds to interaction with the O-end or H-end of the

diatom. The pattern described here is typically easier to see for the elastic trajectories. Looking at the inelastic trajectories the bands seen in the figure are wider than in the elastic case, owing in part to the change in magnitude of $\boldsymbol{k}$. In a deviation from the simple structureless Leonard-Jones model above, for some values of b trajectories are observed with a full range of scattering angles from $\theta_{kk'} = 0°$ to 180°. These features likely arise from complex formation since this effectively randomises $\theta_{kk'}$. In the case of OH(A)+Kr complex formation would appear to be more prevalent in inelastic trajectories, and over a range of b of approximately $2.0 - 4.5$ Å. There is also some degree of complex formation seen for elastic trajectories in OH(A)+Kr, albeit over a smaller range of impact parameters.

The OH(A)+H_2 data deviate more from the simple model as there is less recognisable structure in the deflection functions. Firstly, since the reduced mass of this system is considerably smaller, owing to the light hydrogen collider, the particles are more easily deflected. Consequently, the variation from an exact relationship between b and $\theta_{kk'}$ seen for a structureless particle is more exaggerated than with a Kr collider. Secondly, an even greater role is thought to be played by complex formation. Complex formation is common in this system over a larger range of b, and is observed in elastic as well as inelastic trajectories. However, at large b, where trajectories are elastic only, complex formation is not possible and forward scattering dominates. At $N_{\mathrm{OH}} = 10$, the inelastic collisions no longer show any evidence of rainbow scattering. Therefore, at high N_{OH}, it is clear that RET either results from complex formation or repulsive backward scattered trajectories, and typically long range attractive forces do not play a role. The elastic deflection function is more resemblant than at $N_{\mathrm{OH}} = 2$ to that for OH(A)+Kr, indicating that complex formation plays less of a role in elastic collisions at high N_{OH}. This figure supports the discussion of figure 4.8.

4.2.2 The Delay Time

In order to better quantify the role played by long-lived or complex forming trajectories it is useful to consider the time duration of the trajectories. A classical quantity known as the delay time can be defined for trajectory n as [275]

$$\tau_n = t_n - \frac{\mu_{\mathrm{OH,H_2}}\sqrt{\sum_{i=1}^{3}\left(q_{i+3}^{\mathrm{int},n}\right)^2}}{\sqrt{\sum_{i=1}^{3}\left(p_{i+3}^{\mathrm{int},n}\right)^2}} - \frac{\mu_{\mathrm{OH,H_2}}\sqrt{\sum_{i=1}^{3}\left(q_{i+3}^{\mathrm{fin},n}\right)^2}}{\sqrt{\sum_{i=1}^{3}\left(p_{i+3}^{\mathrm{fin},n}\right)^2}}, \tag{4.6}$$

where t_n is the length of time for trajectory n, and $\mu_{\mathrm{OH,H_2}}$ is the reduced mass of the collision system. Remembering from section 3.2.1, that q_4, q_5 and q_6, are the position of the H_2 diatom centre of mass relative to that for the OH diatom, and p_4, p_5 and p_6, are the conjugate momenta. The superscript 'int' refers to the initial values of these co-ordinates at the start of the trajectory, and the superscript 'fin' at the end. The delay time, τ_n, then gives the time the trajectory takes to complete (moving from its initial to final position) relative to its duration in the absence of a potential [275]. This is a useful property to describe the duration of the trajectory as it discounts the relative velocity of the colliding species. Consequently, this is a helpful measure when comparing the duration of trajectories with vastly different reduced masses and relative velocities, such as in the comparison of OH(A)+H_2 and OH(A)+Kr trajectories.

Figure 4.10 plots a histogram for the trajectory delay times of elastic and inelastic trajectories with starting OH(A) rotational angular momentum $N_{\mathrm{OH}} = 2$, with Kr and H_2 colliders. It should be noted that in the case of a H_2 collider approximately 10% of all inelastic trajectories and 5% of all elastic trajectories had $\tau > 1600\,\mathrm{fs}$, and these are not included in the chosen scale. In contrast, 4% of inelastic trajectories with a Kr collider had $\tau < -1100\,\mathrm{fs}$, and are similarly not included. These details are representative of the general pattern - the delay times for OH(A)+H_2 trajectories are

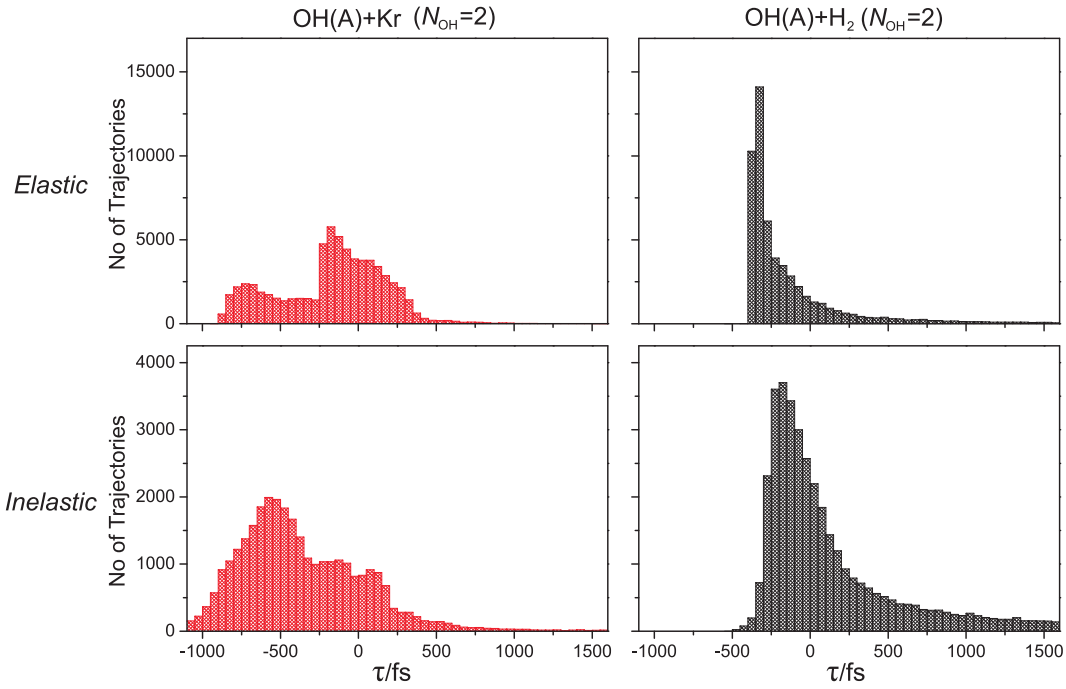

Figure 4.10: Histogram plots of the delay time for trajectories with initial rotational angular momentum quantum number for OH, $N_{\mathrm{OH}} = 2$. The left-hand panels show data with a Kr collider, whilst the right-hand panels with a H_2 collider of initial rotational quantum number, $N_{\mathrm{H_2}} = 1$. The top panels display trajectories that were judged elastic in QCT calculations with respect to OH diatom angular momentum, and the bottom where they were judged inelastic. The delay time is given in femtoseconds and the histogram bins are of width 50 fs with the first positive bin running from 0 to less than 50 fs, and the first negative bin from -50 fs to less than 0 fs. Note in most cases some trajectories are not included in the scale of the graph as described in the main text. 1×10^5 trajectories were run and included for both Kr and H_2 colliders.

more likely to be greater than for OH(A)+Kr trajectories. The rotational period of 392 fs for the OH(A) diatom in $N_{\mathrm{OH}} = 2$, is worth noting when analysing this graph.

There is no strict definition on what constitutes a long-lived or complex forming trajectory. For example, in a study of the H+H_2 collision system by Muga and Levine [276] all trajectories with a delay time greater than -100 fs were considered trapped collisions. In these OH(A) collision studies, positive values for delay time have been chosen as signifying a long-lived trajectory.

Looking first at the elastic histogram data, a warning is provided that applies to other figures on elastic data. Since elastic cross sections cannot be converged, there is the potential for these plots to be dominated by those collisions that essentially do

not experience any interaction, perhaps arbitrarily more so in the case of one collision system than the other. Consequently, it is difficult to make any strong conclusions on the basis of this comparison. There is no such difficulty for elastic DCS's or deflection functions, where it is possible to see in the figure which trajectories result from a limited interaction. In both collision systems negative delay times dominate, although 21% with a H_2 collider or 30% with a Kr collider are positive, suggesting long-lived trajectories do still play some role in the minority of these collisions. With a H_2 collider around 10% of all elastic trajectories have delay times longer than 400 fs or greater than one rotational period, versus only around 2% of OH(A)+Kr collisions in this category. So whilst there are more long-lived trajectories with Kr in this figure, there does appear some tendency for some elastic collisions with H_2 to be particularly long-lived.

The pattern in the inelastic data is more discernible, whilst around 50% of the trajectories for OH(A)+H_2 have negative delay times (corresponding to some of the classic character seen in the deflection function scatter plot in figure 4.9), 50% have positive delay times. Of this 26% have a delay time longer than one rotational period and 18% more than 800 fs (approximately 2 rotational periods). This is in contrast to the Kr data, where 81% of trajectories have negative delay times and only around 5% last longer than 400 fs (roughly a rotational period), and around 2% more than 800 fs. Whilst the Kr collision system does seem to form complexes on occasion, this is clearly a much more important feature in the H_2 collision system.

4.3 $\boldsymbol{N}$-$\boldsymbol{N}'$ Correlation

The $\boldsymbol{N}_{\mathrm{OH}}$-$\boldsymbol{N}'_{\mathrm{OH}}$ correlation describes the rotational tilt following a collision and can be expressed as a Legendre polynomial expansion, where the coefficients are the depolarisation moments. The correlation can be derived from the QCT calculations and is another vector property used in probing the PES, along with the DCSs just explored.

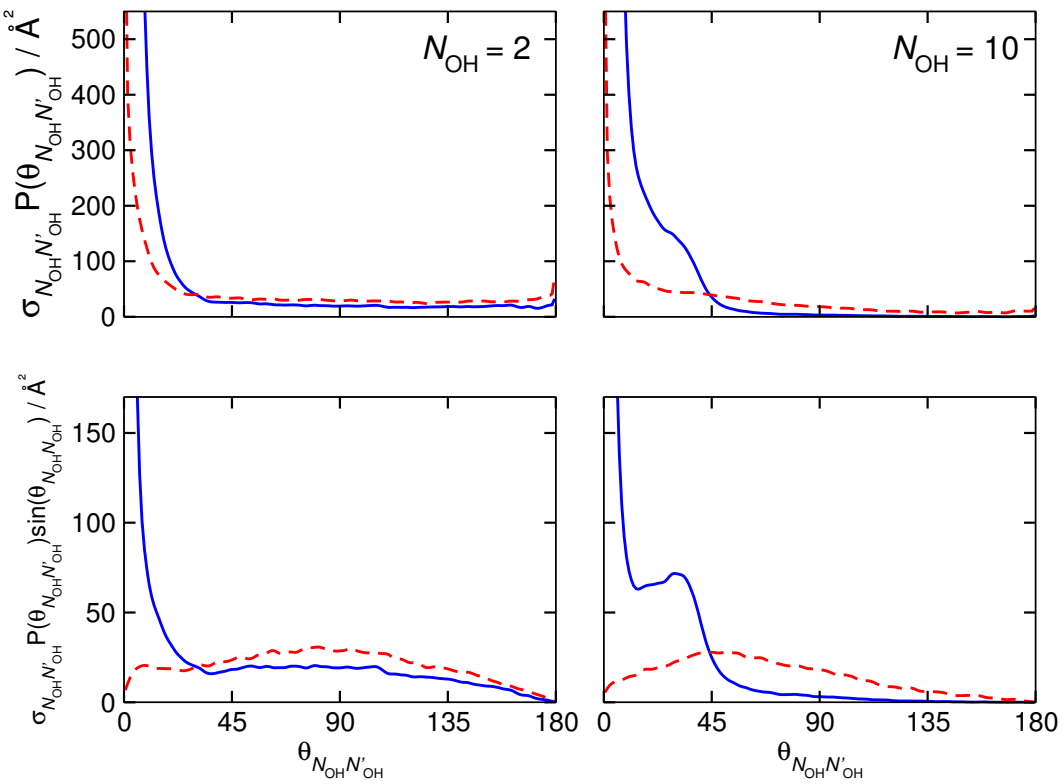

Figure 4.11: The upper and lower panels display in two different forms the $\boldsymbol{N}_{\mathrm{OH}}$-$\boldsymbol{N}'_{\mathrm{OH}}$ correlation as a function of $\theta_{N_{\mathrm{OH}}N'_{\mathrm{OH}}}$ analogous to the DCS. Red dashed lines are from trajectories that are inelastic in N_{OH} whilst the full blue lines are elastic. The left-hand panels show the results of cross sections with initial $N_{\mathrm{OH}} = 2$ and the right-hand panels $N_{\mathrm{OH}} = 10$. In both cases $N_{\mathrm{H_2}} = 1$.

Figure 4.11 demonstrates the $\boldsymbol{N}_{\mathrm{OH}}$-$\boldsymbol{N}'_{\mathrm{OH}}$ correlation in one of two ways: the upper panels as a function analogous to the DCS; the lower panels in a manner equivalent to that used for the DCS in the previous section where the DCS is multiplied by $\sin(\theta_{N_{\mathrm{OH}}N'_{\mathrm{OH}}})$. The correlations for elastic and inelastic OH(A) collisions are displayed for initial $N_{\mathrm{OH}} = 2$ and $N_{\mathrm{OH}} = 10$. The elastic collisions predominantly have small amounts of rotational tilt, associated with strong peaks near $\theta_{N_{\mathrm{OH}}N'_{\mathrm{OH}}} = 0°$. The flux at larger $\theta_{N_{\mathrm{OH}}N'_{\mathrm{OH}}}$ gives rise to elastic depolarisation. Above $\theta_{N_{\mathrm{OH}}N'_{\mathrm{OH}}} = 45°$ the correlation is larger for smaller N_{OH}, since it is easier to redirect the angular momentum of a slower rotating diatom by a larger angle. Small $\theta_{N_{\mathrm{OH}}N'_{\mathrm{OH}}}$ are more popular with inelastic collisions too, though to nowhere near the same extent. Indeed, the lower panels show correlations that resemble the $\sin(\theta_{N_{\mathrm{OH}}N'_{\mathrm{OH}}})$ weighting, indicating a fairly uniform

distribution of $\theta_{N_{\rm OH}N'_{\rm OH}}$ post collision and a randomisation of the angular momentum polarisation. This is to be expected when complex formation plays a substantial role in trajectories, as it does for inelastic collisions.

The correlation can also be resolved into the contributions from different rotational angular momenta transferred, $K_{\rm X}$, similar to the resolution of RET cross sections in $K_{\rm X}$ presented in figure 4.6. The upper panel of figure 4.12 shows the $\sin(\theta_{N_{\rm OH}N'_{\rm OH}})$ weighted angular momentum distribution associated with a particular inelastic collision ($N_{\rm OH} = 2 \rightarrow N'_{\rm OH} = 3$) on the right, and the elastic collision
($N_{\rm OH} = 2 \rightarrow N'_{\rm OH} = 2$) on the left. The figure resolves the distributions into contributions from different $K_{\rm OH}$. Note that each value of $K_{\rm OH}$ corresponds to a particular region of the $\boldsymbol{N}_{\rm OH}$-$\boldsymbol{N}'_{\rm OH}$ angular momentum distribution, just as would be expected given the relationship in equation 3.60. Note also that $K_{\rm OH} = 0$ regions are purely elastic in the QCT analysis, and hence cannot be converged.

4.3.1 Role of H_2

The lower panels of figure 4.12 show the $\boldsymbol{N}_{\rm OH}$-$\boldsymbol{N}'_{\rm OH}$ correlation for the same transitions, but this time resolved into angular momentum transfer in the H_2 molecule, $K_{\rm H_2}$. Again, the initial state of H_2 is $N_{\rm H_2} = 1$. When $K_{\rm H_2} > 0$ there is no difference between the shapes of the distributions in each panel, each largely reflects the $\sin(\theta_{N_{\rm OH}N'_{\rm OH}})$ weighting. This suggests that when there is angular momentum transfer in H_2, there is almost complete randomisation of the direction of $\boldsymbol{N}'_{\rm OH}$ in the accompanying OH(A) collider. The progressively smaller size of the correlations with increasing $K_{\rm H_2}$ is a reflection of the smaller cross sections for larger $K_{\rm H_2}$ values (see figure 4.6). When $K_{\rm H_2} = 0$, such that there is no rotational angular momentum transfer in H_2, the
OH(A)+H_2 collision becomes analogous to an atom-diatom collision. With such collisions, there is a strong propensity for only a small change in the direction of $\boldsymbol{N}_{\rm OH}$.

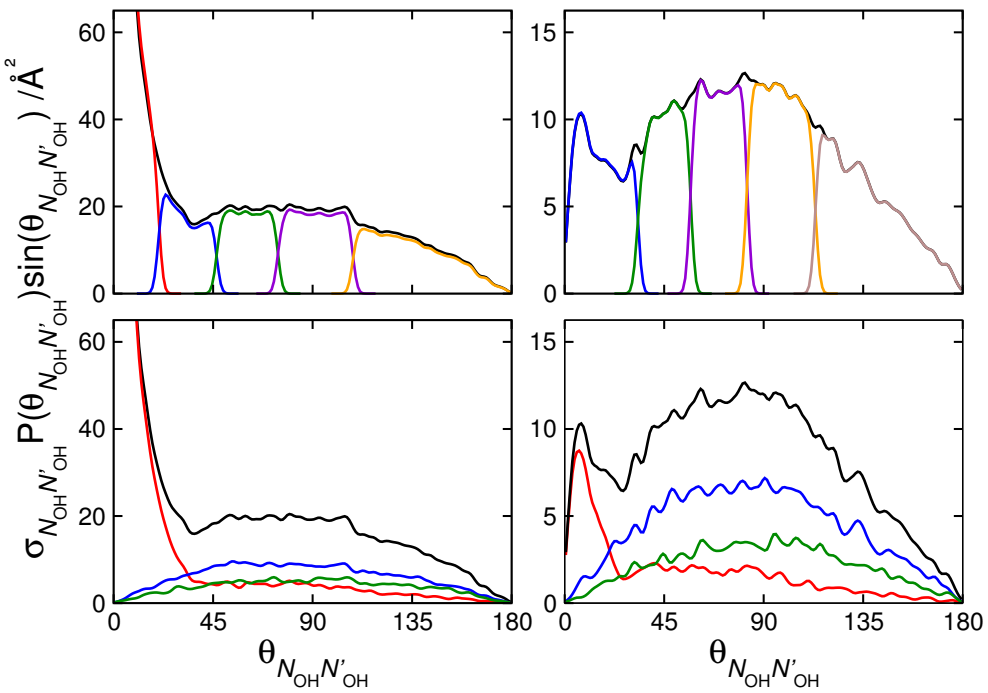

Figure 4.12: Upper panels: $\boldsymbol{N}_{\mathrm{OH}}$-$\boldsymbol{N}'_{\mathrm{OH}}$ correlations for the elastic collision $N_{\mathrm{OH}} = 2 \rightarrow N'_{\mathrm{OH}} = 2$ (left-hand panel) and the inelastic collision $N_{\mathrm{OH}} = 2 \rightarrow N'_{\mathrm{OH}} = 3$ (right) for initial state $N_{\mathrm{H_2}} = 1$ resolved in K_{OH}. Each total $\boldsymbol{N}_{\mathrm{OH}}$-$\boldsymbol{N}'_{\mathrm{OH}}$ correlation is shown in black. The contribution from $K_{\mathrm{OH}} = 0$ is shown in red, $= 1$ in blue, $= 2$ in green, $= 3$ in purple, $= 4$ in orange and $= 5$ in beige. Lower panels: The same correlations as the upper panels for the left-hand and right-hand side but this time resolved in $K_{\mathrm{H_2}}$. The total $\boldsymbol{N}_{\mathrm{OH}}$-$\boldsymbol{N}'_{\mathrm{OH}}$ correlation is shown in black. The contribution from $K_{\mathrm{H_2}} = 0$ is shown in red, $= 1$ in blue, and $= 2$ in green.

According to the QCT calculations, when RET occurs in OH(A) following a collision in which no angular momentum transfer takes place in H_2, there is very little accompanying OH(A) depolarisation. Typically collisions that lead to depolarisation in one diatom have depolarisation in the other. It is likely that this is a consequence of the large number of trajectories that proceed with complex formation, since, when the complex breaks up, the randomisation of the angular momentum for both diatoms should be expected. The $K_{\mathrm{H_2}} = 0$ collisions are likely the smaller number of trajectories that contribute to RET following more glancing collisions that are affected by longer range attractive forces as discussed in subsection 4.2.1. Indeed, the contribution of $K_{\mathrm{H_2}} = 0$ collisions to RET diminishes at higher N_{OH} as shown in figure 4.6, where long range attractive interactions do not lead to RET.

4.3.2 Depolarisation Moments - Open Shell

The first two depolarisation moments that describe the $\boldsymbol{N}_{\rm OH}$-$\boldsymbol{N}'_{\rm OH}$ correlation are of interest as they correspond with the disorientation, $a^{(1)}$, and disalignment, $a^{(2)}$, of $\boldsymbol{N}_{\rm OH}$ following a collision. Figure 4.13 displays open shell depolarisation moments associated with $j_{\rm OH} \rightarrow j'_{\rm OH}$ collisions as a function of final $N'_{\rm OH}$. The cross sections are split into those that are accompanied by a change in the spin-rotation level, and those in which the spin-rotation level is conserved. Cross sections are also resolved into initial f_1 and f_2 spin-rotation levels.

The spin-rotation changing collisions typically have smaller depolarisation moments, indicating that these collisions are more depolarising. On average, in order to change the spin-rotation level a larger angle, $\theta_{N_{\rm OH}N'_{\rm OH}}$, must accompany the scattering, leading to a smaller depolarisation moment. The difference in the moments is more pronounced for disorientation than disalignment. Consider that, if $\theta_{N_{\rm OH}N'_{\rm OH}} = 180°$, the orientation is reversed and the disorientation moment, $a^{(1)} = -1$, however, the alignment is unchanged and $a^{(2)} = 1$. Collisions with $\theta_{N_{\rm OH}N'_{\rm OH}} = 180°$ are always spin-rotation changing and always lead to large disorientation moments whilst maintaining alignment. A rotational tilt of 180° is an extreme case, but on average spin-rotation changing collisions will give larger amounts of disorientation than disalignment. Consequently, the difference in moments between spin-rotation changing and spin-rotation conserving collisions is more dramatic for orientation than alignment.

Moments are generally more positive (less depolarising) for f_1 than f_2 spin-rotation levels, particularly for spin-rotation conserving collisions. This arises for geometric reasons; since the angle between $\boldsymbol{N}_{\rm OH}$ and $\boldsymbol{j}_{\rm OH}$ is larger in f_2 ($\boldsymbol{j} = \boldsymbol{N} - \boldsymbol{S}$) than in f_1 ($\boldsymbol{j} = \boldsymbol{N} + \boldsymbol{S}$) spin-rotation levels, there is a greater depolarisation of $\boldsymbol{j}_{\rm OH}$ for a given $\theta_{N_{\rm OH}N'_{\rm OH}}$ in f_2 than f_1.

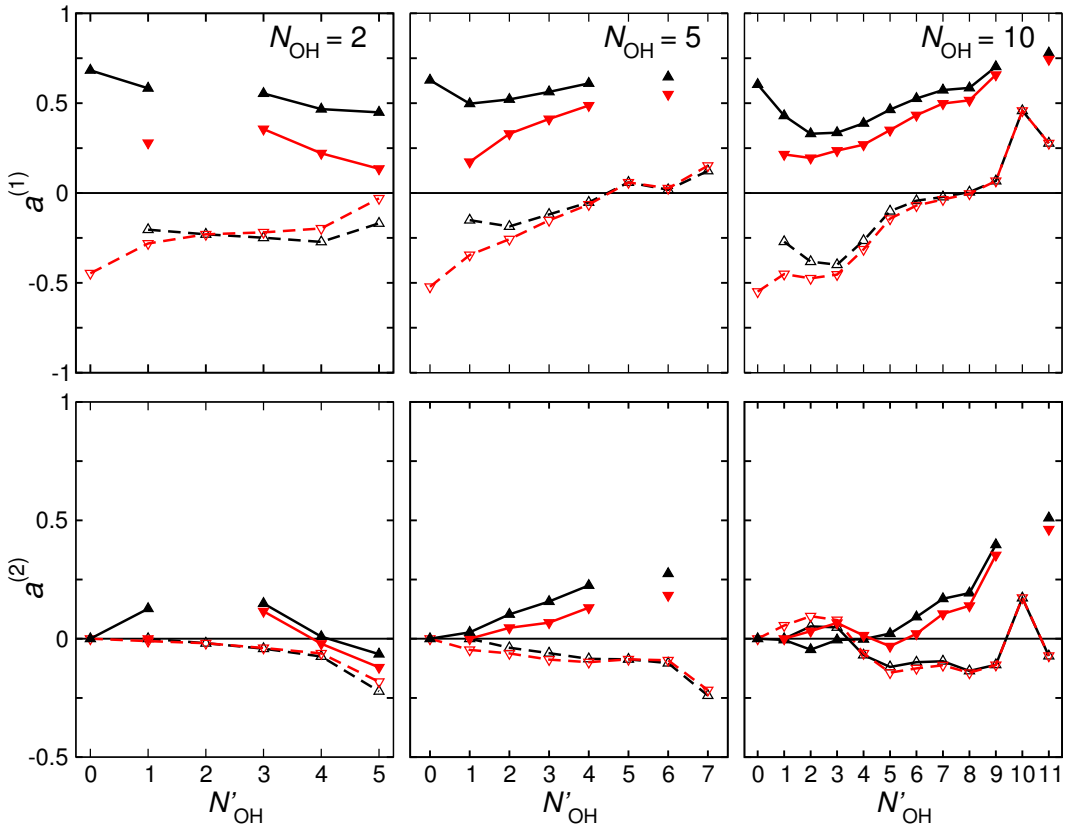

Figure 4.13: Depolarisation moments accompanying various $j_{OH} \rightarrow j'_{OH}$ collisions calculated using an open shell analysis of the QCT calculations on the OH(A)+H_2 collision system. The top row are disorientation moments, $a^{(1)}$, and the bottom row disalignment moments, $a^{(2)}$. Upwards pointing black triangles are data derived from states initially in the f_1 spin-rotation level and downwards pointing red triangles to f_2 spin-rotation levels. The full coloured triangles connected by complete lines are cross sections for processes that conserve the spin-rotation level but only change N_{OH} to N'_{OH}, whilst open triangles connected by dashed lines are spin-rotation changing collisions that change between spin rotation manifolds during the collision. Cross sections are displayed with various initial rotational levels, $N_{OH} = 2$ (left), 5 (middle) and 10 (right). All data are colliding with $N_{H_2} = 1$.

The figure also illustrates the moments as a function of final rotational angular momentum, N'_{OH}, for different starting N_{OH}. Orientation and alignment moments generally decrease with increasing ΔN_{OH}, indicating that collisions with a greater degree of accompanying RET are more depolarising. As already discussed, these trajectories are more likely to have involved the formation of short-lived complexes, which on break up, randomise the direction of the angular momentum polarisation. This pattern of smaller polarisation moments (or, more accurately, closer to zero moments) for larger ΔN_{OH} is

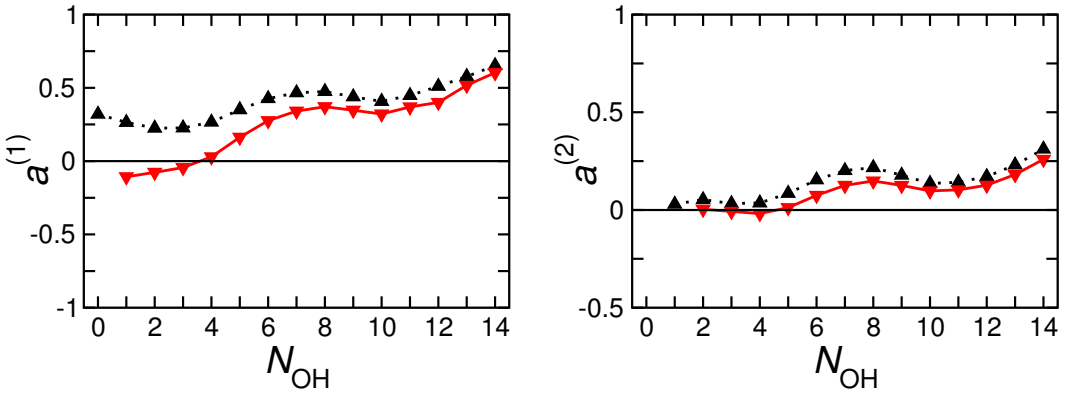

Figure 4.14: Total inelastic depolarisation moments for $j_{OH} \rightarrow j'_{OH}$ collisions where $j'_{OH} \neq j_{OH}$ determined from QCT calculations for the OH(A)+H_2 system with $N_{H_2} = 1$. The left-hand panel shows depolarisation moments for orientation, $a^{(1)}$, and the right-hand panel for alignment, $a^{(2)}$. In both figures, upwards pointing black triangles connected by dotted lines relate to the f_1 spin-rotation level ($j_{OH} = N_{OH} + S$), and downwards pointing red triangles connected by full lines the f_2 spin-rotation level ($j_{OH} = N_{OH} - S$).

more pronounced with spin-rotation conserving collisions, since spin-rotation changing collisions typically require a larger degree of depolarisation regardless of ΔN_{OH}.

Figure 4.14 presents the total inelastic depolarisation moments for different initial N_{OH}, effectively derived from a weighted average of the depolarisation moments in the previous figure. The figure shows moments from initial f_1 and f_2 spin-rotation manifolds and, as expected from the previous figures, the moments are smaller in the case of f_2. In general, at low N_{OH}, the depolarisation moments are close to 0. This indicates that the angular momentum polarisation is effectively randomised following these collisions. The result is an isotropic distribution of $\boldsymbol{N}'_{OH}$. At higher N_{OH} the moments become progressively more positive as collisions become less depolarising. This can be seen for $N_{OH} = 10$ in figure 4.11, where inelastic collisions are more likely to involve smaller than larger $\theta_{N_{OH}N'_{OH}}$ (it is still a fairly isotropic distribution). This is demonstrated by the fact that the peak in the distribution shown in the lower panel for $N_{OH} = 10$ is at $\sim 45°$, as opposed to in the $N_{OH} = 2$ distribution where the peak is at $\sim 90°$. This pattern reflects the fact that it is harder to change the direction of the rotational angular momentum of a faster rotating diatom. However, even at

$N_{\mathrm{OH}} = 14$, collisions are extremely disaligning, and orientation is by no means conserved (for which $a^{(1)}$ would equal unity). The figure demonstrates clearly that, even at higher N_{OH}, collisions are relatively depolarising, as would be expected for a system described by an extremely anisotropic and attractive potential.

4.4 Opacity Functions

Figure 4.15 displays opacity functions $P(b)$ from closed shell QCT calculations for collisions starting in $N_{\mathrm{OH}} = 2$, 5 and 10. The upper panel shows opacity functions for RET, $P^{(0)}(b)$, along with inelastic disorientation, $P^{(1)}(b)$, and inelastic disalignment, $P^{(2)}(b)$. The depolarisation opacity functions are related to the RET opacity functions via

$$P^{(k)}(b) = P^{(0)}(b)(1 - a^{(k)}). \tag{4.7}$$

The lower panel gives opacity functions for elastic collisions $P^{(0)}(b)$. Unlike the inelastic cross sections, these do not fall to 0 at large b, reflecting the inability to converge elastic cross sections classically. The panel also gives depolarisation opacity functions accompanying these elastic collisions.

The opacity functions reflect the fall in RET cross section with N_{OH}. The functions also demonstrate that this is a consequence both of a reduction in the probability of inelastic collisions at all b, and a restriction of inelastic collisions to a progressively smaller range of collision parameters. At the smallest of impact parameters, there is a steep increase in $P^{(0)}(b)$ for inelastic collisions tending to 1 at $b = 0$, indicating inelastic collisions are the only outcome from head-on trajectories. Aside from this feature though, the probability of an inelastic versus elastic collision is fairly uniform over the range of b that inelastic collisions are observed. This insensitivity to the impact parameter may indicate that on this highly anisotropic surface the trajectories are drawn

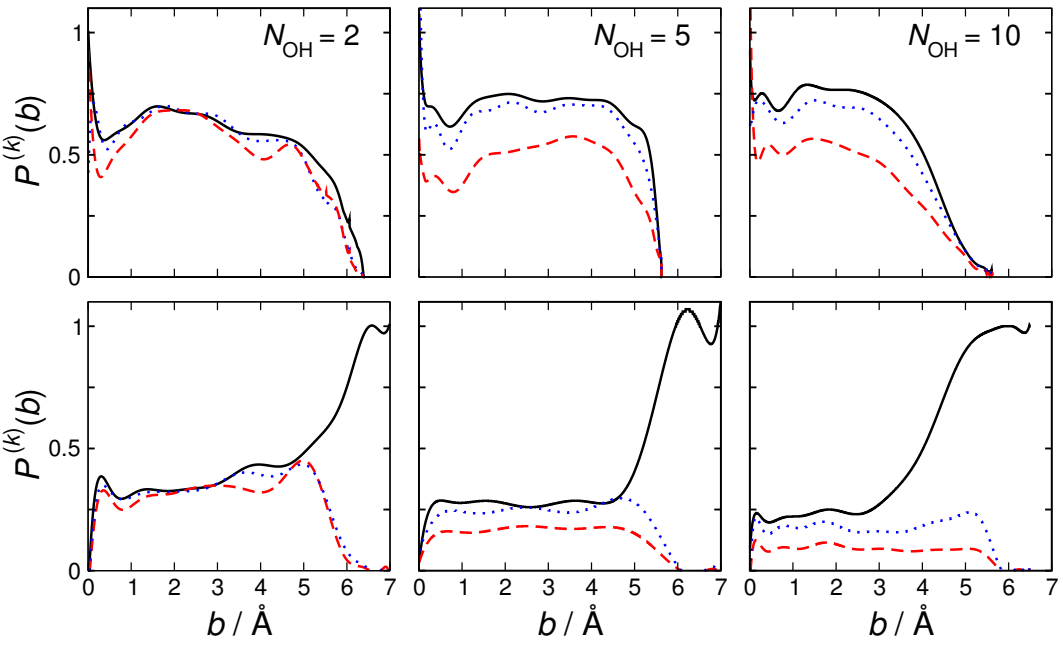

Figure 4.15: The top panels give opacity functions for collisions that are inelastic in terms of N_{OH} and the bottom panels opacity functions for collisions that are elastic. This assessment follows a closed shell treatment of QCT calculations on the OH(A)+H_2. Black complete lines are for opacity functions for either inelastic or elastic collisions, $P^{(0)}(b)$. The red dashed line are opacity functions associated with disorientation cross sections, $P^{(1)}(b)$, and the blue dotted line an opacity function associated with disalignment cross sections, $P^{(2)}(b)$. The initial N_{OH} is varied in the panels from left to right panels, and in all cases $N_{\mathrm{H_2}} = 1$.

to the same (deeply attractive) regions of the PES regardless of this initial condition, and the outcomes of the trajectories are similar. This conclusion was also reached in considering the deflection functions, which demonstrated that complex formation involving specific regions of the PES occurred irrespective of the impact parameter. The opacity functions for depolarisation, $P^{(1)}(b)$ and $P^{(2)}(b)$, are also fairly uniform over this range of b in both elastic and inelastic cases. Note also that the probability of a collision being inelastic is high over the range of b for which they are possible, with greater than 50% of all collisions having an inelastic outcome.

The inelastic and elastic opacity functions, $P^{(0)}(b)$, necessarily sum to unity for a given b. Consequently, at large b, when inelastic collisions are no longer possible, the elastic opacity functions tend to 1. However, the degree of depolarisation accompanying

these elastic collisions typically begins to fall as the proportion of elastic collisions as a whole increases. Regardless of N_{OH}, above approximately 6 Å there is no accompanying depolarisation with elastic collisions and the collisions are purely elastic.

4.5 Depolarisation Cross Sections

Total depolarisation cross sections with varying initial N_{H_2} and N_{OH} are shown in figure 4.16, and allow for comparison with experimental results. The cross sections include contributions from elastic and inelastic depolarisation. The latter contributions are dependent on the inelastic depolarisation moments and the RET cross sections, consequently these cross sections largely reflect patterns already discussed.

The differences between OH(A) total depolarisation cross sections with different

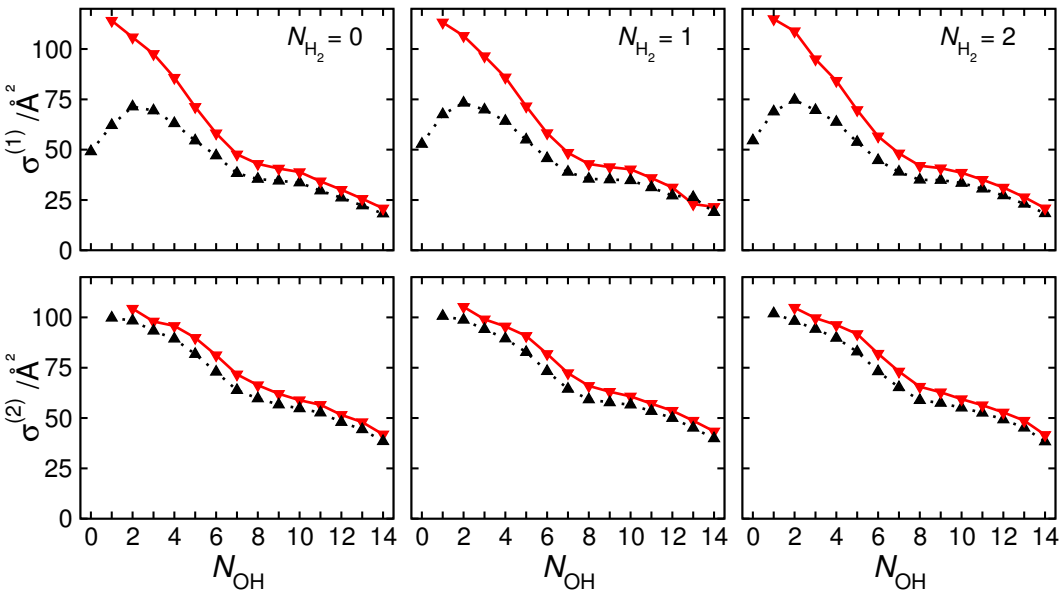

Figure 4.16: Open shell total depolarisation cross sections for the OH(A) radical from OH(A)+H_2 QCT calculations. The initial N_{OH} and N_{H_2} are shown. The upper panels are for disorientation and the lower disalignment. Black upwards pointing triangles connected by dotted lines are for OH(A) radicals beginning in the f_1 spin-rotation manifold, whilst red downwards pointing arrows connected by full lines begin in the f_2 spin-rotation manifold. $N_{H_2} = 0$ (left), $= 1$ (middle) and $= 2$ (right).

initial N_{H_2} are negligible. The slight differences in RET cross sections observed for $N_{H_2} = 0$ compared to other N_{H_2} in figure 4.4 have not translated to any differences in the depolarisation cross sections, indicating that the reduced amount of depolarising RET collisions for $N_{H_2} = 0$ at low N_{OH} is compensated for by increased elastic depolarisation. The depolarisation cross sections are larger for f_2 than f_1, reflecting patterns seen for depolarisation moments and RET cross sections. This difference is comparatively small for disalignment compared to disorientation, due to both the smaller differences between f_1 and f_2 inelastic disalignment moments and the lack of both f_1 and f_2 disalignment cross sections at $N_{OH} = 0$ and 1 (where the differences in RET cross sections between f_1 and f_2 are at their greatest).

The depolarisation cross sections fall with increasing N_{OH} as it becomes progressively harder to change the direction of rotation of a faster rotating diatom, and because rotational averaging of the PES reduces the number of complex forming trajectories (likely to be highly depolarising). f_1 disorientation cross sections rise initially between $N_{OH} = 0$ and 2, before falling. This pattern reflects that seen for RET cross sections in figure 4.7, and the lack of contributions from pure spin-rotation changing collisions when $j_{OH} = 0.5$, $N_{OH} = 0$. This relationship between f_1 disorientation cross sections and N_{OH} has been seen with other OH(A) collision systems before, including Kr [111] and Ar [37].

4.5.1 Elastic versus Inelastic

Figure 4.17 separates the elastic and inelastic contributions to depolarisation as a function of the initial OH(A) radical angular momentum. In these calculations, the initial rotational angular momentum state of H_2 is $N_{H_2} = 1$.

For all N_{OH}, inelastic depolarisation is the larger of the two contributions to the total depolarisation. The elastic contributions become relatively more important at

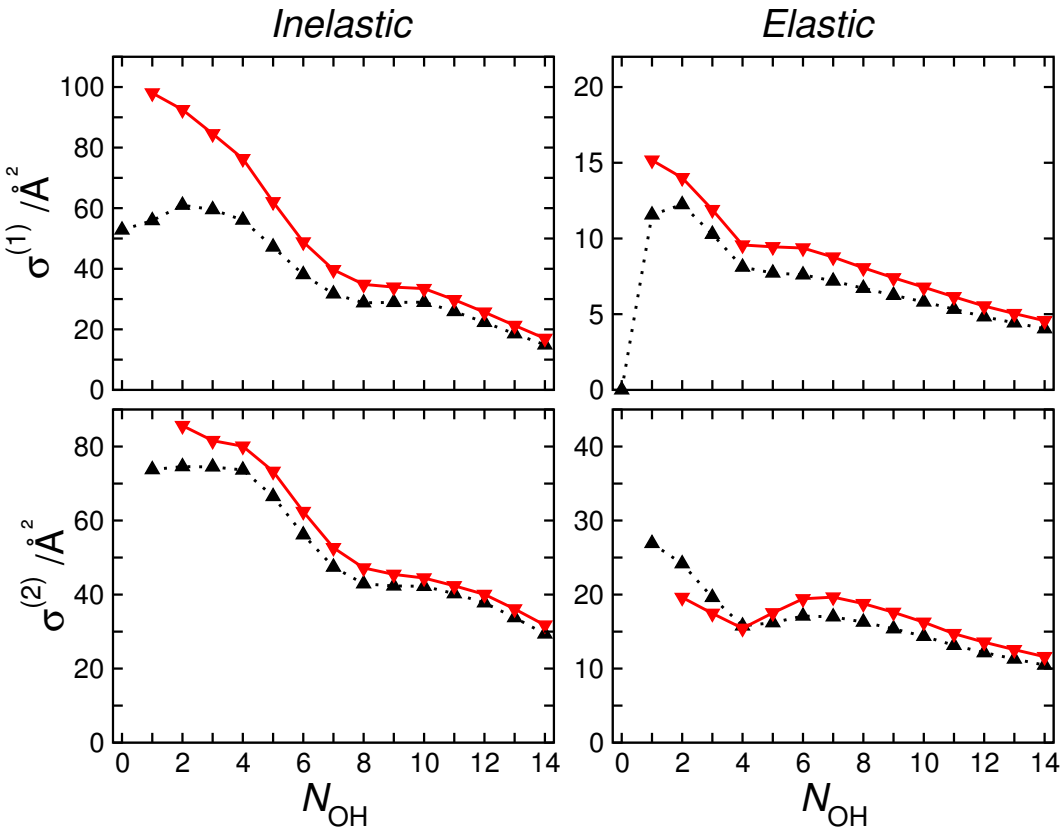

Figure 4.17: Open shell collisional depolarisation cross sections resolved into initial OH(A) rotational state with initial $N_{H_2} = 1$. Upwards pointing black triangles connected by dotted lines relate to the f_1 spin-rotation level, and downwards pointing red triangles connected by full lines the f_2 spin-rotation level. The top row are the disorientation cross sections and the bottom row disalignment. The left column shows the inelastic depolarisation cross sections and the right column the elastic depolarisation.

higher N_{OH}. This is as seen in other systems previously, and results largely from falling levels of RET at higher N_{OH}, whilst the collisions remain very depolarising.

The elastic disorientation cross section at $N_{OH} = 0$ for f_1 is necessarily zero, as the only contribution to the angular momentum is the intrinsic spin of the electron, $\boldsymbol{S}$, which is a spectator in the QCT treatment. Generally, elastic depolarisation cross sections fall with N_{OH} - the faster rotating OH(A) diatom is harder to knock out of its rotational plane even if there is no accompanying RET. This factor is more important than the increasing amount of elastic collisions at higher N_{OH}. This pattern differs from that with a Kr collider [111], where the elastic depolarisation cross sections are

constant. This is likely because the degree of RET holds up better as N_{OH} increases with an H_2 collider, as discussed in section 4.1. Elastic disalignment cross sections are uniformly larger than their disorientation counterparts since it is easier to change the plane of rotation than its sense, with a smaller $\theta_{N'_{\mathrm{OH}}N_{\mathrm{OH}}}$ rotational tilt being required.

4.6 Summary

The extremely attractive and anisotropic PES that describes the OH(A)+H_2 collision system leads to a high degree of OH(A) angular momentum depolarisation upon collision. Both the $\boldsymbol{k}$-$\boldsymbol{k}'$ and $\boldsymbol{N}_{\mathrm{OH}}$-$\boldsymbol{N}'_{\mathrm{OH}}$ correlations indicate that collisions that lead to the formation of short lived complexes in deep potential wells are extremely important, and plots of the deflection function and delay time demonstrated the presence of these kinds of collision. The availability of rotational energy from the colliding H_2 diatom leads to a larger degree of RET in OH(A) than seen in QCT studies with atomic colliders [37, 111, 114, 116]. The H_2 also allows for a high degree of RET to be maintained at larger N_{OH}. Since a high degree of RET is sustained at high N_{OH}, elastic depolarisation has a smaller role to play than previously seen with atomic colliders [37, 111, 114, 116]. The opacity functions have shown that collisions are extremely depolarising across a range of impact parameters.

The degree of depolarisation and RET in the OH(A) diatom is mostly independent of the initial rotational level of H_2, yet a degree of correlation is seen in the energy and momentum transfer between the two diatoms during a collision. There is limited RET observed in the H_2 diatom, although, when it is observed, there is a propensity for anti-correlated RET in the OH(A) diatom. Most OH(A) RET collisions see no accompanying RET in the H_2, though there is usually some accompanying angular momentum transfer in H_2, i.e. depolarisation. Likewise, depolarisation in OH(A) is most often accompanied by depolarisation in the H_2 diatom. The conclusion of these

findings is that, within this QCT analysis, the H_2 does not behave like an atomic collider. This is to be expected when the PES describing the system is so anisotropic with respect to rotation of either diatom, and the formation of complexes plays a large role in the collision dynamics.

Chapter 7 expands this analysis of the QCT results, and explores the usefulness of the QCT methodology in understanding this collision system. Cross sections determined from these QCT calculations will be compared with those measured from the experiments set out in the next chapter. The QCT calculations are adiabatic and so do not allow for electronic quenching. However, in chapter 7, the extent to which trajectories enter regions of the PES associated with quenching is explored. Finally, chapter 7 considers alternative methods for binning the final angular momentum based upon a Gaussian weighting rather than a histogram binning treatment.

Chapter 5

OH(A)+H_2 Experimental Method

A laser-induced fluorescence (LIF) technique has been used to determine collision cross sections associated with the dynamics of the thermal OH(A)+H_2 system. Through recording the fluorescence decay of the excited OH(A) radical at different collider pressures, cross sections for quenching and rotational energy transfer (RET) can be found.

Polarised light has been used to create a polarised angular momentum distribution in the excited state as set out in section 1.6. This polarisation is changed following collisions, as set out in this chapter. Section 1.7 introduced the Zeeman quantum beat spectroscopy (ZQBS) technique, whilst chapter 2 demonstrated its use in measuring the angular momentum polarisation of OH(X) fragments following H_2O_2 photolysis. Here ZQBS is a tool for exploring collision dynamics, specifically collisional depolarisation. This technique has been used in this way before in investigating the collisional depolarisation of the NO(A) radical with He and Ar [264], and the OH(A) radical with Ar [57, 114], Kr [111] and water [21]. As explored in section 1.7, the technique is reliant upon excitation with a laser pulse of finite duration and energy levels that are closely spaced. The use of a monochromator has allowed the collisional depolarisation to be resolved into elastic and inelastic contributions.

5.1 Effect of Collisions on a Polarised Distribution of Angular Momentum

Section 1.6 derived a general expression for the angular momentum polarisation in the lab-frame created by polarised light. The final expression was given in equation (1.37) as

$$P(\theta_j) = \frac{1}{2}[1 + 3r_0^{(1)}(j)P_1(\cos\theta_j) + 5r_0^{(2)}(j)P_2(\cos\theta_j)]. \tag{5.1}$$

In this chapter there is an interest in the polarisation in the lab-frame following a collision, $P(\theta_{j'})$, in order to evaluate this the above distribution is combined with that for the rotational tilt, $P(\theta_{jj'})$, discussed in subsection 1.4.2 giving [55]

$$P(\theta_{j'}) = \int_0^\pi P(\theta_j)P(\theta_{jj'})\sin\theta_j \mathrm{d}\theta_j. \tag{5.2}$$

Evaluating this integral and considering the $\boldsymbol{j}$-$\boldsymbol{j}'$ correlation given in equation (1.24) leads to [37]

$$P(\theta_{j'}) = \frac{1}{2}\sum_k [k]a^{(k)}(j', j)r_0^{(k)}(j)P_k(\cos\theta_{j'}). \tag{5.3}$$

The polarisation moments describing the distribution of $\boldsymbol{j}'$ after the collision, equivalent to the $h_0^{(k)}$ moments in equation (1.19), are labelled $\rho^{(k)}$. Comparing the above expression with equation (1.19) makes clear that the $\rho^{(k)}$ moments are the product of the extrinsic polarisation parameters arising from the initial creation of a polarised distribution, and the depolarisation moments that define the $\boldsymbol{j}$-$\boldsymbol{j}'$ correlation in the molecular-frame, i.e.

$$\rho^{(k)}(j') = a^{(k)}(j', j)r_0^{(k)}(j). \tag{5.4}$$

The experiments performed here only probe the dipolar and quadrupolar polarisation moments, $\rho^{(1)}(j')$ and $\rho^{(2)}(j')$, and the distribution reduces to

$$P(\theta_{j'}) = \frac{1}{2}[1 + 3a^{(1)}(j', j)r_0^{(1)}(j)P_1(\cos\theta_{j'}) + 5a^{(2)}(j', j)r_0^{(2)}(j)P_2(\cos\theta_{j'})]. \quad (5.5)$$

Unlike in the QCT studies, which are restricted to single collisions, following excitation the radicals can undergo multiple collisions before fluorescing, or being electronically quenched, to the ground state. In the simple case of elastic collisions, after undergoing n such collisions the $\boldsymbol{j}'$ distribution can be expressed as

$$P(\theta_{j'}; n) = \frac{1}{2}\left[1 + 3r_0^{(1)}[a^{(1)}(j, j)]^n P_1(\cos\theta_{j'}) + 5r_0^{(2)}[a^{(2)}(j, j)]^n P_2(\cos\theta_{j'})\right]. \quad (5.6)$$

In actuality, the collisions are a mix of elastic and inelastic in nature. The pseudo-first-order rate constant for any collision $j \to j'$ may be written as

$$k'_{j\to j'} \equiv k_{j\to j'}[\mathrm{Q}], \quad (5.7)$$

where $k_{j\to j'}$ is the rate constant and [Q] the collider gas pressure.

Collisions can be modelled by a Poisson distribution [57] with the probability of n collisions inducing $j \to j'$ in time t given by

$$P(n \mid t) = \frac{(k'_{j\to j'})^n}{n!}\exp(-k'_{j\to j'}t). \quad (5.8)$$

In the absence of population decay, polarisation of rank k decays according to [57]

$$\begin{aligned}\rho^{(k)}(j) &= \sum_n P(n \mid t) r_0^{(k)}(j)[a^{(k)}(j)]^n \\ &= r_0^{(k)}(j) \sum_n \frac{(k'(j))^n}{n!} \exp(-k'(j)t)[a^{(k)}(j)]^n \\ &= r_0^{(k)}(j) \exp(-k'(j)t) \sum_n \frac{(k' a^{(k)}(j))^n}{n!}, \end{aligned} \tag{5.9}$$

where weighted averages for all collisions $j \rightarrow j'$ are taken to give the depolarisation moments, $a^{(k)}(j)$ and rate constant, $k'(j)$. Since the sum is a Taylor expansion of an exponential it follows that [57]

$$\rho^{(k)} = r_0^{(k)} \exp[-k'(1 - a^{(k)})t], \tag{5.10}$$

where the j in parentheses has been dropped for further simplicity. This demonstrates that the rate constant for depolarisation, $k_d^{(k)}$, is equivalent to $k'(1 - a^{(k)})$. Note that here elastic and inelastic contributions to the depolarisation are included.

Collision cross sections are more intuitive than pseudo-first-order rate constants and are the property that has been calculated in the accompanying theoretical results presented in chapter 4. As discussed in section 1.2, assuming the collision cross section is independent of the mean relative velocity of the system, a rate constant k can be converted via [22, 272]

$$\sigma \approx \frac{k}{\upsilon_{\text{rel}}}. \tag{5.11}$$

It follows that $\sigma_d^{(k)} = \sigma(1 - a^{(k)})$, and this result was used in calculating depolarisation cross sections in QCT calculations as detailed in section 3.3.4. Here this equivalence has been demonstrated classically but can also be arrived at through quantum mechanics with the consideration of state multipoles and tensor cross sections (see reference [169]) and this result was stated earlier in equation (1.30).

5.2 Experimental Apparatus

The basic experimental arrangement is shown in figure 5.1. The lasers and reaction chamber are the same as those used for the H_2O_2 studies described in chapter 2. Polarised light is used to create a polarised angular momentum distribution of OH(A) radicals which precesses in the presence of a magnetic field. Fluorescence from this distribution is similarly polarised and the intensity of the fluorescence decay signal contains a quantum beat since it is observed via a polariser. The fluorescence decay is recorded for a variety of accompanying H_2 collider pressures and on evaluating the rate of loss of polarisation and population, depolarisation and quenching cross sections can be determined.

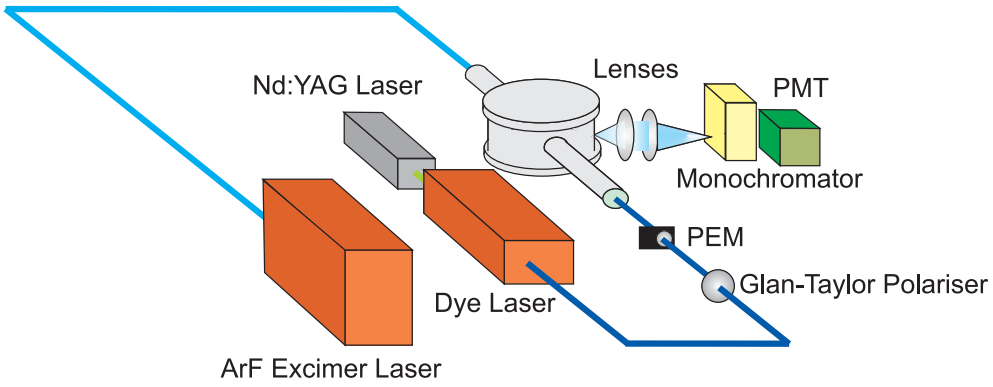

Figure 5.1: Experimental set-up for OH(A)+H_2 experiments.

As described in chapter 2, a magnetic field is produced by a pair of Helmholtz coils at the centre of the reaction chamber. Fields in the range from 0 to 30 Gauss are generated for these experiments. The strength of the field chosen reflects a careful balancing of factors. Firstly, the field must not be so large that the magnetic sub-levels are too separated for coherent excitation by the laser. Conversely, the Larmor frequency must be sufficiently large that the polarisation completes at least one, but preferably three or four, revolutions during the time that the fluorescence decay is detectable i.e. the beat period should be less than the fluorescence lifetime. However, the beat period

must be sufficiently large, and the field sufficiently small that a quantum beat can be resolved by the PMT. Collectively these factors mean beat periods should be of the order of 100 ns, with the exact field strength chosen dependent on the spin-rotation level excited N, j. The coils are rotated when switching between orientation and alignment measurements. For alignment experiments the field axis is parallel to the detection direction [21], and is perpendicular for orientation experiments [83].

5.2.1 Introduction of Collision Partners - OH(A) and H_2

Unlike previous experiments with NO(A) [72, 264], the OH(A) radical is not stable and must be made in-situ from a suitable precursor. This precursor was usually hydrogen peroxide; however, in cases where signal was limited, nitric acid was used.

A 50:50 mixture of water and hydrogen peroxide, H_2O_2, or a 70:30 mixture of water and nitric acid, HNO_3, is prepared in a fume hood and added to a 250 ml vacuum-sealed glass bomb. The bomb is attached to the vacuum chamber via a teflon tube, and entry into the chamber is controlled by an inlet valve. The pressure in the chamber is below the vapour pressure of the water, acid and peroxide, so the gases slowly enter. The partial pressure of the gas from the bomb is maintained below 5 mTorr throughout the experiments, this way the collider gas is vastly in excess. A pump-probe laser process is used to generate OH radicals in their first excited state, OH(A $^2\Sigma^+$). The pump laser initially photolyses the peroxide or acid before the probe laser excites the resultant OH(X $^2\Pi$) radicals to OH(A).

H_2 collider gas flows into the chamber via an inlet valve. A series of three needle valves are used to control the partial pressure of the collider gas in the chamber. In order to determine collision cross sections for depolarisation, rotational energy transfer and quenching experiments are repeated at a variety of partial pressures, typically six over the range 100-600 mTorr.

5.2.2 Laser System

OH(X $^2\Pi$) ground state radicals are produced following the photolysis of H_2O_2, as described in chapter 2 and in references [55, 208, 219, 224], or HNO_3 as described in references [277, 278], using a 193 nm laser. This wavelength is generated by an ArF excimer laser. The photolysis gives a mix of OH(A) and OH(X) products in the case of HNO_3 photolysis, but purely OH(X) products in the case of H_2O_2. Additionally, the products of photolysis are translationally hot. Leaving a delay of 20 μs between this pump laser and a subsequent probe laser allows for translational moderation of the radicals through collisions with the H_2 collider [21]. The translational moderation of the radicals was modelled using a simple hard sphere model developed previously [21, 279], and the 20 μs delay time found to be more than sufficient. This delay also allows OH(A) radicals produced via photolysis to relax to their ground state. As a consequence of this delay the probed OH(X) radicals have thermal translational energies and all OH(A) radicals result from the probe laser.

These OH(X) radicals are excited to their first electronic excited state, OH(A $^2\Sigma^+$), in a range of different spin-rotation levels. This is achieved via probing a variety of (A $\leftarrow$ X) transitions in the range 306-309.5 nm using the tunable dye laser described in chapter 2. The finite pulse time of the laser leads to a coherence width due to the restrictions of energy-time uncertainty. In this experiment the pulse duration is approximately 5 ns, giving a coherence width of 30 MHz, and any levels separated by less than this can potentially be coherently excited, provided both levels are accessible according to optical selection rules. The coherence width of the laser is sufficient for the coherent excitation of Zeeman sub-levels in OH(A) radicals upon the application of a magnetic field 1-30 Gauss in magnitude.

As in the H_2O_2 photolysis experiment, the lasers enter the vacuum chamber through silica windows in counterpropagating directions. The flat silica window at the entry

point for the excimer laser is replaced with a slanted window in these collision experiments. This window prevents the reflection of the probe beam back into the chamber upon exit and since the excimer laser does not need to be plane polarised its impact on the polarisation of the pump beam can be ignored. The light from the dye laser is partially linearly-polarised, but it passes through a Glan-Taylor polariser on its route to entering the reaction chamber which purifies the initial polarisation. Further along the path to the reaction chamber the probe laser passes through a photoelastic modulator (PEM) which flips the laser polarisation on alternate shots. The potential applied to the PEM is selected depending upon whether orientation or alignment is being studied, flipping on alternate laser shots between left- and right-circularly-polarised light for orientation or vertically and horizontally polarised light for alignment studies. The necessary PEM setting is found by observing the quality of the separation of the two polarisations after the light passes through a Rochon polariser in the case of alignment, or a Fresnel rhomb and Rochon polariser in the case of orientation.

5.2.3 Detection and Data Recording

OH(A) radicals fluoresce back to their ground electronic state and, as in the H_2O_2 photolysis experiments, this fluorescence is focused onto the entrance of a monochromator. Subsequent to the focusing lenses but prior to the monochromator the fluorescence passes through one or two polarisers depending on whether orientation or alignment is being measured. If orientation is being measured, the fluorescence passes through a quarter-wave plate followed by a linear polariser, whilst for alignment the fluorescence only passes through the linear polariser. This lens set-up is demonstrated in figure 5.2. The linear polariser is arranged for the preferred alignment of light for the monochromator.

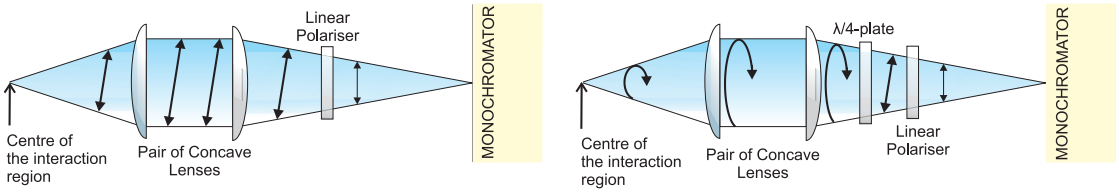

Figure 5.2: A pictorial depiction of the optics involved in focusing and polarisation filtering the emission onto the monochromator. On the left is the set-up for disalignment experiments and on the right the set-up for disorientation experiments.

Figure 5.3 demonstrates the evolution of the angular momentum precession, fluorescence and resultant decay detected, following excitation with a vertically or horizontally aligned probe laser [21]. Note there is no beat for excitation with light aligned parallel to the detection direction. Figure 5.4 demonstrates the same evolution but with the experimental geometry for disorientation experiments and excitation via left- or right-circularly-polarised light [83].

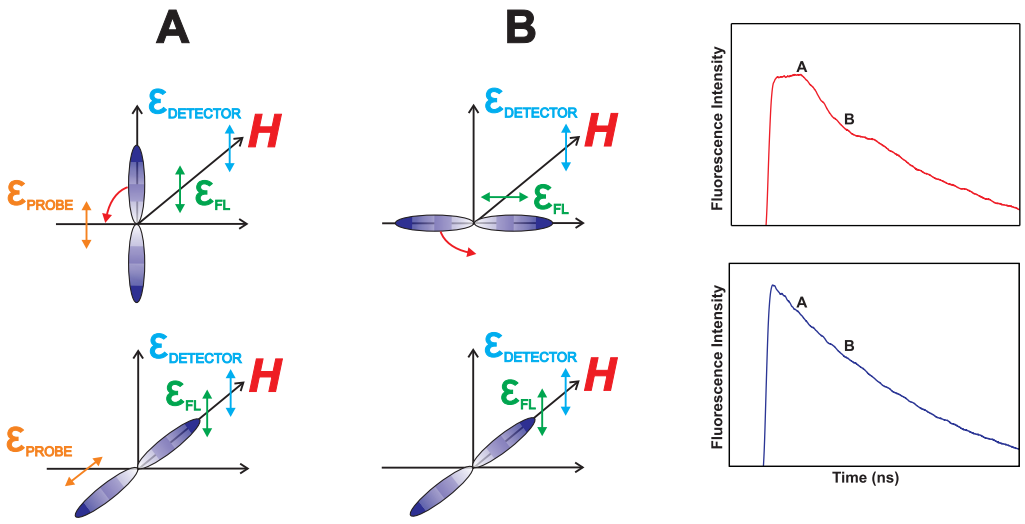

Figure 5.3: A pictorial depiction of an aligned distribution precessing in time and the polarisation of the resultant fluorescence. The preferred polarisation for the detection geometry is also shown. To the right a decay signal is shown with labels to indicate points in time that correspond with the picture.

Following passage through the monochromator the emission is focused onto the PMT. The signal from the PMT is sent to the digital oscilloscope which records the signal from alternate laser shots in different channels, thus recording the fluorescence

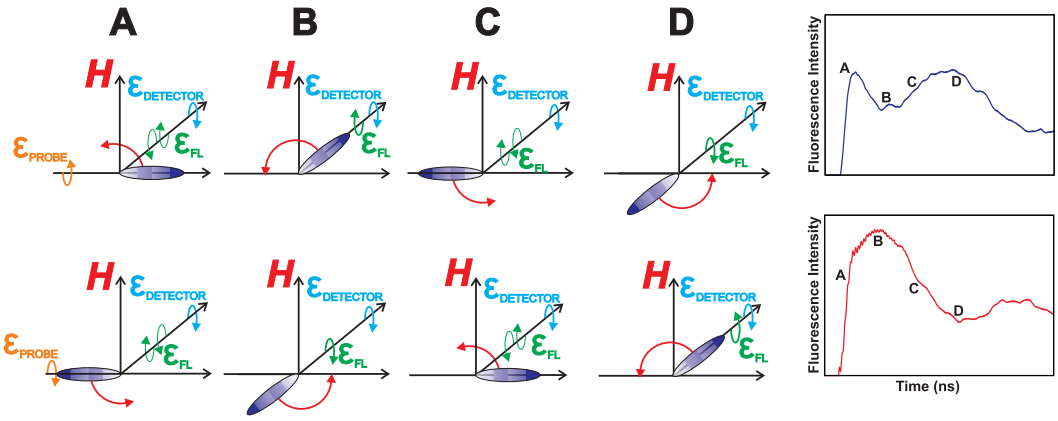

Figure 5.4: A pictorial depiction of an oriented distribution precessing in time and the polarisation of the resultant fluorescence. The preferred polarisation for the detection geometry is also shown. To the right a decay signal is shown with labels to indicate points in time that correspond with the picture.

decay from the two different light polarisations in different channels. The oscilloscope averages the decays over 532 laser shots then passes them to a computer, which itself averages 12-20 such decay traces so that at least 3000 laser shots contribute to the signal for each polarisation at one pressure in each experimental run.

5.2.4 Monochromator

The emission passes through a Bethan M300 monochromator which acts as a filter, selecting only a narrow band of fluorescence wavelengths. The monochromator position is adjusted by a step per motor for the grating, controlled by a module that can be adjusted manually or by a PC, whilst the slit width is adjusted manually. The grating of the monochromator has 2400 lines/mm, giving a theoretical maximum resolution of 0.7 Å with a minimum slit width of 0.05 mm. In practice, the maximum resolution is 1.0 Å [114]. The true resolution is obtained by considering the intensity profile obtained by experimentally scanning the monochromator. The signal is recorded with a purpose-built LabVIEW program [228] on a PC that interfaces with the monochromator via a RS232 port. This recorded spectrum is compared with that from a simulated spectrum produced by a LabVIEW program [55, 228] or LIFBASE [227].

In this experiment the monochromator is employed for one of two purposes, depending on whether elastic or total depolarisation is being studied and if the studies are of an aligned or oriented distribution. Q branch emission is insensitive to OH(A) orientation, and therefore no quantum beat is observed. Meanwhile the beats in emission from P and R branches are equal in magnitude, but of opposite phase. In order to measure total disorientation the monochromator is set such that emission from only one of these branches is recorded. The monochromator slit width and position is selected to also ensure that emission is detected from all levels populated following RET.

With alignment experiments, quantum beats in the P and R emission branches are the same phase, but opposite to the phase of beats in the Q branch. Q branch emission is much more intense than P and R branch emission, so it is possible to observe a beat and thus measure polarisation with unresolved emission. Given this, the monochromator is often held at its minimum resolution in total disalignment experiments.

In elastic depolarisation, it is necessary to further resolve the emission so LIF from just the initially excited spin-rotation level is recorded. This is possible for experiments with OH(A) radicals as transition lines are sufficiently far apart.

Total Depolarisation

When studying total depolarisation, emission from all rotational levels that can reasonably be populated following collisions of the OH(A) radical in its initially excited rotational level are detected. These experiments not only determine total depolarisation cross sections, but electronic quenching cross sections through consideration of population decay.

A variety of spin-rotation levels are excited in these studies. Tables 5.1 and 5.2 list the rotational quantum number N and the spin-rotation quantum number j for these excited states. The tables also list the excitation line used and the position of the monochromator for collecting the fluorescence signal - the monochromator is centred

N	j	Excitation Line	Emission Line	Slit Width/mm	Bandwidth /Å	Field /Gauss
0	0.5	$P_{12}(1)$	$P_{12}(1)$	1.0	12.0	2
1	1.5	$P_{11}(2)$	$P_{11}(2)$	1.0	12.0	3
2	2.5	$P_{11}(3)$	$R_{11}(1)$	2.0	23.4	5
2	1.5	$R_{22}(1)$	$P_{22}(3)$	1.5	17.5	7
4	3.5	$R_{22}(3)$	$P_{22}(3)$	3.0	35.0	10
5	5.5	$R_{11}(4)$	$P_{11}(6)$	5.0	59.0	15
5	4.5	$R_{22}(4)$	$P_{22}(6)$	5.0	59.0	10
6	5.5	$R_{22}(5)$	$P_{22}(7)$	6.0	70.0	18
7	7.5	$R_{11}(6)$	$P_{11}(8)$	6.0	70.0	24
8	7.5	$R_{22}(7)$	$P_{22}(9)$	4.0	47.0	10
10	10.5	$R_{11}(9)$	$R_{11}(9)$	3.0	35.0	30
10	9.5	$R_{22}(9)$	$P_{22}(11)$	Open	77.0	30

Table 5.1: Table detailing the excitation lines and monochromator settings for different starting spin-rotation levels for total disorientation studies.

on a particular emission line. The lines are labelled as $\Delta N_{F_\Pi f_\Sigma}(N'')$ where N'' is the ground state rotational quantum number, ΔN is O, P, Q, R, S for $\Delta N = -2, -1, 0, 1, 2$ respectively, F_Π gives the spin-orbit manifold of the ground electronic state: 1 for $^2\Pi_{3/2}$ and 2 for $^2\Pi_{1/2}$, and f_Σ the spin-rotation manifold of the excited electronic state: 1 for $j = N + S$ or 2 for $j = N - S$. The tables also list the magnetic field strength used in each case, and finally the monochromator slit width and resultant bandwidth in each experiment. Table 5.1 lists these settings for total disorientation experiments and table 5.2 for disalignment experiments. In the latter case the monochromator slit is fully opened and its effective resolution is 77 Å.

Elastic Depolarisation

Unlike with NO(A) emission, for which the emission lines are too close together to be resolved with the monochromator, in some cases OH(A) emission lines can be fully resolved. This allows emission from a single spin-rotation level to be studied. By resolving just the emission from the initially excited spin-rotation level the depolarisation

N	j	Excitation Line	Emission Line	Slit Width/mm	Bandwidth /Å	Field /Gauss
1	1.5	$Q_{11}(1)$	$Q_{11}(1)$	Open	77.0	0
2	1.5	$R_{22}(1)$	$Q_{22}(2)$	Open	77.0	0
3	3.5	$Q_{11}(3)$	$P_{11}(4)$	Open	77.0	0
4	3.5	$R_{22}(3)$	$P_{22}(5)$	Open	77.0	5
5	5.5	$R_{11}(4)$	$P_{11}(6)$	Open	77.0	7
5	4.5	$R_{22}(4)$	$P_{22}(6)$	Open	77.0	5
6	5.5	$R_{22}(5)$	$P_{22}(7)$	Open	77.0	12
7	7.5	$R_{11}(6)$	$P_{11}(8)$	Open	77.0	12
8	7.5	$R_{22}(7)$	$P_{22}(9)$	Open	77.0	15
10	10.5	$R_{11}(9)$	$R_{11}(9)$	Open	77.0	15

Table 5.2: Table detailing the excitation lines and monochromator settings for different starting spin-rotation levels for total disalignment studies.

with respect to collisions that are elastic in OH(A) can be measured [114]. The emission decay is only analysed for the first 200 ns to eliminate the possibility of including emission from OH(A) radicals that have undergone two or more inelastic collisions which act to return them to the initially excited spin-rotation level. The exact grating position of the monochromator is checked before every set of data by scanning the emission spectra.

By considering the total population decay associated with these measurements, and the quenching cross section determined in the total depolarisation cross sections, it is possible to determine RET cross sections as their difference. Table 5.3 and table 5.4 detail the spin-rotation levels studied, excitation and emission lines, and monochromator settings for elastic depolarisation experiments for disorientation and disalignment respectively, in the same way as the tables in the previous subsection. With some rotational levels it is not possible to fully resolve every individual emission line perfectly, and the overlapping lines are included in a new column of the table along with their distance in Å from the emission line. Except with low spin-rotation levels these are mostly satellite lines with small emission coefficients when compared with the main line studied.

N	j	Excitation Line	Emission Line	Bandwidth /Å	Field /Gauss	Overlapping Lines (/Å)
0	0.5	$P_{12}(1)$	$P_{12}(1)$	1.0	2	$Q_{22}(7)$ (0.90)
4	3.5	$R_{22}(3)$	$R_{22}(3)$	1.4	10	
5	4.5	$R_{22}(4)$	$R_{22}(4)$	1.4	10	
8	7.5	$R_{22}(7)$	$P_{22}(9)$	2.7	10	$P_{12}(9)$ (0.19), $O_{12}(6)$ (0.23)

Table 5.3: Table detailing the excitation lines and monochromator settings for different starting spin-rotation levels for elastic disorientation studies.

N	j	Excitation Line	Emission Line	Bandwidth /Å	Field /Gauss	Overlapping Lines (/Å)
1	1.5	$Q_{11}(1)$	$Q_{11}(1)$	1.0	0	$Q_{21}(1)$ (0.04)
2	1.5	$R_{22}(1)$	$P_{22}(3)$	1.0	0	$O_{12}(2)$ (0.02), $P_{12}(3)$ (0.06), $Q_{22}(9)$ (0.18)
4	3.5	$R_{22}(3)$	$R_{22}(3)$	1.4	5	
5	4.5	$R_{22}(4)$	$R_{22}(4)$	1.4	5	
8	7.5	$R_{22}(7)$	$P_{22}(9)$	2.7	10	$P_{12}(9)$ (0.19), $O_{12}(6)$ (0.23)

Table 5.4: Table detailing the excitation lines and monochromator settings for different starting spin-rotation levels for elastic disalignment studies.

5.3 Data Analysis and Fitting

The fluorescence decays recorded in the experiment can be fit to the following phenomenological expression:

$$I(t) = I(0)\,\mathrm{e}^{-k_n t}\left(1 + \sum_F C_F\,\mathrm{e}^{-k_p^{(k)} t}\cos(k\,\omega_F\,t + \phi)\right), \tag{5.12}$$

where C_F is the beat amplitude proportional to the initial polarisation, and ω_F the Larmor frequency associated with the F^{th} hyperfine level. This phenomenological expression resembles equation (1.46) and the equations for P, Q and R branch emission in subsection 1.7.3 of the introduction chapter introducing quantum beats. However the earlier equations did not account for the exponential decay of polarisation presented in subsection 5.1. The sum is over all hyperfine levels that contribute to the quantum beat. To clarify, different hyperfine levels are not excited coherently, which would lead to hyperfine quantum beats [280, 281], but more than one discrete superposition

of Zeeman levels can emerge from exciting more than one hyperfine level within the bandwidth of the laser (as hyperfine levels are not resolved). Additionally, following inelastic collisions more hyperfine levels, potentially of different spin-rotation levels, will be populated. Fluorescence from these newly occupied levels will also be detected, depending upon the monochromator settings. ϕ refers to the phase of each superposition at the start of the beat. k is the polarisation moment being considered, with $k = 1$ for orientation and $k = 2$ for alignment. k_n is the rate constant for the population decay and k_p the rate constant for the decay of the initial polarisation.

Both rate constants can be written as a sum of components that are the result of collisions with the collider gas, H_2, and another independent of those collisions. For population decay [111]

$$k_n = k_0 + k_1[Q], \tag{5.13}$$

where $[Q]$ is the concentration of the collider gas and the collision based rate constant is determined by varying the pressure of the collider gas in the experiment. k_0 is the fluorescence rate constant, the reciprocal of the fluorescence lifetime. The fluorescence lifetime for the OH(A) radical is of the order of 680-760 ns for the rotational levels excited in these experiments ($N = 0-10$) [227]. k_1 quantifies the rate of quenching mediated population loss, either for the excited state OH(A) or a particular spin-rotation state of that electronic state depending upon the resolution of the fluorescence. If total depolarisation is being studied $k_1 = k_Q$, the electronic quenching rate constant. When emission is resolved to explore elastic depolarisation, k_1 has an additional contribution from the RET rate constant: $k_1 = k_Q + k_{\mathrm{RET}}$.

Likewise the rate constant for radical depolarisation can be written as [111]

$$k_p^{(k)} = k_2^{(k)} + k_3^{(k)}[Q], \tag{5.14}$$

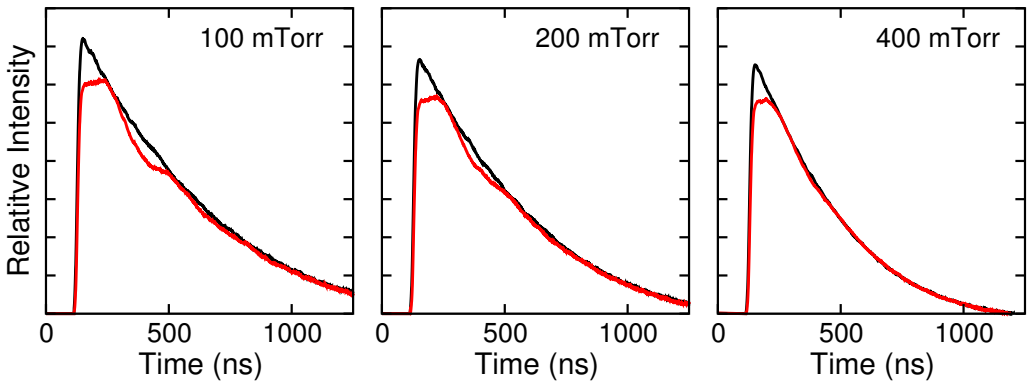

Figure 5.5: Fluorescence decays recorded following excitation of OH radicals to their first excited state by horizontal and vertically polarised light are shown in black and red respectively. Each decay is produced with a different pressure of H_2 present. The excitation is to the $j = 7.5, N = 8$ spin-rotation level. The settings for collecting this data are as shown in table 5.2.

where $k_2^{(k)}$ takes account of polarisation loss in the absence of collisions and includes contributions arising from field inhomogeneity. $k_3^{(k)}$ accounts for the loss of quantum beat amplitude through collisions, and is equated with the collisional depolarisation rate constant, although there is a small contribution from collisional dephasing (see section 5.4).

Figure 5.5 displays OH(A) fluorescence decays recorded following excitation with linear-polarised light of two orthogonal polarisations at a series of H_2 collider pressures. Qualitatively, this figure shows that with increased collider pressure the fluorescence decays faster due to the increased collisional quenching that competes with fluorescence. The faster decay of the quantum beat with increased pressure can also be seen.

Using equations (5.12) to (5.14) these fluorescence decays can be fit to

$$I(t) = A\,\mathrm{e}^{-(k_0+k_1[Q])t}\left(1+\sum_F C_F\,\mathrm{e}^{-(k_2+k_3^{(k)}[Q])t}\cos(k\,\omega_\mathrm{F}\,t+\phi)\right), \qquad (5.15)$$

using a genetic algorithm program written in Fortran77 [282, 283]. All four rate constants are treated as variables within the fitting program, along with the beat amplitude, phase factor and magnetic field associated with the Z-axis. The magnetic fields

of the other axes are set to 0. Since the size of the field in the Z-axis is known, the accuracy of the fit in this respect can be considered and can be helpful when making a judgement as to the quality of the overall fit. This gives a total of 9 variables that are fit between set limits.

Genetic algorithms provide a stochastic rather than deterministic methodology for finding solutions to a problem, in this case fitting experimental data [284]. The algorithms take their name from biology as the methodology involves procedures analogous to chromosomal crossover, mutations and evolution. The first iteration of the program produces a set number of strings (analogous to chromosomes), with each variable (gene) chosen randomly between set limits for each string. In fitting this data an initial population of 1000 strings was produced and the 'chi-squared' value for each string is evaluated via [34]:

$$\chi^2 = \frac{1}{n_{\max}} \sum_n \int (I^n_{\text{expt}}(t) - I^n_{\text{str}}(t))^2 \text{dt}, \tag{5.16}$$

where $n_{\max}$ is the number of pressures and the subscript n signifies the n^{th} pressure decay recorded in the experimental run. $I^n_{\text{expt}}(t)$ is the intensity at time t from the experimental signal for pressure n. $I^n_{\text{str}}(t)$ is the intensity at time t, for pressure n, for that particular string as calculated in equation (5.15). The best χ^2 value for the first population is noted along with the string responsible, and the average χ^2 value is determined.

The next step of the algorithm is to generate a new set of strings for the second iteration (analogous to generation). The χ^2 value for each string is a measure of its 'fitness' as a solution to the problem and for passing on to the next iteration. In generating the new population of a further 1000 strings an adaptation to the basic genetic algorithm procedure is used known as the stochastic remainder selection [284], which guarantees that strings with smaller than average χ^2 values (better fits) for the iteration are carried over to the next iteration at least once. After each of these strings is

replicated the remaining strings are selected randomly from all the initial strings, with the likelyhood of a string being chosen weighted by how small its χ^2 value is. In this way strings with the smallest values of χ^2 are more prevalent in the new population, and those which are less good fits are less prevalent. Over a number of iterations strings that are poor fits are lost from the population [284].

At this stage the population of the new generation clearly contains more strings that produce smaller χ^2 values, but it does not involve new values for variables or new combinations of those variables. In order to create more diversity in the new population processes analogous to chromosomal crossover and mutation occur. In crossover each string is partnered and for each randomly selected pair a position in the list of nine variables is chosen randomly. The values of the variables after this position are switched between the two strings, generating two new strings. In this way variables responsible for a good fit are mixed amongst the new strings.

Again at this point the new strings do not contain any variable values not in the initial population, these are introduced through mutations. The algorithm randomly selects a string along with randomly selecting one of its nine variables, the value of this variable is then changed. In this algorithm half of mutations change the value to another randomly selected between the two initial limits, whilst in the other half there is a bias towards the values associated with the best fit string thus far. In the algorithm used in this analysis 400 mutations in total occur in each iteration, a high number of mutations such as this is common when as here strings are short [284].

The new population of 1000 strings is used in the second iteration and the procedure described above repeated. A total of 20,000 iterations of this genetic algorithm were used in fitting the data from each experimental run, and the variables for the lowest final χ^2 define the equation for the final fit, including the collision rate constants. One advantage of this genetic algorithm method is that typically the global minimum is found as opposed to local minima, as several solutions are explored in each step [284].

The experiment was run and data fitted for each transition at least three times, with the average of the fit collision rate constants used in forming the collision cross sections presented in the next chapter. All the rate constants from each experimental run were within the error bars of the average. Error bars represent 95% confidence levels.

Finally, the rate constants determined for electronic quenching, RET and depolarisation are converted to collision cross sections through equation (5.11). These experiments were carried out in thermalised conditions at 300 K where the relative velocity, $v_{\mathrm{rel}} = 1884\,\mathrm{ms}^{-1}$, as given by the mean of the Maxwell-Boltzmann distribution in equation (1.6).

5.3.1 Orientation Quantum Beats

Figure 5.6 shows the fluorescence decays recorded experimentally following excitation with left- and right-circularly-polarised light for different collider pressures. The decay occurs faster at higher gas pressures as a consequence of increased collisional quenching of the excited state in the presence of more collider gas.

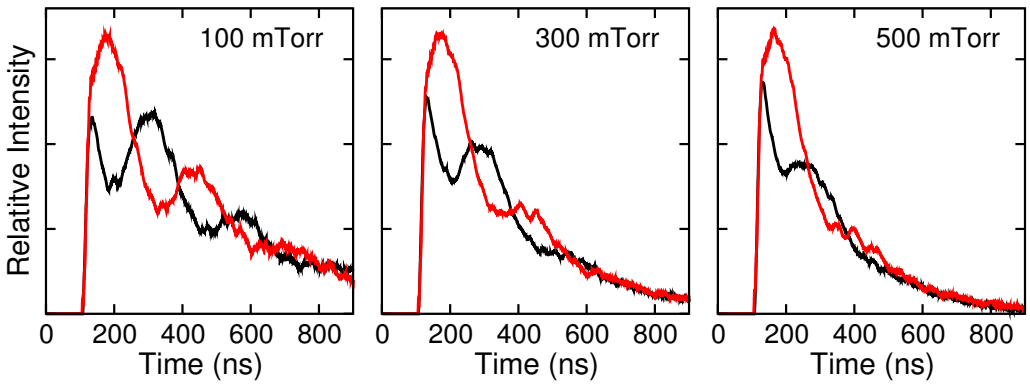

Figure 5.6: Fluorescence decays recorded following excitation of OH radicals to their first excited state by opposite circular polarisations of light shown in red and black. Each decay is produced with a different pressure of H_2 present. The excitation is to the $j = 7.5, N = 8$ spin-rotation level. The settings for collecting this data are as shown in table 5.1.

Rather than fitting the full decay from one of the polarisations with equation (5.15), the normalised difference of the signal from both decays can be fit as [261]

$$\frac{I_{\circlearrowleft\circlearrowleft}(t) - I_{\circlearrowright\circlearrowright}(t)}{I_{\circlearrowleft\circlearrowleft}(t) + I_{\circlearrowright\circlearrowright}(t)} \simeq \mathrm{e}^{-(k_2+k_3^{(1)}[Q])} \sum_F C_F \cos(\omega_F t + \phi), \tag{5.17}$$

which is comparable to equation (1.61) introduced for circular polarisation in section 1.7.3, but sums over hyperfine levels and accounts for exponential decay of the polarisation. The fitting procedure is identical to that for the full decays except for the loss of two variables, k_0 and k_1, as this expression is independent of the population loss. The summed signal $I_{\circlearrowleft\circlearrowleft}(t) + I_{\circlearrowright\circlearrowright}(t)$ is independent of the polarisation loss but dependent on the population loss, so this expression can be used to fit for k_1 and the quenching or RET cross section.

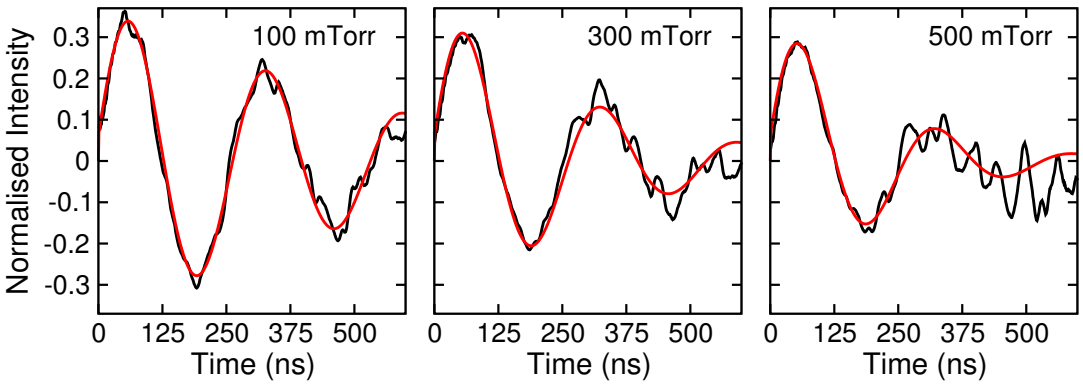

Figure 5.7: Orientation Zeeman quantum beats for OH(A)+H_2 following $R_{22}(7)$ excitation for three different collider gas pressures. The experimental data are shown in black with the best fit in red. The settings for collecting this data are as shown in table 5.1.

Figure 5.7 displays this normalised difference for experimentally-recorded fluorescence decays of OH(A)+H_2 at three different pressures. These are the same data as for the decays in figure 5.6. The best fit of the data compared to equation 5.17 is also shown. From these data it is clear that the beat amplitude falls faster at higher pressures of collider gas since more collisional depolarisation occurs. Note that initially, at $t = 0$, there is no polarisation in the detection direction, and a magnetic field is

required to rotate the initial polarisation so that it is parallel to the detection axis, as demonstrated in figure 5.4.

5.3.2 Alignment Quantum Beats

When fitting alignment data, $I_\perp(t)$ contains no quantum beat, the magnetic field H can be set to 0, and $\phi = \frac{\pi}{2}$, whilst $I_\parallel(t)$ experiences the magnetic field, has a quantum beat, and ϕ should be set to 0. Again, rather than fitting the full equation for each decay the normalised difference can be fit instead such that

$$\frac{I_\parallel(t) - I_\perp(t)}{I_\perp(t)} = \frac{\mathrm{e}^{-(k_2^{(k)}+k_3^{(k)}[\mathrm{Q}])\sum_\mathrm{F} \mathrm{C_F}(1+\cos 2\omega_\mathrm{F} t)}}{1 - \mathrm{e}^{-(k_2^{(k)}+k_3^{(k)}[\mathrm{Q}])\sum_F C_F}}, \tag{5.18}$$

which is only dependent on the polarisation decay, not the population loss.

Figure 5.8 compares the normalised difference from experimentally-recorded fluorescence decays of OH(A)+H_2 at three different pressures with that from the best fit. These are the same data as for the decays in figure 5.5. Once again the beat amplitude falls faster with higher collider pressure due to the increased levels of collisional depolarisation.

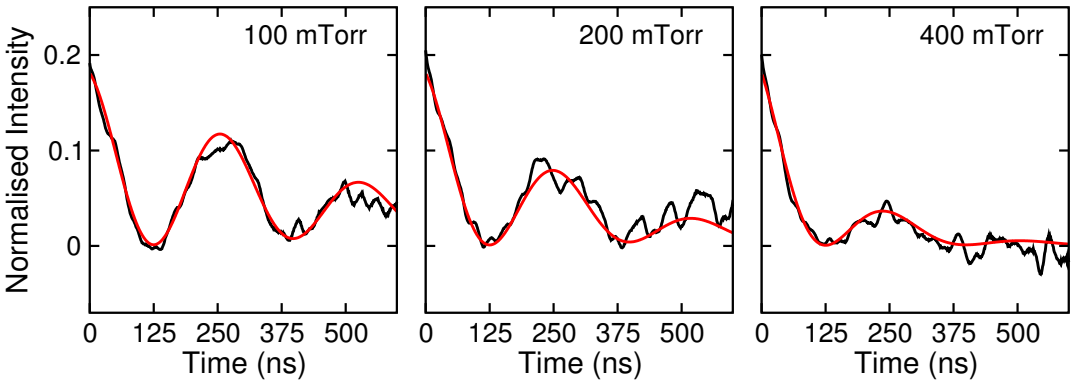

Figure 5.8: Alignment Zeeman quantum beats for OH(A)+H_2 following $R_{22}(7)$ excitation for three different collider gas pressures. The experimental data are shown in black with the best fit in red. The settings for collecting this data are as shown in table 5.1.

The degree of alignment is at its maximum at $t = 0$, and as such a magnetic field is not neccessarily required to determine rate constants for disalignment. If no field is used, there is of course only detectable polarisation decay in $I_{\parallel}(t)$ and either this can be fit to the full equation or fit as a normalised difference by

$$\frac{I_{\parallel}(t) - I_{\perp}(t)}{I_{\perp}(t) + 2I_{\perp}(t)}, \tag{5.19}$$

which is dependent on polarisation and not population decay. The denominator $I_{\perp}(t) + 2I_{\perp}(t)$ can be fit separately in a field off environment to identify the population loss rate constants as it is independent of polarisation decay. A field off environment was used to acquire RET cross sections and elastic disalignment cross sections for low N.

5.4 Depopulation, Depolarisation and Dephasing in the Excited State

Following the formation of the ensemble of coherently excited molecules there is a polarised distribution in a single spin-rotation level of the excited state. The excited state as a whole is depopulated by spontaneous fluorescence and collisions that cause electronic quenching. Such processes do also depolarise the system, but can be separated out, as shown in equation (5.15), from processes that preserve the excited state population, but still change the direction of the angular momentum.

The QCT formalism outlined in chapter 3 only considers the collisions that remain in the excited state. It is these collisional causes of depolarisation that are of particular interest experimentally as processes behind $k_3^{(k)}$ rate constants. There are elastic and inelastic contributions to this depolarisation as in the QCT studies.

Elastic collisions conserve the translational kinetic energy of the system and the magnitude of its angular momentum. However, they may change the direction of this angular momentum by changing the relative population of the various M_F levels. This causes a loss in the degree of polarisation in the precessing distribution and a loss of beat amplitude. Inelastic collisions can also be accompanied by a change in angular momentum direction and cause a loss of polarisation. The variety of different types of inelastic collisions are defined in section 3.4, though once again note the experiment is insensitive to collisions that maintain spin-rotation level but change hyperfine level.

Inelastic collisions also lead to a change in the Larmor frequency of the diatom due to a change in the g_F value. This means that the diatom precesses out of phase with the initial distribution, leading to a weakening of the amplitude of the beat even though the level of depolarisation may actually be small. This dephasing phenomenon contributes to $k_3^{(k)}$, and cannot be separated out from the true depolarisation. As a consequence, the rate constant $k_3^{(k)}$ is an overestimate of the true depolarisation rate constant $k_d^{(k)}$ introduced in subsection 5.1. Collisions that lead to a change in the spin-rotation manifold are the most dephasing, as they change the sign of the g_F value and so the direction of precession.

In previous studies of the OH(A)+Kr and OH(A)+Ar systems, the results of QCT calculations have been used to simulate the experiment and account for dephasing [57, 117]. These simulations have shown that including dephasing leads to only a small change in the calculated $\sigma_3^{(k)}$ relative to $\sigma_d^{(k)}$. This is characteristic of highly depolarising systems, since if following a collision the angular momentum is almost completely randomised, dephasing has very little additional effect on the value of $\sigma_3^{(k)}$. As the OH(A)+H_2 QCT calculations have revealed that the collisions are extremely depolarising, the effect of dephasing on the value of $\sigma_3^{(k)}$ will once again be small. Consequently, for the rest of this thesis the dephasing effect has been assumed negligible, and the collision cross section $\sigma_3^{(k)}$ is approximated as the depolarisation cross section $\sigma_d^{(k)}$.

5.5 Summary

The creation of an aligned or oriented distribution with circularly- or linearly-polarised laser excitation has been demonstrated, along with the evolution of this distribution with collisions. The potential for Zeeman quantum beat spectroscopy to monitor this evolution has been demonstrated and the experimental apparatus to carry out this experiment detailed. A monochromator has been used to filter out emission that would act to eliminate the quantum beat or further resolve the emission to observe only the initially populated spin-rotation level. A data analysis approach has been demonstrated that fits a function to the recorded fluorescence decays and this calculates collision cross sections for quenching, RET and depolarisation.

Chapter 6 will present experimental results from OH(A)+H_2 collisions observed with this method. Chapter 7 will compare these results with those calculated from the quasi-classical trajectories.

Chapter 6

OH(A)+H_2 Experimental Results

In this chapter, experimental results collected with the Zeeman quantum beat spectroscopy based method are presented and analysed. Quenching cross sections, rotational energy transfer (RET) and depolarisation cross sections are shown in terms of their relationship to the spin-rotational level investigated. Total depolarisation cross sections (for all collisions) and elastic depolarisation cross sections ($j' = j$) are presented.

The chapter continues by comparing the depolarisation and RET cross sections measured in this study with results from previous Zeeman quantum beat studies [24, 34, 57]. These previous studies focused on OH(A) collisions with noble gases, but are nonetheless useful. Helium is a collider of similar mass, and the heavier noble gases provide a comparison with a system that is also associated with a strongly attractive potential energy surface (PES). These comparisons allow for some elucidation of the relative importance of kinematic and dynamic effects in determining the magnitude of the various cross sections.

6.1 Electronic Quenching

Electronic quenching cross sections have been recorded following excitation to a number of spin-rotation levels. Figure 6.1 compares the experimentally-determined quenching cross sections from this work with those from previous studies by Hemming *et al.*[91], German [90], and Copeland *et al.*[92]. The rotational population of the OH(X) radicals is largely thermalised during the large pump-probe time delay time of 20 μs and consequently the population at high rotational levels is small. With only a small population of radicals to excite to high N_{OH}, the signal was insufficient to record quenching cross sections above $N_{OH} = 10$. High N_{OH} experiments were possible in the work of Hemming *et al.* [91], in which a smaller pump-probe time delay of 8 μs was used, and data from these measurements are included in the figure.

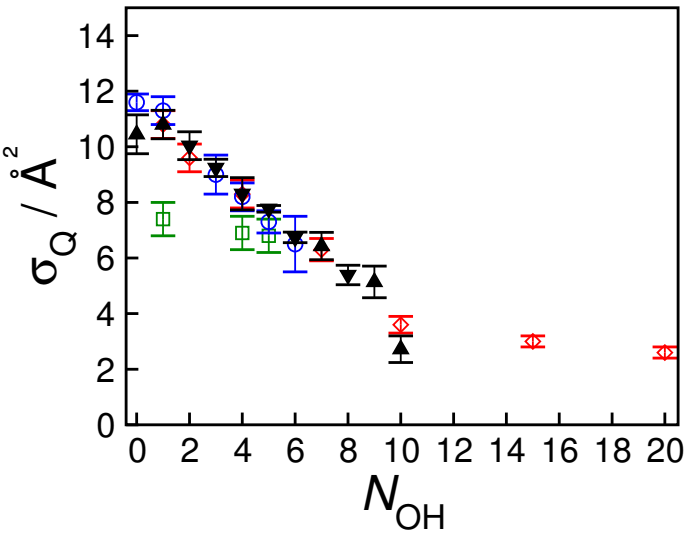

Figure 6.1: Experimentally-measured electronic quenching cross sections for OH(A)+H_2 compared with those from other work. The black triangles are from these studies with upwards pointing triangles relate to quenching of OH(A) radicals excited to the f_1 spin-rotation manifold and downwards pointing arrows those excited to the f_2 spin-rotation manifold. The green squares are from the work of German [90], blue open circles from Copeland [92] and red diamonds from Hemming *et al.* [91], in these three previous studies the spin-rotation manifold was unspecified.

The results from these experiments compare favourably with those from previous studies, with a fall in cross section observed with increasing OH(A) rotational quantum number, N_{OH}. The exception to this agreement is the German study [90], which did not identify any rotational level dependence unlike the more recent studies. This fall is indicative of a process that is defined by anisotropy in the PES, since it is sensitive to the orientation of the OH(A) radical. As discussed in subsection 1.9.3, electronic quenching is widely believed to occur along a seam of conical intersections between the excited state $2A'$ and ground state $1A'$ PESs [107, 126, 177, 178]. This tallies with the products of the non-reactive quenching primarily being OH(X) in its A' lambda doublet level, as observed experimentally in references [101, 259]. The identified conical intersections are at geometries where the oxygen end of the OH(A) radical is directed towards the hydrogen molecule, hence the sensitivity of the quenching cross section to the diatom orientation. The concept of rotational averaging or washing out of the PES has already been introduced, but is particularly important in the case of electronic quenching, which is associated exclusively with a certain region of the PES. As the radical rotates faster, the approaching hydrogen collider experiences the attractive regions less, and is less likely to be drawn into the attractive oxygen wells associated with quenching. The importance of attractive features of the potential in bringing about electronic quenching is further evidenced by the temperature dependence of the cross sections, explored previously by Heard and Henderson [100] and Hemming and Crosley [94]. Cross sections were seen to increase with decreasing temperature as would be expected if the process depended on attractive areas of the PES.

The experimental results also suggest no difference between the quenching cross sections on changing spin-rotation level. Similarly, Copeland *et al.* concluded that the quenching cross sections for the f_1 and f_2 spin-rotation levels were the same within experimental error, whilst Hemming *et al.* did not indicate if their studies had focused on one or other spin-rotation level.

Though not evident in the results from this experiment, which do not extend to high N_{OH}, results from others show that the quenching cross sections plateau at higher N_{OH} to a constant value of around 2 Å^2. This is possibly because at a certain point the rotational speed of the diatom is considerably faster than the intermolecular approach velocity and the potential experienced is almost completely isotropic. At this point any further increase in rotational speed cannot further reduce the quenching cross sections. Another possibility is that there is more than one mechanism by which quenching occurs: a larger contribution from an N_{OH} dependent mechanism that disappears at high N_{OH}, along with a smaller contribution from an N_{OH} independent mechanism. One possible secondary mechanism is that the system could overcome barriers to the conical intersections via non-classical dynamics, e.g. quantum tunneling.

6.1.1 Comparison with other Collision Environments

Table 6.1 compares the thermal quenching cross sections for this system with those for OH(A) with other atomic and molecular colliders. Falling quenching cross sections with increased OH(A) rotation are typical of these systems, indicating sensitivity to the OH(A) approach orientation and the involvement of regions of attractive potential [285]. Copeland *et al.* demonstrated a qualitative relationship for a number of colliders between complex formation cross sections and the quenching cross sections, with the former being estimated from various multipole moment parameters [92]. This analysis provides evidence for the clear role of attractive forces in the quenching processes.

OH(A) electronic quenching to ground state OH(X) with rare gas colliders, as with H_2, occurs through conical intersections [93]. Figure 6.2 displays cuts of the excited and ground state A' diabatic PESs for the linear HO-Rg approach geometry, and is a composite of figures provided by J. Kłos [286]. The conical intersections thought to be responsible for electronic quenching are clearly visible in the Ar, Kr and Xe panels.

N_{OH}	H_2	Kr	Xe	O_2	N_2
0	10.5±1.1	10.1±1.0	22.3±0.4	20.7±0.8	6.7±1.4
1	10.8±0.5	11.1±1.0	28.2±2.7	21.0±2.5	4.8±0.5
2	10.0±0.5	7.8±1.5	28.1±1.0	20.6±0.6	3.2±0.2
3	9.2±0.3	5.3±0.8	26.5±2.5	16.6±0.7	2.5±0.5
4	8.3±0.6	3.4±0.8	32.1±2.6		2.9±0.2
5	7.8±0.1	3.2±1.2	29.7±0.7	13.9±0.9	
6	6.7±0.2	2.9±0.4	21.1±1.7	12.9±0.9	1.7±0.5
7	6.4±0.5	1.4±0.1	25.3±1.4	11.9±0.8	0.6±0.3
8	5.3±0.4	2.0±1.0	24.6±2.0		
9	5.1±0.6		25.9±1.3		
10	2.7±0.5	0.4±0.3	22.3±3.8		0.3±0.2
15	3.0±0.2		12.1±0.8	6.0±0.4	
20	2.6±0.2	0.8±0.3	12.1±0.8	6.7±0.3	

Table 6.1: Table comparing the thermal (300 K) quenching cross sections of the OH(A) radical with various quenching species. The data for H_2 is mostly from this study. Data for Krypton is taken from Brouard *et al.* [93] and from reference [91] for $N_{\mathrm{OH}} = 10, 20$. Xenon data was obtained via the method used here for H_2 quenching and is taken from reference [24, 112] except for $N_{\mathrm{OH}} = 15, 20$ which is again taken from reference [91]. O_2 data is taken from a mix of reference [92] for $N_{\mathrm{OH}} = 0 - 5$, and reference [91] for higher N_{OH}. N_2 data is also taken from a mix of these two sources; $N_{\mathrm{OH}} = 0, 1, 3$ from reference [92] and all others from reference [91]. The cross sections vary little with spin-rotation level and this is not specified here. All data are in Å^2.

The crossings for the lighter rare gases (seen here for Ar) occur within the repulsive wall of the excited surface and are not generally accessible at thermal collision velocities. Consequently, the electronic quenching cross sections are very small, 0.047 Å^2 for Ar and 0.004 Å^2 for He [287–289]. With Kr and Xe colliders the conical intersection lies within the potential well, and is readily accessed in thermal collisions leading to much larger quenching cross sections. There are further conical intersections in OH-Rg geometries but these are not energetically accessible [93].

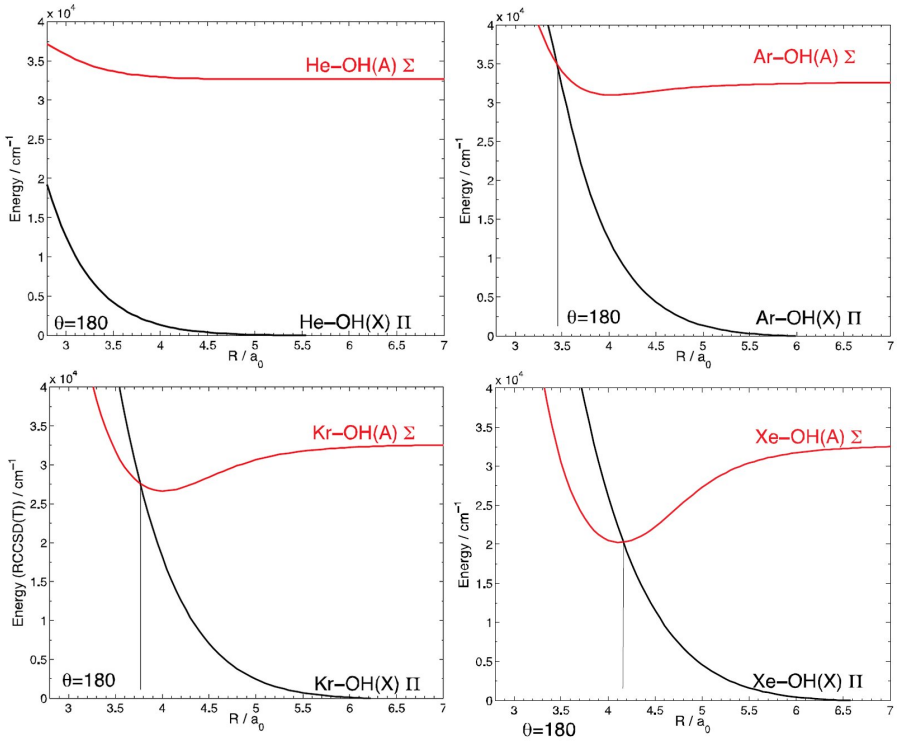

Figure 6.2: Cuts through the potential energy surface of OH(X,A)+Rg collision systems. The cuts are at a linear HO-Rg geometry ($\theta = 180°$). The red curves are for the excited $2^2A'$ state and the black curve for the ground state $1^2A'$. In the top left Rg=He, the top right Rg=Ar, the bottom left Rg=Kr and the bottom right Rg=Xe. Figure is a composite of figures provided by J. Kłos [286].

The quenching cross sections for Kr and Xe were for the most part calculated with the same experimental approach as here for OH(A)+H_2 [24, 93]. The cross sections for Xe are significantly larger than those for Kr as a result of differences in the relevant interaction potentials. Firstly, the well in Xe is significantly deeper, ∼12000 cm^{-1} [24],

compared with $\sim$6000 cm^{-1} [93, 110] for Kr. Consequently, the attractive forces drawing collisions towards the crossing region are stronger, resulting in larger quenching cross sections. Secondly, whilst both intersections lie in the region of the potential well, with attractive potentials (relative to the infinitely separated diatoms), in the Kr case the crossing is in a rising part of the potential beyond the deepest point in the well. In contrast, the intersection in the Xe case is almost exactly at the base of the well. More collisions will pass through the intersection in the latter case, especially when the possibility of the formation of a short-lived complex is considered. Again, this will lead to larger quenching cross sections. As with OH(A)+H_2, the cross sections fall with N_{OH} due to the rotational averaging of the anisotropy. Unfortunately, this precise description of the location of the conical intersection is not possible with OH+H_2 as there is a 4 dimensional seam of intersections which is still the subject of characterisation [189, 290, 291].

An adapted QCT study using trajectory surface hopping, of the kind first proposed by Tully and Preston [192, 292, 293], has been carried out on the excited state OH(A $2A'$)-Kr surface and the coupled ground state OH(X $1A'$)-Kr surface by Brouard, Perkins and co-workers [24, 111]. This provided a very good estimation of the rotational product state distribution and the variation of quenching cross sections with N_{OH}, demonstrating the role of the conical intersection and surface hopping near the linear HO(A)-Kr geometry in electronic quenching.

In the case of the Kr collider, the cross sections fall close to zero by around $N_{OH} = 10$. Likewise the cross sections seem to fall to zero for N_2. However, the cross sections with Xe and O_2 behave like those with a H_2 collider, falling and then plateauing to a constant level at higher N_{OH}. This plateau is as observed for OH(A)+H_2, and again may indicate that more than one mechanism is involved in the quenching, with a smaller contribution from a N_{OH} independent mechanism. With these heavier systems, quantum mechanical tunnelling is highly improbable, suggesting that the explanation

of the plateau has a different origin.

The deepest point in the OH(A)+H_2 occurs in a O-end C_{2v} geometry, with a well depth of $\sim$11000 cm^{-1}, a similar size to the Xe potential energy well. However, the quenching cross sections are much smaller than those with a Xe collider, and are more comparable to Kr at low N_{OH}. This is likely because the surface as a whole for H_2 is more repulsive (see section 3.1) limiting the number of collisions pulled to the intersection. Additionally the interaction with Xe is longer range than with H_2 due to the much larger size of the collider. The reduction of quenching cross sections with increasing N_{OH} is less pronounced with H_2 than Kr. At first sight this may be a result of the more attractive PES with a H_2 collider, however, it is more likely due to the larger relative velocity for H_2. The relative velocity of the H_2 system is 1875 ms^{-1} compared to 670 ms^{-1} for Kr. At $N_{OH} = 5$ the angular frequency of the OH(A) radical is $\approx 3.6 \times 10^{13}$ rad/s. In the time it takes for the Kr collider to move 0.1 Å the radical rotates through 32° versus only 11° for H_2, i.e. the potential is more averaged with the Kr collider.

For N_2 a conical intersection is found in the linear HO-N_2 $C_{\infty v}$ geometry, which lies $\sim$2300 cm^{-1} below the asymptote [107]. This is not the most attractive region of the excited state PES, which is actually the other linear geometry OH-N_2 with a well depth of $\sim$ 3770 cm^{-1}. However, the conical intersection in this geometry lies high up the repulsive inner wall. A further intersection is associated with a C_{2v} geometry where the oxygen atom is pointed towards the midpoint of the N_2 bond, but this lies above the asymptote for separated OH(A) and N_2 so again is not thermally accessible [107]. There are both relatively few accessible conical intersections, and the associated regions are much less attractive than with Kr, Xe and H_2 colliders, hence the much smaller cross sections for quenching observed. The products of the quenching are vibrationally cold, rotationally hot, and with a propensity for production in the A' Λ doublet [294].

This is, as observed with H_2, because the dynamics involve crossing from the OH(A $2A'$)+N_2 surface to the OH(X $1A'$)+N_2 surface close to a conical intersection. As with H_2, the lower surface is highly anisotropic with respect to OH(X) rotation, hence the rotational excitation [294].

With an O_2 collider there has been little previous work on the PES describing the system. The quenching of the OH(A) radical with O_2 is known to give a mix of O_3+H and H_2O+O reactive products along with non-reactive OH(X)+O_2 products [295]. The large quenching cross sections and N_{OH} dependence suggest a potential very similar to H_2, with conical intersections lying in strongly attractive regions of the excited state surface. It is likely that these regions are even more strongly attractive or more accessible than those of the OH+H_2 potential, hence the larger quenching cross sections.

6.2 Rotational Energy Transfer

Rotational energy transfer (RET) cross sections have been measured experimentally for a number of different initial spin-rotation levels. These experiments are sensitive to all changes in spin-rotation level, so the cross sections include contributions from collisions $j_{OH}, N_{OH} \rightarrow j'_{OH}, N'_{OH}$, where $j'_{OH} \neq j_{OH}$, $N'_{OH} = N_{OH}$, and also where $N'_{OH} \neq N_{OH}$.

Table 6.2 details experimentally-measured flux-averaged thermal RET cross sections at 300 K for OH(A)+H_2 collisions. These data are comparable with those measured previously by Crosley and Lengel [109], although that set only included cross sections for $N_{OH} = 1$ and 3, both with a cross section of 15 ± 1 Å^2. Within the experimental errors, the RET cross sections are almost constant, with only modest dependence on N_{OH}. This is unexpected. Previous studies of OH(A) collisions with light rare gases, including Kr, Ar and He, have shown a fall in RET cross section with N_{OH}, as the energy required to change the rotational level increases [55, 57, 110, 114]. As set out

N_{OH}	j_{OH}	f_1/f_2	$\sigma_{RET}/Å^2$
0	0.5	f_1	28.7 ± 6.1
2	1.5	f_2	13.8 ± 8.5
4	3.5	f_2	14.7 ± 1.9
5	4.5	f_2	18.5 ± 6.8
8	7.5	f_2	17.6 ± 1.8
10	10.5	f_1	16.1 ± 2.5

Table 6.2: Table detailing the RET cross sections observed experimentally following excitation to various different spin-rotation levels, N_{OH}, j_{OH}, of the OH(A) radical in the presence of a H_2 collider.

in equation 4.3, the total energy must be conserved after the collision, this ultimately limits the size of j'_{OH} after the collision. This restricts the amount of RET possible where the outcome is an increase in j_{OH}. However, there is the possibility of a reduction in j_{OH} not subject to this restriction. The accompanying QCT studies indicated that collisions that reduce j_{OH} were vastly dominant in inelastic collisions at high N_{OH}, as detailed in section 4.1.

As set out in equation (4.4), the source or sink for OH(A) rotational angular momentum following RET is either the rotational angular momentum of the accompanying H_2 diatom, or the orbital angular momentum, $\boldsymbol{\ell}$. At high initial N_{OH}, larger amounts of rotational energy are transferred in RET collisions. At least in OH(A)+Rg systems, transfer of angular momentum from orbital angular momentum is more efficient at smaller impact parameters, and thus smaller cross sections result. Opacity functions from the QCT calculations in section 4.4 demonstrated that the reduction in impact parameter over which RET was possible happens very slowly as N_{OH} increases for this system. In the QCT calculations this pattern was observed because angular momentum transfer to or from the H_2 diatom can augment that from the orbital angular momentum, and sustain RET at larger b and N_{OH}. H_2 could be acting as a source/sink of angular momentum in the experimental case too, sustaining larger RET cross sections to higher N_{OH}. H_2 is particularly effective because its rotational

constant, $B_{H_2} = 60.92\,\mathrm{cm}^{-1}$ [46], is much larger than for OH(A), $B_{OH} = 17.36\,\mathrm{cm}^{-1}$ [46], so it is a large store/sink of rotational energy with energy levels that are much more widely spaced than in OH(A).

The experiments are not sensitive to the final rotational level of H_2, so whether transfer of rotational angular momentum occurs between the two diatoms cannot be determined. However, it is a possible kinematic cause for the larger than anticipated cross sections at high N_{OH}.

As discussed in chapter 4, previous studies have demonstrated that RET is associated with attractive regions of a PES. The most attractive regions of the OH(A)+H_2 potential surface are associated with geometries with the oxygen end of the OH diatom directed at the H_2 molecule, but as discussed in the previous section these are the site of conical intersections responsible for electronic quenching. The possibility then arises that the process of RET and electronic quenching are in direct competition. Since electronic quenching is N_{OH} dependent, this competition could account for the relative lack of N_{OH} dependence seen in the experimentally-measured RET cross sections.

6.2.1 Comparison with other Colliders - Helium and Argon

Figure 6.3 compares the experimentally-measured RET cross sections from collisions with H_2 with those measured with helium [55] and argon colliders [34, 57]. These systems were chosen for comparison as to some extent they reflect the competing kinematic and dynamic factors influencing the outcome of OH(A)+H_2 collisions. Helium provides a system with similar kinematics to those in the OH(A)+H_2 system, whilst the Ar system a much more attractive surface reflecting the more anisotropic and attractive potential OH(A) experiences with H_2.

The large difference between the RET cross sections of He and Ar arises through a combination of kinematic and dynamic factors. Table 6.3 lists some of the important

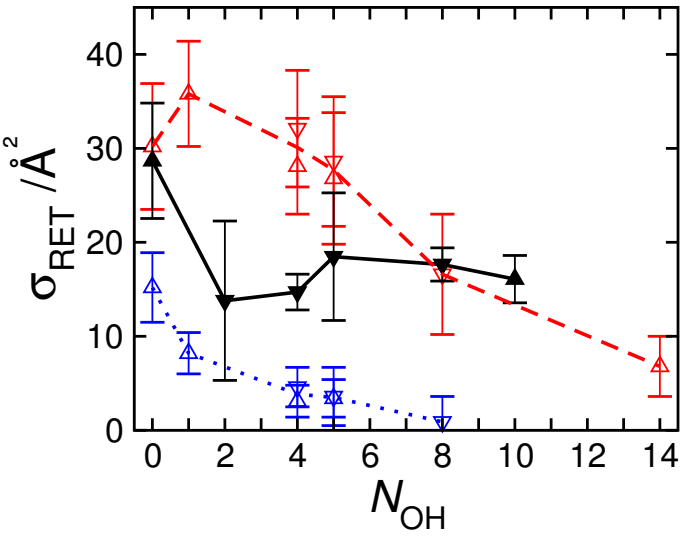

Figure 6.3: Experimentally-measured RET cross sections for OH(A) with various colliders - H_2 in filled black triangles connected by full lines, He in open blue triangles connected by dotted lines, and Ar in red triangles connected with dashed lines. Upwards pointing triangles are cross sections determined following excitation to the f_1 spin-rotation level and downwards pointing triangles are cross sections determined following excitation to the f_2 spin-rotation level.

properties in determining cross sections for the various OH(A)+X systems used in the comparisons of this chapter. The heavier reduced mass, μ, with the Ar collider leads to a larger orbital angular momentum, $\boldsymbol{\ell}$, facilitating angular momentum transfer and RET. When the OH(A) radical is hit with a heavier atom a greater torque is applied, speeding up or slowing down the rotation of the radical. The PES associated with He

X	μ/ amu	ν_{rel}/ ms^{-1}	V_{well}(HO-X)/ cm^{-1}	V_{well}(OH-X)/ cm^{-1}
He	3.24	1400	122	51
Ar	11.93	730	1717	1219
Kr	14.14	670	6079	1949
Xe	15.06	650	12648	3500
H_2	1.80	1877	C_{2v}: 10158 $C_{\infty v}$: 10046	C_{2v}: 3818

Table 6.3: Table detailing kinematic and dynamic properties for OH(A)+X collision systems. These include the reduced mass (in atomic mass units), and the relative velocity. Listed alongside this are the deepest points in the potential energy wells of the associated PESs for two different planar geometries. The well depths are taken from PESs used in QCT studies, similar to those in this thesis for He [55], Ar [113], Kr [110] and Xe [286].

is only weakly attractive and very isotropic. This weak preference for a particular orientation of the OH(A) radical in the collision means relatively little torque is applied. In contrast, the PES for OH(A)+Ar (presented in figure 6.4) contains two strongly attractive regions [113], with well depths of $\sim$1200 cm^{-1} and $\sim$1700 cm^{-1} for the two linear approach geometries: OH-Ar and HO-Ar respectively, separated by a repulsive potential for side-on collisions. There is a strong preference for particular approach orientations for the diatom, and this dynamic effect induces torque and facilitates RET.

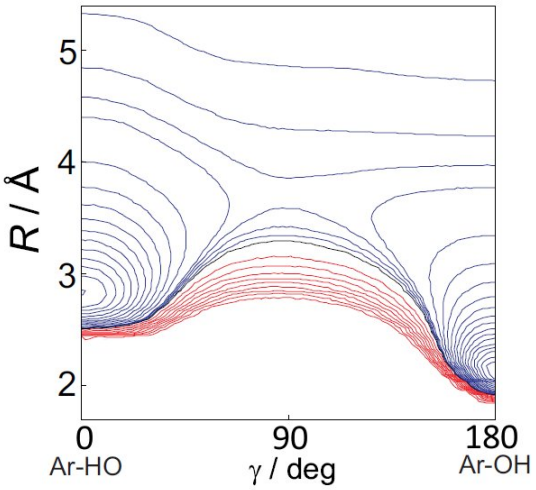

Figure 6.4: The OH(A)+Ar PES. Blue contours correspond to attractive regions and are 100 cm^{-1} apart at energies above 100 cm^{-1}, but 25 cm^{-1} apart below. Red contours designate repulsive regions, and are separated by 100 cm^{-1}. This figure was adapted from reference [34]. The angle γ describes the angle between the OH bond vector, $\boldsymbol{r}_{\mathrm{OH}}$, and the vector between the OH centre of mass and the Ar collider, $\boldsymbol{R}_{\mathrm{CM}}$. The angles 0° and 180° correspond to linear geometries OH-Ar and HO-Ar respectively.

The H_2 RET cross sections lie between those of He and Ar. On the basis of kinematic arguments, the larger reduced mass of the He system would be expected to lead to larger cross sections. However, the much more attractive and anisotropic nature of the H_2 PES, and the additional possibility of angular momentum exchange with the H_2 diatom clearly overrides this factor. However these factors are not clinching in the comparison with OH(A)+Ar RET, which is larger for $N_{\mathrm{OH}} < 8$ in spite of the fact that the most attractive parts of the OH(A)+H_2 PES are nearly 10 times those of the

OH(A)+Ar PES. Two factors are important in explaining this pattern; the first is the larger reduced mass with an Ar collider, which unlike with a He collider is considerably (rather than slightly) larger than that with H_2. Secondly, there are competing quenching processes with an H_2 collider which may act to reduce the degree of RET.

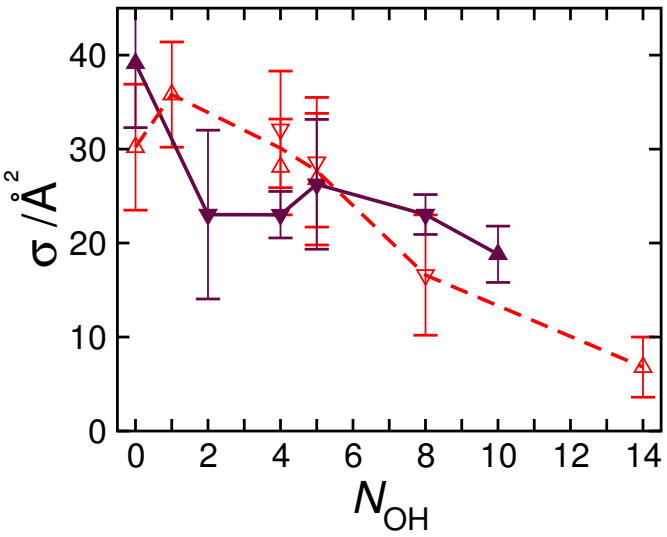

Figure 6.5: Experimentally-measured RET cross sections for OH(A) with Ar are shown in red connected with dashed lines. The filled purple triangles connected with full lines are the combined experimental cross sections of RET and electronic quenching for OH(A)+H_2. Upwards pointing triangles are cross sections determined following excitation to the f_1 spin-rotation level and downwards pointing triangles are cross sections determined following excitation to the f_2 spin-rotation level.

For OH(A)+H_2, quenching cross sections are comparable in size to those for RET at low N_{OH}. Figure 6.5 sums the experimentally-determined electronic quenching and RET cross sections for OH(A)+H_2, and compares these with the OH(A)+Ar RET cross sections. The cross sections are of similar size and the combined OH(A)+H_2 cross sections show a more typical N_{OH} dependence. However, given the kinematics involved in the OH(A)+H_2 system these cross sections are relatively high. In this experimental study, it is not clear whether this is solely the result of the very attractive and anisotropic potential, or the availability of rotational energy exchange between the two diatoms. The QCT study suggests both factors have a role to play.

6.2.2 Comparison with other Colliders - Nitrogen and Oxygen

Studies by Burris *et al.* provide a comparison with RET cross sections determined for OH(A) collisions with N_2 and O_2, though their data are limited to a small range of N_{OH} [296]. This comparison is shown in figure 6.6, and the data source did not specify whether the f_1 or f_2 spin-rotation level was probed, although all the other studies presented in this chapter suggest spin is a spectator to the collision.

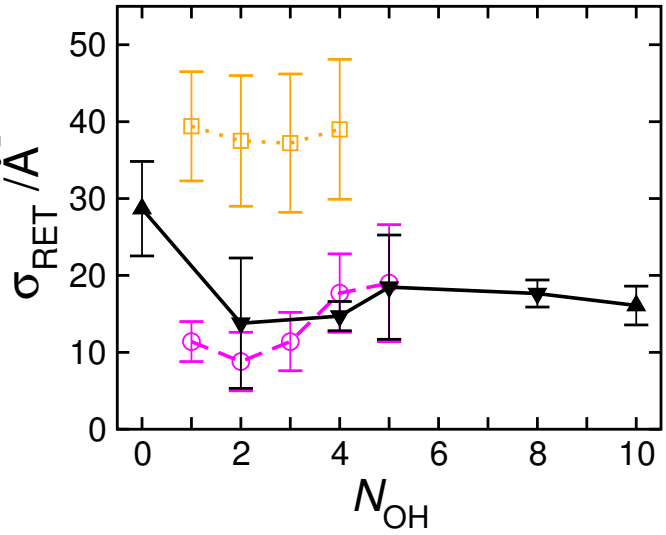

Figure 6.6: Experimentally-measured RET cross sections for OH(A) with various molecular colliders - H_2 in filled black triangles connected by full lines, N_2 are shown by open orange squares connected by dotted lines [296], and O_2 by open pink circles connected with dashed lines [296]. For a H_2 collision partner the spin-rotation state was specified and upwards pointing triangles correspond to excitation to the f_1 spin-rotation level, and downwards pointing triangles to the f_2 spin-rotation level.

The largest OH(A) RET cross sections are observed with N_2. This collider is not only heavier than H_2, but the surface is more attractive, with a maximum well depth of $\sim 3770\,\mathrm{cm}^{-1}$ [107]. The surface also stretches over a longer range, owing to the strong dipole-quadrupole interaction between the diatoms [107]. As stated in subsection 6.1.1, there is relatively little information on the OH(A)+O_2 PES, but the cross sections observed here are comparable to those with H_2, despite the larger mass of O_2. However, the quenching cross sections with an O_2 collider are approximately twice those with H_2. The RET cross sections for N_2, like those for H_2, appear largely

independent of N_{OH} (although the available data range is small), whilst in the O_2 case the cross sections actually appear to increase with N_{OH}. These patterns all suggest that, in each case, quenching and RET collisions are in competition. In the O_2 case, where electronic quenching cross sections are nearly twice the size of those for RET at low N_{OH}, this actually results in the RET cross sections increasing as the quenching cross sections fall.

6.3 Depolarisation Cross Sections

6.3.1 Elastic Depolarisation

Some collisions do not result in a change in the spin-rotation level and are elastic. These can be separated into those that are purely elastic, where there is no change in the angular momentum direction, and those that lead to a change in the direction of the angular momentum. Cross sections for this elastic depolarisation can be obtained from the spin-rotation level resolved fluorescence decay of excited state OH(A) radicals as described in the previous chapter. The experiment is only sensitive to the elasticity of the OH(A) radical and so the collision might be inelastic with respect to the H_2 rotation.

Table 6.4 details the experimentally-determined elastic depolarisation cross sections following excitation to a number of spin-rotation levels. Data are shown for both the depolarisation of oriented and aligned distributions. The spin-rotation level $N_{OH} = 0, j_{OH} = 0.5$ cannot be aligned, and its disorientation cross section is close to zero, indicating the initial orientation cannot be depolarised on collision. As explained previously, the intrinsic spin of the electronic motion of the OH(A) radical is the sole source of angular momentum in this spin-rotation level. As expected in the tensor

N_{OH}	j_{OH}	f_1/f_2	$\sigma_{\mathrm{el}}^{(1)}/\mathrm{\AA}^2$	$\sigma_{\mathrm{el}}^{(2)}/\mathrm{\AA}^2$
0	0.5	f_1	0.0 ± 0.1	
1	1.5	f_1		32.9 ± 3.1
2	1.5	f_2		36.7 ± 3.2
4	3.5	f_2	4.1 ± 2.4	12.2 ± 3.0
5	4.5	f_2	2.9 ± 1.1	14.4 ± 3.3
8	7.5	f_2	1.7 ± 0.7	12.6 ± 3.1

Table 6.4: Table showing the elastic depolarisation cross sections observed experimentally following excitation to various different spin-rotation levels, $N_{\mathrm{OH}}, j_{\mathrm{OH}}$, of the OH(A) radical in the presence of a H_2 collider.

opacity formalism used in the theoretical calculations, this spin must act as a spectator to the collisions, as has been seen previously with rare gas colliders [111, 114].

The disorientation cross sections are smaller than for disalignment. This, as previously discussed, is because the rotational tilt angle, $\theta_{N_{\mathrm{OH}}N'_{\mathrm{OH}}}$, required to completely depolarise orientation is larger than for alignment; this pattern will be seen once again in the experimental total depolarisation cross sections. The less dramatic collisions associated with elastic outcomes are less likely to bring about such a large change in the direction of polarisation so are more disaligning than disorienting.

Both sets of cross sections fall with increased rotational level. There is a particularly pronounced fall in the disalignment cross sections from $N_{\mathrm{OH}} = 2$ to 4. However, the lowest two disalignment cross sections will be affected by unresolved satellite lines, as shown in table 5.4. These satellite lines mean the cross sections for $N_{\mathrm{OH}} = 1$ and 2 include contributions from states populated by pure spin-rotation changing collisions ($j'_{\mathrm{OH}} \neq j_{\mathrm{OH}}, N'_{\mathrm{OH}} = N_{\mathrm{OH}}$), and are likely larger than the pure elastic depolarisation cross sections. This effect has been accounted for previously with experimental simulations [114]. In the OH(A)+Ar case, approximately a third of the disalignment cross sections at $N_{\mathrm{OH}} = 0$ could be attributed to these satellite lines [114]. At higher N_{OH}, the impact of satellite lines is negligible [114]. Whilst far from insignificant, the impact of unresolved satellite lines is insufficient to detract from the qualitative conclusion that

the experimental elastic disalignment cross sections decrease with N_{OH}. This dependence is partly because, as previously discussed, a larger torque is required to change the direction of rotation of a faster rotating diatom, leading to a smaller cross section.

There is insufficient data to make any judgements about whether the nature of the spin-rotation level initially excited affects the elastic depolarisation cross section. However, as the electron spin behaves as a spectator, it is unlikely to make a significant difference beyond the geometric one discussed in section 4.3.2.

6.3.2 Total Depolarisation

Table 6.5 lists the experimentally-determined total disorientation and disalignment cross sections following excitation of various spin-rotation levels in the OH(A) excited state. These depolarisation cross sections include the contributions to depolarisation accompanying RET collisions as well as elastic depolarisation. As with the RET cross sections there is at best only weak dependence on the rotational quantum number N_{OH}, with a slight decline observed. Many of the arguments for the pattern of RET cross sections apply here, because depolarisation accompanying RET is a major contributor to the depolarisation cross sections. This includes explaining the relative lack of N_{OH} dependence, since elastic depolarisation cross sections have already been demonstrated as dependent upon N_{OH}, though they make a comparatively small contribution to total depolarisation. The depolarisation cross sections are consistently larger than the RET cross sections because of additional elastic depolarisation, and they do appear somewhat more dependent on N_{OH} than RET due to that contribution. There is once again little appreciable difference between cross sections measured following excitation to different spin-rotation manifolds. Indeed for $N_{\mathrm{OH}} = 5$, the f_1 and f_2 cross sections lie almost on top of one another.

N_{OH}	j_{OH}	f_1/f_2	$\sigma^{(1)}$/Å^2	$\sigma^{(2)}$/Å^2
0	0.5	f_1	29.8 ± 12.1	
1	1.5	f_1	28.1 ± 14.5	65.8 ± 11.7
2	2.5	f_1	17.6 ± 10.6	
2	1.5	f_2	28.1 ± 7.9	40.1 ± 22.4
3	3.5	f_1		30.0 ± 6.76
4	3.5	f_2	21.8 ± 6.6	29.9 ± 8.7
5	5.5	f_1	19.9 ± 3.4	22.1 ± 4.8
5	4.5	f_2	19.4 ± 5.1	23.4 ± 12.9
6	5.5	f_2	18.2 ± 9.5	22.8 ± 5.3
7	7.5	f_1	16.1 ± 8.5	25.9 ± 4.3
8	7.5	f_2	12.2 ± 4.6	23.5 ± 9.4
10	10.5	f_1	18.9 ± 2.6	17.6 ± 4.0
10	9.5	f_2	16.4 ± 12.5	

Table 6.5: Table showing the total depolarisation cross sections observed experimentally following excitation to various different spin-rotation levels, N_{OH}, j_{OH}, of the OH(A) radical in the presence of a H_2 collider.

As expected total disalignment cross sections are larger than total disorientation, but this difference is only pronounced at low N_{OH}. In order to explain this, it is worth considering the size of the inelastic depolarisation cross sections, determined from the difference of the total depolarisation and elastic depolarisation cross sections. These inelastic depolarisation cross sections are given in table 6.6. The data set is extremely limited, as only in three cases are there cross sections available for both disalignment and disorientation. Additionally the low N_{OH} inelastic disalignment cross sections are difficult to determine because of the contribution of satellite lines in the elastic depolarisation cross sections.

The inelastic depolarisation cross sections for disalignment and disorientation are within the error bars of one another. Additionally, they are comparable in size to the RET cross sections. Consequently, it is clear that inelastic collisions lead to both complete disalignment and disorientation (at least for these mid value N_{OH} levels). Furthermore, the difference in total depolarisation cross sections for disorientation and disalignment largely arises from the difference in their elastic depolarisation cross

N_{OH}	j_{OH}	f_1/f_2	$\sigma_{\mathrm{in}}^{(1)}/\mathrm{\AA}^2$	$\sigma_{\mathrm{in}}^{(2)}/\mathrm{\AA}^2$
4	3.5	f_2	17.7 ± 6.6	17.7 ± 8.7
5	4.5	f_2	16.5 ± 5.1	9.0 ± 12.9
8	7.5	f_2	10.5 ± 4.6	10.9 ± 9.4

Table 6.6: Table showing the inelastic depolarisation cross sections determined experimentally from total and elastic depolarisation measurements. Measurements follow excitation to various different spin-rotation levels, $N_{\mathrm{OH}}, j_{\mathrm{OH}}$, of the OH(A) radical in the presence of a H_2 collider. Only data where a cross section for both disalignment and disorientation have been included.

sections. Since the elastic depolarisation cross sections fall with N_{OH}, the difference between the total depolarisation cross sections for alignment and orientation similarly falls.

6.3.3 Comparison of Cross Sections with other Colliders - Helium and Argon

As with the RET cross sections, figures 6.7 and 6.8 compare the depolarisation cross sections for OH(A)+H_2 with those with He and Ar colliders [34, 57, 114].

Firstly, considering the elastic depolarisation in figure 6.7; as with the RET cross sections those for H_2 typically lie between those of He and Ar. Again, the Ar cross sections are larger than those for He, and this pattern arises for both kinematic and dynamic reasons [34]. For He the cross sections are seen to fall with increased N_{OH}, whilst they remain approximately constant in the case of Ar. For the Ar collision system, it has been suggested in reference [114] that whilst collisions in the plane of the rotating OH radical will induce RET, out of plane collisions lead to elastic depolarisation or RET. Along with studies by Alexander and Dagdigian [169, 170], this study suggested that elastic depolarisation is most efficient with 'following'-type trajectories where the PES is sufficiently attractive and anisotropic to trap the colliding atom in a complex. Furthermore, it was suggested that in this approach geometry the anisotropy of the potential was less rapidly washed out, helping to sustain elastic depolarisation

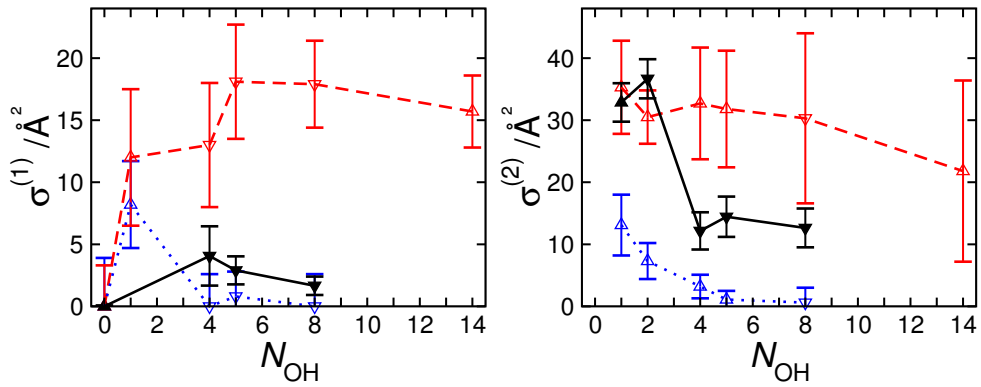

Figure 6.7: Experimentally-measured elastic depolarisation cross sections for OH(A) with various colliders - H_2 in filled black triangles connected by full lines, He in open blue triangles connected by dotted lines, and Ar in red triangles connected with dashed lines. Upwards pointing triangles are cross sections determined following excitation to the f_1 spin-rotation level and downwards pointing triangles are cross sections determined following excitation to the f_2 spin-rotation level. The left-hand panel shows data for disorientation and the right-hand panel for disalignment.

to higher N_{OH} with Ar colliders. The He PES is insufficiently attractive to create complexes so this system has very poor levels of elastic depolarisation, which also fall with N_{OH}. Kinematically, once again a heavier collider species (here Ar rather than He) is capable of applying more torque and so leads to a larger depolarisation cross section.

The explanation for the OH(A)+H_2 elastic depolarisation cross sections lying between those of OH(A)+He and OH(A)+Ar is similar to that put forward to explain this pattern for RET; the more attractive and anisotropic PES is sufficient to more than overcome the advantage for elastic depolarisation He draws from its greater mass, but not when compared to the considerably larger mass of Ar. Despite the very different surfaces, both H_2 and He show a fall in the elastic depolarisation cross section with N_{OH}, though this is far more pronounced for He. The more complex PES describing the OH(A)+H_2 collision system (arising from the fact that two diatoms are involved), may mean that arguments about particular kinds of approach geometries leading to RET and elastic depolarisation are not appropriate. If, however, it were the case that the H_2 collider needed to approach out of the plane of the OH(A) rotation, this would imply that the middle panel of figure 3.2 is the most relevant in considering the dynamics

involved. This 2D slice of the PES has a well depth of $-1344\,\mathrm{cm}^{-1}$ which is comparable to well depths for the OH(A)+Ar system, but the surface here is considerably less anisotropic than the OH(A)+Ar PES suggesting the anisotropy can more easily be washed out. If these approach geometries were significant for OH(A)+H_2 elastic depolarisation as they are for OH(A)+Rg systems, this may explain why the elastic depolarisation cross sections for OH(A)+H_2 are N_{OH} dependent. The QCT calculations are supportive of this argument, unlike in OH(A)+Kr or OH(A)+Ar QCT calculations [37, 111, 116, 117], depolarisation cross sections are seen to fall with increasing N_{OH} in section 4.5.1. The deflection functions in subsection 4.2.1 indicate this is precisely because there are fewer following or complex forming collisions with elastic trajectories at high N_{OH}.

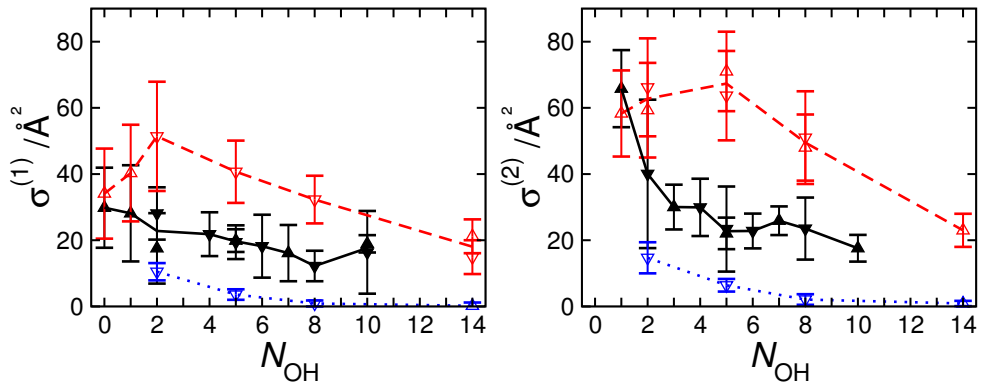

Figure 6.8: Experimentally-measured total depolarisation cross sections for OH(A) with various colliders - H_2 in filled black triangles connected by full lines, He in open blue triangles connected by dotted lines, and Ar in red triangles connected with dashed lines. Upwards pointing triangles are cross sections determined following excitation to the f_1 spin-rotation level and downwards pointing triangles are cross sections determined following excitation to the f_2 spin-rotation level. The left-hand panel shows data for disorientation and the right-hand panel for disalignment.

Figure 6.8 compares the total depolarisation cross sections for the three colliders, and it comes as no surprise to see the OH(A)+H_2 cross sections lying between those with He and Ar colliders once again. This pattern can again be explained by consideration of the more attractive and anisotropic OH(A)+H_2 PES, its light reduced mass, and the role of quenching processes that compete with inelastic collisions.

Once the contribution to the total depolarisation from elastic depolarisation is accounted for, it is clear that for the Ar collider the RET and remaining (inelastic) depolarisation cross section are comparable in size. As with OH(A)+H_2, OH(A)+Ar collisions lead to the complete randomisation of the direction of the angular momentum. For He collisions the depolarisation moments are slightly larger than 0, but RET collisions are nonetheless extremely depolarising. Total depolarisation cross sections with He and Ar colliders fall with N_{OH} whilst with H_2 this dependence is weak. As noted in the discussion on RET cross sections in section 6.2, this behaviour is best explained by considering the competing electronic quenching process in the OH(A)+H_2 system not seen in the other cases, which is itself N_{OH} dependent.

As with the previous cross section comparisons, the error bars for the H_2 data are generally slightly larger than those with the rare gas atoms. This is to be expected as there is less signal in the OH(A)+H_2 experiments, owing to the larger pump-probe delay time required with a less effective translational moderator - H_2. This larger delay time allows more of the OH(X) radical products of the H_2O_2 photolysis to leave the interaction region. Immediately following photolysis the OH(X) radicals have considerable translational energy and their concentration is focused in the interaction region. The longer delay time allows a larger population of OH(X) to leave the reaction chamber through pumping, or simply leave the interaction region through diffusion. The OH(X) radicals are also translationally excited immediately following photolysis and 'fly out' of the interaction region. Since H_2 is a poor translational moderator, they move at this superthermal speed for longer and more OH(X) radicals will leave the interaction region. Collectively these factors mean there is a smaller concentration of OH(A) radicals in the interaction region for probing, and consequently reduced signal in the experiments.

6.4 Comparison of Cross Sections with other Colliders - Xenon

Comparison with the cross sections determined experimentally for OH(A)+Xe is useful for two reasons. Unlike the lighter noble gas colliders, this system has appreciable electronic quenching cross sections, larger in fact than for OH(A)+H_2. Secondly, the system has a very deep potential well ($\sim$12000 cm^{-1}) comparable to the deepest well in the OH(A)+H_2 PES, although the potentials are still vastly different. The OH(A)+Xe PES is shown in figure 6.9. The potential extends over a longer range due to the large polarisable Xe atom, whilst the OH(A)+H_2 involves four rather than three atoms and is consequently considerably more complex, with 6 rather than 3 internal co-ordinates. The Xe collision potential consists of two attractive wells for linear geometries, separated by a repulsive region which is essentially an extension of the inner repulsive wall seen in most PESs. As set out in section 6.1.1 and shown in figure 6.2, a conical

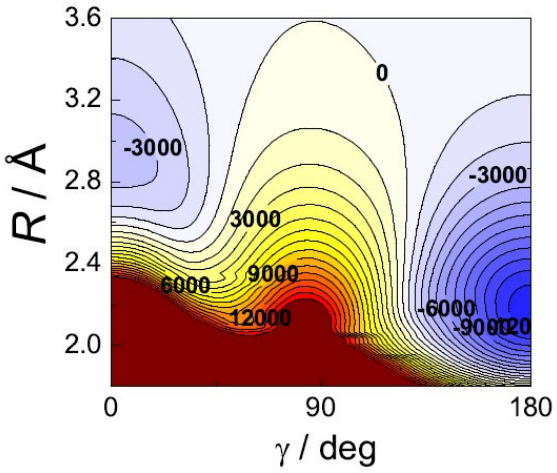

Figure 6.9: Potential energy surface for OH(A)+Xe. Contours are separated by 1000 cm^{-1}, blue shaded regions are attractive, whilst repulsive regions are coloured in a yellow-red spectrum. Quoted energies are given in cm^{-1}. Figure is adpated from that provided in reference [24] and the surface provided by Jacek Kłos [112, 286].

intersection has been identified in the deep potential well in the HO-Xe linear geometry. The PES used in the theoretical calculations in this thesis, as well as alternative calculations describing the OH(A)+H_2 potential outlined in section 1.9.3, demonstrate that this surface contains seams of conical intersections in valleys of attractive regions, stretching over multiple geometries. There are also considerable repulsive barriers to these attractive regions, and as with the OH(A)+Xe surface, deep potential wells not associated with conical intersections. The resulting surface is considerably anisotropic, comparable to the OH(A)+Xe surface.

Studies by Perkins [24] have used the same Zeeman quantum beat spectroscopy technique employed here in studying OH(A)+H_2, to determine cross sections for the OH(A)+Xe system. The RET cross sections for the OH(A)+H_2 and OH(A)+Xe [24, 112] collision systems are compared in the left-hand panel of figure 6.10. The two sets of cross sections are very similar, suggesting a balance between a number of different factors that affect the size of RET cross sections for each system. This is at first surprising, because the OH(A)+Xe system has a more favourable PES and more favourable kinematics for RET. The OH(A)+H_2 surface can be considered less favourable because, as presented in chapter 2, it contains several repulsive regions which hinder access to the attractive regions thought responsible for RET. Additionally, the heavier mass of Xe is able to apply a larger torque during collisions. Both colliders show little variation in the RET cross section with increasing N_{OH}. However, in both cases there are competing quenching processes also associated with the most attractive regions of the PES.

The right-hand panel of figure 6.10 compares the sum of measured RET and quenching cross sections. The larger quenching cross sections for Xe lead to combined cross sections that are now larger than those for H_2, typically by over 20 Å^2. This pattern would seem to reflect the more favourable kinematics and PES for OH(A)+Xe collisions. These combined cross sections slowly reduce with increasing N_{OH} as the

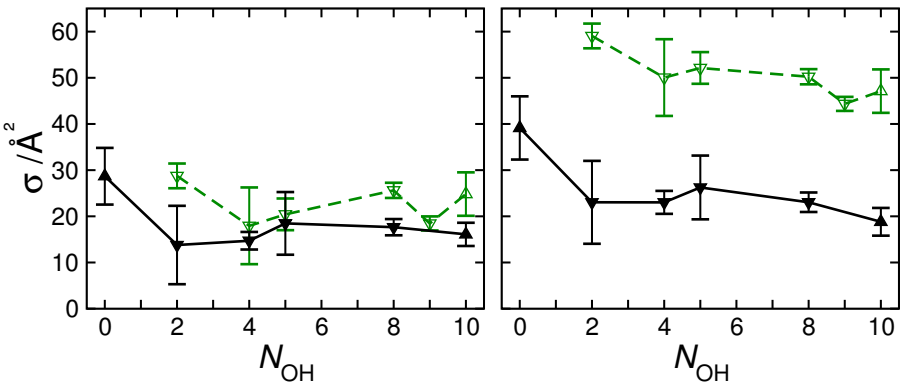

Figure 6.10: Experimentally-measured cross sections for OH(A) with various colliders - H_2 in filled black triangles connected by full lines, and Xe in open green triangles connected by dashed lines. The left-hand panel compares RET cross sections for the two systems, the right-hand panel sums the quenching and RET cross sections measured for each system. Upwards pointing triangles are cross sections determined following excitation to the f_1 spin-rotation level and downwards pointing triangles are cross sections determined following excitation to the f_2 spin-rotation level.

anisotropy associated with these inelastic processes is washed out. Both surfaces are extremely anisotropic, so this washing out is much slower than seen with other OH(A)+Rg surfaces.

Figure 6.11 compares the disalignment cross sections for Xe [24] and H_2 colliders. The figure displays total disalignment on the left, and elastic disalignment cross sections on the right. Disorientation cross sections have not been measured for Xe. For the total depolarisation cross sections, there is a dramatic difference in the relationship with increasing N_{OH}; Xe cross sections increase in magnitude, whilst H_2 cross sections decline. With Xe, falling competition from electronic quenching leads to more depolarising collisions occurring at higher N_{OH}. This reduction in quenching competition is also expected for H_2 but the depolarisation cross sections still fall slightly. The reduction in elastic depolarisation cross section is likely behind this.

For elastic depolarisation, the cross sections fall with H_2, but remain constant for Xe. This pattern is as seen in the comparison with the OH(A)+Ar system, and its explanation is likely the same. Note that in both collision systems elastic depolarising collisions and electronic quenching do not appear to be in competition.

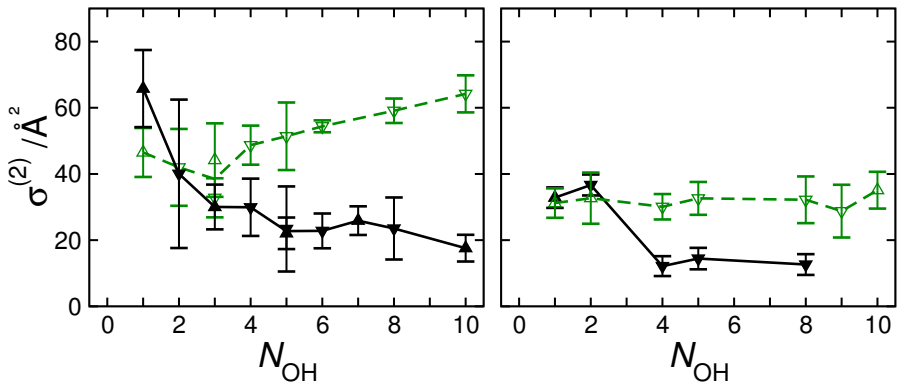

Figure 6.11: Experimentally-measured disalignment cross sections for OH(A) with various colliders - H_2 in filled black triangles connected by full lines, and Xe in open green triangles connected by dashed lines. Upwards pointing triangles are cross sections determined following excitation to the f_1 spin-rotation level and downwards pointing triangles are cross sections determined following excitation to the f_2 spin-rotation level. The left-hand panel shows data for total disalignment and the right-hand panel for elastic disalignment.

6.5 Summary

Experimentally-determined cross sections for electronic quenching, RET, elastic depolarisation and total depolarisation of OH(A) in collisions with H_2 have been presented. Where there are previous OH(A)+H_2 studies available for comparison, the results have agreed well. A rotational dependence has been observed for electronic quenching, as is characteristic of other OH(A) collision systems. However, only a weak rotational dependence has been seen for RET and total depolarisation. This is an unusual result when compared to light rare gas colliders. Elastic depolarisation cross sections show some rotational dependence.

Qualitatively it has been demonstrated that the magnitude of the various experimentally-determined cross sections result from competing kinematic and dynamic factors, by comparing with results acquired with monoatomic colliders, He and Ar. The competing quenching process, and the non-adiabatic nature of the full potential, clearly have an impact on the H_2 RET and total depolarisation cross sections not seen for the light rare gases. This has been considered further by comparing with the heavier Xe

collider, which also shows considerable electronic quenching.

The experimental results are discussed further in chapter 7, where they are compared with the predictions of theoretical quasi-classical trajectory calculations.

Chapter 7

Comparison and Further Analysis

This chapter continues the discussion of the OH(A)+H_2 collision system. It compares the cross sections determined from QCT calculations with those determined through experimental measurements. There is also an analysis of the extent to which the classical trajectories can account for the quenching cross sections observed experimentally.

An energy difference arises between the energy at the end of the trajectory, and the energy after binning the final rotational quantum states of the diatoms. This is suggested as a cause of the discrepancies between QCT calculations and the experimental results. To attempt to correct for this, a variety of alternative binning methods based upon Gaussian binning are developed and applied to the calculations. The chapter concludes by considering the relative importance of different factors that may explain the discrepancies between theoretical and experimental results.

7.1 Comparison of Experiment and Theory

In the analysis of QCT results in chapter 4, the initial N_{H_2} was a specified integer value, corresponding to a specific rotational quantum state of the H_2. In comparison with the experiment the initial N_{H_2} in each trajectory is instead chosen from a weighted distribution - a product of the nuclear spin statistics for hydrogen and the Boltzmann

distribution, as described in equation (3.9). Final cross sections are determined from this weighted distribution.

As shown in Figures 7.1 to 7.3, there is in general rather poor agreement between the adiabatic QCT cross sections and the experimental data. In particular, the calculated RET and total depolarisation cross sections are systematically larger than those found experimentally.

7.1.1 Rotational Energy Transfer

Figure 7.1 compares RET cross sections determined from experiments with those from QCT calculations on the OH(A)+H_2 first excited state PES. The agreement is both qualitatively and quantitatively poor. Qualitatively, whilst the cross sections fall with increased initial N_{OH} in the QCT calculations, the experimental cross sections are approximately constant. Quantitatively, the calculated cross sections are systematically larger than those found experimentally, in excess of twice the size.

One potential reason for the discrepancy, is that the QCT calculations do not

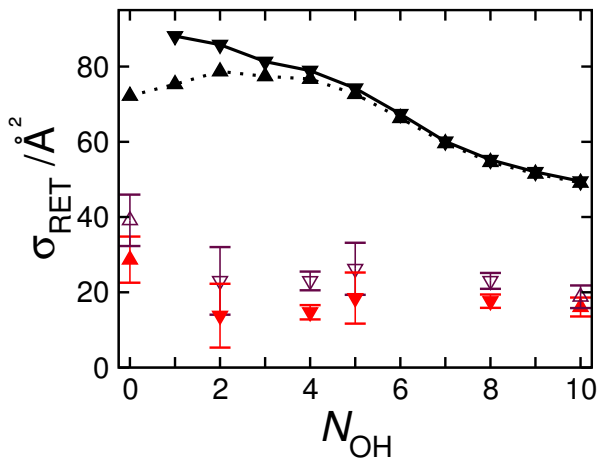

Figure 7.1: Experimentally-measured RET cross sections, shown in red, are compared with those from adiabatic QCT calculations in black. The open purple triangles sum the experimentally-determined RET and electronic quenching cross sections. Upwards pointing triangles are for OH(A) initially in an f_1 spin-rotation level and downwards pointing triangles where the initial OH(A) is in the f_2 spin-rotation level.

account for competing quenching processes. As discussed in the previous chapter, electronic quenching in OH(A)+H_2 occurs via conical intersections located in extremely attractive potential energy wells in the excited state surface [126, 178, 187, 189, 259]. These wells are likely to be responsible for considerable RET and depolarisation in the adiabatic QCT calculations. Therefore, the competing electronic quenching process is likely to reduce the RET and collisional depolarisation cross sections compared with the adiabatic theory.

QCT surface hopping studies of OH(A)+Kr, approximately account for non-adiabatic coupling to the ground electronic state in that system [24, 93]. In these studies, the RET and depolarisation cross sections were suppressed somewhat compared to those calculated from purely adiabatic QCT calculations [93]. Future studies could attempt to carry out similar surface hopping studies on the OH(A)+H_2 system.

In order to make some estimate of the impact this competing quenching may have, figure 7.1 also compares the results of QCT calculations with the sum of the experimentally-observed quenching and RET cross sections. Whilst this is a simplistic comparison, the cross sections from QCT calculations are still considerably larger than these combined cross sections, suggesting additional sources of error in the QCT calculations which will be discussed throughout this chapter.

7.1.2 Total Depolarisation

Figure 7.2 extends the comparison of experiment and theory to total depolarisation cross sections. As with RET cross sections, there is considerable disagreement between experiment and theory. Generally the QCT calculated cross sections fall more rapidly than experimentally, for which the decline is slight. The QCT calculated cross sections are also much larger than those found experimentally, with this difference typically more pronounced at low N_{OH}. However, QCT calculated cross sections at high N_{OH}

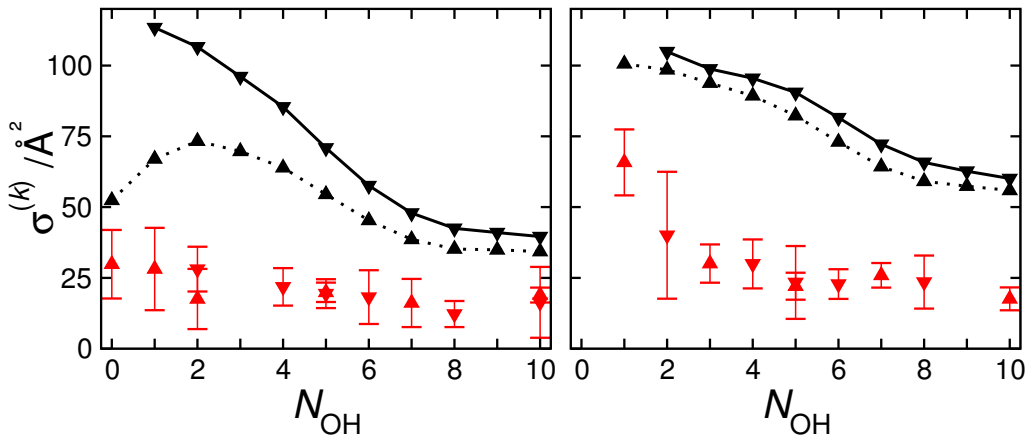

Figure 7.2: Comparison of total depolarisation cross sections determined from experiment (red triangles) and QCT calculations (black triangles). The left-hand panel compares total depolarisation cross sections for orientation ($k = 1$), whilst the right-hand panel compares total depolarisation cross sections for alignment ($k = 2$). Upwards pointing triangles are for OH(A) initially in an f_1 spin-rotation level and downwards pointing triangles where the initial OH(A) is in the f_2 spin-rotation level.

are still more than twice those measured experimentally.

Competing electronic quenching collisions, not accounted for in the adiabatic QCT calculations, likely play some part in the disagreement between experiment and theory. In addition to the neglect of non-adiabatic effects, discrepancies may also arise from errors in the classical binning methodology detailed later in section 7.3. Alternatively, the observed disparities may arise from inadequacies in the way the forces or dynamics of the system are considered in the classical trajectories. Any inaccuracies in the adiabatic PES would lead to deficiencies in the calculation of the forces governing collisions. The constraint on the dynamics introduced on fixing the bond lengths in the QCT calculations could also present problems. This may restrict trajectories from entering the deep well regions of the PES most likely to cause RET, collisional depolarisation, and also electronic quenching. These two factors are considered further in section 7.2.

There is also the possibility that errors arise from the experimental data, although this seems unlikely on the basis of agreement between results determined from this ZQBS method and other experiments, and secondly because of the good previous

agreement between experiment and theory in simpler systems. Where the experimental measurements of this study can be compared with those from previous studies, as in the case of electronic quenching cross sections [91, 92] and limited RET cross sections [109], there has been good agreement. Cross sections determined from the ZQBS method have also proved reliable relative to other experiments in previous studies. For example, RET cross sections determined for OH(A)+Ar [57] agreed with those determined by Jorg *et al.* [297], whilst the elastic depolarisation cross sections [55] showed strong agreement with those measured by Brinkman and Crosley [20]. Likewise, the combined elastic depolarisation and RET cross sections measured for OH(A)+Ar and OH(A)+He systems using ZQBS, agreed strongly with those measured for the analogous property of bulk polarisation loss, $\sigma_{\mathrm{PS}}^{(k)}$, determined using a polarisation spectroscopy technique in studies by McKendrick and co-workers [114].

Systems such as NO(A)+Ar or OH(A)+Ar/He have been simpler to investigate theoretically because consideration of only one electronic state is appropriate, and there are 6 rather than 9 internal co-ordinates [34, 37]. In these cases there has been broad agreement between the results of ZQBS experiments and those from QCT calculations for elastic depolarisation, total depolarisation and RET cross sections, suggesting that ZQBS techniques are appropriate in the determination of these properties [57, 264].

7.1.3 Elastic Depolarisation

Figure 7.3 extends the comparison of cross sections from experiments and QCT calculations to the elastic depolarisation cross sections. In the case of elastic disorientation, the QCT calculations, once again, give a larger than expected cross section compared to experiment. However, there is reasonable agreement between the two data sets for disalignment. More generally, it is noteworthy that experiment and theory are in somewhat better agreement for the elastic depolarisation cross sections than for the RET

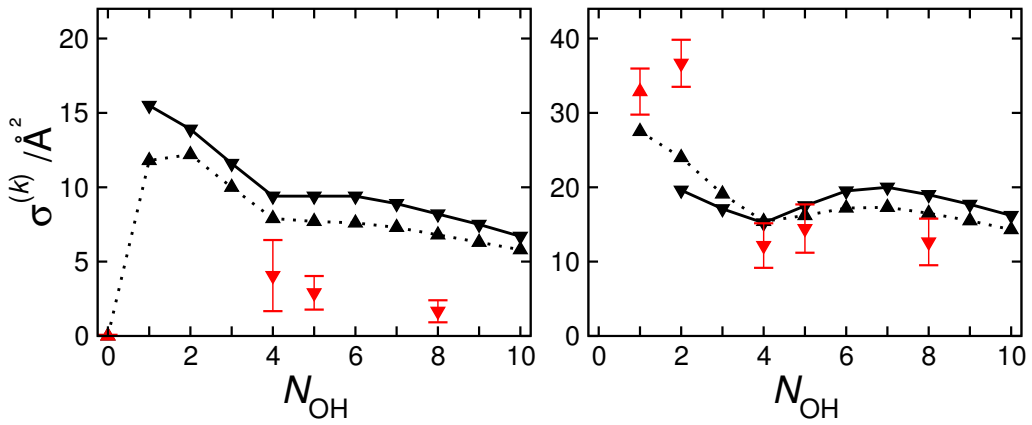

Figure 7.3: Comparison of elastic depolarisation cross sections determined from experiment (red triangles) and QCT calculations (black triangles). The left-hand panel compares elastic depolarisation cross sections for orientation ($k = 1$), whilst the right-hand panel compares elastic depolarisation cross sections for alignment ($k = 2$). Upwards pointing triangles are for OH(A) initially in an f_1 spin-rotation level and downwards pointing triangles where the initial OH(A) is in the f_2 spin-rotation level.

and total depolarisation cross sections.

The consideration of elastic depolarising collisions in the QCT calculations of chapter 4 drew a number of conclusions. Firstly, based on the opacity functions presented in section 4.4, elastic depolarisation is slightly more prevalent than inelastic collisions at higher initial impact parameters. At these larger initial impact parameters, the trajectory is more likely to explore longer range attractive regions of the PES, and undergo collisions of a more glancing nature, these regions are not those responsible for quenching. Secondly, there was a reduced amount of complex forming collisions at higher N_{OH}, and that this was likely responsible for the declining elastic depolarisation cross sections. Finally, the discussion in subsection 6.3.3 speculated that elastic depolarising collisions may involve H_2 approach out of the plane of rotation of the OH(A) radical. All these observations suggest that the collisions that cause elastic depolarisation are less likely to explore the extremely attractive well regions of the PES thought responsible for electronic quenching compared with inelastic collisions. Consequently, the adiabatic nature of the QCT approach is less likely to have an impact on calculations concerning elastic depolarisation.

7.2 Electronic Quenching and the PES

In this work, trajectories are confined to a single adiabatic PES, but as already discussed this is an insufficient way to characterise the OH(A)+H_2 collision system with non-adiabatic effects being important, not least in explaining electronic quenching collisions [126, 178, 187–189, 259]. Whilst electronic quenching cannot take place in the QCT calculations, it is possible to investigate how often trajectories sample geometries which are known to be associated with electronic quenching.

As discussed previously, the deepest parts of the excited state PES, and those associated with electronic quenching, occur in geometries with the H_2 molecule approaching the oxygen end of the radical [126]. By recording the lowest potential energy sampled by the trajectories it is possible to track the number of trajectories entering these well regions of the PES. Figure 7.4 displays distributions of the minimum energy reached by trajectories in QCT calculations, for different initial OH(A) angular momenta. Oxygen well regions correspond to the far left of these graphs, with energies at around $-10000\,\mathrm{cm}^{-1}$, and are not shown because the trajectories do not sample this well. This is quite surprising, given that explanations for electronic quenching involve the OH(A) radicals passing through conical intersections in this region of the PES.

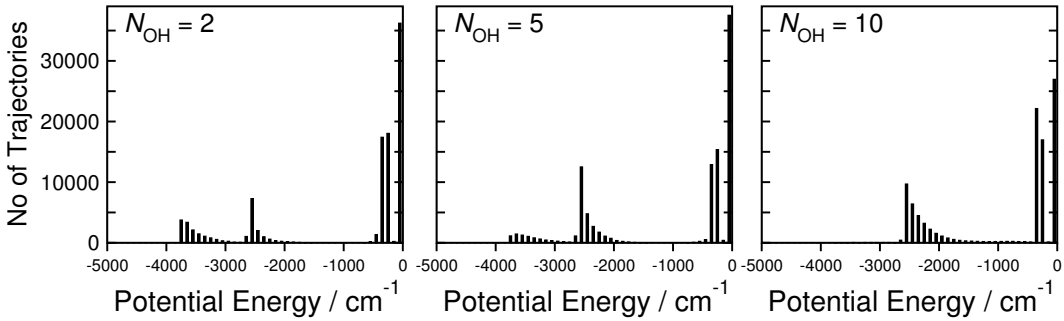

Figure 7.4: Histograms showing the distribution of deepest energy points reached in the course of trajectories. The left-hand panel has an initial OH(A) angular momentum of $N_{\mathrm{OH}} = 2$, the middle panel $N_{\mathrm{OH}} = 5$, and the right-hand panel $N_{\mathrm{OH}} = 10$. The initial state of H_2 was $N_{\mathrm{H_2}} = 1$. Each bar represents the number of trajectories with a minimum energy $50\,\mathrm{cm}^{-1}$ either side of the central value. There are in total 1×10^5 trajectories for each panel.

Figure 7.5 presents cuts through the potential energy surface for the O-end approaches associated with the deepest potential wells and electronic quenching. In the linear $C_{\infty v}$ approach, there is a considerable potential barrier to entering the well of $5606\,\mathrm{cm}^{-1}$. Likewise in the C_{2v} geometry there is a potential barrier of $432\,\mathrm{cm}^{-1}$, which is the smallest identified potential barrier on this PES prior to the O-end wells associated with collisional quenching. These barriers are larger than the thermal collision energy of $315\,\mathrm{cm}^{-1}$, so cannot be accessed classically. It is possible that the smaller barriers could be penetrated through quantum mechanical tunnelling, which the QCT method would not account for.

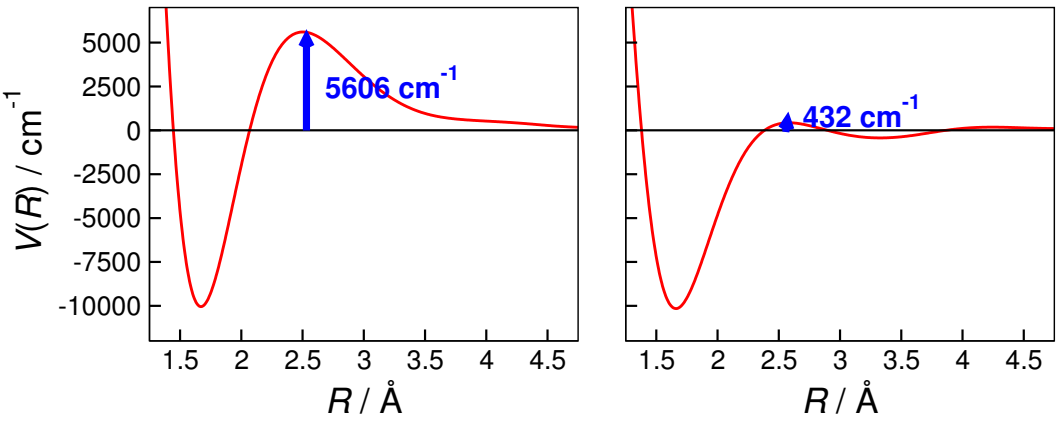

Figure 7.5: Potential energy curves for different approach geometries for the OH(A)+H_2 system derived from the surface used in QCT calculations. Bond lengths are fixed at the equilibrium values for infinitely separated diatoms. Both curves are for geometries where the oxygen end of the OH(A) diatom is directed at the H_2. The left curve is for a C_{2v} approach geometry whilst the right curve is for an O-end co-linear approach. R is the diatom separation distance.

Alternatively, it could be that these barriers are penetrated at higher collision energies. The QCT calculations presented thus far have been carried out for a fixed collision energy of $315\,\mathrm{cm}^{-1}$ (39 meV), yet the true collision energy follows a thermal distribution. It could be that the barriers discussed here are penetrated at the higher collision energies within the tail of the Maxwell-Boltzmann distribution of energies. In order to consider this possibility further QCT calculations were carried out at a higher collision energy. $1\mathrm{x}10^5$ trajectories were run at a higher collision energy of $1613\,\mathrm{cm}^{-1}$

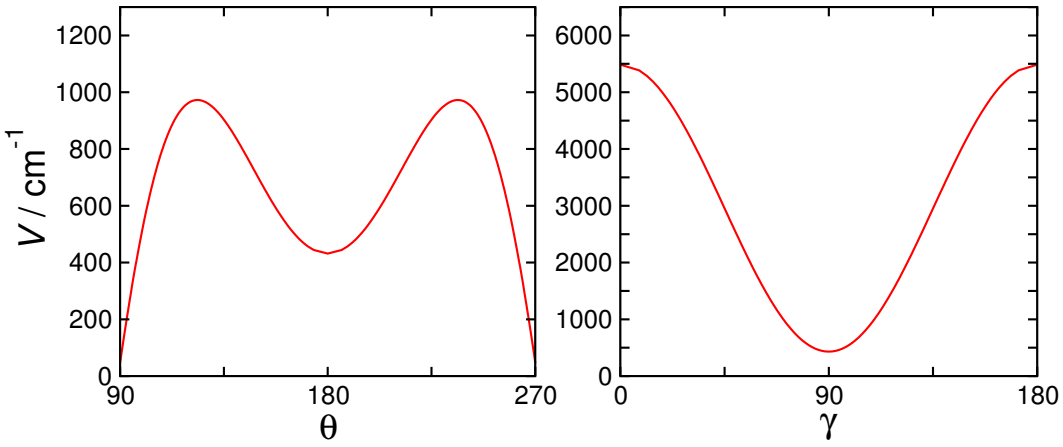

Figure 7.6: Potential energy curves displaying the variation of the OH(A)+H_2 potential on rotating the diatoms away from the barrier to the O-end potential well in the C_{2v} approach geometry. The angles are as described in subsection 3.1: θ the rotation of the OH(A) diatom (shown in the left-hand panel), and γ the H_2 diatom (shown in the right-hand panel). The O-end C_{2v} geometry is at $\theta = 180°$, $\gamma = 90°$, and the diatoms are held in the same plane.

(200 meV) for $N_{OH} = 2$, but still no trajectories entered the O-end potential energy well. This is likely because, whilst this would be sufficient energy to circumvent the barrier in a precise C_{2v} geometry, the rotation of the two diatoms makes this difficult to achieve.

Figure 7.6 demonstrates the angular dependence of the potential as the diatoms rotate away from the C_{2v} geometry (corresponding to $\theta = 180°$, $\gamma = 90°$) at the intermolecular distance for the minimum barrier ($R = 4.88$Å). θ relates to OH(A) rotation and γ to H_2 rotation. The potential rapidly grows with diatom rotation (especially H_2) and the point of the minimum barrier is a tight valley in the PES that rotating molecules are unlikely to pass through, even at collision energies of 200 meV. The left-hand panel shows the potential falling to 0 cm^{-1} at angles lower than 135° or greater than 225° but these more side-on approaches do not lead to O-end wells. The situation is more stark when the rotation with respect to the dihedral angle, ϕ, is considered, as this also raises the barrier height.

Figure 7.4 demonstrates that other well regions of the PES are sampled by the trajectories. These can be considered alongside the slices of the PES presented in figures 3.1 and 3.2 of chapter 3. Wells in which the H_2 approaches the hydrogen end of the OH(A) radical in a C_{2v} geometry account for the trajectories at around $-3500\,\mathrm{cm}^{-1}$. The C_{2v} H-end well depth is $-3882\,\mathrm{cm}^{-1}$ but this is for a co-planar geometry and there are slightly smaller well depths for similar geometries that are either slightly off planar, or planar but slightly out of the C_{2v} geometry - hence the spread in energies. The trajectories experiencing deepest energy points of around $-2500\,\mathrm{cm}^{-1}$ correspond with those in geometries close to $\theta = 53°$, $\gamma = 90°$, $\phi = 0°$ in the top panel of figure 3.1 which has a well depth of $-2656\,\mathrm{cm}^{-1}$. The geometry of the deepest point of this well is contiguous with the shallower well shown in the middle panel of figure 3.2. These geometries shall be described as resulting from side-on collisions. The number of trajectories entering these different well regions is sensitive to N_{OH}. As N_{OH} increases (see middle and right-hand panels) fewer trajectories enter the hydrogen wells, with none entering at $N_{\mathrm{OH}} = 10$, and there is a corresponding increase in the number of trajectories experiencing the side-on wells as their deepest potential.

Figure 7.7 replicates the 'lowest energy point reached' histogram, but this time in

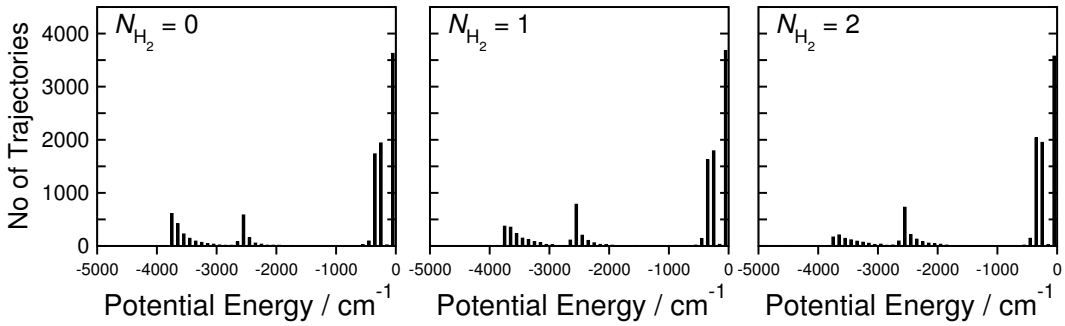

Figure 7.7: Histograms showing the distribution of deepest energies experienced over the course of the trajectory. The left-hand panel has an initial H_2 angular momentum of $N_{H_2} = 0$, the middle panel $N_{H_2} = 1$, and the right-hand panel $N_{H_2} = 2$. The initial state of OH was $N_{\mathrm{OH}} = 2$. Each bar represents the number of trajectories with a minimum energy $50\,\mathrm{cm}^{-1}$ either side of the central value. There are a reduced total of 1×10^4 trajectories for each panel.

terms of N_{H_2}. The pattern is very similar to that seen with increasing N_{OH}, with the C_{2v} geometry H-end well being probed less with increasing N_{H_2}. The potential in this region is clearly anisotropic with respect to rotation of either diatom. Given that OH(A) RET was seen as largely independent of initial N_{H_2} in the QCT calculations, it would seem that entry into either well is equally capable of bringing about an RET collision. This is hardly surprising given even the shallowest well has a depth comparable to that of the OH(A)+Ar PES [113].

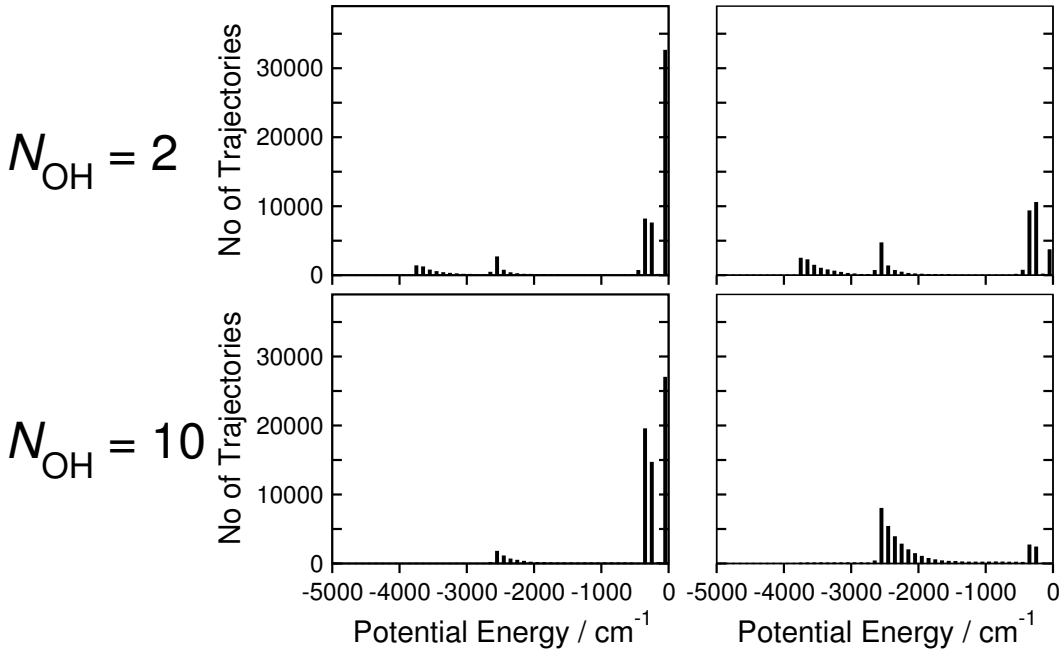

Figure 7.8: Histograms showing the distribution of deepest point energies reached in the course of trajectories. Trajectories are split into collisions that are considered elastic and inelastic in OH(A) on the left and right respectively. This analysis is of a closed shell nature. The top two panels are for trajectories starting in $N_{OH} = 2$ and the lower panels $N_{OH} = 10$, in each case $N_{H_2} = 1$. Each bar represents the number of trajectories with a minimum energy $50\,cm^{-1}$ either side of the central value. There are a total of 1×10^5 trajectories for each row of panels.

Figure 7.8 demonstrates the importance of the potential wells to inelastic and elastic collisions, where inelasticity is defined in terms of N_{OH}. The deepest potential experienced for trajectories starting in $N_{OH} = 2$ (top panels) and $N_{OH} = 10$ (bottom panels) are shown for elastic (left) and inelastic collisions (right). All parts of the potential energy surface are probed by trajectories included in each category. It is also clear that

trajectories entering into the potential wells are much more likely to be inelastic and that these wells are often important in bringing about RET.

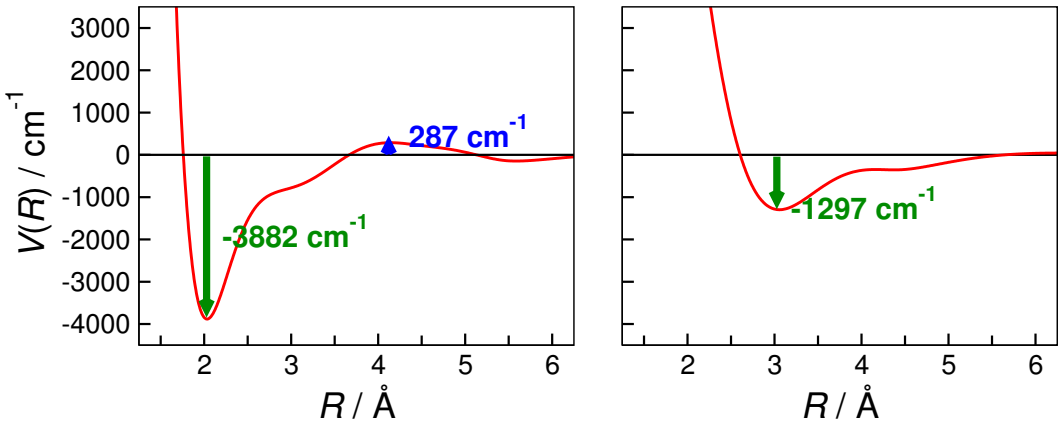

Figure 7.9: Potential energy curves for different approach geometries for the OH(A)+H_2 system, derived from the surface used in QCT calculations. Bond lengths are fixed at the equilibrium values for infinitely separated diatoms. The left curve is for a C_{2v} approach geometry where the H-end of the OH(A) diatom is directed at the H_2 diatom, whilst the right curve is for the co-parallel approach of the two diatoms (the bonds approaching side by side). R is the diatom separation distance.

Figure 7.9 shows the potential at approaches similar to those responsible for entry into these wells. The left-hand panel shows the potential for the H-end C_{2v} approach, whilst the right-hand panel shows a planar side-on approach with $\theta = 90°$, $\gamma = 90°$ and $\phi = 0°$. At the shorter separation distances associated with the H-end well, the surface is very anisotropic with considerable barriers to OH(A) and H_2 rotation. As a consequence, at higher N_{OH} (or N_{H_2}) the trajectories are unable to probe these wells as molecular rotation leads to the trajectory experiencing a more isotropic repulsive potential. Note that there is also a radial barrier to the H-end approach, but, unlike the barriers to O-end approaches, this barrier is smaller in height than the collision energy and so can be breached by classical dynamics. The side-on wells are at a larger intermolecular separation than those for the H-end approach. At these larger separations the PES is fairly isotropic with respect to OH(A) rotation, and the well can continue to be easily accessed at higher N_{OH}. The side-on approaches, whilst less attractive than the C_{2v} or $C_{\infty v}$ approaches, are still extremely attractive. Therefore, the high RET

and depolarisation seen in QCT calculations at high N_{OH} should be expected with this potential.

Earlier it was suggested that fixing the bond lengths in the dynamics calculations may be a cause of differences between experimental and QCT calculated cross sections, because it could prevent sampling of the oxygen well regions which are associated with electronic quenching. For example, it is known that on this PES the lowest energy conical intersections occur at slightly different bond lengths to those of OH(A) and H_2 at equilibrium [126]. Consequently, it might be that the barriers are also overcome at different bond lengths. The H_2 bond is the most relevant to consider, as several studies have reported that at points of intersection the OH(A) bond length does not vary much from equilibrium [126, 178].

Figure 7.10 shows the variation in the potential energy for the O-end $C_{\infty v}$ approach geometry with the H_2 diatom bond length. The black curve is that used in the QCT calculations, whilst the red is that which leads to the smallest barrier to the deep potential well. A third curve is also shown for further comparison. The bond length affects the depth of the well, the potential at large separation distances, and the height

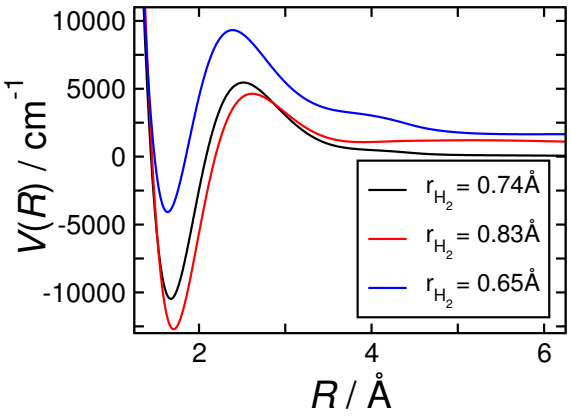

Figure 7.10: Potential energy curves for the O-end $C_{\infty v}$ approach geometry for the OH(A)+H_2 system, derived from the surface used in QCT calculations. The bond length of the H_2 diatom varies between the three curves as shown in the inset legend. The black curve corresponds to the H_2 equilibrium bond length used in trajectory calculations, r_{H_2}=0.741 Å. The bond length of the OH(A) diatom is fixed at the equilibrium length used in the trajectory calculations, r_{OH}=1.012 Å. R is the diatom separation distance.

of the potential barrier. Note, the potential curve only tends to zero at high intermolecular separation distances for the equilibrium bond lengths. Whilst a larger bond length lowers the barrier slightly, it is still over 4000 cm^{-1}. Consequently, if going via this geometry, the potential well is still inaccessible at thermal collision energies.

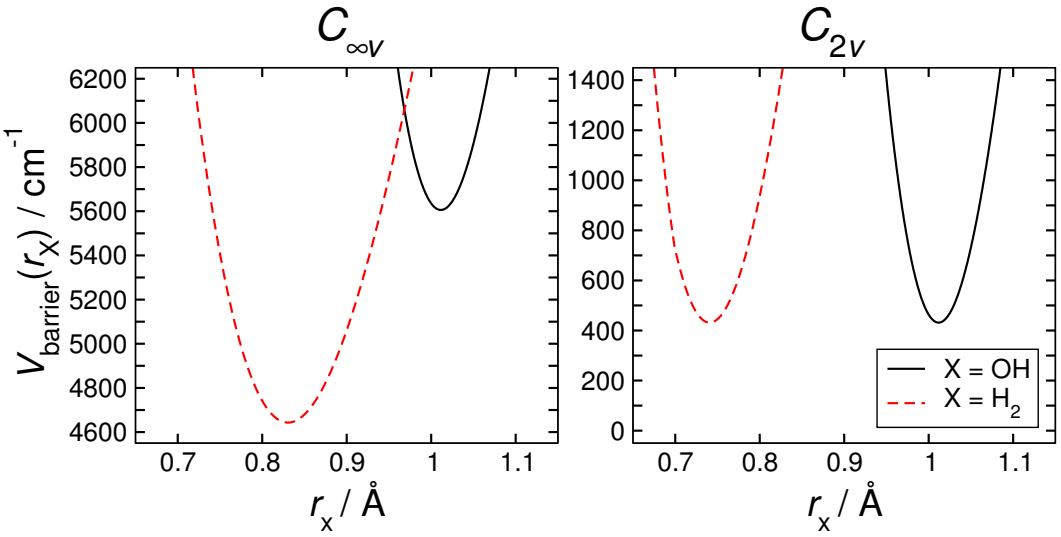

Figure 7.11: Potential energy curves that show the variation in the size of the potential barrier, with the bond lengths of each diatom in the OH(A)+H_2 system. The barrier is the largest potential at a separation distance larger than that of the potential wells in the O-end approach geometries - $C_{\infty v}$ on the left, and C_{2v} on the right. Red dashed curves show a variation in the length of the H_2 bond, whilst the black curve shows variation in the OH(A) bond length. In each case the bond length of the accompanying diatom in the potential is at the equilibrium length used in the QCT calculations here.

Figure 7.11 extends this analysis of the PES, by showing the variation with bond length of the potential barriers experienced on approach in both the O-end $C_{\infty v}$ and O-end C_{2v} geometries. It is clear that the size of the barrier is a function of the bond length, but for both geometries the barrier remains larger than the collision energy regardless. In the figure the bond length of the diatom accompanying that being varied in the potential curves is at its equilibrium length. However, the global minimum of the barriers has been found by varying the bond length of both diatoms. In the $C_{\infty v}$ case, the minimum barrier was found to be 4631 cm^{-1}, and in the C_{2v} approach, 432 cm^{-1}. The latter case is the minimum barrier identified in this study to the deep

potential wells associated with electronic quenching, and occurs at equilibrium bond lengths. Note that in this figure the intermolecular distance at the barrier's maximum height varies. However, the angles - θ, ϕ and γ - of the approach are fixed, therefore it is possible that there are routes around these barriers at different geometries at non-equilibrium bond lengths which have not been found.

Whilst considerable effort has been made to find smaller barriers, ultimately a full multi-dimensional analysis of the PES is beyond the scope of this thesis. However, several previous theoretical studies have concluded that there are barrierless approaches to the conical intersections [105, 107, 130, 178, 190, 298, 299]. This includes studies by Clary, Lester and co-workers, which stated that there were no barriers to entering conical intersections whilst remaining in an O-end C_{2v} geometry [105, 107, 130, 190, 299]. In this study it has been demonstrated that this is not the case with the Bowman *et al.* PES [126]. Additionally, the QCT calculations have probed the potential at fixed bond lengths that correspond to the smallest identified barrier to the O-end potential wells on the surface (in the O-end C_{2v} geometry). Therefore, the absence of trajectories entering into potential wells associated with electronic quenching is unlikely to be a fault of fixing the bond lengths in the QCT method, but more likely inaccuracies in the potential itself.

The analysis presented here has been complicated by recently published work [290, 291]. Several previous studies have concluded or been based upon the assumption that conical intersections are restricted to planar geometries. However, Yarkony and Dillon have recently demonstrated that conical intersections between the OH(A $2A'$)+H_2 and OH(X $1A'$)+H_2 PESs exist in off-planar geometries [290, 291]. Moreover, these conical intersections are within far shallower wells than the ones identified previously, but have bond lengths close to equilibrium for both diatoms. However, consistent with previous studies, all the identified conical intersections involve the O-end of the OH(A) radical directed at the H_2 diatom. The shallower conical intersections

do raise a concern that these regions are probed in the trajectories. However, the potentials calculated in the Yarkony study [290] do not agree with those in the PES used in this study, again raising questions about the quality of the PES employed here.

Due to errors in the PES, the QCT studies presented here have not explained the presence of quenching in the system. Whilst electronic quenching was not a possible outcome in the calculations of these studies, these inaccuracies will also have an impact on the outcome of adiabatic dynamics. The inappropriateness of this PES is therefore likely to be a major factor in the disagreement observed between RET and depolarisation cross sections found experimentally, and those found from the QCT calculations.

7.3 Problems with Histogram Binning

Over the course of a classical trajectory, energy and angular momentum are conserved. However, in binning final angular momenta to their nearest allowed quantum numbers, this conservation is no longer maintained. This is not unique to the OH(A)+H_2 system, and is intrinsic to QCT calculations, including similar studies on atom-diatom systems: NO(A)-Rg [115, 264] and OH(A)-Ar/He [37, 114, 115]. However, in these cases there was excellent agreement between experiment and theory. In OH(A)+H_2, there is the quantisation of angular momentum in two diatoms to be concerned about.

In the atom-diatom case, the principal concern is that trajectories with final angular momenta far away from their binned values contribute to depolarisation just as much as those trajectories that have final angular momenta close to the quantum-mechanically allowed value. The extra energy added when rounding up is usually small and comparable to that which could come from the translational motion, except at high N_{OH}, where there is minimal RET anyway. The energy removed from the system on rounding down could be considered to be additional to the translational energy. However, in OH(A)+H_2, these energy differences could allow for unrealistic RET in the partner

diatom. The problem is especially acute because of the much larger rotational constant of H_2 compared to that of OH(A) ($B_{H_2} = 60.853\,\mathrm{cm}^{-1}$ versus $B_{OH} = 17.358\,\mathrm{cm}^{-1}$ [46]). The H_2 can transfer rotational energy to the OH(A) diatom without having to undergo RET itself. Alternatively, it can become a recipient of rotational energy from the OH(A) diatom, without this being accounted for in a change in N_{H_2}. To be clear, that whilst the issues in this section are talked about as problems arising from binning, it is not the binning process that is the potential source of error. Rather, the potential error is the assumption that a quantised system can be propagated classically and that its true quantum nature can be accounted for by binning the final angular momenta at the end of the trajectory.

For the remainder of this chapter, new nomenclature is introduced to distinguish between classical properties associated with the trajectory, and the binned properties of the trajectory (subject to energy and angular momentum quantisation). As such, classical angular momentum at the end of the trajectory is given by

$$|\boldsymbol{\mathcal{L}'}| = \sqrt{\mathcal{L}'(\mathcal{L}'+1)}\hbar \tag{7.1}$$

where $\mathcal{L}'$ is a classical equivalent to the angular momentum quantum number. The classical angular momentum has associated energy $\mathcal{E}'$. N' refers to the final angular momentum quantum number following binning (as in the previous chapters) with corresponding energy E'.

If the initial conditions of a trajectory are $N_{OH} = 2$ and $N_{H_2} = 1$, a collision would be considered inelastic in H_2, and binned to $N'_{H_2} = 2$, with classical angular momentum $\mathcal{L}'_{H_2} = 1.5$ at the end of the trajectory. The classical energy is $136.9\,\mathrm{cm}^{-1}$ smaller than the value it is rounded to ($N'_{H_2} = 2$). At the same time, to bin $\mathcal{L}'_{OH}$ to $N_{OH} = 3$ requires only an increase to $\mathcal{L}'_{OH} = 2.5$, or $47.7\,\mathrm{cm}^{-1}$ of additional rotational energy. Both the $N_{OH} = 2 \rightarrow N'_{OH} = 3$ and $N_{H_2} = 1 \rightarrow N_{H_2} = 2$ transitions will be considered to have

taken place with only $154.2\,\mathrm{cm}^{-1}$ transferred to the diatoms from translational energy. In reality these transitions would require a total of $347.6\,\mathrm{cm}^{-1}$ in translational energy to be transferred to the two diatoms. This is greater than the total energy available, as the collision energy is $315\,\mathrm{cm}^{-1}$ at $300\,\mathrm{K}$. Whilst this is an extreme example, it illustrates how the QCT method can lead to the inclusion of RET collisions that are clearly not physical.

A second example makes clearer the way that the disparity between the rotational constants of the two diatoms increases this problem. Using the same initial conditions as above, the H_2 can gain up to $106.5\,\mathrm{cm}^{-1}$ of energy without being considered to undergo any transition, i.e. the trajectory is considered elastic for H_2. If rather than being taken from the translational energy this $106.5\,\mathrm{cm}^{-1}$ is taken from the rotational energy of the OH(A) radical, this brings about a reduction in rotational level of $N_{\mathrm{OH}} = 2$ to $N'_{\mathrm{OH}} = 0$. Observations in section 3.3.1 demonstrated that H_2 will readily behave as a sink for OH(A) rotational energy, particularly at high N_{OH}, indicating the importance of this example. Alternatively, (with the same initial conditions as before) the H_2 diatom can lose up to $76.1\,\mathrm{cm}^{-1}$ in rotational energy and the trajectory will still be considered elastic with respect to this diatom. This is again enough additional energy for $\mathcal{L}'_{\mathrm{OH}}$ to be binned to $N'_{\mathrm{OH}} = 3$. So when the angular momentum of OH(A) or H_2 is rounded down, energy has in effect been removed from the system, and when rounding up, energy has been created. The result of all these examples is to increase the levels of RET seen in the system for both OH and H_2. This could go some way to explaining the disagreements seen between experiment and theory, remembering that these are far smaller in the case of elastic depolarisation cross sections. The problem is heightened because the H_2 can release or gain considerable rotational energy without being considered to have undergone any RET, and that these energy changes are large enough to bring about RET in the OH(A) radical.

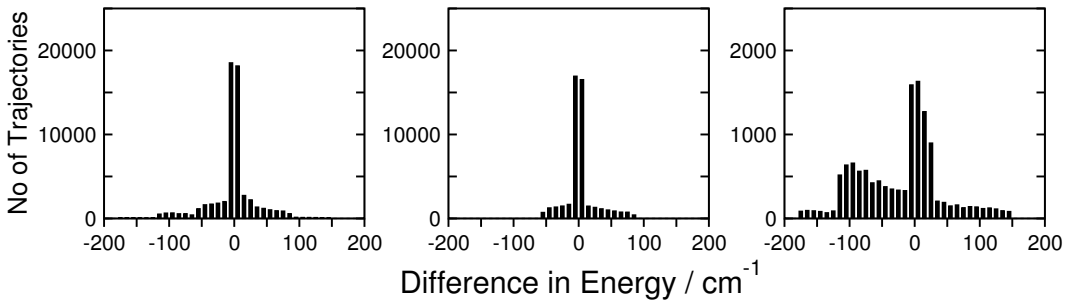

Figure 7.12: Histogram plots showing the difference in energy between the actual final rotational angular momentum of the H_2 following a classical trajectory, $\mathcal{L}'_{\rm OH}$, and the energy it has after histogram binning to $N'_{\rm H_2}$. Negative values indicate H_2 has less energy than suggested by $N'_{\rm H_2}$ and positive values more. All trajectories have initial angular momentum quantum numbers $N_{\rm OH} = 5$ and $N_{\rm H_2} = 1$. The left-hand panel includes all trajectories with initial H_2 angular momentum, $N_{\rm H_2} = 1$. The central panel includes just the collisions that are considered elastic in H_2, i.e. $N'_{\rm H_2} = N_{\rm H_2} = 1$. The right-hand panel includes trajectories that are inelastic in H_2 and note has a different scale. Each bar is the sum of the trajectories with energy differences 5cm^{-1} either side of the central value on which the bars sit.

Figure 7.12 demonstrates the scale of this problem, showing the range and spread of differences in energy between the final classical rotational energy of the H_2 diatom at the end of the trajectory, and the H_2 rotational energy after binning ($E_{\rm H_2} - \mathcal{E}'_{\rm H_2}$). The figure looks at the binning of trajectories with initial conditions, $N_{\rm H_2} = 1$ and $N_{\rm OH} = 5$. The energy differences for all such trajectories are shown alongside just those that are considered elastic or inelastic in H_2. Looking at the panel for all the trajectories, it is clear that in the majority of cases there is only a small difference in energy which would not cause a problem, and likely these differences are no more substantial than unaccounted for energy seen in histogram binning of OH(A) in OH(A)+Rg systems.

The middle panel of figure 7.12 displays the histogram for just the collisions that are considered elastic in H_2, and a considerable spread of energy differences is still seen. There is a natural limit on the spread of energies, no lower than -76 cm^{-1} arising from rounding up from $\mathcal{L}'_{\rm H_2} = 0.5$, and no greater than 106 cm^{-1} arising from rounding down from $\mathcal{L}'_{\rm H_2} = 1.5$. Several thousand trajectories have energy differences greater than 50 cm^{-1} - a considerable amount of energy, though not enough to lead to RET in

the OH(A) (with $N_{OH} = 5$) diatom alone. However, the availability of this energy reduces the energy transfer required from translation to bring about RET in the OH(A) diatom, potentially increasing the size of the cross section.

The right-hand panel of figure 7.12 shows the energy differences histogram for just the trajectories that are inelastic in N_{H_2} from the left-hand panel. The energy difference distribution spread is greater than in the elastic case and, although small differences are the most likely, large differences are still very prevalent. It should be noted that there are far fewer trajectories in this set overall than in the elastic set. The distribution could be considered bimodal with a smaller maximum around $-100\,\mathrm{cm}^{-1}$. This corresponds with rounding to $N'_{H_2} = 2$ from $\mathcal{L}'_{H_2} = 1.5$, the minimum final classical angular momentum for an increase in N_{H_2}. The maximum around $0\,\mathrm{cm}^{-1}$ is predominantly made up of transitions to $N'_{H_2} = 0$. There is a tendency in this graph for the trajectories to have negative energy differences, which correspond to creating energy in the system upon binning the trajectories.

This discussion has not considered the possible need to conserve parity in the H_2, and in assigning the final angular momentum of the H_2, N'_{H_2}, parity has been allowed to change. However, the argument extends to analyses that conserve parity, with the situation worsened by the larger energy gaps between allowed rotational levels in the H_2.

In both the parity conserving and parity changing case, it is likely that the levels of RET in H_2 observed in QCT calculations are greater than they should be. Experimentally, only OH(A) RET cross sections are measured, and this is the only comparison with theory available. In the QCT calculations, whether parity is conserved or allowed to change in the histogram binning of the final angular momentum of H_2 is irrelevant to the final rotational state of OH(A). The problem is that the large energy gaps in H_2 allow it to act as a very large source of rotational energy to bring about an increase in rotational quantum number in OH(A), or provide a large sink for rotational energy and

reduce the rotational quantum number in OH(A). Both potentially act to increase the amount of RET seen in the QCT calculations. It is clear from these distributions that this problem is potentially considerable, and far outstrips the problem of unaccounted for energy in OH(A) binning alone, which is also a concern in previous OH(A)+Rg studies.

Alternative binning techniques have been developed to attempt to ascertain the impact of this problem on the QCT calculated RET and depolarisation cross sections. However, it strengthens the case for attempting quantum mechanical (QM) calculations on this surface, where energy and angular momentum quantisation are accounted for throughout the trajectory.

7.4 One-Dimensional Gaussian Binning

In histogram binning, all trajectories are weighted equally regardless of how unrealistic their final classical rotational energy or angular momentum are relative to their quantum-mechanically allowed values. Alternatively, the trajectories could be weighted differently on the basis of the variance in one or more of these properties. Previous studies have focused on applying a weighting determined from a Gaussian distribution, centred on the quantum-mechanically allowed values of a property [300–305]. Alternative weightings from Gaussian distributions centred on the rotational angular momentum quantum numbers, N_{OH}, have been determined in a previous QCT study of OH(A)+Ar [37, 113]. In that study, the cross sections calculated using this procedure were indistinguishable from those calculated using the simple histogrammatic binning method.

Histogram binned inelastic cross sections are calculated in QCT via the equation (see subsection 3.3.1)

$$\sigma_{NN'} = \frac{\pi b_{\mathrm{max}}^2 \mathcal{N}_{NN'}}{\mathcal{N}_{\mathrm{tot}}}. \tag{7.2}$$

With alternative weightings, $W(\mathcal{L}'_i)$, for each trajectory i, the cross section is instead calculated as

$$\sigma_{NN'} = \frac{\pi b_{\max}^2}{\mathcal{N}_{\text{tot}}} \sum_{i=1}^{\mathcal{N}_{\text{tot}}} W(\mathcal{L}'_i; N'). \tag{7.3}$$

Many previous studies have divided by the sum of the weights for all trajectories rather than the total number of trajectories [302–304], however Aoiz has demonstrated that in doing so the cross sections will not converge [306]. In short, if the sum of the weights is used then this includes weightings for all elastic trajectories, which will have sharply defined angular momentum and rotational energy, and would dominate the sum of the weights. Given that elastic cross sections cannot be converged in QCT calculations, nor can this sum of the weightings, and the result would be cross sections that similarly cannot be converged. Many previous studies deal with systems that are reactive without elastic trajectories, so this problem does not arise.

7.4.1 Gaussian Binning in Angular Momentum

Replicating the Gaussian binning approach centred on the angular momentum of the OH(A) used in OH(A)+Rg studies [34, 37, 113], the weighting is determined from a Gaussian distribution, such that

$$W(\mathcal{L}'_i; N') = g(\mathcal{L}'_i; N, \sigma) = a\mathrm{e}^{-\left(\frac{\mathcal{L}'_i - N'}{\sqrt{2}\sigma}\right)^2}, \tag{7.4}$$

where $g(x; b, u)$ is a Gaussian function of variable x, with mean value b, and standard deviation u. The Gaussian is normalised such that

$$a = \frac{1}{\sigma\sqrt{2\pi}}. \tag{7.5}$$

Commonly, when determining the weightings for the trajectories, an appropriate full-width-half-maximum (FWHM) of the Gaussian is chosen. This is directly related to

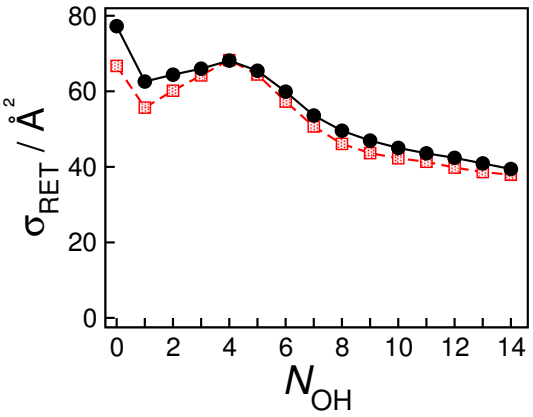

Figure 7.13: OH(A)+H_2 RET cross sections for the OH(A) diatom from QCT calculations determined using histogram binning (black filled circles), and angular momentum Gaussian binning approaches (red lightly shaded squares). The Gaussian weightings for each trajectory were determined from distributions with a full width half maximum equal to 0.25.

the standard deviation, σ, of the Gaussian distribution by

$$\text{FWHM} = 2\sqrt{2\ln 2}\sigma. \tag{7.6}$$

Figure 7.13 compares OH(A) RET cross sections determined from QCT calculations using histogram binning with those determined with this Gaussian binning approach applied. Weightings for the Gaussian binning are determined using the final classical angular momentum of the OH(A) diatom, $\mathcal{L}'_{\text{OH}}$, as the variable. The figure clearly demonstrates that there is little variation between the results with histogram binning and angular momentum Gaussian binning. The Gaussian binning leads to a small reduction in the RET cross sections, but this alternative binning process does not improve the agreement with experiment to any meaningful extent. Given this approach has not considered the variation of the final classical angular momentum of H_2 relative to its binned value, this lack of improvement is not surprising.

Figure 7.14 compares inelastic cross sections calculated via this Gaussian binning approach with those determined by applying a histogram binning approach to the QCT calculations. The cross sections are resolved into final N'_{OH} with initial $N_{\text{OH}} = 5$ for

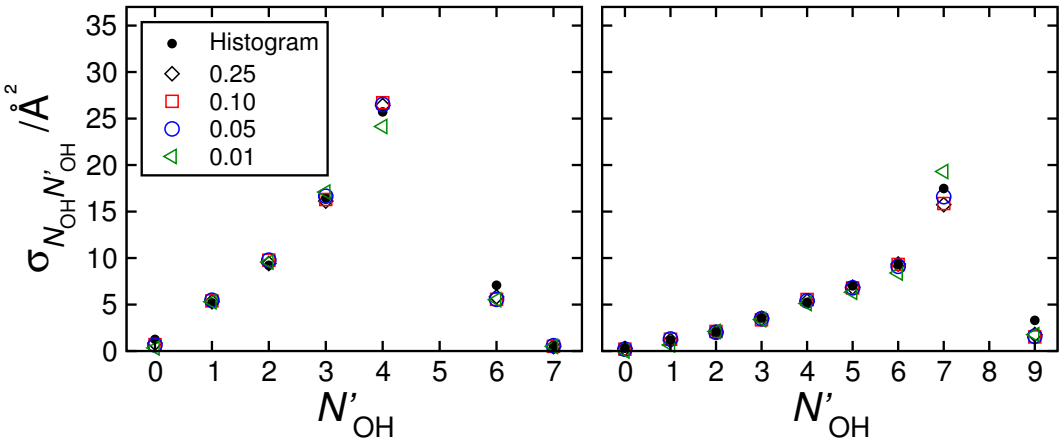

Figure 7.14: QCT calculated cross sections for $N_{OH} \rightarrow N'_{OH}$ inelastic collisions in the OH(A)+H_2 system resolved into N'_{OH}. The panels compare cross sections determined with Gaussian binning and histogram binning (shown with black filled circles) approaches. The full width half maximum for the Gaussian distributions used to determine the weighting is varied as detailed in the inset legend of the left-hand panel. Results for $N_{OH} = 5$ are shown on the left and for $N_{OH} = 8$ on the right.

the left-hand panel and $N_{OH} = 8$ in the right-hand panel. There is little observable difference between the cross sections determined from each approach with this resolution. The FWHM of the Gaussian weighting function is varied between 0.25 and 0.01, and the effect this has on the calculated cross section is shown in the figure. By varying the FWHM in this way the convergence of this weighting approach can be determined. The figure confirms that the cross sections determined with this methodology are converged over this FWHM region.

Whilst this alternative binning approach has not led to any substantial change in the calculated cross sections, this does not mean there are not still concerns about the histogram binning approach. The concerns raised focused on the impact the presence of a second diatom had on the histogram binning, but this alternative angular momentum Gaussian binning scheme has not considered the H_2 diatom.

7.4.2 Gaussian Binning in Energy

It is not possible to weight trajectories on the basis of the variance of $\mathcal{L}'_{\mathrm{H_2}}$ from $N'_{\mathrm{H_2}}$ and determine RET cross sections resolved in N_{OH}, as this would require the weighting of trajectories which are elastic in H_2. Such weightings cannot be converged for reasons already discussed.

However, trajectories can be binned with respect to the total internal energy. In this way both diatoms are considered in determining the weighting of trajectories. A similar approach has been used previously to bin the final ro-vibronic states, ν', j', of a reaction product [301, 307]. Alternatively, the approach has been used in QCT calculations that involve binning to the different vibrational modes of a reaction product[303, 304]. Studies of this kind include those by Bowman *et al.* considering the H_2O product of the OD(A)+H_2 $\rightarrow$ H_2O+D reaction [308]. The trajectories in this study were run on the OH(X A')+H_2 PES calculated alongside the excited state PES used in this thesis. In these previous studies, the results agreed well with those from QM calculations. This may be the first time that the method has been utilised in binning the final rotational levels of two separate species following a non-reactive collision, however, the principles are very similar.

The classical final total rotational energy of trajectory i, is given by

$$\mathcal{E}'_i = B_{\mathrm{OH}}\mathcal{L}'_{\mathrm{OH},i}(\mathcal{L}'_{\mathrm{OH},i}+1) + B_{\mathrm{H_2}}\mathcal{L}'_{\mathrm{H_2},i}(\mathcal{L}'_{\mathrm{H_2},i}+1). \tag{7.7}$$

The contribution of a trajectory ending with classical rotational angular momenta $\mathcal{L}'_{\mathrm{OH},i}$, $\mathcal{L}'_{\mathrm{H_2},i}$, to the final state N'_{OH}, is given by a weighting that is a function of a Gaussian distribution centred on $E' = B_{\mathrm{OH}}N'_{\mathrm{OH}}(N'_{\mathrm{OH}}+1) + B_{\mathrm{H_2}}N'_{\mathrm{H_2}}(N'_{\mathrm{H_2}}+1)$ such that

$$W(\mathcal{L}'_{\mathrm{OH},i}; N'_{\mathrm{OH}}) = f(\mathcal{E}'_i; E') = J(E') \times g(\mathcal{E}'_i; E', \sigma). \tag{7.8}$$

A Jacobian, $J(E')$, is introduced connecting E' and N'_{OH}, $\frac{\partial E'}{\partial N'_{\mathrm{OH}}}$. $g(\mathcal{E}'_i; E', \sigma)$ is a Gaussian distribution centred on E, so that

$$W(\mathcal{L}'_{\mathrm{OH},i}; N'_{\mathrm{OH}}) = \frac{\partial E'}{\partial N'_{\mathrm{OH}}} \times g(\mathcal{E}'_i; E', \sigma) = B_{\mathrm{OH}}(2N'_{\mathrm{OH}} + 1) \times \frac{1}{\sigma\sqrt{2\pi}} \exp\left[-\frac{(\mathcal{E}'_i - E')^2}{2\sigma^2}\right]. \tag{7.9}$$

Once again, inelastic cross sections are calculated using the equation

$$\sigma_{N_{\mathrm{OH}}N'_{\mathrm{OH}}} = \frac{\pi b_{\mathrm{max}}^2}{\mathcal{N}_{\mathrm{tot}}} \sum_{i=1}^{\mathcal{N}_{\mathrm{tot}}} W(\mathcal{L}'_{\mathrm{OH},i}; N'_{\mathrm{OH}}). \tag{7.10}$$

In this method, the weighting of a trajectory to any combination, N'_{OH}, $N'_{\mathrm{H_2}}$, where E' is greater than the total initial energy of the system, E_{tot}, is set to 0. Here, E_{tot} is the sum of the energy from initial rotation, E, and the collision energy (that available from translation), $E_{\mathrm{coll}} = 39\,\mathrm{meV}$ (just as in equation 4.3). This ensures that binning does not lead to cross sections that are physically impossible in energy conservation terms. Finally, this method allows for a consideration of parity conservation in H_2, by comparing $\mathcal{E}'_i$ exclusively with E' values derived from N'_{OH}, $N'_{\mathrm{H_2}}$ combinations where $N'_{\mathrm{H_2}}$ is of the same parity as $N_{\mathrm{H_2}}$.

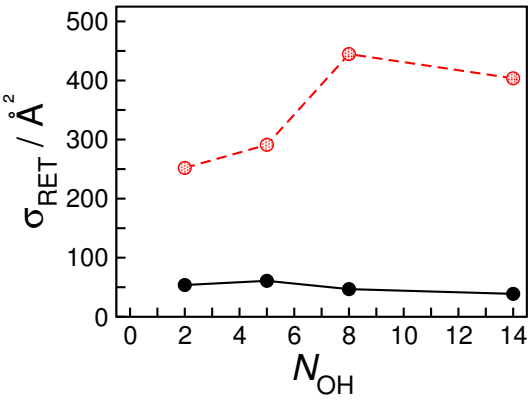

Figure 7.15: OH(A)+H_2 RET cross sections for the OH(A) diatom from QCT calculations determined using histogram binning (black filled circles), and total rotational energy Gaussian binning approaches (red lightly shaded squares). The Gaussian weightings were determined from distributions with a full width half maximum equal to $20\,\mathrm{cm}^{-1}$.

Figure 7.15 compares the OH(A) RET cross sections determined in this way for a selection of initial states, N_{OH}, with those previously determined using histogram binning. The results in the figure have applied parity conservation constraints. It is clear from this figure that this methodology is not satisfactory, as the cross sections are several times larger than those from histogram binning.

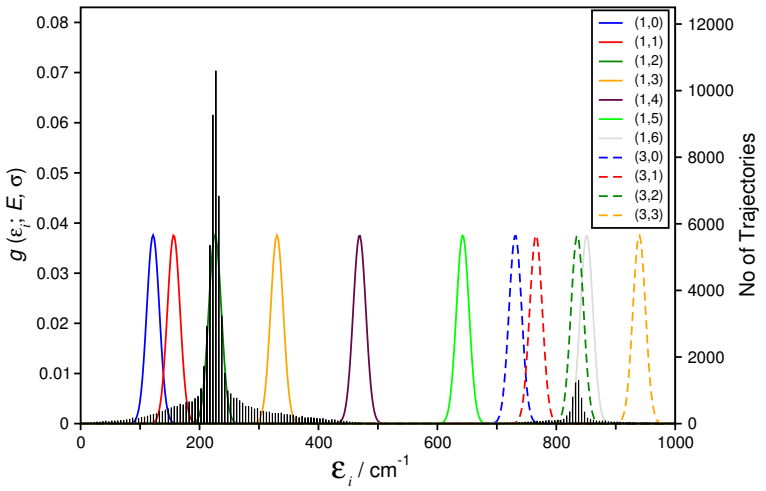

Figure 7.16: In black are histogram bins of trajectory final internal rotational energy, $\mathcal{E}_i$, of width $10\,\mathrm{cm}^{-1}$. The coloured distributions are Gaussian functions (note that no Jacobian is applied here) centred on allowed energies $E(N'_{\mathrm{H}_2}, N_{\mathrm{OH}})$ (as labelled in the panel legend) with FWHM of $25\,\mathrm{cm}^{-1}$. Here N'_{H_2} is restricted to odd values. Note the bimodal structure corresponding to the initial condition of $N_{\mathrm{OH}} = 2$, and a Boltzmann distribution of initial N_{H_2} =1 and 3.

Figure 7.16 is a histogram of classical final total rotational energy, $\mathcal{E}'$, for quasi-classical trajectories on the OH(A)+H_2 PES, alongside the Gaussian distribution used in determining weightings for the RET cross sections. The trajectories displayed start in odd N_{H_2} and $N_{\mathrm{OH}} = 2$. The figure demonstrates that the very large cross sections observed in figure 7.15 arise because there can be considerable overlap between different Gaussian distributions, and effectively a double counting of trajectories to several different final N'_{OH}. In this figure, this is best demonstrated by the overlap of $N'_{\mathrm{OH}} = 2$, $N'_{\mathrm{H}_2} = 3$ with $N'_{\mathrm{OH}} = 6$, $N'_{\mathrm{H}_2} = 1$, an area in which there are considerable number of trajectories because of elastic collisions starting in $N_{\mathrm{OH}} = 2$, $N_{\mathrm{H}_2} = 3$.

7.4.3 Conditional One-Dimensional Gaussian Binning in Energy

The problem of overlapping Gaussian distributions in energy binning can be overcome by pre-assigning the final angular momentum of the H_2 diatom, N_{H_2}, using the histogram binning approach. This method will be referred to as conditional one-dimensional Gaussian binning in energy or conditional 1D GB. Within this approach, parity is conserved, i.e. if N_{H_2}, is odd, $\mathcal{L}'_{H_2}$ is binned to the nearest odd N'_{H_2} or the nearest even N'_{H_2}, if N_{H_2} is even.

	FWHM (cm^{-1})				
N_{OH}	*20*	*10*	*5*	*2*	*1*
2	51.01	50.31	49.98	50.22	49.22
5	53.32	52.80	52.24	52.53	52.82
10	40.41	40.37	39.88	38.61	38.27

Table 7.1: Closed shell RET cross sections from QCT calculations using conditional 1D GB, given in units of $Å^2$. The full width half maximum (FWHM) of the Gaussian weighting involved is varied between $1\,cm^{-1}$ and $20\,cm^{-1}$. These tables are used to consider whether the cross sections converge with changing FWHM.

Table 7.1 shows the variation in closed shell RET cross sections when changing the FWHM of the Gaussian distribution. For there to be confidence in the results with this weighting methodology, the cross sections should converge around reasonable FWHM values. In this case the FWHM has units of cm^{-1} and reasonable values are smaller than the energy spacing between energy levels. Variation is less than $3\,Å^2$ over the range 2 - $20\,cm^{-1}$ for all N_{OH}, which is reasonable in demonstrating convergence.

Open Shell Extension

The method sketched earlier can be extended to consider open shell cross sections, rather than closed shell cross sections. This has required the weighting of tensor opacities based on the rotational energy. No weighting has been applied on the basis of the non-integer value of angular momentum transfer from the trajectories, κ, compared to the restricted integer values, K. K and κ are as defined in subsection 3.4.1 which also details the role of tensor opacities in calculating open shell cross sections.

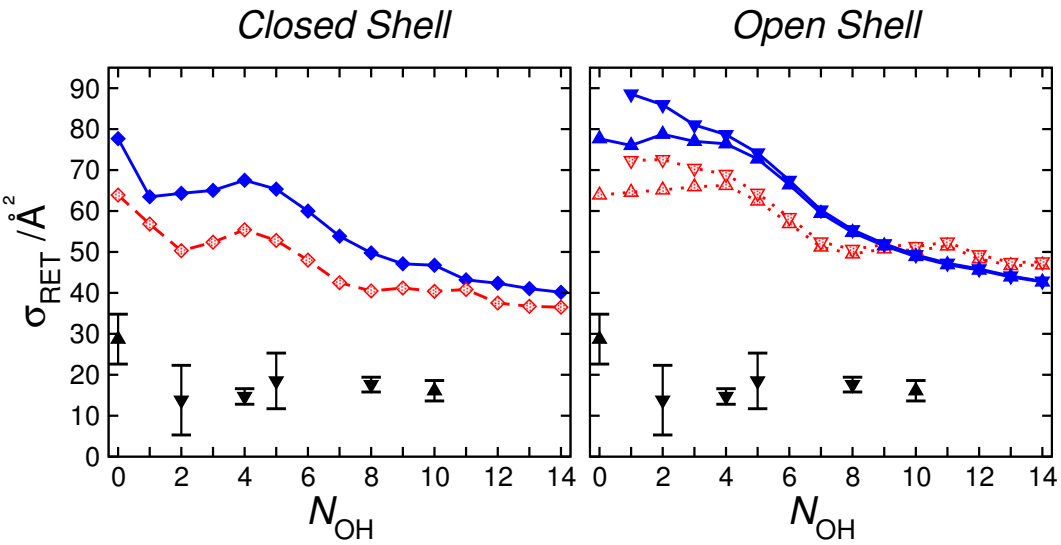

Figure 7.17: Comparison between QCT RET cross sections obtained using histogram binning (blue, fully shaded symbols connected by full lines) and conditional 1D GB (red, lightly shaded symbols connected by broken lines). Experimentally-determined RET cross sections are shown for comparison where available (black, fully shaded triangles complete with error bars). The left-hand panel shows closed shell RET cross sections (diamonds) whilst the right open shell RET results (triangles), the latter includes pure spin-rotation changing collisions. Where spin-rotation is resolved upward pointing triangles relate to the f_1 spin-rotation level, and downwards pointing triangles the f_2 spin-rotation level. A FWHM=10 cm^{-1} is utilised in determining the conditional 1D GB cross sections. A constraint that H_2 parity is conserved has been applied when pre-selecting N'_{H_2}.

Figure 7.17 compares RET cross sections determined from conditional 1D GB of QCT calculations, with those from histogram binning and from experiments. Both open and closed shell data are shown. This methodology leads to a slight reduction in the cross sections compared to those calculated with histogram binning. The exception

to this pattern is the open shell cross sections at high N_{OH}, which are slightly larger in the Gaussian binned case. There is still a considerable difference between the QCT calculated cross sections and those determined from the experiment. However, the effect of the slightly increased cross sections at high N_{OH} and smaller cross sections at lower N_{OH} is a flattening of the reduction in RET cross section with increasing N_{OH}, comparable to the pattern seen experimentally.

		FWHM (cm^{-1})				
N_{OH}	j_{OH}	*20*	*10*	*5*	*2*	*1*
2	1.5	73.01	72.55	72.38	72.17	70.41
	2.5	65.68	65.14	64.91	64.85	63.37
5	4.5	64.54	64.34	64.02	64.33	64.42
	5.5	62.67	62.42	62.05	62.37	62.49
10	9.5	50.48	51.31	51.31	50.77	52.02
	10.5	49.56	50.32	50.27	49.66	50.77

Table 7.2: Open shell RET cross sections from QCT calculations using conditional 1D GB, given in units of $Å^2$. The FWHM of the Gaussian weighting involved is varied between $1\,cm^{-1}$ and $20\,cm^{-1}$. A constraint that H_2 parity is conserved has been applied when pre-selecting N'_{H_2}.

Table 7.2 demonstrates the variation in open shell RET cross sections with varying FWHM of the Gaussian function used. The cross sections would appear to be converged over the FWHM range used.

The use of the conditional 1D GB method in determining open shell cross sections opens up the possibility of extending the approach to determine depolarisation properties. Figure 7.18 compares total and elastic depolarisation cross sections determined from histogram binning or conditional 1D GB of QCT calculations, with those from experiment.

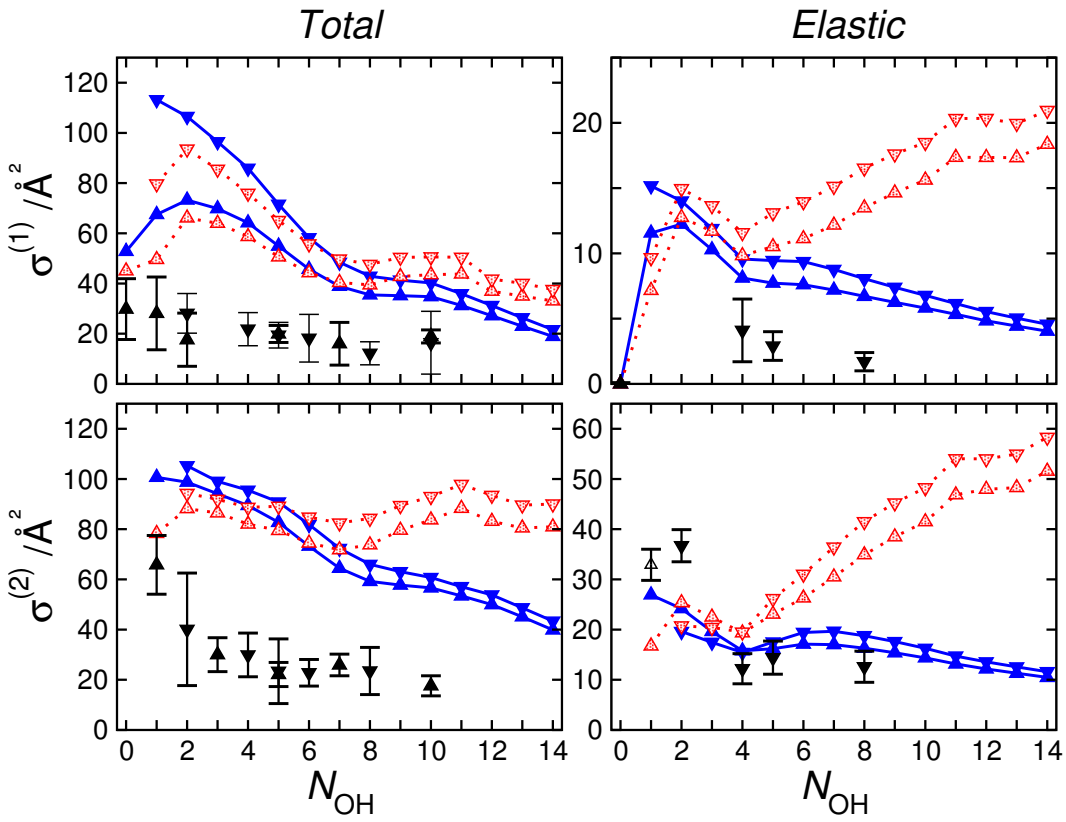

Figure 7.18: Comparison between QCT depolarisation cross sections obtained using histogram binning (blue, fully shaded symbols connected by full lines) and conditional 1D GB (red, lightly shaded symbols connected by dotted lines). Experimentally-determined depolarisation cross sections are shown for comparison where available (black, fully shaded triangles complete with error bars). The left-hand panels show total depolarisation cross sections, whilst the right-hand panels display elastic depolarisation cross sections, the former includes contributions pure spin-rotation changing collisions. The top panels are for disorientation and the bottom panels for disalignment. Upward pointing triangles relate to the f_1 spin-rotation level and downwards pointing triangles the f_2 spin-rotation level. A FWHM=10 cm^{-1} is utilised in determining the conditional 1D GB cross sections. A constraint that H_2 parity is conserved has been applied when pre-selecting N'_{H_2}.

For total depolarisation at low N_{OH}, the cross sections are generally smaller with conditional 1D GB compared to histogram binning. At high N_{OH}, the cross sections are larger with conditional 1D GB. For disalignment this has the effect of making the cross sections constant with increasing N_{OH} and making the decline with N_{OH} shallower for disorientation - this pattern is more similar to that seen experimentally. However, given that competing quenching processes are not being accounted for, and these seem

		Inelastic Disorientation					Inelastic Disalignment				
		FWHM (cm^{-1})									
N_{OH}	j_{OH}	*20*	*10*	*5*	*2*	*1*	*20*	*10*	*5*	*2*	*1*
2	1.5	79.20	78.59	78.52	77.67	73.94	73.75	73.53	73.56	73.38	71.16
	2.5	53.86	53.37	53.34	52.68	49.69	63.16	62.81	62.88	62.72	60.15
5	4.5	52.33	52.01	51.34	50.40	48.68	63.37	62.94	62.58	63.02	63.22
	5.5	40.35	40.09	39.56	38.73	37.03	56.82	56.41	55.91	56.22	55.91
10	9.5	32.03	32.10	31.60	30.06	30.63	44.23	44.76	44.57	44.31	45.40
	10.5	27.88	27.90	27.42	25.90	26.32	41.76	42.22	42.02	41.53	42.20

Table 7.3: Open shell inelastic depolarisation cross sections from QCT calculations using conditional 1D GB, given in units of $Å^2$. The FWHM of the Gaussian weighting involved is varied between $1\,cm^{-1}$ and $20\,cm^{-1}$. The left-hand cross sections are for disorientation, and the right disalignment cross sections.

the likely explanation of the lack of N_{OH} dependence in the experimental total depolarisation cross sections, this is not necessarily a good thing. In any case, quantitatively there is still a large discrepancy between total depolarisation cross sections from experiment and theory.

When conditional 1D GB is employed in determining elastic depolarisation cross sections, the agreement with experiment becomes much worse. The cross sections are very similar at low N_{OH} to those from histogram binning, but increase with N_{OH} - a pattern not observed experimentally.

Tables 7.3 and 7.4 once again show the variation of cross sections for depolarisation determined from conditional 1D GB with varying FWHM of the Gaussian distribution. The tables separate contributions to depolarisation into inelastic (table 7.3) and elastic (table 7.4).

A significant problem with the Gaussian binning method emerges in table 7.4, where it is shown that it is not possible to converge elastic depolarisation cross sections, a

		Elastic Disorientation					Elastic Disalignment				
		FWHM (cm^{-1})									
N_{OH}	j_{OH}	*20*	*10*	*5*	*2*	*1*	*20*	*10*	*5*	*2*	*1*
2	1.5	14.62	14.96	15.06	14.92	14.49	20.32	20.73	20.76	20.41	19.83
	2.5	12.56	12.75	12.83	12.62	12.19	24.93	25.36	25.52	25.15	24.33
5	4.5	12.37	13.10	13.76	14.57	14.91	24.05	26.16	27.94	30.16	31.39
	5.5	10.01	10.52	10.95	11.43	11.57	21.58	23.07	24.34	25.91	26.62
10	9.5	16.89	18.49	19.71	21.60	23.91	43.73	48.24	51.92	57.89	63.92
	10.5	14.28	15.62	16.62	18.17	20.13	37.70	41.49	44.53	49.39	54.62

Table 7.4: Open shell elastic depolarisation cross sections from QCT calculations using conditional 1D GB, given in units of Å^2. The FWHM of the Gaussian weighting involved is varied between 1 cm^{-1} and 20 cm^{-1}. The left-hand cross sections are for disorientation, and the right disalignment cross sections.

problem seen more clearly at high N_{OH}. As the Gaussian FWHM is decreased, the elastic depolarisation cross sections increase significantly, and at small FWHM the cross sections become unrealistically large and inconsistent with histogram binning results. This divergence is responsible for the large elastic depolarisation cross sections.

Consideration of OH(A)+Kr

In order to ascertain whether the issues faced with divergence in elastic depolarisation cross sections are unique to the OH(A)+H_2 collision system, the conditional 1D GB method, developed here, was applied to earlier QCT calculations on the OH(A)+Kr collision system [111, 117]. In this way, it is possible to ascertain if the problem arises for a reason linked to the introduction of a second diatom, or the large rotational energy spacing in that diatom.

Table 7.5 looks at the cross sections for RET and depolarisation that result from calculations with varying FWHM of the weighting function. In the case of closed shell

RET cross sections, convergence has been demonstrated and the cross sections are slightly smaller than those from histogram binning - just as with OH(A)+H_2. However, there is a clear increase in the three open shell cross sections calculated as the FWHM of the weighting function decreases. As with OH(A)+H_2, cross sections that include elastic $N'_{OH} = N_{OH}$, $j'_{OH} = j_{OH}$ do not converge, in the OH(A)+Kr case this extends to cross sections that include pure spin-rotation changing collisions, where $N'_{OH} = N_{OH}$, $j_{OH} \neq j'_{OH}$.

			FWHM (cm^{-1})					
	N	j	*20*	*10*	*5*	*2*	*1*	HB
Closed Shell RET	2		26.62	27.92	27.49	27.23	26.48	30.56
	8		8.56	8.76	8.83	8.53	8.18	9.76
Open Shell RET	2	1.5	54.85	59.18	65.06	74.49	82.04	49.23
	8	7.5	142.42	210.66	307.44	513.53	769.99	30.17
Total Disorientation	2	1.5	80.65	91.29	105.65	128.78	148.63	66.10
	8	7.5	276.47	414.81	612.41	1035.83	1564.55	49.03
Elastic Disorientation	2	1.5	27.78	37.03	50.23	73.10	93.61	16.28
	8	7.5	148.44	234.77	367.34	668.55	1060.25	20.39

Table 7.5: Cross sections from QCT calculations using conditional 1D GB for OH(A)+Kr trajectory calculations, given in units of Å^2. The FWHM of the Gaussian weighting involved is varied between 1 cm^{-1} and 20 cm^{-1}. The cross sections from histogram binning (HB) are included for comparison.

Figure 7.19 demonstrates the spread of final classical angular momenta, $\mathcal{L}'_{OH}$, from the trajectories that would be histogram binned as elastic in a closed shell analysis, along with the value of κ associated with the collision. The figure shows this correlation for trajectories with initial OH(A) rotational quantum number $N_{OH} = 8$ in both the OH(A)+Kr and OH(A)+H_2 studies. All values of K greater than 0 contribute to spin-rotation changing collisions. Similarly, all values of K greater than 0 contribute

to elastic depolarisation following spin-rotation conserving collisions. However, high values of K make a greater contribution for spin changing collisions than low values of K, with the weighting determined by the 6-j symbol in equation 3.74.

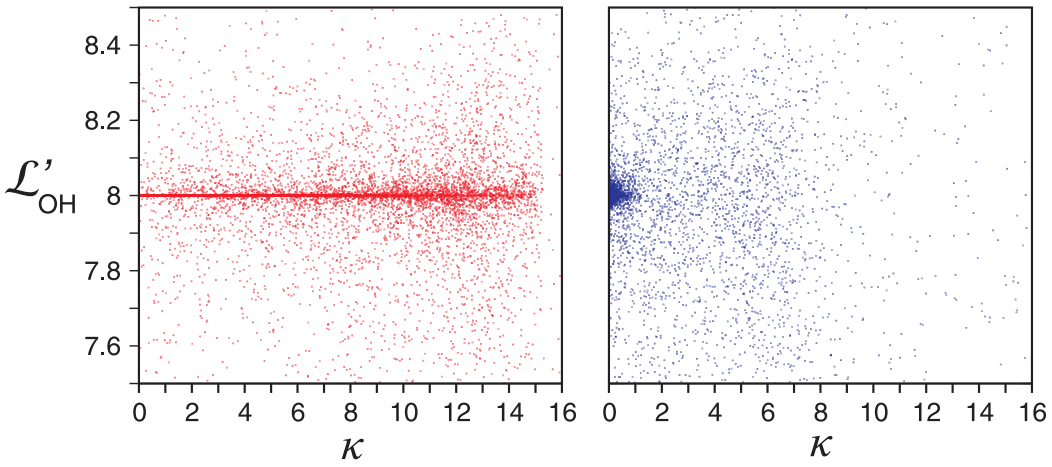

Figure 7.19: Plot of the final classical angular momentum of the OH(A) radical, $\mathcal{L}'_{OH}$, against the classical angular momentum transferred over the course of the collision, κ. The left-hand panel show the results from OH(A)+Kr QCT calculations. The right-hand panel shows the results from OH(A)+H_2 trajectories. A total of 10,000 trajectories were run to produce these plots though many had final angular momenta outside the range of the y-axis here (i.e. they would be considered inelastic in histogram binned QCT). The y-axis is focused on $7.5 \leq \mathcal{L}'_{OH} < 8.5$ - the trajectories that would be considered elastic in histogram binning with a closed shell analysis.

In the case of OH(A)+Kr, even at high κ, the trajectories are extremely elastic. They are not only binned as elastic in a quasi-classical approach (as all trajectories in either box are), but are close to being classically elastic, where $\mathcal{L}'_{OH} = 8$. In a Gaussian binning approach these trajectories would be given a large weighting which would not converge after reducing the FWHM of the Gaussian. This prevents cross sections for pure spin-rotation changing collisions from being converged for OH(A)+Kr. In the case of OH(A)+H_2 trajectories there is a much more even spread of $\mathcal{L}'_{OH}$ at high κ and subsequently pure spin-rotation changing cross sections can be converged with changing FWHM. However, the low κ trajectories are highly elastic for OH(A)+H_2, and these make a sizeable contribution to the elastic depolarisation (although no contribution if

κ is less than 0.5). Consequently, elastic depolarisation cross sections cannot be converged in either OH(A)+H_2 or OH(A)+Kr Gaussian binned QCT calculations.

More generally it is not possible to converge cross sections in which heavy contributions come from trajectories that are close to being classically elastic, just as it is not possible to converge elastic collision cross sections classically. It is possible to converge elastic depolarisation cross sections in regular histogram binned QCT calculations, as then all trajectories with $\kappa \geq 0.5$ contribute equally regardless of their elasticity. In the conditional 1D GB approach these trajectories are weighted on the basis of their final angular momentum and, as stated earlier, weightings for elastic processes do not converge.

Since elastic depolarisation cross sections do not converge with a Gaussian weighting, total depolarisation and elastic depolarisation cross sections determined in this way cannot be considered reliable.

7.5 Two-Dimensional Gaussian Binning

Another approach in the QCT analysis is to determine the weighting with a 2D rather than 1D Gaussian distribution. In this way no pre-binning of the angular momentum of either diatom is required because there are no overlaps in energy. With this method the weightings are calculated as [309]

$$\begin{aligned} W(\mathcal{L}'_{\mathrm{OH},i}\mathcal{L}'_{\mathrm{H_2},i}; N'_{\mathrm{OH}}N'_{\mathrm{H_2}}) &= f(x_i, y_i) \\ &= \frac{1}{2\pi s_x s_y \sqrt{1-\rho^2}} \exp\left(-\frac{1}{2(1-\rho^2)}\left[\frac{x_i^2}{s_x^2} + \frac{y_i^2}{s_y^2} - \frac{2\rho x_i y_i}{s_x s_y}\right]\right), \end{aligned} \tag{7.11}$$

where the variables x_i and y_i can either refer to the distribution of final diatom angular momentum or final rotational energy. In the angular momentum case, $x_i = \mathcal{L}'_{\mathrm{OH},i} - N'_{\mathrm{OH}}$ and $y_i = \mathcal{L}'_{\mathrm{H_2},i} - N'_{\mathrm{H_2}}$, whilst for energy, $x_i = \mathcal{E}'_{\mathrm{OH},i} - E'_{\mathrm{OH}}$ and $y_i = \mathcal{E}'_{\mathrm{H_2},i} - E'_{\mathrm{H_2}}$, where

$\mathcal{E}'_{\mathrm{A},i}$ and E'_{A} are the classical and binned energy associated with diatom A in trajectory i. s_x and s_y are the set standard deviations for the Gaussian weighting for the x and y variables. To retrieve the weighting, $W(\mathcal{L}'_{\mathrm{OH},i}, N'_{\mathrm{OH}})$, used in the equations in earlier subsections, the above weighting is merely summed over $N'_{\mathrm{H_2}}$. Once again, weightings can be determined with or without the constraint of parity conservation. In the examples in this text, cross sections were determined in such a way that parity conservation constraints were applied. When the weighting is determined from the spread in energies a Jacobian determinant multiplier is once again introduced,

$$\begin{vmatrix} \frac{\partial E_{\mathrm{OH}}}{\partial N_{\mathrm{OH}}} & 0 \\ 0 & \frac{\partial E_{\mathrm{H_2}}}{\partial N_{\mathrm{H_2}}} \end{vmatrix} = B_{\mathrm{OH}}(2N'_{\mathrm{OH}}+1) \times B_{\mathrm{H_2}}(2N'_{\mathrm{H_2}}+1). \tag{7.12}$$

The interdependence of the two variables is accounted for within the correlation ρ. Here ρ is estimated from the Pearson's product moment sample correlation coefficient for the angular momenta of the two diatoms as [309]

$$\rho = \frac{\sum_{i=1}^{\mathcal{N}_{\mathrm{tot}}} (\mathcal{L}'_{\mathrm{OH},i} - \bar{\mathcal{L}}'_{\mathrm{OH}})(\mathcal{L}'_{\mathrm{H_2},i} - \bar{\mathcal{L}}'_{\mathrm{H_2}})}{\sqrt{\sum_{i=1}^{\mathcal{N}_{\mathrm{tot}}} (\mathcal{L}'_{\mathrm{OH},i} - \bar{\mathcal{L}}'_{\mathrm{OH}})^2} \sqrt{\sum_{i=1}^{\mathcal{N}_{\mathrm{tot}}} (\mathcal{L}'_{\mathrm{H_2},i} - \bar{\mathcal{L}}'_{\mathrm{H_2}})^2}}, \tag{7.13}$$

where $\bar{\mathcal{L}}'_{\mathrm{H_2}}$ is the mean final H_2 classical momentum following the trajectories. The correlation can alternatively be expressed in terms of the rotational energy of the two diatoms, by replacing $\mathcal{L}'$ with $\mathcal{E}'$.

The variation of these correlations with different initial H_2 and OH(A) rotational angular momenta are given in table 7.6. It is notable that, with the exception of $N_{\mathrm{H_2}} = 0$, the negative correlation is stronger for energy than angular momentum. Due to this stronger energy interpendence, the subsequent cross sections will be determined with 2D Gaussian binning in energy.

	$N_{\mathrm{OH}} = 2$		$N_{\mathrm{OH}} = 8$	
$N_{\mathrm{H_2}}$	ρ_{energy}	ρ_{angmom}	ρ_{energy}	ρ_{angmom}
0	-0.256	-0.295	-0.642	-0.669
1	-0.325	-0.308	-0.586	-0.548
2	-0.525	-0.448	-0.466	-0.363
3	-0.616	-0.538	-0.313	-0.208

Table 7.6: Table presenting Pearson's product moment sample correlation coefficient for the correlation, ρ_{angmom}, between the classical final angular momentum of H_2 and that of OH(A), following classical trajectories on a OH(A)+H_2 PES with initial angular momentum $N_{\mathrm{H_2}}$ and N_{OH}. These are shown alongside the Pearson's product moment sample correlation coefficient for the related final rotational energies of the two diatoms following the trajectories, ρ_{energy}.

Figure 7.20 compares cross sections determined with this method against those from experiment, standard histogram binning, and the conditional 1D GB method. The cross sections are close to agreement with those from the experiment at high N_{OH},

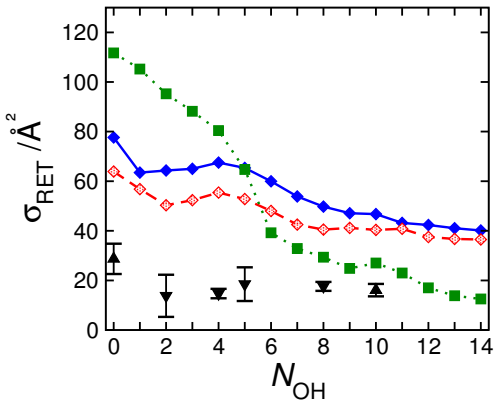

Figure 7.20: Comparison between QCT RET cross sections obtained using histogram binning (blue, fully shaded diamonds connected by full lines), conditional 1D GB (red, lightly shaded diamonds connected by broken lines), and 2D Gaussian binning in energy (green filled squares connected by dotted lines). Experimentally-determined RET cross sections are shown for comparison where available (black fully shaded triangles complete with error bars). In the experiments, spin-rotation is resolved, and upward pointing triangles relate to the f_1 spin-rotation level, whilst downwards pointing triangles the f_2 spin-rotation level. A FWHM=10 cm^{-1} is utilised in determining the conditional 1D GB cross sections. The standard deviations for the 2D case were selected as s_{OH}=2.5 cm^{-1} and $s_{\mathrm{H_2}}$=10 cm^{-1}. The parity of the H_2 diatom was conserved in binning $N'_{\mathrm{H_2}}$.

but at low N_{OH} the agreement is far worse than with standard binning, with the predicted cross sections being considerably larger.

Table 7.7 tests whether the cross sections are converged when varying the standard deviation. The two standard deviations are varied together in the top row, where clearly the cross sections do not converge with the changing s_{x} of the Gaussian weighting. Similarly, the cross sections diverge when decreasing each standard deviation separately, since the variables are treated interdependently.

	s_{x} (cm^{-1})				
	10	*5*	*2.5*	*1*	*0.5*
$\sigma_{\mathrm{RET}}(s_{\mathrm{OH}}{=}s_{\mathrm{x}},\ s_{\mathrm{H_2}}{=}s_{\mathrm{x}})$	60.58	65.92	68.46	68.50	64.31
$\sigma_{\mathrm{RET}}(s_{\mathrm{OH}}{=}2.5\,\mathrm{cm}^{-1},\ s_{\mathrm{H_2}}{=}s_{\mathrm{x}})$	64.71	67.69	68.46	79.60	94.62
$\sigma_{\mathrm{RET}}(s_{\mathrm{OH}}{=}s_{\mathrm{x}},\ s_{\mathrm{H_2}}{=}10\,\mathrm{cm}^{-1})$	60.58	62.56	64.71	66.33	72.10

Table 7.7: QCT calculated RET cross sections given in units of Å^2. These cross sections are calculated using the 2D Gaussian weighting with energy method, for the initial OH(A) state $N_{\mathrm{OH}} = 5$ and a thermal population of $N_{\mathrm{H_2}}$. The standard deviations of the two dimensions, s_{OH} and $s_{\mathrm{H_2}}$, are varied or fixed as presented in the table. These are closed shell calculations.

The cross sections diverge faster when varying $s_{\mathrm{H_2}}$ than when varying s_{OH}. This can be understood by considering equation (7.11) for the weighting as the product of three exponential factors. When varying the standard deviation with respect to OH, s_{OH}, it is the exponential factor $\exp(2\rho x_i y_i / s_{\mathrm{OH}} s_{\mathrm{H_2}})$ that is divergent; the other two factors are converged. When varying $s_{\mathrm{H_2}}$ both this factor and $\exp(-y_i^2/s_{\mathrm{H_2}}^2)$ are divergent. In both cases, the divergent factors involve both the varying standard deviation, and the variable for the H_2 diatom, $y_i = \mathcal{E}'_{\mathrm{H_2},i} - E'_{\mathrm{H_2}}$. For extremely elastic collisions in H_2, y_i tends to 0 and these trajectories dominate increasingly as s_{OH} or $s_{\mathrm{H_2}}$ are decreased; consequently, the cross sections will not converge. Note it is for this reason (that trajectories that are elastic need to be weighted in H_2 on the basis of their energy

or angular momentum) that cross sections for OH(A) RET cannot be determined by 1D Gaussian binning in H_2 final angular momentum as stated at the start of section 7.4.2. This 2D Gaussian binning method has not worked in practice as an alternative approach to binning the final angular momenta of the trajectories and, consequently, is considered no further. A theme has emerged throughout the possible weightings presented in this chapter that, when properties are elastic, they cannot be weighted in QCT binning procedures.

7.6 Closing Remarks on Gaussian Binning

A number of different Gaussian binning approaches have been developed and presented, most have either been unsuccessful or have not accounted for the role of the second diatom. Limited sucesses have been achieved with the conditional one-dimensional Gaussian binning approach described in section 7.4.3. The development of the conditional 1D GB approach has allowed the contribution of the unphysical trajectories described in section 7.3 to be reduced in three ways:

- The contribution/weighting of a trajectory to a final state N'_{OH}, $N'_{\mathrm{H_2}}$, where the sum of the rotational energy of the two diatoms is greater than the total energy in the system E_{tot}, is set to zero

- The weighting of a trajectory to a final state N'_{OH}, $N'_{\mathrm{H_2}}$ is dependent upon how close $\mathcal{E}'(\mathcal{L}'_{\mathrm{OH}}, \mathcal{L}'_{\mathrm{H_2}})$ is to $E'(N_{\mathrm{OH}}, N_{\mathrm{H_2}})$, with trajectories that are closer getting a larger weighting

- In pre-binning $N'_{\mathrm{H_2}}$ only values of the same parity as $N_{\mathrm{H_2}}$ have been considered (although it is unclear whether the parity conservation constraint is actually applicable when the collisions of H_2 are with a paramagnetic molecule, on an extremely attractive surface, describing a system with considerable non-adiabaticity)

In spite of this, the method has only brought about a very small reduction in the RET cross sections compared to those determined from standard histogram binned QCT calculations. Quantitatively however, this slight reduction does not bridge the gap with the experimental results.

It can either be concluded that the issues set out in section 7.3 are not readily surmounted by the choice of binning method, or that these issues concerning unphysical transfer of rotational energy between H_2 and OH(A) are not a major problem in the QCT calculations. The second possibility should not be quickly dismissed, since issues with the appropriateness of the PES for the study of this system have been raised extensively in section 7.2, and the use of histogram binning has not led to differences between QCT and QM calculations in OH(A)+Rg systems. In any case, comparing the current QCT results with those from a corresponding QM study would be highly desirable.

7.7 Summary

This chapter has shown that the QCT calculations agree poorly with experimentally-determined results for rotational energy transfer and collisional depolarisation. The disagreement between experimentally-determined elastic depolarisation cross sections and those from QCT calculations is somewhat smaller. However, the QCT calculations and PES should be generally seen as a poor model for the non-quenched collision dynamics in this system.

In considering the deepest potentials experienced in trajectories, it became clear that the O-end regions that are associated with collisional quenching were not explored. Essentially, this meant that the calculations or surface could not adequately account for electronic quenching either. Barriers on the surface prevented entry into these regions and it seems unlikely that these barriers always exist in reality. Investigations did not

indicate that these barriers could be overcome by varying bond lengths, as would be allowed in the true dynamics.

Alternative binning procedures for the QCT calculations rather than the standard histogram binning procedure were considered. In doing so an alternative approach - conditional one-dimensional Gaussian binning was developed. The aim of these alternative binning procedures was to attempt to reduce problems that arise through including non-physical trajectories, where energy and angular momentum conservation is not obeyed. The new approach did not lead to drastically different cross sections, and it is quite possible that this is not a major source of error in the calculation.

Essentially, there are three potential contributors to the disagreement between experiment and theory. The most important is that the model attempts to account for the dynamics with an adiabatic calculation when non-adiabatic activity is known to be important in OH(A)+H_2 collisions. Whilst non-quenched collisions may not undergo non-adiabatic dynamics themselves, they are in competition with collisions that do, and this will have a significant effect on collision cross sections for various processes. Secondly, there are considerable questions around the quality of the PES used in exploring the dynamics of this system. Finally, there are lingering questions about the appropriateness of some of the assumptions made in the QCT methodology, namely the fixing of the bond lengths of the diatoms and the binning procedure. Carrying out quantum scattering calculations would allow for the elimination of the latter of these two.

The final chapter will present some overriding conclusions for the OH(A)+H_2 study, and suggest future avenues for research that may further elucidate the dynamics involved in quenching and non-quenching collisions in this system.

Chapter 8

Conclusions and Future Work

In this final chapter the main conclusions of the study into the OH(A)+H_2 collision system are drawn together. Proposals for extending this study, as well as extending the work to consider other systems, are made. These proposals for future work, include both theoretical and experimental approaches. Finally, the chapter and thesis conclude by introducing a new compact crossed-molecular-beam experiment. The concept behind the design is explored and preliminary measurements introduced.

8.1 Conclusions

Experimental and theoretical investigations of the OH(A)+H_2 collision system have both been carried out. The central focus has been the outcome of the non-quenching collisions that remain in the excited OH(A) state, the quenching processes having been extensively studied previously.

Circularly-polarised light was used to photolyse H_2O_2, and the lab-frame orientation of the photofragments was probed with LIF techniques. This study demonstrated the ability of the Zeeman quantum beat spectroscopy method to probe angular momentum polarisation. This technique was used again to determine collisional depolarisation cross sections for OH(A) in collisions with H_2. Alongside exploring collisional

depolarisation, cross sections for RET and collisional quenching were determined experimentally. The use of a monochromator allowed the contribution to depolarisation from elastic collisions to be isolated.

Experimentally-determined quenching cross sections are seen to fall with increasing OH rotational angular momentum, N_{OH}, indicating the involvement of an anisotropic potential sensitive to OH rotation. These quenching cross sections strongly agreed with those from previous studies, and added to the available data. It was also noted that the quenching cross sections were independent of whether the f_1 or f_2 spin-rotation level is the subject of the experiment.

The experiments performed have added significantly to the quantity of data available on the electronically elastic, rotationally inelastic OH(A) RET cross sections. These are substantial in size, comparable to cross sections for OH(A) collisions with the heavier rare gas atoms. The RET cross sections remain constant with increasing OH(A) rotation; this is unexpected given that the PES used to describe the system is both extremely attractive and anisotropic. Note that, even if the full 6D PES used here is considered inadequate for the purposes of this study, it is still well known that the potential describing this system is very anisotropic and attractive. It seems likely that RET competes with quenching collisions, and the sum of these experimentally-determined cross sections does fall with increasing N_{OH}. It is unclear whether RET occurs in the H_2 collision partner as the experiment is insensitive to $N_{\mathrm{H_2}}$ and $N'_{\mathrm{H_2}}$. Furthermore, it is unclear whether a parity conservation constraint is appropriate in understanding this system, or whether the highly attractive interactions and paramagnetic nature of OH(A) allow parity changing collisions in H_2. If RET does take place in the H_2 collision partner, this would be a substantial contributor to the available energy for RET in OH(A).

This is the first time depolarisation cross sections have been measured comprehensively for OH(A) with a molecular collider. Depolarisation occurs extensively during collisions, and the angular momentum direction is effectively randomised during RET; this suggests the involvement of the formation of complexes that survive for several rotational periods during the course of the collision. Total depolarisation cross sections are constant with increasing OH(A) rotational angular momentum, but again it is likely this is partly because they are in competition with quenching processes.

Surprisingly for a system with a very attractive PES, elastic depolarisation is not a substantial contributor to the depolarisation. The size of the contribution is seen to decrease slowly with N_{OH}, indicating that these collisions are associated with an anisotropic region of the PES that is subject to rotational averaging. This decrease in elastic depolarisation with N_{OH} is also unexpected, given that, in OH(A)+Rg systems, attractive, anisotropic surfaces lead to elastic depolarisation that is independent of N_{OH}. The decrease in elastic depolarisation cross sections with N_{OH} does, however, indicate that this process does not compete with electronic quenching.

Collectively, a large body of additional experimental data on the OH(A)+H_2 non-quenched collisions has been produced, and a number of surprising conclusions concerning these data present challenges to theoretical models attempting to describe this system. In this thesis, a QCT approach has been applied. To this end, a new four-atom QCT method and code was developed, but the PES was provided from elsewhere [126]. This technique, and the potential employed, are adiabatic in nature, but the OH(A)+H_2 collision system has marked non-adiabaticity, with conical intersections to the ground state explaining electronic (reactive and non-reactive) quenching. Despite not accounting for the true non-adiabatic nature of the collision system, the PES and QCT technique were used to help rationalise the results of the non-quenching collisions.

In the QCT results, RET was observed in both OH(A) and H_2 diatoms, with substantially more occurring in the OH(A) diatom, as expected given its smaller rotational

energy spacing. In cases in which H_2 underwent RET, anti-correlated RET was evident in the OH(A) diatom. In this way, if one diatom was rotationally excited, the angular momentum of the other had a propensity to fall. Extensive depolarisation accompanied elastic as well as inelastic collisions of OH(A). More often than not, accompanying depolarisation was also seen in the H_2 diatom, suggesting that H_2 does not behave as an atomic spectator. Whilst it is unclear if H_2 RET occurs in the true experimental case, it seems highly unlikely that the angular momentum polarisation of H_2 is not depolarised on a PES that is highly anisotropic with respect to H_2 rotation.

In the QCT calculations, total depolarisation, elastic depolarisation and RET cross sections for OH(A) were all predicted to fall with increased N_{OH}, though the decline is more gradual than seen for the OH(A)+Rg systems. The formation of complexes between the two diatoms during the collision was important in explaining these patterns.

These QCT calculated cross sections were all larger than those observed experimentally, although in the elastic depolarisation case the agreement was more reasonable. The fact that the theory does not take account of competing quenching processes, and the non-adiabatic nature of the true interaction, is one possible cause for the observed disagreement. Since elastic collisions are thought not to compete with quenching processes, and there is less disagreement here, this at least appears to be part of the answer. However, the disagreement between combined experimental RET and quenching cross sections, compared to QCT calculated RET cross sections, suggests there are additional reasons for the disagreement. Likewise, the trajectories do not actually probe the parts of the potential thought responsible for the electronic quenching.

It was hypothesised that the larger RET cross sections from QCT calculations may arise from deficiencies in the histogram binning approach. With this in mind, alternative Gaussian binning methods were developed. Gaussian weighting rather than traditional histogram binning has become increasingly popular in QCT studies recently, and several approaches have been applied here with varied success. A conditional

1D Gaussian binning in energy method was developed, and with this approach it has been possible to calculate inelastic depolarisation and RET cross sections. These cross sections show improved agreement with experiment compared with those determined using standard binning, but only slightly.

In other QCT studies, Gaussian weightings have typically been applied to reaction or electronic quenching products. In contrast, applying a full Gaussian binning treatment to the OH(A)+H_2 non-quenched collisions requires the application of Gaussian weightings to elastic depolarisation cross sections. This is problematic, as weightings for elastic trajectories cannot be converged, a problem linked to the inability of QCT methods to converge integral cross sections for elastic collisions classically.

The fact that alternative binning procedures did not dramatically change the calculated cross sections suggests that the binning procedure is not the cause of discrepancy between the theory and experiment. Instead, alongside the fundamentally non-adiabatic nature of the true collision system, the largest cause of disagreement between the experiment and theoretical cross sections is likely the inadequacies of the PES for describing the full OH(A)+H_2 dynamics.

8.2 Further Work

There are a number of possible future avenues of investigation to further the work of this thesis. These future possibilities touch on both further advancing the theoretical study, and designing and implementing alternative experiments. Further work could also consider other diatom-diatom collision systems, both for systems in which there are non-adiabatic effects present and in others in which they are absent.

8.2.1 Theory

Evidently, repeating this work using a PES that is more accurate, particularly at higher separation distances, would be a fruitful line of enquiry. The likely inaccuracies of the current surface have made it difficult to evaluate to what extent the differences between experimental and QCT calculated cross sections are a result of the application of an adiabatic QCT method. With respect to the authors of the current surface, it is the only full 6D OH(A)+H_2 PES currently available for dynamics calculations, reflecting the difficulty in producing PESs for systems larger than triatomics.

Performing scattering calculations with a method based on quantum mechanics employing the current PES, for example with the HIBRIDON code, would also be worthwhile. The HIBRIDON suite of codes [310] uses a hybrid propagator consisting of the log-derivative propagator of Manopoulos at short range [311], and the Airy propagator over longer range [312] to solve the close-coupled (CC) equations. The HIBRIDON code has been used previously to run fully quantum CC calculations in OH(A)+Rg studies [37, 110, 114, 313], although in those cases there was very little difference between the resulting QM and QCT calculated cross sections. Here, though, there are potentially large problems with binning the final angular momenta of the diatoms following a classical trajectory, so a QM theoretical approach may be helpful. Certainly a QM approach would allow for a determination of how much impact binning the final angular momentum has on the calculated cross sections, since attempts to apply an alternative Gaussian binning approach made relatively little difference. HIBRIDON [310], or alternatively the MOLSCAT code [314], have been used extensively in the past to run CC scattering calculations on molecule+molecule collisions. These include collisions involving the H_2 diatom with, for example, OH(X) [132], HCl [159], NH_3 [315] and HCN [148, 149]. A proper consideration of H_2 parity conservation can also be made in these calculations, as it can be allowed to vary or stay fixed. QM

calculations would also elucidate what role, if any, quantum mechanical effects like tunnelling or resonances have on the dynamics of this system.

The OH(A)+Kr and OH(A)+Xe systems have also been investigated with QCT calculations in a similar way to OH(A)+H_2, although in those studies theoretical calculations were carried out that account for the electronic quenching pathway [24, 93, 112, 313, 316]. In these systems the QCT method was adapted, so trajectories have the possibility of 'hopping' from the excited state surface OH(A A')+Rg to either of the ground state surfaces, OH(X A')+Rg and OH(X A'')+Rg. Put simply, at each point in the trajectory the probability of the radical being quenched by hopping to another surface is determined, and the trajectory propagated accordingly. The inclusion of the ground state A'' symmetry surface accounts for Coriolis and Renner-Teller coupling. The inclusion of this different symmetry state was demonstrated to be important in determining the quenching cross sections in calculations performed by Perkins [24]. Similar, though significantly more challenging, trajectory surface hopping calculations could be carried out here on OH(A)+H_2. However, with the current surface, the trajectories do not explore the areas of the potential associated with surface hopping to the ground state(s), so this surface would first need replacing. Further calculations would also be required to determine a PES for the additional A'' ground state, along with the couplings between the three states ($1A''$, $1A'$ and $2A'$).

Another possibility is to run the QCT calculations again, but averaging the potential over all H_2 orientations, and fixing the rotational angular momentum of the H_2. In this way the potential is reduced to two-dimensions. This might be fruitful as the much smaller experimental cross sections and possible parity conservation constraint suggest that H_2 might not be able to transfer its rotational angular momentum in the collision. This averaging of the potential over H_2 orientation has been tried previously in CC scattering calculations on the HCN+H_2 [151] and O_2+H_2 [158] systems. In the O_2 case, the results were almost identical to those found with a full 4D PES, but in the

HCN case, this approach was considered unsatisfactory in subsequent work by Lique *et al.* [149]. The O_2+H_2 PES is fairly isotropic with respect to H_2 rotation, so the fact this averaging makes no difference is perhaps to be expected. However, the HCN+H_2 surface is much more anisotropic with respect to H_2 rotation [150]. The OH(A)+H_2 surface is even more anisotropic than HCN+H_2 for some geometries, so it seems likely this approach would be unsuccessful here also.

The ultimate goal would be full CC three state quantum scattering calculations on non-adiabatic OH(X,A)+H_2 surfaces. Current unpublished work by Kłos, Alexander and Dagdigian is exploring this problem for the OH+Kr and OH+Xe systems, but the OH+H_2 collision system is significantly more difficult. This type of calculation is both computationally extremely expensive and far from easy at the present time.

Exploration of other diatom-diatom systems would further test the four-atom QCT code. A system without non-adiabatic effects, or in which electronic quenching is known to be of limited importance, would allow for a more direct challenge on other assumptions involved in the QCT method. These assumptions include the fixing of diatom bond lengths, the subsequent fixing of vibrational energy, and those arising from binning the final angular momentum. A system in which the reduced masses of the two diatoms were more similar, so that neither has the ability to supply a large amount of rotational energy to the other without accompanying RET, would also be worthy of study. Certainly, the consideration of a system with two heterodiatomics would simplify the study by removing the need (or not) to account for parity conservation.

8.2.2 Experiment

Due to the large discrepancy between theory and experiment, and the problems that may arise from binning final angular momentum, it has not been possible to reach any conclusion about whether or not parity is conserved in H_2 during a collision. This could

be explored experimentally in a number of ways. Firstly, the results of the present study could be compared with data from a study employing a HD rather than H_2 collider, where there are no nuclear spin statistics or parity constraints. If OH(A) RET cross sections were similar to those found in these studies it would indicate either that spin parity was not conserved or that no RET occurs in the colliding diatom. However, with this comparison there are kinematic differences to account for so the results may prove inconclusive. Alternatively, the experiment could be carried out using a collider of only one spin-isomer (e.g *para*-H_2). If the OH(A) RET cross sections are similar to those in these studies, it would indicate there is no RET in H_2 during the collision.

Recent studies have used a LIF based technique, similar to that used in these studies, to consider the collisions between Kr and the first vibrationally excited state of OH(A, $\nu = 1$) [24]. This could be extended to look at collisions with H_2, calculating cross sections for vibrational energy transfer (VET) along with RET and electronic quenching, noting that relatively little work has been carried out on the electronic quenching previously [287–289, 317, 318].

With the introduction of a third tunable laser the quenching products could be analysed. The first laser is used to photolyse the H_2O_2 or HNO_3 precursor and the second to pump the resultant ground state radicals into specified spin-rotation states of the first excited state, OH(A). The additional third laser would probe the products of non-reactive quenching collisions, OH(X), exciting them into a vibrationally excited OH(A) state, and then recording the resultant fluorescence decay. The product state distribution of the reactive quenching products, H+H_2O, could also be investigated, as these products are amenable to both Rydberg tagging and REMPI detection approaches. Studies of this kind have been carried out previously [101, 102, 108, 259], but tended to focus on the quenching of OH(A) from the ground rotational state, $N_{OH} = 0$. By using a tunable dye laser in the second step the variation in quenched product state distribution with the spin-rotation level of OH(A) can be explored. Together with the

results of the experiments in this thesis, a full understanding of the dependence of the products of OH(A)+H_2 collisions on the initial OH(A,j,ν) state could be determined.

A newly developed crossed-molecular-beam (CMB) machine, introduced briefly in section 8.3, can be used to explore the correlation between other vectors that characterise the collision. The simplest challenge would be to measure the differential cross section for OH(A)+H_2 collisions, a property closely related to the $\boldsymbol{k}$-$\boldsymbol{k}'$ correlation. Such an experiment would be carried out in a similar way to recent CMB experiments on the excited NO(A) radical with rare gases by McKendrick, Costen, Chandler and Alexander [319–322], though in this case it would require the development of a usable REMPI scheme for OH(A). Going further, the $\boldsymbol{k}$-$\boldsymbol{k}'$-$\boldsymbol{j}'_{\mathrm{OH}}$ correlation could be explored by considering the polarisation of the collision products [321]. Finally, with a beam of initially polarised OH(A) diatoms the full $\boldsymbol{k}$-$\boldsymbol{k}'$-$\boldsymbol{j}_{\mathrm{OH}}$-$\boldsymbol{j}'_{\mathrm{OH}}$ correlation can be explored.

The present work represents the first time a detailed study of collisional depolarisation using Zeeman quantum beat spectroscopy has been carried out with a molecular collider, although some preliminary results were found for the OH(A)+H_2O collision system [21], and McKendrick and co-workers [124] explored collisions of the OH radical in the ground state with molecular N_2 and O_2. Other systems with molecular colliders could also be studied including, but not limited to: OH(A)+N_2, OH(A)+H_2O, NO(A)+N_2, NO(A)+H_2 and NO(A)+O_2. However, further studies are clearly more useful when there is an accompanying theoretical study. Previous collisional depolarisation studies have proved a useful probe of the accuracy of calculated PESs, and when the experimental and theoretical cross sections agree some confidence can be had in any conclusions drawn on the mechanics of collisions seen theoretically.

8.3 Introducing a New Experiment

In this final section, the design and development of a new molecular-beam experiment is briefly described. The concept behind the initial design and the apparatus are detailed. Additionally, it is demonstrated that the molecular-beam generates rotationally cold molecules. Finally, ion-images are produced from the products of OCS photolysis that are comparable with those from previous experiments.

8.3.1 Concept

Two experiments have been proposed in this thesis that require the use of molecular-beam apparatus. This first is to repeat the photolysis of H_2O_2 experiments detailed in chapter 2 in a cold molecular-beam. By repeating measurements under these conditions, the effect of parent molecule rotation on the observed lab-frame orientation can all but be eliminated. The model proposed in section 2.5 would imply that under these circumstances the measured lab-frame orientation would be close to zero. This experiment would require a single-beam LIF arrangement.

The second experiment is proposed in relation to the OH(A)+H_2 collision system with the hope of exploring the $\boldsymbol{k}$-$\boldsymbol{k}'$-$\boldsymbol{j}'_{\mathrm{OH}}$ correlation, necessitating the development of a crossed-molecular-beam (CMB) experiment. It is more likely that such an experiment will first be applied to extending studies by Brouard *et al.* on the collisions of OH(A) and rare gases. However, in either case a crossed-molecular-beam velocity-mapped ion imaging (VMI) set-up is required.

More broadly, there is a desire to further advance recent studies on simple diatom-atom and diatom-diatom collisions and consider a wider range of vector correlations. The above $\boldsymbol{k}$-$\boldsymbol{k}$-$\boldsymbol{j}'_{\mathrm{OH}}$ correlation is just one such example. An alternative example would make use of an electric field to orient a heterodiatom bond axis and investigate the scattered products produced upon selectively approaching one or other end of the diatom.

Another hope is to utilise the quantum beat spectroscopy technique under molecular-beam conditions. With this range of experiments in mind the design of an experiment that could easily be adapted from one arrangement to another was desirable.

Traditional CMB machines have required the use of large diffusion or turbomolecular pumps to remove the large amount of gas injected by the molecular-beam valve, this was particularly true when the valves were of the continuous flow variety [1, 323]. Large vacuum pumps and vacuum chambers are both financially and spatially expensive, and it is difficult to differentially pump source and scattering chambers whilst maintaining a short distance between the nozzle and interaction region. Increases in this distance reduce the density of particles in the interaction region, which is especially problematic in experiments where signal is expected to be low.

A recent study by Chandler and co-workers has demonstrated that advances in pumping and molecular-beam technology allow for CMB apparatus of a much smaller scale, with advantages of cost, space and signal [323]. The experiment designed, developed, and explained here draws heavily upon their ideas. Further compact CMB machines were developed concurrently with that developed in this study, in Nijmegen by Parker and co-workers [324], and in Bristol by Greaves and co-workers [325]. In the Greaves experiment, the scattering chamber sits within the source chamber and is differentially pumped through the time of flight tube, in this way the distance between the nozzle and interaction region was reduced considerably [325].

The advantages of building a compact CMB experiment are threefold. Firstly, a compact design should allow for a reduction in the distance between the nozzle and interaction region, increasing the density of the beams in that region and supporting the investigation of systems with otherwise low signal. Secondly, a compact design can be more easily adapted and reconfigured, as the parts are light and small enough to be moved easily, this is useful when a range of different experiments are envisaged as set out at the beginning of this section. Finally, a small set-up is financially less expensive

to produce.

Chandler *et al.* identified the principal concern in the design of CMB experiments as maintaining steady-state pressure, that is the average pressure in the vacuum chamber with the valve in operation, low enough to ensure that the flow of the gases is described by molecular flow [323]. In the molecular flow regime the mean free path of the gases is much larger than a relevant length (for instance the distance between the chamber walls or between the skimmer and nozzle), such that the primary collisions particles undergo are with the walls of the chamber or the skimmer. In these circumstances the particles move through diffusion. Chandler *et al.* postulate that the critical element in achieving a sufficient pumping speed in these circumstances is maximising the ratio of the pump opening to the surface area of the chamber walls [323].

The source chambers in the design presented in this section are of a more traditional nature, having a larger volume than those in the Chandler CMB experiment, but also a larger pump with a pumping area that, whilst larger than for the source chambers in the Chandler CMB instrument, makes up a lower proportion of the total surface area of the chamber. The scattering chamber meanwhile has a pumping area that takes up most of one face of the chamber. It is important therefore to ascertain whether, under these circumstances, the new experiment introduced here produces a beam that is rotationally cold.

8.3.2 Experimental Apparatus

The experimental set-up produced is illustrated in figure 8.1. The apparatus is shown in the arrangement used for velocity-mapped ion imaging crossed-molecular-beam experiments, where products of inelastic scattering are ionised and velocity-mapped onto a multi-channel plate (MCP) detector.

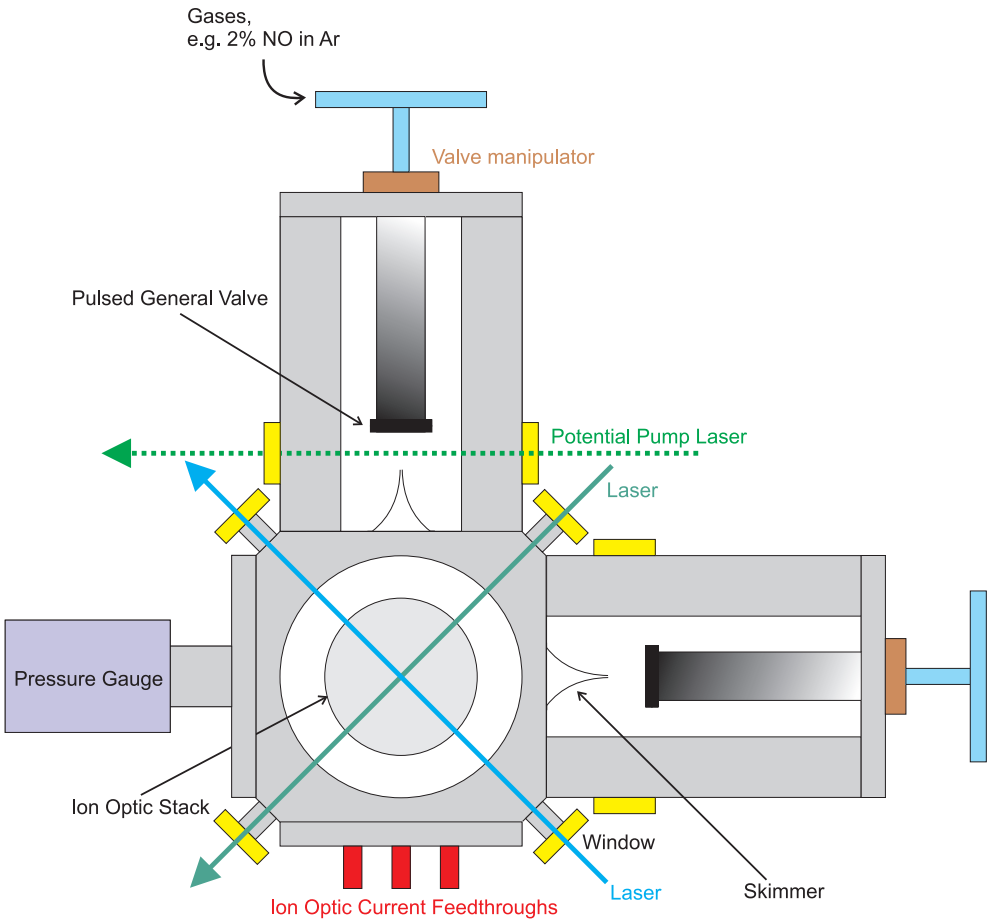

Figure 8.1: Experimental apparatus for a new compact molecular-beam machine in the arrangement for crossed-molecular-beam velocity-mapped ion imaging experiments. The time of flight tube is above the plane of the page and the turbo pumps below. The experiment is viewed from above in this pictoral description.

Vacuum Chambers

The scattering chamber is a stainless steel 120 mm sided cube hollowed out from top to bottom with a cylinder of diameter 100 mm through the centre of one side. The cube is further hollowed out by two cylinders of diameter 70 mm for each of the horizontal axes, again initiated at the centre of each square face. The resultant internal volume of the chamber is around 1100 cm^3. Whilst the initial conception for this experiment and that developed by Chandler *et al.* were the same, their internal volume is significantly smaller at $\sim$ 400 cm^3. This larger size amounts to less than 3 cm in each dimension and allows a larger pump to be accommodated (the pumping speeds of all turbomolecular

pumps in the Chandler experiment were $31\,\mathrm{ls}^{-1}$). The 4 vertical edges of the cube are trimmed at a 45° angle relative to the cube faces as shown in figure 8.1. A small window is attached halfway down these new edges via 10 mm tubing. These windows will allow for the entry and exit of a laser beam in the crossed-molecular-beam ion imaging set-up.

The six faces of the cube are the same, in so far as they all allow the attachment of stainless steel flanges or vacuum chambers of size 100x120 mm. This uniformity gives the experiment in-built flexibility, as different components can be attached and detached with ease depending upon the experiment. Such flexibility is much more difficult to achieve in a traditional larger molecular-beam set-up, where this interchangeability has not been pre-designed, or where the components are likely to be heavier and moving them becomes undesirable.

The scattering chamber is pumped by a Oerlikon Leybold SL300 turbomolecular pump capable of pumping N_2 at a speed of $240\,\mathrm{ls}^{-1}$ at pressures below 10^{-1} mbar. The turbomolecular pump is attached from below the scattering chamber via a ISO 100-KF flange. This turbomolecular pump is rough pumped by a Oerlikon Leybold TRIVAC D8B rotary pump with a pumping speed of $8.5\,\mathrm{m}^3\mathrm{hr}^{-1}$.

A 100x120 mm plate with a ISO 25-KF flange is usually attached to one side of the chamber to which an Oerlikon Leybold IONIVAC E90 hot cathode ion gauge is connected. This allows the pressure to be monitored in the experiments. In the absence of the molecular-beam a background pressure of 5×10^{-8} mbar is achieved by the turbomolecular pump. Further plates for the sides of the scattering cube include one with a window and feedthroughs for ion optics, and another with a larger window connected to a DN 63-CF flange.

Two identical source chambers have been produced, each is a stainless steel rectangular prism of length 130 mm and sides of 120×100 mm. This way the source chamber

can be attached to any face of the scattering chamber as required. The chamber is hollowed out by a 70 mm diameter cylinder along its length and another cylinder from the bottom to the top of diameter 63 mm, the internal volume is approximately 660 mm^3, again significantly larger than the Chandler *et al.* source chamber internal volume of $\sim 200\,cm^3$ [323]. A manipulator for the pulsed valve is attached to the back face of each chamber, and another stainless steel plate connected to a hot cathode pressure gauge is attached to the top.

The source chamber is pumped by a Oerlikon Leybold SL80 turbomolecular pump capable of pumping N_2 at a speed of $65\,ls^{-1}$ below 10^{-1} mbar. The turbomolecular pump is attached to the bottom of the source chamber via a ISO 63KF flange. Each of these smaller turbomolecular pumps is rough pumped by a Oerlikon Leybold TRIVAC D4B rotary pump with a pumping speed of $4.2\,m^3/hr$. A background pressure of 9×10^{-8} mbar was recorded for each source chamber. Two 1 cm diameter windows are placed centrally on each side of the source chamber, approximately 3.5 cm down its length. These windows lie between the nozzle and the skimmer, and allow for the possibility of a pump laser interacting with the supersonic expansion prior to its collimation. The proposed experiments for OH(A) scattering envisage a 193 nm laser photolysing HNO_3 at this point [326].

Pulsed Valve and Skimmer

The theory and application of molecular-beams is the subject of considerable review by Scoles [1], and shall not be detailed here. In this experiment a Sensor Technics (Series 9) general valve is held in the source chamber by the valve manipulator. In order to avoid the pumping system becoming overloaded by the gas and a loss of molecular-beam conditions, a face plate with a small orifice was chosen (0.1 mm). However, in practice sufficiently low steady-state pressures, and a cold molecular-beam were demonstrated with a valve face plate with an orifice of 0.51 mm.

A valve pulser unit triggers the opening and closing of the molecular valve. The pulser determines the length of time the valve stays open for, and the force with which it is opened, by applying a voltage. The pulser is capable of voltages up to 230 V and in the experiments described here this maximum was used. Typically the valve was opened for 200 μs and a backing pressure of 1.5 bar of gas was used. Under these conditions, the steady-state pressures in the scattering and source chambers were $\sim 1 \times 10^{-6}$ mbar and $\sim 7.5 \times 10^{-5}$ mbar respectively. This indicated that fears about pumping in the source chamber were unfounded, as the pressure in the source chamber is significantly lower than the $\sim 1 \times 10^{-3}$ mbar [323] reported for the Chandler CMB machine. However, the scattering chamber pressure in the Chandler apparatus was somewhat lower at $\sim 9 \times 10^{-7}$ mbar [323] than that reported in this experiment.

The mean free path, l, is given by [25]

$$l = \frac{1}{\sqrt{2}} \frac{RT}{\pi d^2 N_A P} \tag{8.1}$$

where P is the pressure, R the ideal gas constant, $T = 300$ K is the temperature, N_A is the Avogadro constant, and d is the hard sphere diameter of the gas molecule. An arbitrary, but typical, diameter for a hard sphere of 3.5×10^{-10} m is used in a demonstrative calculation [323]. For the recorded pressures, and under this assumption, the mean free path in the source chamber of the new experiment is ~ 1 m, and ~ 85 m for the scattering chamber. In both cases these distances are at least an order of magnitude greater than any relevant distance in the experiment, and a molecular flow regime can be assumed.

The gas load entering the chamber is dependent upon the length of time the valve is opened, the force with which it is opened (voltage applied), the stagnation (backing) pressure of the valve, and the aperture of the nozzle. At backing pressures at 3 bar or above, and when the valve was opened with both the maximum voltage (230 V) and

for maximum time period (400 μs) allowed by the pulser unit, then the pressure in the source chamber would rise to the order of 1×10^{-2} mbar. Under these circumstances, background gases will exhibit the characteristics of viscous rather than molecular flow (mean free path $l \sim 7.6$ mm). The rapid momentum transfer between particles will cause the loss of the supersonic expansion. Such settings were quite obviously not used, but demonstrated what can happen if the gas load in these small chambers became too high for the pumps to maintain a high vacuum.

The molecular-beam is collimated by a skimmer (Beam Dynamics model 2) prior to entering the scattering chamber. The skimmer has an orifice diameter of 1 mm, and following optimisation the valve lies approximately 4.1 cm back from the entrance to the skimmer. As a result, the total distance from the valve to the interaction region is just 10.1 cm. This is lower than the distance reported in Chandler *et al.*'s experimental set-up, of 13.9 cm.

Laser-Induced Fluorescence Set-Up

Whilst no LIF experiments were performed when initially characterising the new set-up, the components to carry out LIF experiments were nonetheless produced. These included the possibility of performing Zeeman quantum beat spectroscopy with the use of Helmholtz coils. These coils could be placed in the centre of the scattering chamber either by suspending them from above, or from one of the sides of the chamber. Furthermore, the coils could easily be turned to switch the magnetic field from a horizontal to vertical direction. A cylinder of μ-metal shielding of diameter 100 mm has been produced for when the magnetic field is used, and fits into the centre of the scattering chamber. Holes are cut into the shield to allow for the passage of laser and molecular-beams. Finally, a flange containing a window to allow external observation of fluorescence emission can be attached to the scattering chamber. This flange places the window slightly within the chamber and also allows for the usage of the pre-existing

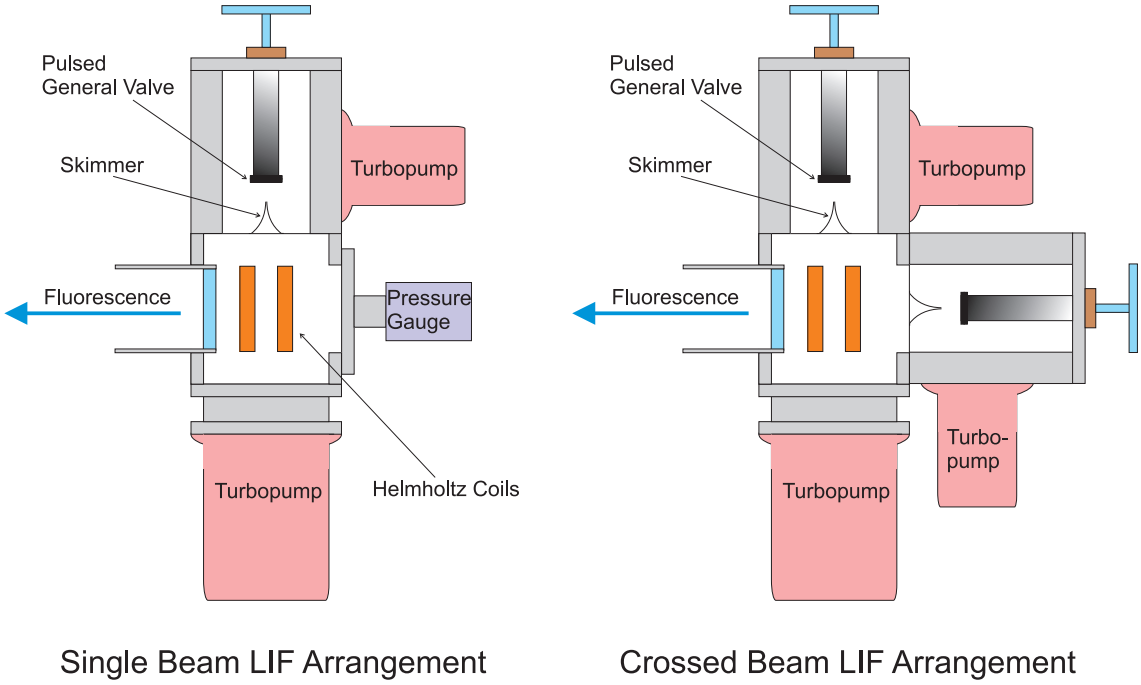

Figure 8.2: Experimental apparatus for a new compact molecular-beam machine in arrangements for LIF detection experiments. The lasers enter and exit the chamber orthogonal to the plane of the page.

lenses and monochromator described in the experiment of chapters 2 and 5.

The experimental geometry (directions of lasers, molecular-beams and detection axis) can be changed depending upon the experiment, as shown in figure 8.2. Any polarisation of the lasers is more easily defined if their propagation is orthogonal to the direction of detection and the direction of the molecular-beams. The geometries shown allow this to be achieved whilst still allowing the magnetic coils to be placed at the centre of the scattering chamber if desired.

Velocity-Mapped Ion Imaging Set-Up

The concepts behind the velocity-mapped ion imaging (VMI) technique have already been described extensively in other sources [5, 6, 327]. In brief, molecules or atoms are ionised in between charged plates, described variously as ion optics or electrostatic lenses. The different voltages applied to these plates create an electric field gradient

with which the particles interact. The charges applied to the plates are typically positive, and the positively charged ions are repelled by the most positively charged plate towards that with the lower charge. As they travel through the potential gradient the ions are accelerated and continue with their new speed after leaving the region of the plates. The ions then travel along a time of flight (TOF) tube before hitting a detector. The charges on the plates are carefully chosen to velocity map the ions, onto the detector. Ions of the same mass, moving with the same velocity in the image plane prior to ionisation are mapped onto the same point of the detector irrespective of their initial position within the laser interaction region. Thus the velocities of the particles are *mapped* onto the detector. The voltages applied to the plates are therefore arrived at through a careful consideration of the length of the TOF tube, the mass of the charged particles, and the distance between the plates. Since the initial relative velocity of the molecules is well described in a molecular-beam experiment, and the velocity after the chemical process (photolysis or collision) is well recorded in VMI, the technique allows for the determination of the differential cross section and kinetic energy release distribution.

The arrangement of the various chambers and lasers for crossed-molecular-beam scattering experiments are shown in figure 8.1. VMI can also be used to record the velocity distribution of photofragments following photolysis. This involves a single-beam arrangement. This single-beam arrangement is used to characterise the rotational temperature of the beam and to record images of the products of OCS photolysis at the end of this section. The single-beam arrangement is shown in figure 8.3, and in this figure the TOF tube and ion optic arrangements are also clearer. The details of the various components for a VMI experiment are now detailed.

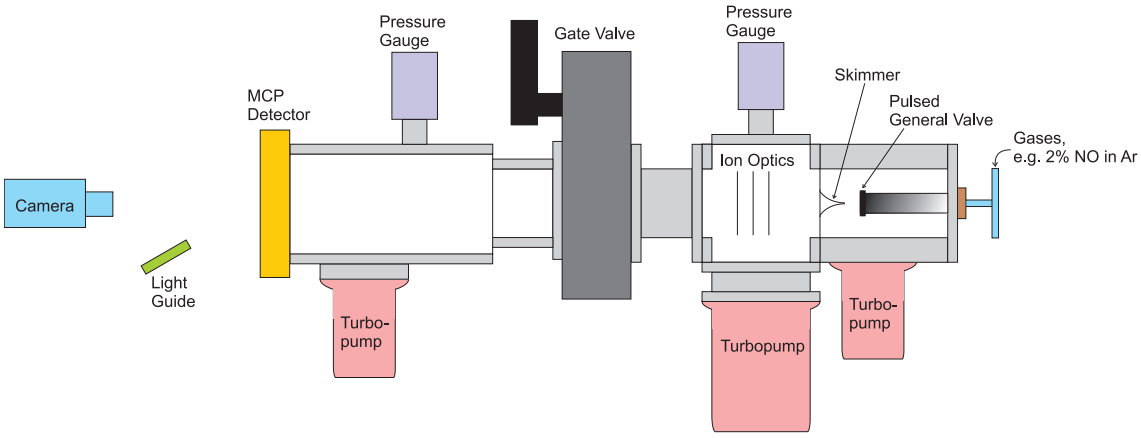

Figure 8.3: Experimental apparatus for a new compact molecular-beam machine in the arrangement for single-beam velocity-mapped ion imaging experiments. The laser enters the interaction region orthogonal to the plane of the paper.

Optics

Whilst two lenses would be satisfactory in principle, in practice three electrodes are used to generate the field, named the extractor, repeller and ground plate. These three plates are made from 1 mm thick stainless steel and have a diameter of 65 mm. The plates are held on a ring placed in the groove of one of the faces of the scattering chamber. Three long screws descend from this ring and insulated spacers hold the ion optics in place. The height of the stack in the chamber is such that the centre of the chamber lies between the extractor and the repeller. This is where the molecular-beam(s) and laser(s) cross and where ions are formed.

The lenses are 16 mm apart and the extractor and repeller are connected to electrical feedthroughs in one of the windowed side panels. The third plate is grounded via the ring holding the lenses. Each plate has a hole at its centre to allow the ions to pass through. The repeller plate has a hole of 2 mm diameter, the extractor of 4 mm diameter and the ground plate has a hole of 8 mm diameter.

A simulation of the experiment was created with SIMION [328] and the velocity mapping of ions of varying masses and velocities was demonstrated. This confirmed

that the electric field gradient experienced by the ions was uniform within the interaction region and did not display any abnormalities owing to the relatively small size of the ion optics and their close proximity, not only to each other, but to the scattering chamber walls. The power supplies for the ion optics were capable of applying a voltage of up to 5000 V. In practice the voltages used were of the order of 1000-2500 V. The voltage required for velocity mapping was indicated by the SIMION simulations [328].

Time of Flight Tube

Figure 8.3 demonstrates that the TOF tube has three constituent stainless steel parts. A short cylinder of length 55 mm connects the scattering chamber to a gate valve. The gate valve has a width of 70 mm and acts to isolate the main section of the TOF tube from the rest of the experimental set-up. This allows the detector to be protected under vacuum when the VMI set-up is not in use, or when the scattering and source chambers are brought up to atmospheric pressure to make an adjustment.

The main section of the TOF tube is 275 mm in length. The diameter changes approximately a quarter of the way down its length from 76 mm to 102 mm. The TOF tube is attached to the gate valve via a ISO 63-KF flange, and at the other end a DN 150-CF flange attaches to the detector housing. An ISO 63-KF flange lies two thirds of the way down the TOF tube for the attachment of another SL80 turbomolecular pump rough pumped by another TRIVAC D4B. A pressure gauge is also attached, and a pressure of 9×10^{-8} mbar achieved on pumping. The total distance between the detector and the interaction region in the scattering chamber is 455 mm.

MCP Detector

The accelerated positive ions travel down the TOF tube before hitting the detector. The detector consists of two multi-channel plates (MCPs) mounted in a chevron configuration, and a P47 phosphor screen (MCPs, PHOTONIS USA). When an ion enters a channel/pore in the front MCP a cloud of electrons is produced which travel down an electric field gradient generated between the first and second MCP. Each electron

entering a pore in the second MCP produces a further cloud of electrons which travel down another electric field gradient to the phosphor screen. In this way the MCPs act to amplify the signal. The phosphor screen phosphoresces upon electron impact. The light from this phosphorescence is subsequently recorded with a CCD camera or a photomultiplier tube (PMT).

Each MCP along with the phosphor screen are circular in shape and 40 mm in diameter. For VMI the voltages on the ion optics are chosen such that the Newton sphere maps onto around two thirds to three quarters of this area. Each channel in the MCP is 10 μm in diameter and the centre to centre spacing of nearest neighbour pores is 12 μm, consequently there are $\approx 10^7$ pores on the surface of the detector. The cascading electrons lead to each ion hit being detected in more than one pore, so the resolution is not as high as this would suggest, but in any case the light emitted from the phosphor screen is isolated to the area where the ion hit.

Feedthroughs in the flange holding the detector allow for the application of voltages to the faces of the MCPs and the phosphor screen, generating the required electric field gradients between them. The external power supply for the MCP detector is capable of generating voltages up to 5000 V. Typically the front face of the front MCP is grounded, whilst a voltage of 700 V is applied to the back face. The same 700 V voltage is applied to the front face of the back MCP and a voltage of 1400 V applied its the back face. A voltage of 4400 V is applied to the phosphor screen. These voltages are sometimes decreased when signal is strong, but the ratio of the voltage at the interplate faces is maintained at half that for the back face of the back MCP.

If too many ions are produced on each laser shot there is a risk of electrostatic interactions between the ions at the surface of the detector which would reduce resolution. However, if too few ions are produced the signal to noise ratio of the experiment would be poor. To balance these conditions a signal of around 10-100 ion hits per laser shot was targeted. In order to produce an image with a strong signal to noise ratio it

is usually necessary to sum the intensity over several thousand laser shots.

CCD Camera and PMT Detector

The detector is imaged by a intensified charge coupled device (CCD) camera (Photonic Science). The camera sensor has 1392 x 1040 pixels, and the signal is digitised to 12 bits. At the focal length of the camera lens (15 mm) the detector takes up 350 x 350 pixels in the centre, so only this sub area is imaged in the experiment.

A 18 mm intensifier precedes the CCD surface coupled by high efficiency fibre optics. The intensifier contains an MCP that amplifies photon flux when the signal is low. This acts to improve signal-to-noise in low signal experiments. Alongside this intensifier gain, the camera also allows for video gain that amplifies the signal but does not improve the signal to noise ratio. The camera and its software is capable of applying up to 10x gain set on a logarithmic scale of 100 steps which is usually set at 70 steps.

The digital signal from the camera is sent via a Camera Link interface to a Camera Link frame grabber. This communicates with a purpose-built LabVIEW program for operating the camera, analysing, and saving the images [228]. Camera parameters are controlled via a RS232 interface integrated in the Camera Link frame grabber cable. The computer sets, amongst other parameters, the exposure time of the camera (typically 10 μs), the triggering scheme (internal or external), the intensifier and video gain, any sub-array of pixels to be looked at, and any binning that will be applied (typically none).

In the experiment the camera's intensifier is gated as is the camera shutter. These are triggered externally by a TTL pulse from a Quantum Composer 9520 Series Pulse Generator, which is synchronised with the triggering of the laser and pulsed valve. The experiment was operated at 10 Hz. There is a minimum limit of 70 ns on the camera gate length. Typically the camera shutter is opened for 1 μs, and the intensifier for 100 ns, centred in both cases on the point at which the ions hit the detector, which is discerned from observing the PMT signal (see below).

The purpose-built LabVIEW program can perform a number of operations on the recorded image. One setting in the program thresholds the signal so that it must be of sufficiently high intensity to be seen in the processed image. Another setting removes noise by only including signal which lights up a certain number of adjacent pixels (typically 4), thus removing any noise that lights just the one pixel. Each remaining signal recorded within these parameters is considered an ion 'hit'. Another setting centroids the signal converting each ion hit to a single pixel by taking the average position of all the pixels lit up by that hit. Both the final and unprocessed image can be saved by the program.

Additionally, a light guide is pointed at the phosphor screen of the detector (in such a way as not to obscure the view of the camera). This transmits light from the phosphor screen and directs it to an external PMT. This signal is recorded on an oscilloscope, as set out in earlier experiments. The PMT in effect measures the integrated light signal across the whole MCP detector. The oscilloscope is set to average the signal over a certain number of laser shots.

8.3.3 Determining the Rotational Temperature

It was necessary to determine the rotational temperature of the molecular-beam and confirm that, despite the compact size of the experiment, the beam was rotationally cold and suitable for resolved crossed-molecular-beam experiments. In order to confirm this, the experiment was arranged to image a single molecular-beam. A cylindrical bomb of volume 500 cm^3 was filled with a gas mixture of 2% NO(X) seeded in Ar. The cylinder was attached to the molecular-beam valve via a combination of teflon tubing and a series of 3 valves. The 3 valves were used to control the flow of the gas mixture to the molecular-beam valve, with a pressure gauge attached to the teflon tube to monitor this. The backing pressure was maintained at approximately 2 bar throughout

the scan. In the future a multi-purpose gas regulator will be introduced to perform this task.

The neutral NO($X^2\Pi, \nu = 0$) molecules enter the interaction region between the repeller and extractor plate where they are ionised in a one colour (1+1) resonance-enhanced multi-photon ionisation (REMPI) process, at wavelengths close to 226 nm, via the NO($A^2\Sigma, \nu = 0$) state. The laser set-up was as set out in subsection 2.3.3, except that a Coumarin 450 dye was used to generate wavelengths close to 450 nm, which were frequency doubled to wavelengths in the vicinity of 225 nm. Additionally, the 3rd harmonic rather than 2nd harmonic of the YAG laser was used to pump the dye laser at 355 nm. In a well defined molecular-beam the velocity component of the NO(X) fragment orthogonal to the direction of the beam will be negligible. In the current experimental arrangement this is the velocity component in the detection plane, consequently under velocity mapping conditions the ions will be mapped to a central spot. To avoid the resultant risk of damaging the detector, the voltages applied to the ion optics were slightly adjusted away from those for VMI so the ions were not focussed in this way.

The grating of the probe laser was scanned over a wavelength range of 452.1 − 452.6 nm in steps of 0.0005 nm and each point was repeated for 64 laser shots. As the ions hit the MCP detector the resultant fluorescence was captured by the light guide and channelled to the PMT detector. The oscilloscope was interfaced with a PC running a purpose-built LabVIEW program to record the spectra [228]. Peaks are seen in the spectrum owing to the different spin-rotation levels ionised at different wavelengths.

Figure 8.4 shows an example REMPI spectrum recorded in this way. The high absorption coefficients mean there is the possibility of the signal being saturated, this is particularly true for the intense Q_{11} peaks. This can make determining the rotational temperature from these experiments difficult. Several scans were performed and where

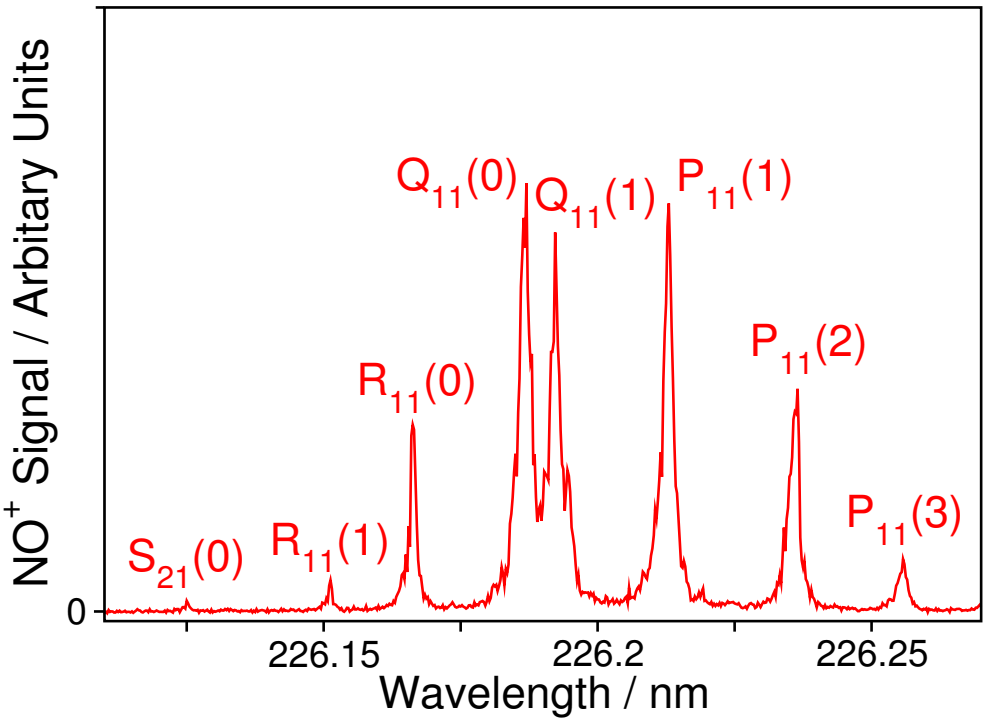

Figure 8.4: Experimentally-recorded NO(X) 1+1 REMPI spectrum.

saturation seemed likely the Q_{11} peaks were ignored in the subsequent analysis.

The relative populations of the states, $P(N_{NO})$, were determined by integrating the area under each peak and dividing by the absorption coefficients. A Boltzmann plot of $\ln[P(N_{NO})/g(N_{NO})]$, where $g(N_{NO}) = 2N_{NO} + 1$ is the degeneracy of the state N_{NO}, against the rotational energy of the state $E_{rot,NO}$ was then produced. The rotational temperature was determined from the gradient of the linear trendline for this data. The gradient itself is $-1/k_B T$ where k_B is the Boltzmann constant and T is the rotational temperature. The rotational temperature was determined to be 10.7 ± 2.2 K following 3 scans, where the error represents 2 standard deviations. Consequently it was concluded that the beam was sufficiently rotationally cold. The experimental apparatus developed by Chandler and co-workers recorded a rotational temperature of approximately 5 K. However this is with an Even-Lavigne valve [329], which has the advantage of allowing for much shorter pulse lengths (by an order of magnitude compared to a General valve) and consequently denser beams that still reduce the gas load on the pumps

[323]. The future acquisition of an Even-Lavigne valve, or alternatively a Nijmegen pulsed valve (NPV) [324], would certainly be desirable in maximising the advantages of an experiment like the one developed. The NPV has a reported minimum pulse width of $\sim 20\,\mu$s and the rotational temperature of NO(X), achieved by the developers Parker and co-workers, is reported as $\sim 1\,$K [324].

8.3.4 Velocity Map Ion Images from Photolysis Experiments

Velocity map ion imaging experiments were carried out to observe the DCS of molecular or atomic photofragments following photodissociation by linearly-polarised light. The object of these studies was not to extensively analyse the systems involved, which have already been the subject of considerable study, but to demonstrate that the new compact CMB machine could adequately reproduce the results of simple VMI photolysis experiments. These experiments only make use of one half of the CMB as they are single-beam photolysis experiments; therefore, the experimental geometry is as set out in figure 8.3. These experiments demonstrate that the new instrument can be used successfully to record images from VMI.

Carbonyl sulphide, OCS, is photolysed at $\sim 230\,$nm, and both the sulphur, S, and carbonyl, CO, products can be ionised at wavelengths close to $\sim 230\,$nm [330, 331], thus allowing images to be recorded from a simple one colour experiment. In the experiments carried out here, the focus was on imaging the CO product. However, on scanning the laser to record a REMPI spectrum for CO, the regions of the spectrum where S was ionised were clearly visible. Additionally, separate peaks on the oscilloscope for the different arrival times of the S^+ and CO^+ ions at the detector could be seen. By using the camera's intensifier gate, it was possible to record images following the photoionisation of either photofragment separately.

The experimental set-up was as set out above for the experiment to determine the rotational temperature of NO(X), although the voltages applied to the ion lenses were carefully selected following consultation with SIMION [328] to ensure the velocity of the photofragments was mapped correctly. Additionally, the Coumarin 450 dye was replaced with Coumarin 460 dye for the generation of wavelengths in the region of 230 nm where CO is ionised by (2+1) REMPI. A REMPI scan of the CO photofragment was recorded, before images were taken at a variety of wavelengths. Each image was recorded over 20,000 laser shots. An example image is shown in figure 8.5.

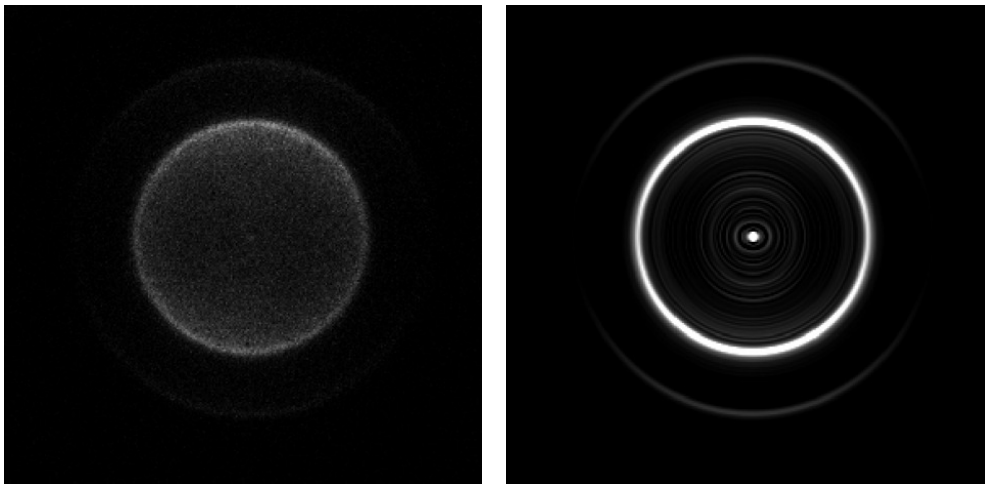

Figure 8.5: Ion image of the CO($X^1\Sigma^+$,J) photofragment produced from the photolysis of OCS at ~ 230 nm. The raw experimental image is shown on the left and the image is processed on the right. The two rings correspond to CO formed in the $J = 66$ state partnered by S(^{3}P) and S(^{1}P).

A number of concentric rings are clearly visible in the image with two of particular significance. The most prominent inner ring and the outermost ring reflect the CO photofragments from two different photofragmentation pathways observed for OCS [330, 331]

$$\begin{aligned} \mathrm{OCS} &\rightarrow \mathrm{CO}(\mathrm{X}^1\Sigma^+, J) + \mathrm{S}(^1\mathrm{D}) \\ \mathrm{OCS} &\rightarrow \mathrm{CO}(\mathrm{X}^1\Sigma^+, J) + \mathrm{S}(^3\mathrm{P}). \end{aligned}$$

The anisotropy of the outer ring and isotropy of the inner ring are also characteristic of the different photodynamics. These images are in excellent agreement with those published previously [330, 331].

Further images were recorded for the photolysis of O_2, imaging the $O(^3P_2)$ photofragment [332, 333], and the photolysis of NO_2 imaging the NO(X) photofragment [334, 335]. Again, these systems have been the subject of considerable previous study, and as with the images from OCS photolysis, the images recorded with the new compact apparatus agreed with those obtained previously.

8.3.5 Next Steps

The next steps for this new experiment are the subject of ongoing work. Firstly, it will be necessary to demonstrate the operation of the experiment in a crossed-molecular-beam arrangement. As with the photolysis experiments carried out to demonstrate single-beam VMI, a well characterised scattering experiment will be used, in this case NO(X)+Ar [336, 337]. Rather than the (1+1) REMPI scheme used to determine the rotational temperature of NO(X) in section 8.3.3, a (1+1′) REMPI scheme utilising a 226 and 308 nm laser will be used. This reduces the concern of saturating the $NO(X \rightarrow A)$ transition in the probe step.

Next, the experiment will be utilised in studying inelastic scattering of OH(X)+Rg, which has been the subject of previous work by McKendrick and co-workers [322]. Subsequent to that work, an original three colour experiment exploring inelastic scattering in OH(A)+Kr, and OH(A)+Xe collisions will be performed [326]. Finally, the experiment will be utilised in furthering the work of this thesis, applying the three colour technique, mastered in the OH(A)+Rg studies, to the more complicated $OH(A)+H_2$ collision problem.

Bibliography

[1] G. Scoles, *Atomic and Molecular Beam Methods*, Volumes 1 and 2, Oxford University Press, 1992.

[2] G. Sanna and G. Tomassetti, *Introduction to Molecular Beams Gas Dynamics*, Imperial College Press, 2005.

[3] K. R. Wilson, G. H. Kwei, J. A. Norris, R. R. Herm, J. H. Birely, and D. R. Herschbach, *J. Chem. Phys.*, **41**, 1154 (1964).

[4] A. G. Suits, L. S. Bontuyan, P. L. Houston, and B. J. Whitaker, *J. Chem. Phys.*, **41**, 8618 (1992).

[5] D. W. Chandler and P. L. Houston, *J. Chem. Phys.*, **87**, 1445 (1987).

[6] D. H. Parker and A. T. J. B. Eppink, *J. Chem. Phys.*, **107**, 2357 (1997).

[7] M. C. van Beek, J. J. ter Meulen, and M. H. Alexander, *J. Chem. Phys.*, **113**, 637 (2000).

[8] M. C. van Beek and J. J. ter Meulen, *J. Chem. Phys.*, **115**, 1843 (2001).

[9] M. C. van Beek, G. Berden, H. L. Bethlem, and J. J. ter Meulen, *Phys. Rev. Lett.*, **86**, 4001 (2001).

[10] D. A. Case, G. M. McClelland, and D. R. Herschbach, *Mol. Phys.*, **35**, 541 (1978).

[11] S. M. Wu, D. C̃. Radenovic, W. J. van der Zande, G. C. Groenenboom, D. H. Parker, C. Vallance, and R. N. Zare, *Nature Chemistry*, **3**, 28 (2010).

[12] H. J. Loesch, *Ann. Rev. Phys. Chem.*, **46**, 555 (1995).

[13] R. N. Zare, *Angular Momentum and Understanding Spatial Aspects in Chemistry and Physics*, Wiley and New York, 1st ed., 1988.

[14] E. A. Wade, K. T. Lorenz, D. W. Chandler, J. W. Barr, G. L. Barnes, and J. I. Cline, *Chem. Phys.*, **301**, 261 (2004).

[15] J. I. Cline, K. T. Lorenz, E. A. Wade, J. W. Barr, and D. W. Chandler, *J. Chem. Phys.*, **115**, 6277 (2001).

[16] K. T. Lorenz, D. W. Chandler, J. W. Barr, W. Chen, G. L. Barnes, and J. I. Cline, *Science*, **293**, 2063 (2001).

[17] A. J. McCaffery, M. J. Proctor, and B. J. Whitaker, *Ann. Rev. Phys. Chem.*, **37**, 223 (1986).

[18] S. R. Jeyes, A. J. McCaffery, and M. D. Rowe, *Mol. Phys.*, **36**, 1865 (1978).

[19] S. R. Jeyes, A. J. McCaffery, and M. D. Rowe, *Mol. Phys.*, **36**, 845 (1977).

[20] E. A. Brinkman and D. R. Crosley, *J. Phys. Chem. A*, **108**, 8084 (2004).

[21] M. Brouard, A. Bryant, I. Burak, S. Marinakis, F. Quadrini, I. Anton Garcia, and C. Vallance, *Mol. Phys.*, **103**, 1693 (2005).

[22] M. Brouard, *Reaction Dynamics*, number 61 in Oxford Chemistry Primers, Oxford University Press, 1998.

[23] M. Brouard and C. Vallance, *Tutorials in Molecular Reaction Dynamics*, RSC Publishing, 2010.

[24] T. Perkins *The effects of electronic quenching on the collision dynamics of OH(A) with Kr and Xe,* DPhil thesis, University of Oxford, (2014).

[25] P. Atkins and J. de Paula, *Atkins' Physical Chemistry*, Oxford University Press, 2002.

[26] A. J. Orr-Ewing and R. N. Zare, *Annu. Rev. Phys. Chem.*, **45**, 315 (1994).

[27] M. L. Costen, S. Marinakis, and K. G. McKendrick, *Chem. Soc. Rev.*, **37**, 732 (2008).

[28] R. D. Levine, *Molecular Reaction Dynamics*, Cambridge University Press, 2005.

[29] K. Blum, *Density Matrix Theory and Applications*, 2nd Ed., Plenum Press, New York and London, 1996.

[30] M. P. de Miranda and F. J. Aoiz, *Phys. Rev. Lett.*, **93**, 083201 (2004).

[31] F. J. Aoiz, M. Brouard, and P. A. Enriquez, *J. Chem. Phys.*, **105**, 4964 (1996).

[32] R. N. Dixon, *J. Chem. Phys.*, **85**, 1866 (1986).

[33] M. P. de Miranda, F. J. Aoiz, L. Bañares, and V. Saéz. Rábanos, *J. Chem. Phys.*, **111**, 5368 (1999).

[34] C. J. Eyles *An Experimental and Theoretical Study of the Dynamics of Atom-Molecule Scattering,* DPhil thesis, University of Oxford, (2010).

[35] I. V. Hertel and W. Stoll, *Adv. At. Mol. Phys.*, **13**, 113 (1978).

[36] M. P. de Miranda, F. J. Aoiz, V. Sáez-Rábanos, and M. Brouard, *J. Chem. Phys.*, **121**, 9830 (2004).

[37] F. J. Aoiz, M. Brouard, C. J. Eyles, J. Kłos, and M. P. de Miranda, *J. Chem. Phys.*, **130**, 044305 (2009).

[38] G. Paterson, M. L. Costen, and K. G. McKendrick, *Mol. Phys.*, **109**, 2565 (2011).

[39] G. C. Corey, M. H. Alexander, and J. Schaefer, *J. Chem. Phys.*, **85**, 2726 (1986).

[40] G. Paterson, A. Relf, M. L. Costen, K. G. McKendrick, M. H. Alexander, and P. J. Dagdigian, *J. Chem. Phys.*, **135**, 234304 (2011).

[41] G. Paterson, M. L. Costen, and K. G. McKendrick, *Int. Rev. Phys. Chem.*, **31**, 69 (2012).

[42] M. H. Alexander and S. L. Davis, *J. Chem. Phys.*, **78**, 6754 (1983).

[43] M. H. Alexander and P. J. Dagdigian, *J. Chem. Phys.*, **83**, 2191 (1985).

[44] B. Follmeg, P. Rosmos, and H. J. Werner, *J. Chem. Phys.*, **93**, 4687 (1990).

[45] G. C. Corey and A. D. Smith, *J. Chem. Phys.*, **83**, 5663 (1985).

[46] G. Herzberg, *Molecular Spectra and Molecular Structure I: Spectra of Diatomic Molecules*, Kreiger Publishing, 2nd ed., 1989.

[47] J. M. Hollas, *Modern Spectroscopy*, John Wiley & Sons, 4th ed., 2004.

[48] J. M. Hollas, *High Resolution Spectroscopy*, John Wiley & Sons, 2nd ed., 1998.

[49] P. Atkins and R. Friedman, *Molecular Quantum Mechanics*, Oxford University Press, 2005.

[50] G. H. Dieke and H. M. Crosswhite, *J. Quant. Spec. Rad. Trans.*, **2**, 97 (1962).

[51] J. M. Brown and A. Carrington, *Rotational Spectroscopy of Diatomic Molecules*, Cambridge University Press, 2003.

[52] R. C. Weast, *Handbook of Chemistry and Physics*, 53 ed., 1972.

[53] M. H. Alexander, P. Andresen, R. Bacis, R. Bersohn, F. J. Comes, P. J. Dagdigian, R. N. Dixon, R. W. Field, G. W. Flynn, K. H. Gericke, E. R. Grant, B. J. Howard, J. R. Huber, D. S. King, J. L. Kinsey, K. Kleinermanns, K. Kuchitsu, A. C. Luntz, A. J. McCafferty, B. Pouilly, H. Reisler, S. Rosenwaks, E. W. Rothe, M. Shapiro, J. P. Simons, R. Vasudev, J. R. Wiesenfeld, C. Wittig, and R. N. Zare, *J. Chem. Phys.*, **89**, 1749 (1988).

[54] M. Born and E. Wolf, *Principles of Optics*, Pergamon Press, 1970.

[55] Y. P. Chang *Novel Probes of Angular Momentum Polarisation,* DPhil thesis, University of Oxford, (2010).

[56] A. C. Kummel, G. O. Sitz, and R. N. Zare, *J. Chem. Phys.*, **88**, 7357 (1988).

[57] M. Brouard, A. Bryant, Y. P. Chang, R. Cireasa, C. J. Eyles, A. M. Green, and S. Marinakis, *J. Chem. Phys.*, **130**, 044306 (2009).

[58] E. B. Aleksandrov, *Opt. Spectrosc. Engl. Transl.*, **17**, 522 (1964).

[59] J. N. Dodd, D. M. Warrington, and R. D. Kaul, *Proc. Phys. Soc. Lon.*, **84**, 176 (1964).

[60] J. A. Gray, R. L. Farrow, J. L. Durant, and L. R. Thorne, *J. Chem. Phys.*, **99**, 4327 (1993).

[61] H. S. Schweda, A. Renn, H. Busender, and A. Hese, *Chem. Phys.*, **98**, 157 (1985).

[62] R. T. Carter and J. R. Huber, *Chem. Soc. Rev.*, **29**, 305 (2000).

[63] J. Muhlbach, M. Dubs, H. Bitto, and J. R. Huber, *Chem. Phys. Lett.*, **111**, 288 (1984).

[64] H. Watanabe, S. Tsuchiya, and S. Koda, *J. Chem. Phys.*, **82**, 5310 (1985).

[65] J. S. Deech, R. Luypaert, and G. W. Series, *J. Phys. B*, **8**, 1406 (1975).

[66] C. Fabre, M. Gross, and S. Haroche, *Optics. Comm.*, **13**, 393 (1975).

[67] H. Kremmling, P. Dabkiewicz, H. Fischer, H. J. Kluge, and T. Kuhl, *Phys. Rev. Lett.*, **43**, 1376 (1979).

[68] J. R. Brandenberger, *Optics. Comm.*, **30**, 181 (1979).

[69] J. Chaiken, T. Benson, M. Gurnick, and J. D. McDonald, *Chem. Phys. Lett.*, **61**, 195 (1979).

[70] P. J. Brucat and R. N. Zare, *J. Chem. Phys.*, **78**, 100 (1983).

[71] R. T. Carter, I. M. Povey, H. Bitto, and J. R. Huber, *J. Chem. Phys.*, **104**, 5365 (1996).

[72] M. Brouard, H. Chadwick, Y. P. Chang, B. J. Howard, S. Marinakis, N. Screen, S. A. Seamons, and A. La Via, *J. Mol. Spec.*, **282**, 42 (2012).

[73] J. Xin, I. Ionescu, D. Kuffel, and S. A. Reid, *Chem. Phys.*, **291**, 61 (2003).

[74] J. Xin and S. A. Reid, *J. Chem. Phys.*, **112**, 10067 (2001).

[75] J. Xin, S. A. Reid, F. Santoro, and C. Petrongolo, *J. Chem. Phys.*, **115**, 8868 (2001).

[76] J. Xin and S. A. Reid, *J. Chem. Phys.*, **116**, 525 (2002).

[77] H. Y. Fan, I. Ionescu, J. Xin, and S. A. Reid, *J. Chem. Phys.*, **121**, 8869 (2004).

[78] H. Y. Fan, I. Ionescu, J. Xin, and S. A. Reid, *J. Chem. Phys.*, **121**, 8874 (2004).

[79] H. Y. Fan, I. Ionescu, C. Annesley, J. Xin, and S. A. Reid, *J. Chem. Phys.*, **120**, 1164 (2004).

[80] P. J. Brucat and R. N. Zare, *J. Chem. Phys.*, **81**, 2562 (1984).

[81] G. W. Loge, J. J. Tiee, and F. B. Wampler, *J. Chem. Phys.*, **84**, 3624 (1986).

[82] M. L. Costen and G. E. Hall, *Phys. Chem. Chem. Phys.*, **9**, 272 (2007).

[83] M. Brouard, H. Chadwick, Y.-P. Chang, R. Cireasa, and C.J. Eyles, *Physica Scripta*, **80**, 048120 (2009).

[84] A. A. Wolf, *Am. J. Phys.*, **37**, 531 (1969).

[85] M. J. Pilling and P. W. Seakins, *Reaction Kinetics*, Oxford University Press, 1997.

[86] D. R. Crosley, *J. Atmos. Sci.*, **52**, 3299 (1995).

[87] P. O. Wennberg, R. C. Cohen, N. L. Hazen, L. B. Lapson, N. T. Allen, T. F. Hanisco, J. F. Oliver, N. W. Lanham, J. N. Demusz, and J. G. Anderson, *Rev. Sci. Instrum.*, **65**, 1858 (1994).

[88] I. Glassman and R. A. Yetter, *Combustion*, Boston Academic, 2007.

[89] R. P. Wayne, *An introduction to the chemistry of the atmospheres of Earth, the planets and their satellites*, Oxford Univeristy Press, 2000.

[90] K. R. German, *J. Chem. Phys.*, **64**, 4065 (1976).

[91] B. L. Hemming, D. R. Crosley, J. E. Harrington, and V. Sick, *J. Chem. Phys.*, **115**, 3099 (2001).

[92] R. A. Copeland, M. J. Dyer, and D. R. Crosley, *J. Chem. Phys.*, **82**, 4022 (1985).

[93] J. H. Lehman, M. I. Lester, J. Kłos, M. H. Alexander, P. Dagdigian, D. Herráez-Aguilar, F. J. Aoiz, M. Brouard, H. Chadwick, T. Perkins, and S. A. Seamons, *J. Phys. Chem. A*, **117**, 13481 (2013).

[94] B. L. Hemming and D. R. Crosley, *J. Phys. Chem. A*, **106**, 8992 (2002).

[95] D. R. Crosley, *J. Phys. Chem.*, **93**, 6273 (1989).

[96] J. R. Creighton, *J. Phys. Chem.*, **81**, 2520 (1977).

[97] W. C. Gardiner and J. Warnatz, *Combustion Chemistry*, Springer-Verlag, 1984.

[98] J. H. Lehman and M. I. Lester, *Annu. Rev. Phys. Chem.*, **65**, 537 (2014).

[99] M. Alagia, N. Balucani, P. Casavecchia, D. Stranger, G. G. Volpi, D. C. Clary, A. Kliesch, and H. J. Werner, *Chem. Phys.*, **207**, 389 (1996).

[100] D. E. Heard and D. A. Henderson, *Phys. Chem. Chem. Phys.*, **2**, 67 (2000).

[101] L. P. Dempsey, C. Murray, and M. I. Lester, *J. Chem. Phys.*, **127**, 151101 (2007).

[102] J. H. Lehman, J. L. Bertrand, T. A. Stephenson, and M. I. Lester, *J. Chem. Phys.*, **135**, 144303 (2011).

[103] D. T. Anderson, M. W. Todd, and M. I. Lester, *J. Chem. Phys.*, **110**, 11117 (1999).

[104] I. B. Pollack, Y. Lei, T. A. Stephenson, and M. I. Lester, *Chem. Phys. Lett.*, **421**, 324 (2006).

[105] P. A. Cleary, L. P. Dempsey, C. Murray, M. I. Lester, J. Kłos, and M. H. Alexander, *J. Chem. Phys.*, **126**, 204316 (2007).

[106] M. Ortiz-Suarez, M. F. Witinski, and H. F. Davis, *J. Chem. Phys.*, **124**, 201106 (2006).

[107] M. I. Lester, R. A. Loomis, R. L. Schartz, and S. P. Walch, *J. Phys. Chem. A*, **101**, 9195 (1997).

[108] L. P. Dempsey, C. Murray, P. A. Cleary, and M. I. Lester, *Phys. Chem. Chem. Phys.*, **10**, 1424 (2008).

[109] R. K. Lengel and D. R. Crosley, *J. Chem. Phys.*, **67**, 2085 (1977).

[110] H. Chadwick, M. Brouard, Y. P. Chang, C. J. Eyles, T. Perkins, S. A. Seamons, J. Kłos, M. H. Alexander, and F. J. Aoiz, *J. Chem. Phys.*, **137**, 154305 (2012).

[111] H. Chadwick, M. Brouard, Y. P. Chang, C. J. Eyles, G. McCrudden, T. Perkins, S. A. Seamons, J. Kłos, M. H. Alexander, P. J. Dagdigian, D. Herráez-Aguilar, and F. J. Aoiz, *J. Chem. Phys.*, **140**, 054306 (2014).

[112] J. Kłos, M. Brouard, G. McCrudden, M. H. Alexander, T. Perkins, F. J. Aoiz, and D. Herráez-Aguilar, *In Preparation.*

[113] J. Kłos, M. H. Alexander, M. Brouard, and F. J. Aoiz, *J. Chem. Phys.*, **129**, 054301 (2008).

[114] M. L. Costen, R. Livingstone, K. G. McKendrick, G. Paterson, M. Brouard, H. Chadwick, Y. P. Chang, C. J. Eyles, F. J. Aoiz, and J. Kłos, *J. Chem. Phys.*, **113**, 15156 (2009).

[115] M. Brouard, H. Chadwick, C. J. Eyles, F. J. Aoiz, and J. Kłos, *J. Chem. Phys.*, **135**, 084305 (2011).

[116] M. Brouard, H. Chadwick, Y. P. Chang, C. J. Eyles, F. J. Aoiz, and J. Kłos, *J. Chem. Phys.*, **135**, 084306 (2011).

[117] H. Chadwick *Angular Momentum Polarisation Effects in Inelastic Scattering,* DPhil thesis, University of Oxford, (2012).

[118] S. Marinakis, G. Paterson, J. Kłos, M. Costen, and K. G. McKendrick, *Phys. Chem. Chem. Phys.*, **9**, 4414 (2007).

[119] M. L. Costen, H. J. Crichton, and K. G. McKendrick, *J. Chem. Phys.*, **120**, 7910 (2004).

[120] G. Paterson, S. Marinakis, M. L. Costen, and K. G. McKendrick, *Physica Scripta*, **80**, 048111 (2009).

[121] G. Paterson, S. Marinakis, M. L. Costen, K. G. McKendrick, J. Kłos, and R. Toboła, *J. Chem. Phys.*, **129**, 074304 (2008).

[122] H. J. Crichton, M. L. Costen, and K. G. McKendrick, *J. Chem. Phys.*, **119**, 9461 (2003).

[123] G. Paterson, S. Marinakis, J. Kłos, M. L. Costen, and K. G. McKendrick, *Phys. Chem. Chem. Phys.*, **11**, 8004 (2009).

[124] G. Paterson, S. Marinakis, M. L. Costen, and K. G. McKendrick, *Phys. Chem. Chem. Phys.*, **11**, 8813 (2009).

[125] M. L. Costen and K. G. McKendrick, *J. Chem. Phys.*, **122**, 164309 (2005).

[126] B. Fu, E. Kamarchik, and J. M. Bowman, *J. Chem. Phys.*, **133**, 164306 (2010).

[127] R. J. Marsh and A. J. McCaffery, *Chem. Phys. Lett.*, **335**, 134 (2001).

[128] D. P. Dewangan, D. R. Flower, and G. Danby, *J. Phys. B*, **19**, 747 (1986).

[129] R. Schinke and P. Andresen, *J. Chem. Phys.*, **81**, 5644 (1984).

[130] S. M. Miller, D. C. Clary, A. Kliesch, and H. J. Werner, *Mol. Phys.*, **83**, 405 (1994).

[131] A. Offer and E. F. van Dishoeck, *Mon. Not. R. Astron. Soc.*, **257**, 377 (1992).

[132] M. H. Alexander and G. C. Corey, *J. Chem. Phys.*, **88**, 6931 (1988).

[133] A. Offer and D. R. Flower, *J. Phys. B*, **23**, 391 (1991).

[134] K. Kudla, A. G. Koures, L. B. Harding, and G. C. Schatz, *J. Chem. Phys.*, **96**, 7465 (1992).

[135] S. Green, *J. Chem. Phys.*, **62**, 2271 (1975).

[136] T. G. Heil, S. Green, and D. J. Kouri, *J. Chem. Phys.*, **68**, 2562 (1978).

[137] V. Balasubramanian, G. G. Balint-Kurti, and J. H. van Lenthe, *J. Chem. Soc. Faraday. Trans.*, **86**, 1659 (1990).

[138] T. R. Phillips, S. Maluendes, and A. D. McClean, *J. Chem. Phys.*, **101**, 5824 (1994).

[139] T. R. Phillips, S. Maluendes, and S. Green, *J. Chem. Phys.*, **102**, 6024 (1995).

[140] M. L. Dubernet and A. Grosjean, *A&A*, **390**, 793 (2002).

[141] M. L. Dubernet, F. Daniel, A. Grosjean, and C. Y. Lin, *A&A*, **497**, 911 (2009).

[142] M. L. Dubernet, F. Daniel, A. Grosjean, A. Faure, P. Valiron, M. Wernli, L. Wiesenfeld, C. Rist, J. Noga, and J. Tennyson, *A&A*, **460**, 323 (2006).

[143] Y. Scribano, A. Faure, and D. Lauvergnat, *J. Chem. Phys.*, **136**, 094109 (2012).

[144] L. Wiesenfeld, Y. Scribano, and A. Faure, *Phys. Chem. Chem. Phys.*, **13**, 8230 (2011).

[145] G. Sarma, C. H. Yang, A. K. Saha, D. H. Parker, and L. Wiesenfeld, *J. Chem. Phys.*, **138**, 024314 (2013).

[146] A. Offer and D. R. Flower, *J. Chem. Soc. Faraday. Trans.*, **86**, 1659 (1990).

[147] C. Rist, M. H. Alexander, and P. Valiron, *J. Chem. Phys.*, **98**, 4462 (1992).

[148] F. Dumouchel, J. Kłos, and F. Lique, *Phys. Chem. Chem. Phys.*, **13**, 8204 (2011).

[149] M. H. Vera, Y. Kalugina, O. Dennis-Alpizar, and T. Stoecklin, *J. Chem. Phys.*, **140**, 224302 (2014).

[150] O. Dennis-Alpizar, M. H. Vera, Y. Kalugina, T. Stoecklin, and F. Lique, *J. Chem. Phys.*, **139**, 224301 (2013).

[151] D. B. Abdallah, F. Najar, N. Jaidane, F. Dumouchel, and F. Lique, *Mon. Not. R. Astron. Soc.*, **419**, 2441 (2012).

[152] Y. Kalugina, J. Kłos, and F. Lique, *J. Chem. Phys.*, **139**, 074301 (2013).

[153] M. Wernli, L. Wiesenfeld, A. Faure, and P. Valiron, *A&A*, **464**, 1147 (2006).

[154] F. Lique, M. L. Senent, A. Spielfiedel, and N. Feautrier, *J. Chem. Phys.*, **126**, 164312 (2007).

[155] A. Spielfiedel, M. L. Senent, F. Dayou, C. Balança, L. Cressiot-Vincent, A. Faure, L. Wiesenfeld, and N. Feautrier, *J. Chem. Phys.*, **131**, 014305 (2009).

[156] F. Lique and J. Kłos, *J. Chem. Phys.*, **128**, 034306 (2008).

[157] M. Wernli, P. Valiron, A. Faure, L. Wiesenfeld, P. Jankowski, and K. Szalewicz, *A&A*, **446**, 367 (2005).

[158] Y. Kalugina, O. Denis-Alpizar, T. Stoecklin, and F. Lique, *Phys. Chem. Chem. Phys.*, **14**, 16458 (2012).

[159] M. Lanza, Y. Kalugina, L. Wiesenfeld, and F. Lique, *J. Chem. Phys.*, **140**, 064316 (2014).

[160] D. R. Flower and E. Roueff, *J. Phys. B*, **31**, 2935 (1998).

[161] S. Fonseca dos Santos, N. Balackrishnan, S. Lepp, G. Quéméner, R. C. Forrey, R. J. Hinde, and P. C. Stancil, *J. Chem. Phys.*, **134**, 214303 (2011).

[162] A. Bohr, N. Balackrishnan, S. C. Paolini, R. C. Forrey, R. J. Hinde, and P. C. Stancil, *J. Chem. Phys.*, **140**, 064308 (2014).

[163] N. Balackrishnan, G. Quéméner, R. C. Forrey, R. J. Hinde, and P. C. Stancil, *J. Chem. Phys.*, **134**, 014301 (2011).

[164] E. P. Wallis and D. L. Thompson, *J. Chem. Phys.*, **97**, 4929 (1992).

[165] D. W. Schwenke, D. G. Truhlar, and M. E. Coltrin, *J. Chem. Phys.*, **87**, 983 (1987).

[166] A. Faure, N. Crimier, C. Ceccarelli, P. Valiron, L. Wiesenfeld, and M. L. Dubernet, *A&A*, **472**, 1029 (2007).

[167] J. Kłos, F. J. Aoiz, R. Cireasa, and J. J. ter Meulen, *Phys. Chem. Chem. Phys.*, **6**, 4968 (2004).

[168] K. Kudla, G. C. Schatz, and A. F. Wagner, *J. Chem. Phys.*, **95**, 1635 (1991).

[169] P. J. Dagdigian and M. H. Alexander, *J. Chem. Phys.*, **130**, 094303 (2009).

[170] P. J. Dagdigian and M. H. Alexander, *J. Chem. Phys.*, **130**, 164315 (2009).

[171] P. J. Dagdigian and M. H. Alexander, *J. Chem. Phys.*, **130**, 204304 (2009).

[172] D. R. Yarkony, *Rev. Mod. Phys.*, **68**, 985 (1996).

[173] G. A. Worth and L. S. Cederbaum, *Ann. Rev. Phys. Chem.*, **55**, 127 (2004).

[174] E. Teller, *J. Phys. Chem.*, **41**, 109 (1937).

[175] D. R. Yarkony, *Acc. Chem. Res.*, **31**, 511 (1998).

[176] G. J. Atchity, S. S. Xantheas, and K. Ruedenberg, *J. Chem. Phys.*, **95**, 1862 (1991).

[177] D. R. Yarkony, *J. Chem. Phys.*, **111**, 6661 (1999).

[178] B. C. Hoffman and D. R. Yarkony, *J. Chem. Phys.*, **113**, 10091 (2000).

[179] G. C. Schatz and H. Elgersma, *Chem. Phys. Lett.*, **73**, 21 (1980).

[180] G. S. Wu, G. C. Schatz, G. Lendvay, D. C. Fang, and L. B. Harding, *J. Chem. Phys.*, **113**, 3150 (2000).

[181] G. Ochoa de Aspura and D. C. Clary, *J. Phys. Chem. A*, **102**, 9631 (1998).

[182] D. H. Zhang and J. Z. H. Zhang, *J. Chem. Phys.*, **100**, 2697 (1994).

[183] K. S. Bradley and G. C. Schatz, *J. Phys. Chem.*, **98**, 3788 (1994).

[184] D. Wang and J. M. Bowman, *J. Chem. Phys.*, **96**, 8906 (1992).

[185] D. Wang and J. M. Bowman, *J. Chem. Phys.*, **98**, 6235 (1993).

[186] G. C. Schatz, *J. Phys. Chem.*, **99**, 516 (1995).

[187] P. Y. Zhang, R. F. Lu, T. S Chu, and K. L Han, *J. Phys. Chem. A*, **114**, 6565 (2010).

[188] P. Y. Zhang, R. F. Lu, T. S. Chu, and K. L. Han, *J. Chem. Phys.*, **133**, 174316 (2010).

[189] M. A. Collins, O. Godsi, S. Liu, and D. H. Zhang, *J. Chem. Phys.*, **135** (2011).

[190] R. Hernández and D. C. Clary, *Chem. Phys. Lett.*, **244**, 421 (1995).

[191] E. Kamarchik, B. Fu, and J. M. Bowman, *J. Chem. Phys.*, **132**, 091102 (2010).

[192] J.C. Tully, *J. Chem. Phys.*, **93**, 1061 (1990).

[193] H. Sato, *Chem. Rev.*, **101**, 2687 (2001).

[194] G. E. Hall and P. L. Houston, *Ann. Rev. Phys. Chem.*, **40**, 375 (1989).

[195] M. Ahmed, D. S. Peterka, A. S. Bracker, O. S. Vasyuntinskii, and A. G. Suits, *J. Phys. Chem. A*, **110**, 4115 (1999).

[196] A. P. Clark, M. Brouard, F. Quadrini, and C. Vallance, *Phys. Chem. Chem. Phys.*, **8**, 5591 (2006).

[197] A. J. Alexander and R. N. Zare, *Acc. Chem. Res.*, **33**, 199 (2000).

[198] A. G. Smolin, O. S. Vasyuntinskii, G. G. Balint-Kurti, and A. Brown, *J. Phys. Chem. A*, **110**, 5371 (2006).

[199] A. G. Suits and O. S. Vasyuntinskii, *Chem. Rev.*, **108**, 3706 (2008).

[200] A. J. Alexander, Z. H. Kim, S. A. Kandel, R. N. Zare, T. P. Rakitzis, and Y. Asano, *J. Chem. Phys.*, **113**, 9022 (2000).

[201] P. A. Giguère and T. K. K. Srinivasan, *J. Mol. Spec.*, **66**, 168 (1977).

[202] R. H. Hunt, R. A. Leacock, C. W. Peters, and K. T. Hecht, *J. Chem. Phys.*, **42**, 1931 (1965).

[203] R. Block and L. Jansen, *J. Chem. Phys.*, **82**, 3322 (1985).

[204] K. H. Gericke, S. Klee, F. J. Comes, and R. N. Dixon, *J. Chem. Phys.*, **85**, 4463 (1986).

[205] M. Brouard, M. T. Martinez, C. J. Milne, J. P. Simons, and J. X. Wang, *Chem. Phys. Lett.*, **165**, 423 (1990).

[206] C. Chevaldonnet, H. Cardy, and A. Dargelos, *Chem. Phys.*, **102**, 55 (1986).

[207] R. Schinke, *J. Phys. Chem.*, **92**, 4015 (1988).

[208] R. Schinke and V. Staemmler, *Chem. Phys. Lett.*, **145**, 486 (1988).

[209] Z. T. Cai, D. H. Zhang, and J. Z. H. Zhang, *J. Chem. Phys.*, **100**, 5631 (1994).

[210] A. U. Grunewald, K. H. Gericke, and F. J. Comes, *J. Chem. Phys.*, **87**, 5709 (1987).

[211] J. August, M. Brouard, M. P. Docker, A. Hodgson, C. J. Milne, and J. P. Simons, *Ber. Bunsen-Ges. Phys. Chem.*, **92**, 264 (1988).

[212] K. H. Gericke, S. Klee, and F. J. Comes, *Ber. Bunsen-Ges. Phys. Chem.*, **92**, 429 (1988).

[213] M. P. Docker, A. Hodgson, and J. P. Simons, *Chem. Phys. Lett.*, **128**, 264 (1986).

[214] K. H. Gericke, S. Klee, and F. J. Comes, *J. Chem. Phys.*, **85**, 40 (1986).

[215] A. J. Alexander, *J. Chem. Phys.*, **118**, 6234 (2003).

[216] G. T. Drozd, A. Melnichuk, and N. M. Donahue, *J. Chem. Phys.*, **132**, 084304 (2010).

[217] L. D. A. Siebbeles, M. Glass-Maujean, O. S. Vasyutinskii, J. A. Beswick, and O. Roncero, *J. Chem. Phys.*, **100**, 3610 (1994).

[218] T. Perkins *Polarisation Effects in Diatomic Photofragments,* Part II thesis, University of Oxford, (2010).

[219] A. U. Grunewald, K. H. Gericke, and F. J. Comes, *J. Chem. Phys.*, **89**, 345 (1988).

[220] A. J. Alexander, *J. Chem. Phys.*, **123**, 194312 (2005).

[221] T. P. Rakitzis and R. N. Zare, *J. Chem. Phys.*, **110**, 3341 (1999).

[222] T. P. Rakitzis and A. J. Alexander, *J. Chem. Phys.*, **132**, 224310 (2010).

[223] T. P. Rakitzis, *J. Chem. Phys.*, **133**, 204301 (2010).

[224] Y. P. Chang, M. Brouard, R. Cireasa, T. Perkins, and S. A. Seamons, *Phys. Chem. Chem. Phys.*, **13**, 8213 (2011).

[225] G. Paterson, S. Marinakis, M. L. Costen, K. G. McKendrick, J. Kłos, and R. Toboła, *J. Chem. Phys.*, **128**, 021101 (2008).

[226] F. Quadrini *Dynamics of OH Generating Photochemical Reactions,* Part II thesis, University of Oxford, (2004).

[227] J. Luque and D. R. Crosley, *LIFBASE: Database and Spectral simulation Program (Version 1.5)*, SRI international Report MP99-009, 1999.

[228] LabVIEW 2012, Vision Development Module and Vision Acquisition Software; National Instruments.

[229] E. Hasselbrink, J. R. Waldeck, and R. N. Zare, *Chem. Phys.*, **126**, 191 (1988).

[230] K. O. Korovin, B. V. Picheyev, O. S. Vasyuntinskii, H. Valipour, and D. Zimmermann, *J. Chem. Phys.*, **112**, 2059 (2000).

[231] B. V. Picheyev, A. G. Smolin, and O. S. Vasyuntinskii, *J. Phys. Chem. A*, **101**, 7614 (1997).

[232] M. L. Costen and G. E. Hall, *Phys. Chem. Chem. Phys.*, **7**, 1408 (2005).

[233] R. Schinke, *Photodissociation Dynamics*, Cambridge University Press, 1993.

[234] J. S. Baskin and A. H. Zewail, *J. Phys. Chem.*, **93**, 5701 (1989).

[235] J. D. Barnwell, J. G. Loeser, and D. R. Herschbach, *J. Phys. Chem.*, **87**, 2781 (1983).

[236] S. E. Choi and R. B. Bernstein, *J. Chem. Phys.*, **85**, 150 (1986).

[237] R. N. Zare, *Ber. Bunsen-Ges. Phys. Chem.*, **86**, 422 (1982).

[238] G. Herzberg, *Molecular Spectra and Molecular Structure II: Infrared and Raman Specra of Polyatomic Molecules*, Kreiger Publishing, 2nd ed., 1989.

[239] R. Vasudev, R. N. Zare, and R. N. Dixon, *J. Chem. Phys.*, **80**, 4863 (1984).

[240] S. K. Lee, D. Townsend, O. S. Vasyutinskii, and A. G. Suits, *Phys. Chem. Chem. Phys.*, **7**, 1650 (2005).

[241] A. Morita and S. Kato, *J. Phys. Chem.*, **96**, 1067 (1992).

[242] A. F. Tuck, *J. Chem. Soc. Faraday. Trans.*, **73**, 689 (1976).

[243] D. L. Baulch, R. A. Cox, R. F. Hampson, J. A. Kett, J. Troe, and R. T. Watson, *J. Phys. Chem. Ref. Data 9.*, page 295 (1980).

[244] E. de Beer, M. P. Koopmans, C. A. de Lange, Y. Wang, and W. A. Chupka, *J. Chem. Phys.*, **94**, 7634 (1991).

[245] M. E. Greenslade, M. I. Lester, D. C̃. Radenović, A. J. A. van Roij, and D. H. Parker, *J. Chem. Phys.*, **123**, 074309 (2005).

[246] J. M. Beames, F. Liu, M. I. Lester, and C. Murray, *J. Chem. Phys.*, **134**, 241102 (2011).

[247] M. Collard, P. Kerwin, and A. Hodgson, *Chem. Phys. Lett.*, **179**, 422 (1991).

[248] C. McRaven, J. Alnis, B. Furneaux, and N. Shafer-Ray, *J. Phys. Chem. A*, **107**, 7138 (2003).

[249] J. D. Coe, B. G. Levine, and T. J. Martínez, *J. Phys. Chem. A*, **111**, 11302 (2007).

[250] J. D. Coe, B. G. Levine, and T. J. Martínez, *J. Phys. Chem. A*, **113**, 13656 (2009).

[251] H. J. Werner, *Mol. Phys.*, **89**, 645 (1996).

[252] T. H. Dunning Jr., *J. Chem. Phys.*, **90**, 1007 (1989).

[253] R. N. Diffenderfer and D. R. Yarkony, *J. Phys. Chem.*, **86**, 5098 (1982).

[254] H. J. Werner and P. J. Knowles, *J. Chem. Phys.*, **89**, 5803 (1985).

[255] Z. Xie, B. J. Braams, and J. M. Bowman, *J. Chem. Phys.*, **122**, 224307 (2005).

[256] B. J. Braams and J. M. Bowman, *Int. Rev. Phys. Chem.*, **28**, 577 (2009).

[257] M. Yang, D. H. Zhang, M. A. Collins, and S. Y. Lee, *J. Chem. Phys.*, **115**, 174 (2001).

[258] K. P. Huber and G. Herzberg, *Molecular Spectra and Molecular Structure IV: Constants of Diatomic Molecules*, Van Nostrand Reinhold, Princeton, 1979.

[259] J. H. Lehman, L. P. Dempsey, M. I. Lester, B. Fu, E. Kamarchik, and J. M. Bowman, *J. Chem. Phys.*, **133**, 164307 (2010).

[260] M. W. Todd, D. T. Anderson, and M. I. Lester, *J. Phys. Chem. A*, **105**, 10031 (2001).

[261] H. Chadwick, M. Brouard, T. Perkins, and F. J. Aoiz, *Int. Rev. Phy. Chem.*, **33**, 79 (2014).

[262] F. J. Aoiz, V. J. Herrero, and V. S. Rábanos, *J. Chem. Phys.*, **94**, 7991 (1991).

[263] F. J. Aoiz, V. J. Herrero, and V. S. Rábanos, *J. Chem. Phys.*, **97**, 7423 (1992).

[264] M. Brouard, H. Chadwick, Y. P. Chang, R. Cireasa, C. J. Eyles, A. La Via, N. Screen, F. J. Aoiz, and J. Kłos, *J. Chem. Phys.*, **131**, 104307 (2009).

[265] M. Karplus, R. N. Porter, and R. D. Sharma, *J. Chem. Phys.*, **43**, 3259 (1965).

[266] F. J. Aoiz, J. E. Verdasco, V. J. Herrero, V. S. Rábanos, and M. A. Alexander, *J. Chem. Phys.*, **119**, 5860 (2003).

[267] R. A. Loomis and M. I. Lester, *Ann. Rev. Phys. Chem.*, **48**, 643 (1997).

[268] N. M. J. Woodhouse, *Introduction to Analytical Dynamics*, Springer, 1987.

[269] E. Wigner, *Z. Phys. Chem. B*, **23**, 19 (1933).

[270] E. Sartori, M. Ruzzi, R. G. Lawler, and N. J. Turro, *J. Am. Chem. Soc.*, **130**, 12752 (2008).

[271] B. F. Minaev and H. Agren, *J. Phys. Chem.*, **99**, 8936 (1995).

[272] R. D. Levine and R. B. Bernstein, *Molecular Reaction Dynamics and Chemical Reactivity*, Oxford University Press, 1987.

[273] G. C. Corey and F. R. McCourt, *J. Phys. Chem.*, **87**, 2723 (1983).

[274] M. H. Alexander, J. E. Smedley, and G. C. Corey, *J. Chem. Phys.*, **84**, 3049 (1986).

[275] J. G. Muga and R. D. Levine, *Chem. Phys. Lett.*, **162**, 7 (1989).

[276] J. C. Muga and R. D. Levine, *J. Chem. Soc. Faraday. Trans.*, **86**, 1669 (1990).

[277] A. Schiffman, D. D. Nelson Jr., and D. J. Nesbitt, *J. Chem. Phys.*, **98**, 6935 (1993).

[278] R. D. Kenner, F. Rohrer, T. Papenbrock, and F. Stuhl, *J. Phys. Chem.*, **90**, 1294 (1986).

[279] M. Baba, M. Brouard, S. P. Rayner, and J. P. Simons, *Chem. Phys. Lett.*, **220**, 411 (1994).

[280] C. H. Greene and R. N. Zare, *Ann. Rev. Phys. Chem.*, **33**, 119 (1982).

[281] L. Rubio-Lago, D. Sofikitis, A. Koubenakis, and T. P. Rakitzis, *Phys. Rev. A*, **74**, 042503 (2006).

[282] A. Green *Zeeman Quantum Beat Spectroscopy As A Tool For Studies Of Collisional Depolarisation,* Part II thesis, University of Oxford, (2007).

[283] W. H. Press, B. P. Flannery, S. A. Teukolsky, and W. T. Vetterling, *Numerical Recipes*, Cambridge University Press, 1986.

[284] H. M. Cartwright, *Applications of Artificial Intelligence in Chemistry*, number 11 in Oxford Chemistry Primers, Oxford University Press, 1993.

[285] I. J. Wysong, J. B. Jeffries, and D. R. Crosley, *J. Chem. Phys.*, **92**, 5218 (1990).

[286] J. Kłos, Personal Communication.

[287] P. Hogan and D. D. Davis, *J. Chem. Phys.*, **62**, 4574 (1975).

[288] P. Hogan and D. D. Davis, *J. Chem. Phys.*, **64**, 3901 (1976).

[289] R. K. Lengel and D. R. Crosley, *J. Chem. Phys.*, **64**, 3900 (1976).

[290] J. Dillon and D. R. Yarkony, *J. Phys. Chem. A*, **117**, 7344 (2013).

[291] J. Dillon and D. R. Yarkony, *J. Chem. Phys.*, **139**, 064314 (2013).

[292] J. C. Tully, *Int. J. Quantum. Chem.*, **25**, 299 (1991).

[293] J. C. Tully and R. K. Preston, *J. Chem. Phys.*, **55**, 562 (1971).

[294] L. P. Dempsey, T. D. Sechler, C. Murray, M. I. Lester, and S. Matsika, *J. Chem. Phys.*, **130**, 104307 (2009).

[295] J. H. Lehman, M. I. Lester, and D. R. Yarkony, *J. Chem. Phys.*, **137**, 094312 (2012).

[296] J. Burris, J. Butler, T. McGee, and W. Heaps, *Chem. Phys.*, **151**, 233 (1991).

[297] A. Jörg, U. Meier, and K. KohseHöinghaus, *J. Chem. Phys.*, **93**, 6453 (1990).

[298] R. L. Schwartz, D. T. Anderson, M. W. Todd, and M. I. Lester, *Chem. Phys. Lett.*, **273**, 18 (1997).

[299] M. D. Wheeler, D. T. Anderson, M. W. Todd, M. I. Lester, P. J. Krause, and D. C. Clary, *Mol. Phys.*, **97**, 151 (1999).

[300] L. Bonnet and J. C. Rayez, *Chem. Phys. Lett.*, **397**, 106 (2004).

[301] L. Bañares, F. J. Aoiz, P. Honvault, B. Bussery-Honvault, and J. M. Launay, *J. Chem. Phys.*, **118**, 565 (2003).

[302] L. Bonnet and J. C. Rayez, *Chem. Phys. Lett.*, **277**, 183 (1997).

[303] L. Bonnet and J. Espinosa-Garcia, *J. Chem. Phys.*, **133**, 164108 (2010).

[304] T. Xie, J. M. Bowman, J. W. Duff, M. Braunstein, and B. Ramachandran, *J. Chem. Phys.*, **122**, 014301 (2005).

[305] J. F. Castillo, F. J. Aoiz, and L. Bañares, *J. Chem. Phys.*, **125**, 124316 (2006).

[306] J. Aoiz, Personal Communication.

[307] A. J. C. Varandas, *Chem. Phys. Lett.*, **439**, 386 (2007).

[308] R. Conte, B. Fu, E. Kamarchik, and J. M. Bowman, *J. Chem. Phys.*, **139**, 044104 (2013).

[309] H. Cramér, *Mathematical Methods of Statistics*, Asia Publishing House, 1999.

[310] HIBRIDON is a package of programs for the time-independent quantum treatment of inelastic collisions and photodissociation written by M. H. Alexander, D. Manolopoulos, H.-J. Werner, and B. Follmeg, with contributions by P. F. Vohralik, D. Lemoine, G. Corey, R. Gordon, B. Johnson, T. Orlikowski, A. Berning, A. D. Esposti, C. Rist, P. Dagdigian, B. Pouilly, G. van der Sanden, M. Yang, F. de Weerd, S. Gregurick, and J. Kłos.

[311] D. E. Manolopoulos, *J. Chem. Phys.*, **85**, 6425 (1986).

[312] M. H. Alexander and D. E. Manolopoulos, *J. Chem. Phys.*, **86**, 2044 (1987).

[313] G. McCrudden *Non-adiabatic effects on the Collision Dynamics of OH(A),* Part II thesis, University of Oxford, (2013).

[314] The MOLSCAT computer code, version 14, by J. M. Hutson and S. Green (Collaborative Computational Project No. 6 of the Science and Engineering Research Council, United Kingdom, 1994).

[315] A. Offer and D. R. Flower, *J. Phys. B*, **22**, L439 (1989).

[316] T. Perkins, D. Herráez-Aguilar, G. McCrudden, J. Kłos, F. J. Aoiz, and M. Brouard, *J. Chem. Phys.*, **142**, 144307 (2015).

[317] L. R. Williams and D. R. Crosley, *J. Chem. Phys.*, **104**, 6507 (1996).

[318] R. K. Lengel and D. R. Crosley, *J. Chem. Phys.*, **68**, 5309 (1978).

[319] J. J. Kay, J. D. Steill, J. Kłos, G. Paterson, M. L. Costen, K. E. Stecker, K. G. McKendrick, M. H. Alexander, and D. W. Chandler, *Mol. Phys.*, **110**, 1693 (2012).

[320] J. J. Kay, G. Paterson, M. L. Costen, K. E. Strecker, K. G. McKendrick, and D. W. Chandler, *J. Chem. Phys.*, **134**, 091101 (2011).

[321] J. D. Steill, J. J. Kay, G. Paterson, T. R. Sharples, J. Kłos, M. L. Costen, K. E. Strecker, K. G. McKendrick, M. H. Alexander, and D. W. Chandler, *J. Phys Chem. A*, **117**, 8163 (2013).

[322] G. Sarma, S. Marinakis, J. J. ter Meulen, and D. H. Parker, *Nature Chemistry*, **4**, 985 (2012).

[323] P. Jansen, D. W. Chandler, and K. E. Strecker, *Rev. Sci. Instrum.*, **80**, 083105 (2009).

[324] B. Yan, P. F. H. Claus, B. G. M. van Oorschot, L. Gerritsen, A. T. J. B. Eppink, S. Y. T. van der Meerakker, and D. H. Parker, *Rev. Sci. Instrum.*, **84**, 023102 (2013).

[325] S. Greaves, Personal Communication.

[326] G. McCrudden *In Preparation,* DPhil thesis, University of Oxford, (2017).

[327] A. T. J. B. Eppink and D. H. Parker, *Rev. Sci. Instrum.*, **68**, 3477 (1997).

[328] Inc. Scientific Instrument Services, *SIMION*, 2006, `http://simion.com`.

[329] M. Hillenkamp, S. Keinan, and U. Even, *J. Chem. Phys.*, **118**, 8699 (2003).

[330] A. Sugita, M. Mashino, K. Kawasaki, Y. Matsumi, R. Bersohn, G. Trott-Kriegeskorte, and G. Karl-Heinz, *J. Chem. Phys.*, **112**, 7095 (2000).

[331] Y. Sato, Y. Matsumi, M. Kawasaki, K. Tsukiyama, and R. Bersohn, *J. Phys. Chem.*, **99**, 16307 (1995).

[332] A. J. Alexander, Z. H. Kim, and R. N. Zare, *J. Chem. Phys.*, **118**, 10566 (2003).

[333] B. Buijsse, W. J. van der Zande, A. T. J. B. Eppink, D. H. Parker, B. R. Lewis, and S. W. Gibson, *J. Chem. Phys.*, **108**, 7229 (1998).

[334] I. Wilkinson M. P. de Miranda and B. J. Whitaker, *J. Chem. Phys.*, **131**, 054308 (2009).

[335] I. Wilkinson and B. J. Whitaker, *Annu. Rep. Prog. Chem., Sect. C*, **106**, 274 (2010).

[336] A. A. Dixit, P. J. Pisano, and P. L. Houston, *J. Phys. Chem. A*, **105**, 14853 (2001).

[337] C. J. Eyles, M. Brouard, C. H. Yang, J. Kłos, F. J. Aoiz, A. Gijsbertsen, A. E. Wiskerke, and S. Stolte, *Nature Chemistry*, **3**, 597 (2011).